Geofluids

CO2 Geological Storage and Enhanced Oil/Gas Recovery in Unconventional Reservoirs

Lead Guest Editor: Shuyang Liu
Guest Editors: Bin Wang and Kai Zhang

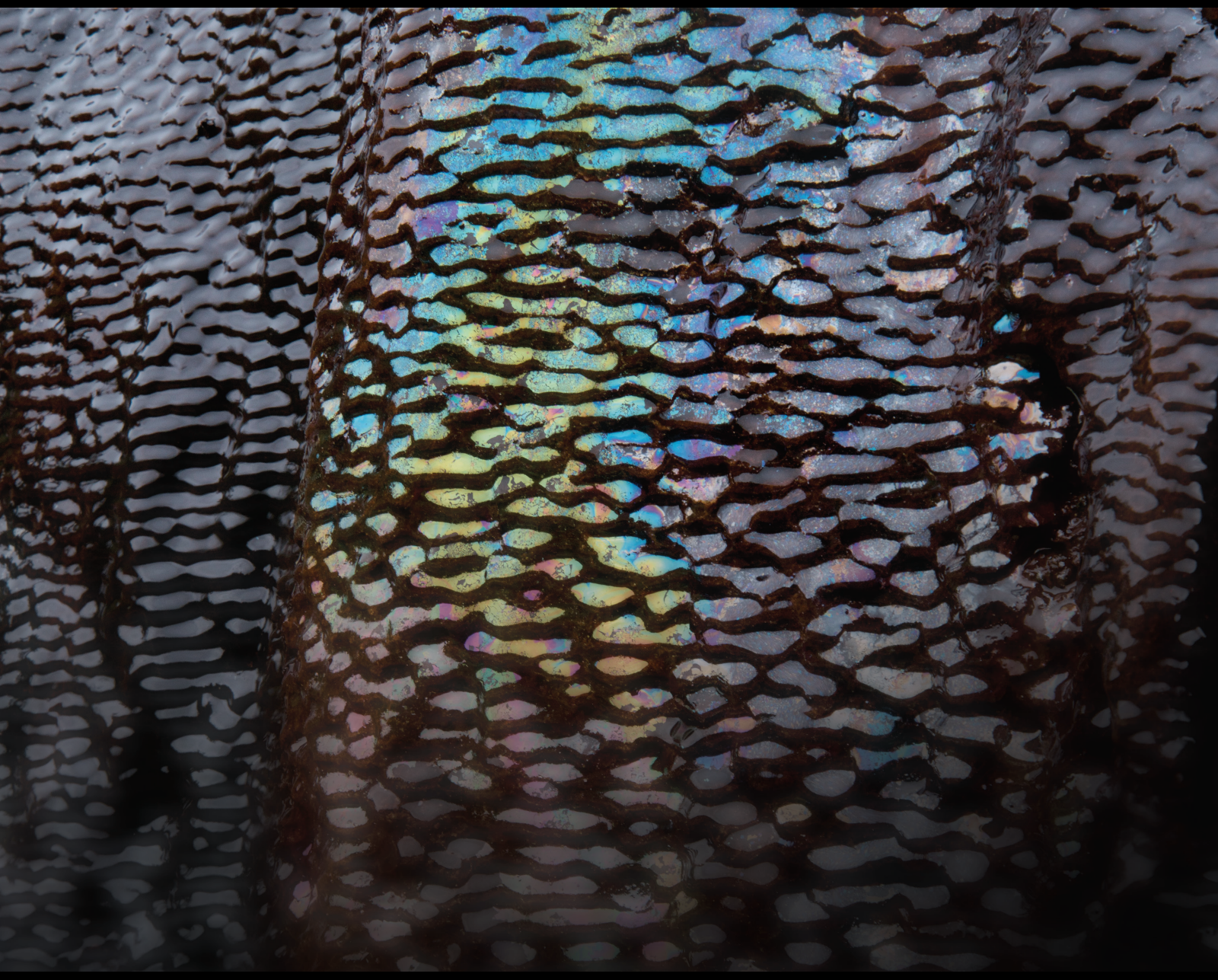

CO2 Geological Storage and Enhanced Oil/Gas Recovery in Unconventional Reservoirs

Geofluids

CO2 Geological Storage and Enhanced Oil/Gas Recovery in Unconventional Reservoirs

Lead Guest Editor: Shuyang Liu
Guest Editors: Bin Wang and Kai Zhang

Copyright © 2022 Hindawi Limited. All rights reserved.

This is a special issue published in “Geofluids.” All articles are open access articles distributed under the Creative Commons Attribution License, which permits unrestricted use, distribution, and reproduction in any medium, provided the original work is properly cited.

Chief Editor

Umberta Tinivella, Italy

Associate Editors

Paolo Fulignati, Italy
Huazhou Li, Canada
Stefano Lo Russo, Italy
Julie K. Pearce, Australia

Academic Editors

Basim Abu-Jdayil, United Arab Emirates
Hasan Alsaedi, USA
Carmine Apollaro, Italy
Baojun Bai, USA
Marino Domenico Barberio, Italy
Andrea Brogi, Italy
Shengnan Nancy Chen, Canada
Tao Chen, Germany
Jianwei Cheng, China
Paola Cianfarra, Italy
Daniele Cinti, Italy
Timothy S. Collett, USA
Nicoló Colombani, Italy
Mercè Corbella, Spain
David Cruset, Spain
Jun Dong, China
Henrik Drake, Sweden
Farhad Ehya, Iran
Lionel Esteban, Australia
Zhiqiang Fan, China
Francesco Frondini, Italy
Ilaria Fuoco, Italy
Paola Gattinoni, Italy
Amin Gholami, Iran
Michela Giustiniani, Italy
Naser Golsanami, China
Fausto Grassa, Italy
Jianyong Han, China
Chris Harris, South Africa
Liang He, China
Sampath Hewage, Sri Lanka
Jian Hou, China
Guozhong Hu, China
Lanxiao Hu, China
Francesco Italiano, Italy
Azizollah Khormali, Iran
Hailing Kong, China
Karsten Kroeger, New Zealand
Cornelius Langenbruch, USA
Peter Leary, USA
Guangquan Li, China
Qingchao Li, China
Qibin Lin, China
Marcello Liotta, Italy
Shuyang Liu, China
Yong Liu, China
Yueliang Liu, China
Constantinos Loupasakis, Greece
Shouqing Lu, China
Tian-Shou Ma, China
Judit Mádl-Szonyi, Hungary
Paolo Madonia, Italy
Fabien Magri, Germany
Micòl Mastrocicco, Italy
Agnes Mazot, New Zealand
Yuan Mei, Australia
Evgeniy M. Myshakin, USA
Muhammad Tayyab Naseer, Pakistan
Michele Paternoster, Italy
Mandadige S. A. Perera, Australia
Marco Petitta, Italy
Chao-Zhong Qin, China
Qingdong Qu, Australia
Reza Rezaee, Australia
Eliahu Rosenthal, Israel
Gernot Rother, USA
Edgar Santoyo, Mexico
Mohammad Sarmadivaleh, Australia
Venkatramanan Senapathi, India
Amin Shokrollahi, Australia
Rosa Sinisi, Italy
Zhao-Jie Song, China
Ondra Sracek, Czech Republic
Andri Stefansson, Iceland
Bailu Teng, China
Tivadar M. Tóth, Hungary
Orlando Vaselli, Italy
Benfeng Wang, China
Hetang Wang, China
Wensong Wang, China
Zhiyuan Wang, China
Ruud Weijermars, Saudi Arabia

Bisheng Wu, China
Da-yang Xuan, China
Yi Xue, China
HE YONGLIANG, China
Fan Yang, China
Zhenyuan Yin, China
Sohrab Zendehboudi, Canada
Zhixiong Zeng, Hong Kong
Yuanyuan Zha, China
Keni Zhang, China
Mingjie Zhang, China
Rongqing Zhang, China
Xianwei Zhang, China
Ye Zhang, USA
Zetian Zhang, China
Ling-Li Zhou, Ireland
Yingfang Zhou, United Kingdom
Daoyi Zhu, China
Quanle Zou, China
Martina Zucchi, Italy

Contents

Hindawi
Geofluids
Volume 2022, Article ID 8215223, 9 pages
https://doi.org/10.1155/2022/8215223

Research Article

Well Pattern and Well Spacing Optimization of Large Volume Water Injection in a Low-Permeability Reservoir with Pressure Sensitivity

Jie Zhan,[1,2] **Yafei Tian**,[3] **Chao Fan**,[1,2] **Xianlin Ma**,[1,2] **Ren-Shi Nie**,[3] **Dongqi Ji**,[4,5] **Teng Li**,[1,2] **and Hongyan Yu**[6]

[1]*School of Petroleum Engineering, Xi'an Shiyou University, Xi'an 710065, China*
[2]*Engineering Research Center of Development and Management for Low to Ultra-Low Permeability Oil & Gas Reservoirs in West China, Ministry of Education, Xi'an Shiyou University, Xi'an 710065, China*
[3]*State Key Laboratory of Oil & Gas Reservoir Geology and Exploitation, Southwest Petroleum University, Chengdu 610500, China*
[4]*Research Institute of Petroleum Exploration and Development, PetroChina, Beijing 100083, China*
[5]*School of Energy Resources, China University of Geosciences (Beijing), Beijing 100083, China*
[6]*State Key Laboratory of Continental Dynamics, Department of Geology, Northwest University, Xi'an 710065, China*

Correspondence should be addressed to Jie Zhan; zhanjie@xsyu.edu.cn and Xianlin Ma; xianlinm@126.com

Received 20 June 2022; Accepted 30 July 2022; Published 19 August 2022

Academic Editor: Shuyang Liu

Copyright © 2022 Jie Zhan et al. This is an open access article distributed under the Creative Commons Attribution License, which permits unrestricted use, distribution, and reproduction in any medium, provided the original work is properly cited.

Even with the fractured wells, the primary oil recovery of low-permeability reservoirs is still poor in Block X of Shengli Oilfield. To further enhance the oil recovery, water is injected into the reservoir. Different from the conventional injection scheme, the maximum daily injection rate of the proposed scheme by Shengli Oilfield reaches 2000 m^3, and the average daily injection rate is around 1500 m^3. Thus, the conventional well spacing of certain well pattern is not suitable for the novel injection scheme. In the paper, the optimal well pattern and well spacing for the large volume water injection scheme to develop a pressure-sensitive low-permeability reservoir is investigated. Firstly, the CMG is employed to build the basic reservoir model developed by fractured vertical wells. To finely depict the pressure sensitivity, the dilation-recompaction geomechanical model is introduced to couple with the basic reservoir model. Based on the established coupled model, the optimal well spacing for the inverted 5-spot well pattern and the inverted 9-spot well pattern is investigated with a total of 80 sets of numerical experiments. The numerical experiments indicate that the optimal well spacing for the inverted 5-spot well pattern is 850 m/350 m and the optimal well spacing for the inverted 9-spot well pattern is 550 m/450 m. To further screen the well pattern, the normalized index of oil production per unit area of each well pattern is proposed. And it is found that the oil production per unit area of the inverted 5-spot well pattern is higher than the inverted 9-spot well pattern. For the reservoir developed with fractured vertical wells coupled with large volume water injection, compared with the inverted 9-spot well pattern, the inverted 5-spot well pattern is better, and the corresponding optimal well spacing is 850 m/350 m. The paper proposes an efficient simulation and optimization workflow for the development of pressure-sensitive low-permeability reservoirs with fractured vertical wells coupled with large volume water injection, providing practical guidance for the efficient and sustainable development of pressure-sensitive low-permeability reservoirs.

1. Introduction

There are abundant low-permeability reservoirs in China and worldwide, which have become a key component in the global energy system. For instance, 46% of China's oil and gas resources are of low quality, which are mostly low-permeability reservoirs [1–4]. Due to the nature of the low-permeability reservoir, the reservoir does not perform well if the EOR/EGR technology, such as fracking and acidizing, has not been applied. Over the years, the technology of

developing low-permeability reservoirs has been significantly improved. But water injection is still the primary method to improve the performance of low-permeability reservoirs [5–8]. Shengli Oilfield proposes an innovative waterflooding scheme with large volume injection to further improve the low-permeability reservoir performance in Block X, which has been depleted for years with low productivity [9]. There are two factors accounting for the improvement of reservoir performance. On one hand, the large volume injection will increase the swept volume. On the other hand, the residual oil located in the region with high seepage resistance can be further mobilized due to the established high-pressure driven system induced by the large volume of injected water so that the displacement efficiency can be further improved. To some extent, the reservoir is rejuvenated due to the novel injection scheme. Different from the conventional injection scheme, the maximum daily injection rate of the proposed scheme by Shengli Oilfield reaches 2000 m^3, and the average daily injection rate is around 1500 m^3. Therefore, the conventional well spacing of certain well pattern is not suitable for the novel scheme, large volume water injection coupled with fractured vertical producers. The inverted 5-spot well pattern and the inverted 9-spot well pattern are widely implemented in the field. Meanwhile, the optimal well pattern and well spacing under different field conditions have been investigated based on machine learning (data-driven modeling) and numerical simulation [10–13]. But few studies have been reported on the optimization of well pattern and well spacing of the novel scheme proposed by Shengli Oilfield to develop the pressure-sensitive low-permeability. In the paper, we build up the coupled reservoir models to represent different scenarios (different well spacing for both the inverted 5-spot well pattern and inverted 9-spot well pattern of the novel scheme to develop a pressure-sensitive low-permeability reservoir) via the advanced reservoir simulator, CMG. With a total of 80 sets of numerical experiments, the optimal well spacing for both the inverted 5-spot well pattern and inverted 9-spot well pattern of the novel scheme is quantified. Then, with the proposed normalized index of oil production per unit area of each well pattern, the optimal well pattern between the inverted 5-spot well pattern and inverted 9-spot well pattern for the novel scheme is studied, as shown in the following flowchart (Figure 1). The study proposes an efficient simulation and optimization workflow for the development of pressure-sensitive low-permeability reservoirs with fractured vertical wells coupled with large volume water injection. With the methodology presented in the study, not only the field test can be further optimized, leading to more efficient and sustainable development, but also the novel scheme proposed by Shengli Oilfield can be promoted and widely applied in China and worldwide.

2. Simulation Methodology and Integrated Workflow

The governing equations of the numerical model are the mass balance equations, including accumulation term and convection term and sink/source term [14, 15]. Darcy's law, which states that fluid flow rate is directly proportional to the pressure gradient, is applied to the fluid flow in the matrix of the model. As to the fluid flow within the hydraulic fracture, the Forchheimer model with the non-Darcy coefficient is implemented to simulate a turbulent flow, accounting for the inertial effects [16–18]. Meanwhile, local grid refinement with logarithmic spacing, discretizing the reservoir to a finer degree region around hydraulic fractures and more coarsely further away from the hydraulic fractures, is coupled with the Forchheimer model to accurately depict the detailed transient fluid flow around the hydraulic fractures [19–21]. To obtain the fluid properties, the Peng-Robinson equation of state is employed. And the oil-water relative permeability of the model is generated by the analytical correlation using the endpoint data [14].

To meet the needs of finely simulating the dynamic evolution of reservoir properties for the pressure-sensitive low-permeability reservoirs, the dilation-recompaction geomechanical model is introduced to couple with the basic reservoir model. Compared with conventional flow-geomechanical coupling models [22], where complex coupling schemes, expensive computational cost, and massive input data, such as rock mechanical data and in situ stress data, get involved, the methodology employed in the study characterizes the dominating mechanism of the physical process while keeping the modeling and computational cost low. The methodology has been applied and validated by previous work to both accurately and efficiently simulate the process [9, 23–26].

The dilation-recompaction model finely depicts the relation between the porosity and reservoir pressure as a piecewise and path-dependent function, illustrated in Figure 2 [9, 27–29]. Different value is given to the compressibility according to the range of reservoir pressure. For instance, small compressibility is given to the line segment *ab*. With the gentle slope, from point *a* to point *b*, the rock experiences an elastic small change of porosity due to the change of pressure, which is reversible. As to the steep line segment *bc*, big compressibility is assigned, leading to the intense change of porosity induced by reservoir pressure, which indicates that the reservoir undergoes irreversible dilation, usually accompanied by the opening of fissures. If the pressure drops at some point during the dilation phase, two phases of compaction will occur. If the pressure remains above the recompaction pressure (P_R), reversible elastic compaction occurs in the reservoir. If the pressure continues to drop until it is below the recompaction pressure (P_R), the reservoir enters the irreversible recompaction phase, which has a larger slope than the elastic compaction. In other words, significant compaction occurs in the reservoir during the recompaction phase. The maximum porosity (ϕ_{max}) in the dilation-recompaction model is correlated with the r_{at}, which is the maximum proportional increase allowed in porosity. The residual dilation fraction (f_r) accounts for the proportion of the total dilation which is permanent and irreversible. If the lower limit of 0 is assigned to the residual dilation fraction, the increase in pore volume as a result of dilation can be fully removed. Conversely, the

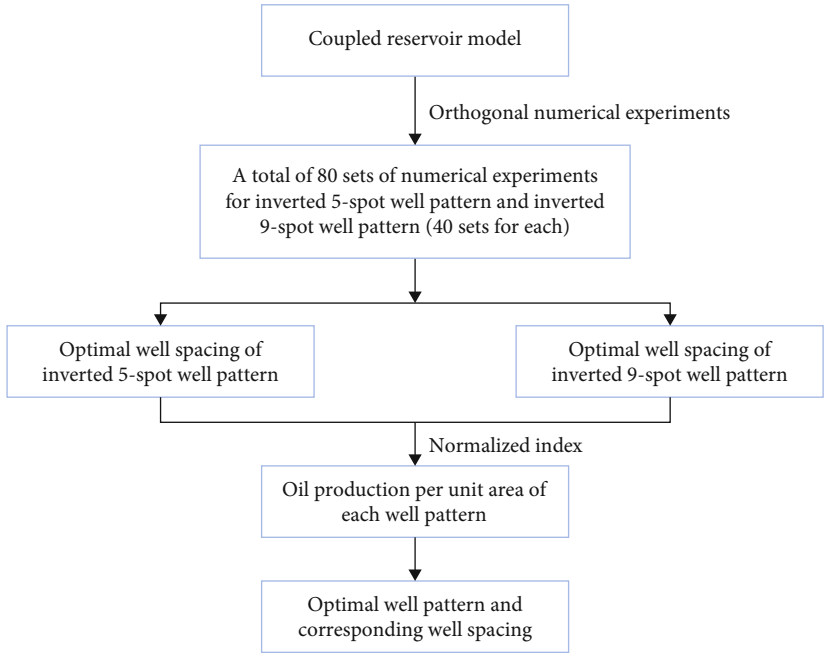

Figure 1: Flowchart of the study.

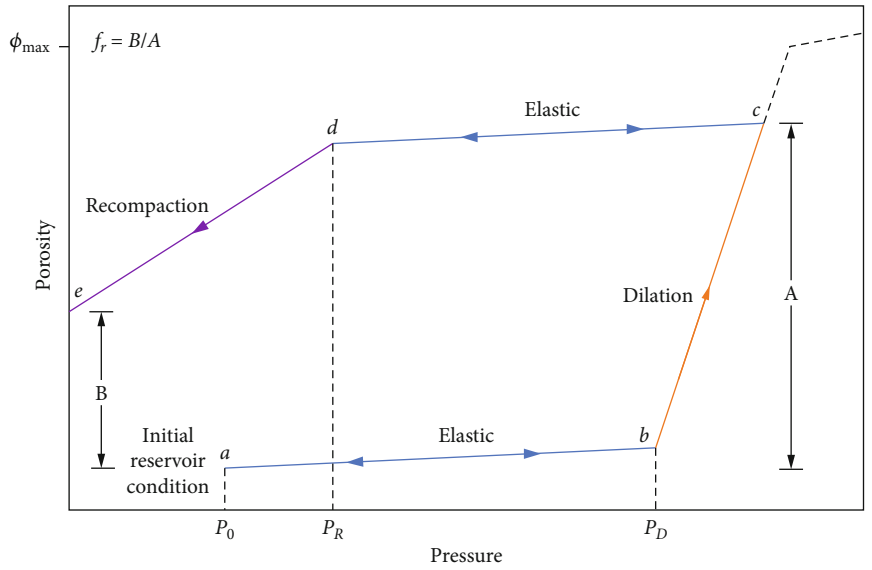

Figure 2: Dilation-recompaction model [9].

increase in pore volume induced by dilation is permanently preserved if the residual dilation fraction takes its maximum value of 1.

There is a correlation between porosity and permeability. Since the porosity evolves with the pressure, so does the permeability, which is also the feature of the low-permeability reservoir with pressure sensitivity [30, 31]. The analytical correlations for the dynamic porosity and permeability are as follows:

$$\phi = \phi_r e^{[c(P-P_R)]}, \tag{1}$$

where c is the compressibility; P_r is reference pressure; and ϕ_r is the porosity at the reference pressure.

$$K = K_0 e^{[K_{MUL}(\phi-\phi_0)/(1-\phi_0)]}, \tag{2}$$

where K_0 is the original permeability; K_{MUL} is a user-defined permeability multiplier; and ϕ_0 is the original porosity.

Based on the above simulation methodology, orthogonal numerical experiments can be conducted to obtain the optimal well spacing of each well pattern. Comparison between two types of objects (different well patterns) cannot be performed directly by the numerical simulation. To obtain the

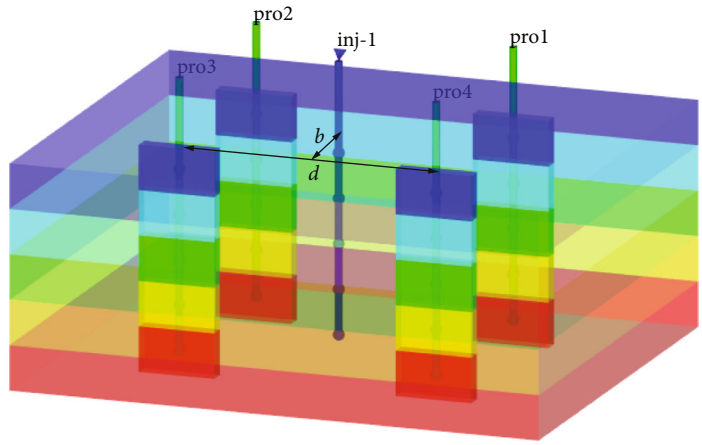

Figure 3: Three-dimensional reservoir model of inverted 5-spot well pattern.

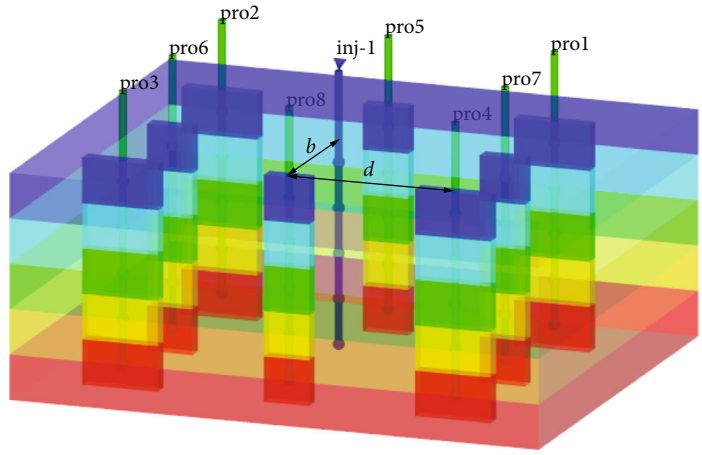

Figure 4: Three-dimensional reservoir model of inverted 9-spot well pattern.

optimal well pattern, the analytical method of reservoir engineering is introduced to couple with the numerical simulation to normalize the performance of each well pattern with optimal well spacing. That is why the normalized index is developed. The process of the analytical calculation of the normalized index is as follows. Firstly, based on the reservoir engineering method, the actual cumulative oil production of each well pattern can be determined with different weighting factors assigned to the corner well and side well, indicating the actual contribution of each well to the group [32]. Then, with the optimal spacing of each well pattern, the corresponding area of each well pattern can be acquired, which is also the area controlled by the injector. Thus, the proposed normalized index of oil production of each well pattern over the corresponding area is quantified so that the optimal well pattern can be determined. With the integrated workflow, combining the analytical method of reservoir engineering with numerical simulation, the well pattern and well spacing can be optimized simultaneously. The detailed analytical calculation will be presented in the results and discussion part.

3. Reservoir Model

Based on the CMG, the reservoir model is developed with the data of Block X. The dimensions of the numerical model are 1750 m × 1450 m × 8 m, corresponding to the length, width, and thickness of the reservoir, respectively. For the inverted 5-spot well pattern, there are one vertical injector and four vertical fractured producers, as shown in Figure 3. For the inverted 9-spot well pattern, there are one vertical injector and eight vertical fractured producers, as shown in Figure 4. d stands for the distance between wells. b stands for the distance between each row. All the wells are perforated from the top to the bottom of the reservoir. The half-length of the hydraulic fracture of the corner producer is 125 m, and the half-length of the hydraulic fracture of the side producer is 75 m. The conductivity of hydraulic fracture is 3.05 mD·m. And the cumulative water injection is 6.0×10^4 m^3. The detailed injection scheme is shown in Figure 5, which is the constraint for the injector of the numerical model. The producer is operated with a minimum bottom-hole pressure of 200 kPa, to fully harness the

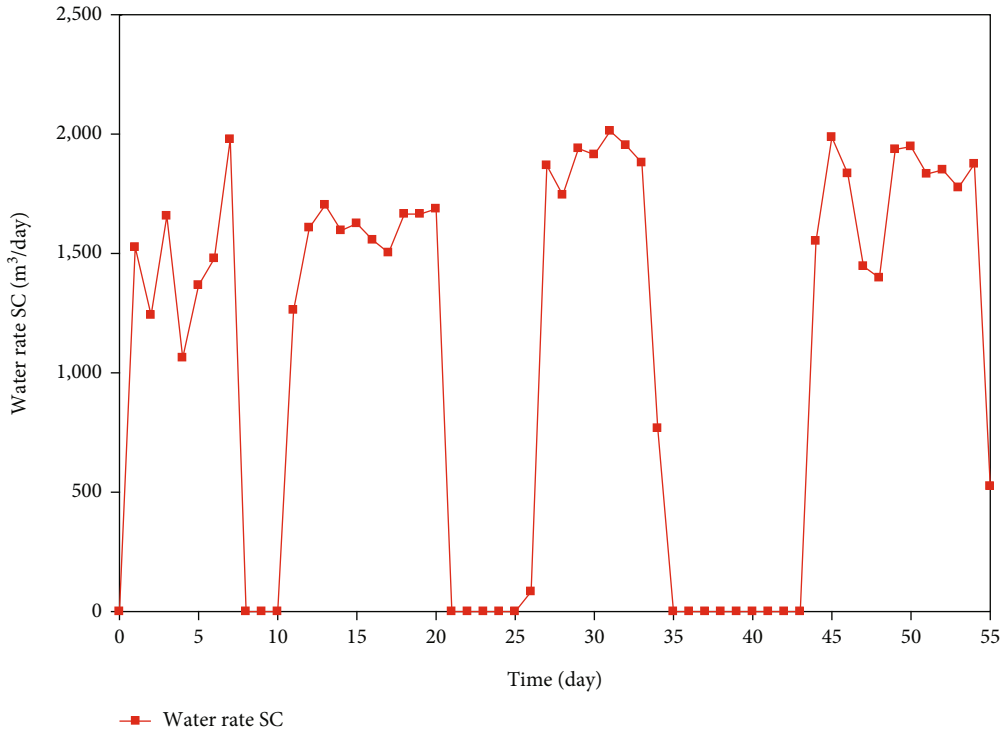

Figure 5: Daily water injection rate.

Table 1: List of model parameters.

Parameters	Value	Unit
Model dimensions	1750 × 1450 × 8	m
Thickness	8	m
Depth	3200	m
Porosity	0.13	/
Permeability	5	mD
Initial reservoir pressure	28	MPa
Reservoir temperature	123	˚C
Hydraulic fracture conductivity	3.05	mD·m
Half-length of hydraulic fracture(corner well)	125	m
Half-length of hydraulic fracture(side well)	75	m

formation energy. Due to the large volume of injected water in each slug within a few days, the bottom-hole pressure is built up rapidly, leading to the increase of the injection pressure. To stabilize the injection pressure at the wellhead within the safe operation limit, the injection is terminated for several days between each slug to facilitate the pressure diffusion outward from the injection spot. Instead of continuous injection, the water slug injection mode is employed in the field. The specific parameters used in the models are listed in Tables 1 and 2.

4. Results and Discussion

Based on the above established model, 40 simulation scenarios are developed with different well spacing for each well pattern, respectively, as shown in Tables 3 and 4. There is a total of 80 sets of numerical experiments. The simulation outcomes are illustrated in Figures 6 and 7, generated with MATLAB.

If the well spacing is too small, it will lead to higher water production with lower oil production. If the well spacing is too large, the supplemental energy by the injection cannot be utilized efficiently to improve the reservoir performance. Based on the cumulative oil production of the well group with different well spacing, the optimal well spacing for the inverted 5-spot well pattern is 850 m/350 m, and the optimal well spacing for the inverted 9-spot well pattern is 550 m/450 m, as shown in the following figures.

With the above optimal well spacing of each well pattern, the optimal well pattern will be determined between the

Table 2: Parameters used in the dilation-recompaction model.

Parameters	Value	Unit
Compressibility coefficient (C_{ab})	9.5×10^{-6}	1/kPa
Dilation compressibility coefficient (C_{bc})	8×10^{-4}	1/kPa
Residual dilation fraction (f_r)	0.1	/
Recompaction pressure (P_R)	30	MPa
Maximum allowed proportional increase in porosity (r_{at})	1.3	/
Dilation pressure (P_D)	50	MPa
Initial reservoir pressure (P_0)	28	MPa
Permeability multipliers (I/J/K) (K_{MUL})	50	/

Table 3: Orthogonal experiment design of well spacing (inverted 5-spot well pattern).

b (m)	d (m)							
	600	650	700	750	800	850	900	950
250	250 × 600	250 × 650	250 × 700	250 × 750	250 × 800	250 × 850	250 × 900	250 × 950
300	300 × 600	300 × 650	300 × 700	300 × 750	300 × 800	300 × 850	300 × 900	300 × 950
350	350 × 600	350 × 650	350 × 700	350 × 750	350 × 800	350 × 850	350 × 900	350 × 950
400	400 × 600	400 × 650	400 × 700	400 × 750	400 × 800	400 × 850	400 × 900	400 × 950
450	450 × 600	450 × 650	450 × 700	450 × 750	450 × 800	450 × 850	450 × 900	450 × 950

Table 4: Orthogonal experiment design of well spacing (inverted 9-spot well pattern).

b (m)	d (m)							
	300	350	400	450	500	550	600	650
300	300 × 300	300 × 350	300 × 400	300 × 450	300 × 500	300 × 550	300 × 600	300 × 650
350	350 × 300	350 × 350	350 × 400	350 × 450	350 × 500	350 × 550	350 × 600	350 × 650
400	400 × 300	400 × 350	400 × 400	400 × 450	400 × 500	400 × 550	400 × 600	400 × 650
450	450 × 300	450 × 350	450 × 400	450 × 450	450 × 500	450 × 550	450 × 600	450 × 650
500	500 × 300	500 × 350	500 × 400	500 × 450	500 × 500	500 × 550	500 × 600	500 × 650

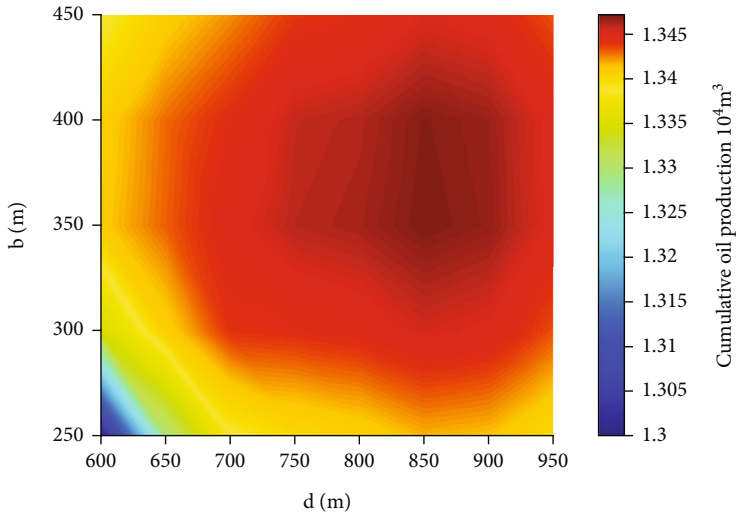

Figure 6: Cumulative oil production for the scenarios with different well spacing (inverted 5-spot well pattern).

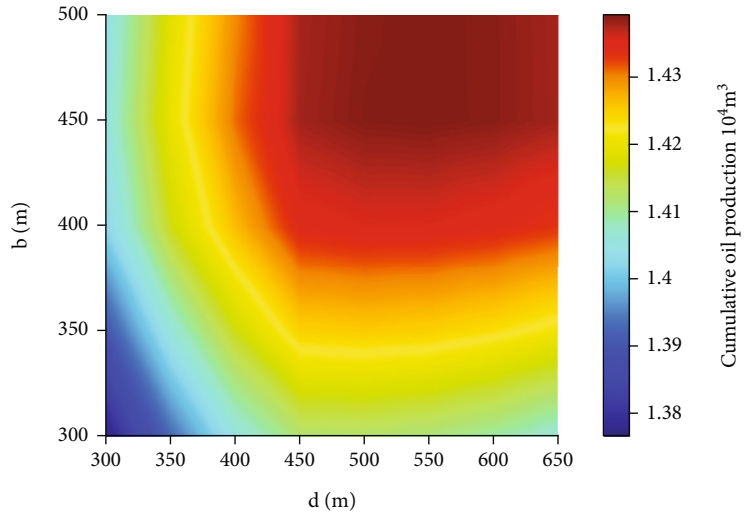

Figure 7: Cumulative oil production for the scenarios with different well spacing (inverted 9-spot well pattern).

Table 5: Evaluation of optimal well pattern.

Parameters	Notation		Inverted 5-spot well pattern	Inverted 9-spot well pattern
Area of well group (m^2)	A		595000	990000
Oil production-corner well (m^3)	N_{pc}	N_{pc1}	3405.21	1867.67
		N_{pc2}	3330.72	1723.95
		N_{pc3}	3330.72	1723.95
		N_{pc4}	3405.24	1867.67
Weighting factor-corner well	/		1/4	1/4
Oil production-side well (m^3)	N_{ps}	N_{ps1}	/	1809.67
		N_{ps2}		1721.00
		N_{ps3}		1869.24
		N_{ps4}		1809.67
Weighting factor-side well	/		/	1/2
Oil production per unit area of each well pattern (m^3/m^2)	N		5.66×10^{-3}	5.45×10^{-3}
Number of producers	n		4	8

inverted 5-spot well pattern and the inverted 9-spot well pattern with the proposed normalized index of oil production per unit area. The normalized index is determined based on the actual cumulative oil production of a well group and the area of a well group. As to the actual cumulative oil production of each well group, different weighting factors will be assigned to the different wells of the group. 1/4 will be the weighting factor of the corner well to account for the oil production contribution to the group. And 1/2 will be assigned to the side well. The analytical correlation for the normalized index is as follows. The detailed info is listed in Table 5. The oil production per unit area of the inverted 5-spot well pattern is higher than the inverted 9-spot well pattern. For the reservoir developed with fractured vertical wells coupled with large volume water injection, based on the normalized index, the inverted 5-spot well pattern is better.

Inverted 5-spot well pattern:

$$N = \frac{1/4\left(N_{pc1} + N_{pc2} + N_{pc3} + N_{pc4}\right)}{A}, \tag{3}$$

$$A = 2bd. \tag{4}$$

Inverted 9-spot well pattern:

$$N = \frac{1/4\left(N_{pc1} + N_{pc2} + N_{pc3} + N_{pc4}\right) + 1/2\left(N_{ps1} + N_{ps2} + N_{ps3} + N_{ps4}\right)}{A}, \tag{5}$$

$$A = 4bd. \tag{6}$$

5. Conclusion

In the study, based on the efficient modeling method, the numerical model of pressure-sensitive low-permeability reservoirs developed with fractured vertical wells coupled with large volume water injection is established. With the coupled model, the well pattern and well spacing optimization workflow is developed with the proposed normalized index, oil production per unit area of a certain well pattern. Based on the integrated optimization workflow, with a total of 80 sets of numerical experiments, it is found that the reservoir developed with fractured vertical wells is coupled with large volume water injection; compared with the inverted 9-spot well pattern, the inverted 5-spot well pattern is better, and the corresponding optimal well spacing is 850 m/350 m. The insights obtained from the paper will shed light on the development of low-permeability reservoirs with the novel scheme proposed by Shengli Oilfield.

Data Availability

Data is available upon request.

Conflicts of Interest

The authors declare no conflict of interest.

Acknowledgments

This research is funded by the Youth Project of the National Natural Science Foundation of China (Grant No. 52004219), the General Project of National Natural Science Foundation of China (Grant No. 51974253), the Natural Science Foundation of Shaanxi Province (Grant Nos. 2020JQ-781 and 2017JM5109), the Scientific Research Program Funded by Shaanxi Provincial Education Department (Grant No. 20JS117), the Open Fund of State Key Laboratory of Shale Oil and Gas Enrichment Mechanisms and Effective Development (Grant No. G5800-20-ZS-KFGY018), and the CNPC Innovation Fund (Grant No. 2020D-5007-0204). School of Petroleum Engineering at Xi'an Shiyou University is highly appreciated.

References

[1] J. Cai, D. A. Wood, H. Hajibeygi, and S. Iglauer, "Multiscale and multiphysics influences on fluids in unconventional reservoirs: modeling and simulation," *Advances in Geo-Energy Research*, vol. 6, no. 2, pp. 91–94, 2022.

[2] Y. Li, H. Luo, H. Li et al., "A brief review of dynamic capillarity effect and its characteristics in low permeability and tight reservoirs," *Journal of Petroleum Science and Engineering*, vol. 189, article 106959, 2020.

[3] W. Hu, Y. Wei, and J. Bao, "Development of the theory and technology for low permeability reservoirs in China," *Petroleum Exploration and Development*, vol. 45, no. 4, pp. 685–697, 2018.

[4] S. Huang, Y. Wu, X. Meng, L. Liu, and W. Ji, "Recent advances on microscopic pore characteristics of low permeability sandstone reservoirs," *Advances in Geo-Energy Research*, vol. 2, no. 2, pp. 122–134, 2018.

[5] D. Wang, D. Niu, and H. A. Li, "Predicting waterflooding performance in low-permeability reservoirs with linear dynamical systems," *SPE Journal*, vol. 22, no. 5, pp. 1596–1608, 2017.

[6] Z. Yuan, J. Wang, S. Li, J. Ren, and M. Zhou, "A new approach to estimating recovery factor for extra-low permeability waterflooding sandstone reservoirs," *Petroleum Exploration and Development*, vol. 41, no. 3, pp. 377–386, 2014.

[7] Z. Aghaeifar, S. Strand, T. Puntervold, T. Austad, and F. M. Sajjad, "Smart Water injection strategies for optimized EOR in a high temperature offshore oil reservoir," *Journal of Petroleum Science and Engineering*, vol. 165, pp. 743–751, 2018.

[8] J. Udy, B. Hansen, S. Maddux et al., "Review of field development optimization of waterflooding, EOR, and well placement focusing on history matching and optimization algorithms," *Processes*, vol. 5, no. 3, p. 34, 2017.

[9] J. Zhan, C. Fan, X. Ma, Z. Zheng, Z. Su, and Z. Niu, "High-precision numerical simulation on the cyclic high-pressure water slug injection in a low-permeability reservoir," *Geofluids*, vol. 2021, 10 pages, 2021.

[10] S. Kalam, U. Yousuf, S. A. Abu-Khamsin, U. B. Waheed, and R. A. Khan, "An ANN model to predict oil recovery from a 5-spot waterflood of a heterogeneous reservoir," *Journal of Petroleum Science and Engineering*, vol. 210, article 110012, 2022.

[11] O. Oluwasanmi, A. N. Pastor, O. Charles, N. Christopher, and O. Seyi, "Optimizing productivity in oil rims: simulation studies on water and gas injection patterns," *Arabian Journal of Geosciences*, vol. 14, no. 7, pp. 1–20, 2021.

[12] E. I. Okon, J. A. Adetuberu, and D. Appah, "Maximising oil recovery in mature water floods using automated pattern flood management," in *Proceedings of the SPE Nigeria Annual International Conference and Exhibition*, Lagos, Nigeria, 2019.

[13] J. E. Onwunalu and L. J. Durlofsky, "A new well-pattern-optimization procedure for large-scale field development," *SPE Journal*, vol. 16, no. 3, pp. 594–607, 2011.

[14] Computer Modelling Group, *User Guide*, Computer Modelling Group Ltd, 2015.

[15] Z. Chen, *Reservoir simulation: mathematical techniques in oil recovery*, Society for Industrial and Applied Mathematics, 2007.

[16] A. Arrarás, F. J. Gaspar, L. Portero, and C. Rodrigo, "Geometric multigrid methods for Darcy-Forchheimer flow in fractured porous media," *Computers & Mathematics with Applications*, vol. 78, no. 9, pp. 3139–3151, 2019.

[17] D. Takhanov, *Forchheimer model for non-Darcy flow in porous media and fractures*, Master's Thesis, Imperial College London, London, UK, 2011.

[18] R. D. Evans and F. Civan, *Characterization of Non-Darcy Multiphase Flow in Petroleum Bearing Formation. Final report*, Oklahoma Univ. School of Petroleum and Geological Engineering, Norman, OK (United States), 1994.

[19] B. Rubin, "Accurate simulation of non-Darcy flow in stimulated fractured shale reservoirs," in *SPE Western regional meeting*, Anaheim, California, USA, 2010Society of Petroleum Engineers.

[20] A. Novlesky, A. Kumar, and S. Merkle, "Shale gas modeling workflow: from microseismic to simulation–a Horn River case study," in *Canadian Unconventional Resources Conference*, Calgary, Alberta, Canada, 2011.

[21] J. Zhan, Z. Niu, M. Li et al., "Numerical simulation and modeling on co2 sequestration coupled with enhanced gas recovery in shale gas reservoirs," *Geofluids*, vol. 2021, 15 pages, 2021.

[22] A. Settari and F. M. Mounts, "A coupled reservoir and geomechanical simulation system," *SPE Journal*, vol. 3, no. 3, pp. 219–226, 1998.

[23] X. Ma, X. Chen, and J. Zhan, "Numerical simulation method for multi-stage hydraulic fracturing based on modified dilation-recompaction model," *Arabian Journal of Geosciences*, vol. 15, no. 7, pp. 1–9, 2022.

[24] R. Gao, X. Wang, Z. Yang et al., "Application of dilation-recompaction model in fracturing optimisation in tight oil reservoir," in *Proceedings of the International Petroleum Technology Conference*, Beijing, China, 2019.

[25] X. Huang, J. Wang, S. Chen, and I. D. Gates, "A simple dilation-recompaction model for hydraulic fracturing," *Journal of Unconventional Oil and Gas Resources*, vol. 16, pp. 62–75, 2016.

[26] X. Huang, *Application of dilation-recompaction model in hydraulic fracturing simulation*, Master's Thesis, University of Calgary, Calgary, Canada, 2015.

[27] C. I. Beattie, T. C. Boberg, and G. S. McNab, "Reservoir simulation of cyclic steam stimulation in the Cold Lake oil sands," in *Proceedings of the SPE California Regional Meeting*, Bakersfield, California, 1989.

[28] Y. Ito, "The introduction of the microchanneling phenomenon to cyclic steam stimulation and its application to the numerical simulator (sand deformation concept)," *Society of Petroleum Engineers Journal*, vol. 24, no. 4, pp. 417–430, 1984.

[29] B. Y. Jamaloei, "Impact of formation dilation–recompaction on cyclic steam stimulation," *SPE Reservoir Evaluation & Engineering*, vol. 24, no. 1, pp. 98–126, 2021.

[30] R. A. Farquhar, B. G. D. Smart, A. C. Todd, D. E. Tompkins, and A. J. Tweedie, "Stress sensitivity of low-permeability sandstones from the Rotliegendes sandstone," in *Proceedings of the SPE annual technical conference and exhibition*, Houston, Texas, 1993.

[31] N. H. Kilmer, N. R. Morrow, and J. K. Pitman, "Pressure sensitivity of low permeability sandstones," *Journal of Petroleum Science and Engineering*, vol. 1, no. 1, pp. 65–81, 1987.

[32] C. Li, *Fundamentals of Reservoir Engineering*, Petroleum Industry Press, Beijing, 2011.

Hindawi
Geofluids
Volume 2022, Article ID 9728261, 15 pages
https://doi.org/10.1155/2022/9728261

Research Article

Tripability Analysis of Casing Strings in Directional Wells Using the Continuous Beam-Column and Buckling Theory

Gang Wang, Gang Liu, Kai Wang, Yichen Li, and Yinan Hu

School of Petroleum Engineering, China University of Petroleum (East China), Qingdao 266580, China

Correspondence should be addressed to Gang Liu; lg_communication@126.com

Received 8 May 2022; Revised 27 June 2022; Accepted 12 July 2022; Published 30 July 2022

Academic Editor: Basim Abu-Jdayil

Copyright © 2022 Gang Wang et al. This is an open access article distributed under the Creative Commons Attribution License, which permits unrestricted use, distribution, and reproduction in any medium, provided the original work is properly cited.

Hindered casing strings are often encountered in unconventional oil and gas exploration during the casing running process. This not only increases the operating costs and time but can also lead to downhole accidents and even abandonment in serious cases. Due to various assumptions, the calculation results of the existing soft models and hard models are different, which causes confusion for field operators when taking friction reduction measures. Moreover, a lowering force is often applied to assist hindered casing string running in a drilling field. However, its application is mainly based on work experience and lacks mechanistic analysis and theoretical guidance. Thus, in this study, a simulation model for the analysis of casing string tripability in a directional well was established and the model was combined with the continuous beam-column theory and buckling theory. The model was used to study how various factors including the friction coefficient, drilling fluid density, and casing diameter could affect the lowering force required when a casing string was hindered by buckling. The results showed that the maximum lowering force and the maximum effective lowering force decreased with the increase in the friction coefficient and the performance of the drilling fluid could be adjusted rapidly, which would be beneficial for ensuring that the casing string could be tripped smoothly by applying a lowering force. The increase in the drilling fluid density caused the maximum lowering force and the maximum effective lowering force to decrease, which was not conducive to hindered casing string running. The larger the casing diameter was, the greater the maximum lowering force and the maximum effective lowering force were. It was more convenient to apply a lowering force for a casing with a large diameter. In addition, the improved model could identify whether the casing string was in contact with the upper or lower borehole walls. Through finite element method verification, the prediction was in line with the actual casing running operation and the improved model has the smallest prediction error, i.e., 6.58%, compared with the existing models. Therefore, the improved model might provide necessary theoretical guidance for casing running operations in directional wells.

1. Introduction

Unconventional oil and gas exploration and development have entered an active period. Directional well technologies such as horizontal wells, extended reach wells, and cluster wells have been widely applied in unconventional oil and gas exploration. Casing strings cannot be tripped at the target depth due to the influence of the formation lithology, well trajectory, and casing running technology. Once the casing string running is hindered, it increases the operating cost and time and can lead to downhole accidents and even abandonment in serious cases [1]. Therefore, to ensure that the casing string reaches the target depth smoothly, it is necessary to predict the friction and applied lowering force.

At present, several models have been established for calculating the drag and torque of a tubular string. The soft-string torque and drag model was initially developed by Johancsik et al. [2] and later put in a standard differential form by Sheppard et al. [3]. This model assumed that the string was in continuous contact with the borehole wall and did not consider the string stiffness [4–7]. It is generally believed that the soft string model sometimes provides poor results for stiff tubular strings, high dogleg severity (small radius of curvature), or narrow radial clearance in the annulus [8].

Because the soft-string model does not consider the influence of the string stiffness, Ho. [9] established a stiff-string model for drag and torque based on the theory of large deformation for a drill string. Mitchell et al. [10] established a differential form that was easy to understand. However, many factors, including the variable stiffness of the tubular strings, the shape of the wellbore, and the clearance, can influence the contact state of the tubular strings and the value of the contact force on the tubular strings. The present stiff string models do not consider these factors, making it difficult to predict accurate results [11–13].

To improve the agreement between the calculation results and the real situation of a casing string running in a wellbore, 3D finite element models have been established to analyze the friction, stress, and deformation of the string in the build-up section and the horizontal section during the tubular string running process [14–20]. The well depth is generally several thousand meters. With the increase of the size of the 3D model, it is necessary to take a long time to complete calculations. The results are difficult to apply in real time in the field; it is often used to provide a reference for the optimal design of the wellbore trajectory and tubular string assembly and verify the accuracy of the new model for prediction drag and torque [21].

The continuous beam-column theory has been increasingly recognized because of its clear physical meaning and relatively simple algorithm [22–24]. When calculating the contact force between the string and the borehole wall in the traditional continuous beam-column theory, the contact point between the string and the borehole wall is first specified but one must generally be very cautious when specifying the contact point. As a result, some real contact points are missed, and in order to find these contact points, it is necessary to judge whether the deflection of the string between the two contact points exceeds the wellbore clearance. However, the traditional model does not consider the effect of a curved borehole on the deflection of the casing string, which cannot be ignored in the curved section.

Therefore, to identify the contact point between the pipe string and the well wall and ensure that the casing string runs smoothly in the directional well, the influence of the initial bending of the casing string on the deflection and deformation of the casing string was considered in this study using the improved continuous beam-column model. In addition, based on buckling theory, a prediction model of the maximum effective lowering force required during hindered casing string running was established. Using the existing friction model for tubular strings and field data verification, the model prediction results were proven to match the actual field data well.

2. Casing String Tripability Analysis Model

A model was established to predict whether a casing string could be run smoothly during the casing running process in a directional well. The primary reason that casing strings cannot be tripped in is the friction force. When the total friction of casing strings is greater than the floating weight of the casing strings above the stuck point, the casing strings are hindered during the casing running process. The friction force is generated by the contact between the casing strings and the wellbore wall. Therefore, the contact force is required to be analyzed first.

2.1. Basic Assumptions

(a) The string, which was composed of a casing, coupling, and centralizer, was regarded as an elastic beam column, and its deformation was within the linear elastic range

(b) The wellbore had a uniform circular cross-section without enlargement or hole shrinkage

(c) The coupling, centralizers, and other parts with relatively large diameters on the string or specified points of a certain length were taken as supports that were in contact with the borehole wall

(d) The casing string rotation and vibration were neglected

2.2. Three-Dimensional Wellbore Trajectory Plane Decomposition. The three-dimensional wellbore could be approximately represented in two dimensions by decomposing it into two planes, plane P and plane Q [25], as shown in Figure 1. The lateral force and deflection of the string were calculated on the two planes separately. Then, the lateral force and deflection of the string in space could be obtained after the corresponding superposition.

2.3. Establishing a Bottom-Hole Coordinate System. Based on the unit vector of the three coordinate axes in the bottom-hole coordinate system [26], the coordinate transformation matrix $[M]$ of the vector from the wellhead coordinate system to the bottom-hole coordinate system could be obtained as follows:

$$[M] = \begin{bmatrix} \cos a_b \cos \phi_b & \cos a_b \sin \phi_b & -\sin a_b \\ -\sin \phi_b & \cos \phi_b & 0 \\ -\sin a_b \cos \phi_b & -\sin a_b \sin \phi_b & -\cos a_b \end{bmatrix}, \quad (1)$$

where a_b and ϕ_b are the well inclination and the azimuth at the casing shoe, respectively. The coordinate transformation was as follows:

$$\begin{Bmatrix} x \\ y \\ z \end{Bmatrix} = [M] \cdot \begin{Bmatrix} N - N_b \\ E - E_b \\ H - H_b \end{Bmatrix}, \quad (2)$$

where H_b, N_b, and E_b are the H, N, and E coordinates of the casing shoe, respectively. H, N, and E are the coordinates of any point in the wellhead coordinate system, and x, y, and z are the x, y, and z coordinates of the corresponding points in the bottom-hole coordinate system, respectively.

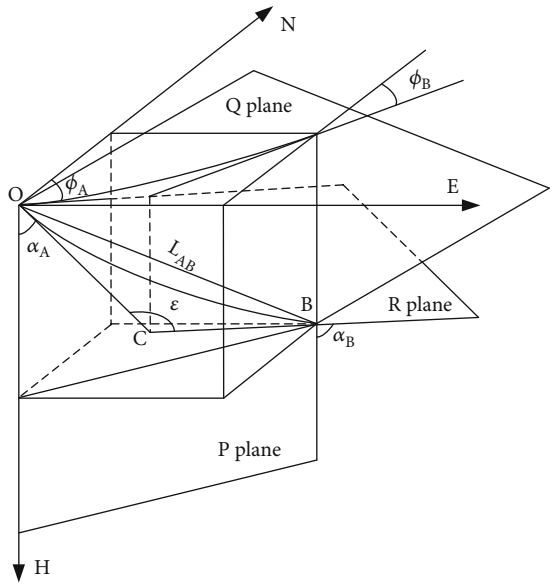

Figure 1: Three-dimensional plane decomposition of borehole trajectory.

2.4. Continuous Beam-Column Model

2.4.1. Three-Moment Equations in Plane P. With the casing string runs in plane P (well inclination plane) as an example, the casing string combination of any number (n) of centralizers was taken as the analysis object. As shown in Figure 2, the centralizers divided the whole casing string into N span beams and the transverse load q_i, bending moments M_{i-1} and M_i, and the axial force F_i acted on the ith span beam. The right deflection angle of the ith span beam was θ_i^R, the shear force was Q_i^R, the transverse load was q_{i+1}, the bending moments were M_i and M_{i+1}, and the axial force F_{i+1} acted on the $(i+1)$th span beam. The right rotation angle of the $(i+1)$th span beam was θ_{i+1}^L, and the shear force was Q_{i+1}^L.

The deflection curves of the two adjacent spans had a common tangent line at the support of the string. Therefore, the rotation angles on both sides of the support were equal:

$$\theta_{i,P}^R = -\theta_{i+1,P}^L. \tag{3}$$

The rotation angle at the support could be obtained from the formula of the end rotation angle and the deformation superposition principle of continuous beam-column theory (Appendix A):

$$\begin{aligned}
\theta_{i,P}^R &= \frac{q_{i,P}L_i^3}{24EI_i}X(u_{i,P}) + \frac{M_{i,P}L_i}{3EI_i}Y(u_{i,P}) + \frac{M_{i-1,P}L_i}{6EI_i}Z(u_{i,P}),\\
\theta_{i+1,P}^L &= \frac{q_{i+1,P}L_{i+1}^3}{24EI_{i+1}}X(u_{i+1,P}) + \frac{M_{i+1,P}L_{i+1}}{3EI_{i+1}}Y(u_{i+1,P}) + \frac{M_{i+1,P}L_{i+1}}{6EI_{i+1}}Z(u_{i+1,P}),\\
\theta_{n+1,P}^R &= \frac{q_{n+1,P}L_{n+1}^3}{24EI_{n+1}}X(u_{n+1,P}) + \frac{M_{n+1,P}L_{n+1}}{3EI_{n+1}}Y(u_{n+1,P}) + \frac{M_{n+1,P}L_{n+1}}{6EI_{n+1}}Z(u_{n+1,P}),
\end{aligned} \tag{4}$$

where L_i is the length of the ith span beam (m), $q_{i,p}$ is the component of the transverse load of the ith span beam in the P plane (N), a_i is the well inclination angle at the ith support (°), w_i is the weight per meter of the ith span beam in mud (kg/m), F_i is the average axial force on the ith span beam (N), E is the elastic modulus of the string (Pa), and I_i is the section moment of inertia of the ith span beam (m^4).

2.4.2. Initial Rotation Angle. For the actual string combination, the diameter of the centralizer was smaller than the diameter of the borehole. Therefore, when the string was tripped in the borehole, the centralizer might have been close to a side of the wellbore wall, which would have caused the displacement of the support due to the elimination of clearance. Therefore, several supports were not in a straight line. This resulted in an additional rotation angle at the end of the beam column due to the displacement of the supports, as shown in Figure 3.

In plane P, the initial additional rotation angle generated by the initial relative displacement of the supports at both ends of the ith span beam was

$$\delta\theta_{i,P}^0 = \arctan\left(\frac{\delta x_i^0 - \delta x_{i-1}^0}{z_i - z_{i-1}}\right). \tag{5}$$

In plane Q, the initial additional rotation angle generated by the initial relative displacement of the supports at both ends of the ith span beam was

$$\delta\theta_{i,Q}^0 = \arctan\left(\frac{\delta y_i^0 - \delta y_{i-1}^0}{z_i - z_{i-1}}\right). \tag{6}$$

2.4.3. Three-Moment Equations. Considering the initial additional rotation angle generated by the displacement of the support, the corresponding three-moment equation of the $(n+1)$th span continuous beam-column in the plane P could be obtained:

$$\begin{aligned}
&M_{i-1,P}\frac{L_iZ(u_{i,P})}{6EI_i} + M_{i,P}\left[\frac{L_iY(u_{i,P})}{3EI_i} + \frac{L_{i+1}Y(u_{i+1,P})}{3EI_{i+1}}\right]\\
&\quad + M_{i+1,P}\frac{L_{i+1}Z(u_{i+1,P})}{6EI_{i+1}} = -\frac{q_{i,P}L_i^3X(u_{i,P})}{24EI_i}\\
&\quad - \frac{q_{i+1,P}L_{i+1}^3X(u_{i+1,P})}{24EI_{i+1}} + \delta\theta_{i+1,P}^0 - \delta\theta_{i,P}^0,\\
&\frac{q_{n+1,P}X(u_{n+1,P})L_{n+1}^3}{24EI_{n+1}} + M_{n+1,P}\frac{Y(u_{n+1,P})L_{n+1}}{3EI_{n+1}}\\
&\quad + M_{n,P}\frac{Z(u_{n+1,P})}{6EI_{n+1}}L_{n+1} = \theta_{n+1,P}^R - \delta\theta_{n,P}^0.
\end{aligned} \tag{7}$$

The boundary conditions at the casing shoe and the upper tangent point in plane P were

$$\begin{aligned}
M_{0,P} &= 0,\\
M_{n,P} &= E\cdot I_n\cdot k_{aT},
\end{aligned} \tag{8}$$

where k_{aT} is the rate of well inclination change at the tangent point.

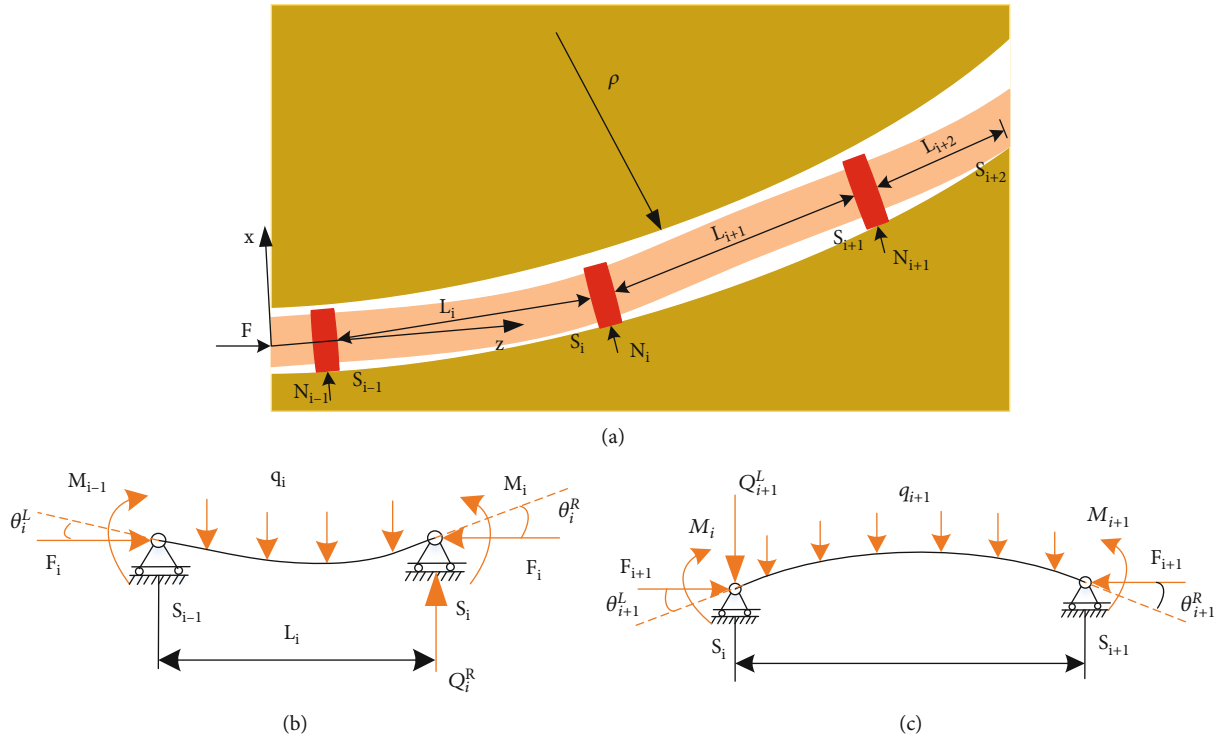

FIGURE 2: Force and deformation of casing string running in a curved section. (a) Schematic diagram of casing string running in a curved section. (b) Force and deformation of the ith span beam. (c) Force and deformation of the $(i+1)$th span beam.

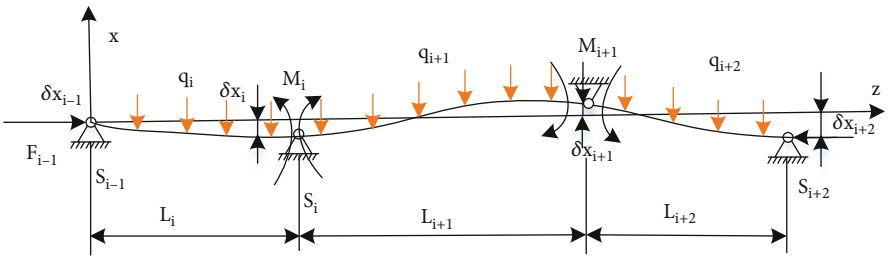

FIGURE 3: Schematic diagram of beam supports not in a straight line under the combined force.

There were $n+1$ equations for the three bending moments, in which the $n+1$ unknowns were $M_1 \sim M_n$ and L_{n+1}. Thus, there was a definite solution. For the ith beam support in plane Q, the left and right sides were the ith and $(i+1)$th span beams, respectively. Based on the continuous condition that the rotation angle of the beams on both sides of the support were equal, the three bending moment equations in plane Q were obtained.

$$M_{i-1,Q}\frac{L_i Z(u_{i,Q})}{6EI_i} + M_{i,Q}\left[\frac{L_i Y(u_{i,Q})}{3EI_i} + \frac{L_{i+1} Y(u_{i+1,Q})}{3EI_{i+1}}\right] + M_{i+1,Q}\frac{L_{i+1} Z(u_{i+1,Q})}{6EI_{i+1}} = \delta\theta^0_{i+1,Q} - \delta\theta^0_{i,Q},$$

$$M_{n+1,Q}\frac{Y(u_{n+1,Q})L_{n+1}}{3EI_{n+1}} + M_{n,Q}\frac{Z(u_{n+1,Q})}{6EI_{n+1}}L_{n+1} = \theta^R_{n+1,Q} - \delta\theta^0_{n,Q}, \quad (9)$$

TABLE 1: Critical load for the helical buckling of the string in different well sections, where F_{hel} is the critical load of helical buckling (N), r is the borehole annulus clearance (m), and R is the string radius (m).

Well section	Critical load for helical buckling
Vertical	$F_{hel} = 5.55\sqrt[3]{EIw^2}$
Straight inclined	$F_{hel} = 2.83\sqrt{EIw \sin a/r}$
Curved	$F_{hel} = 12EI/rR\left[1 + \sqrt{(1 + rR^2 w \sin a/8EI)}\right]$
Horizontal	$F_{hel} = 2\left(2\sqrt{2} - 1\right)\sqrt{EIw/r}$

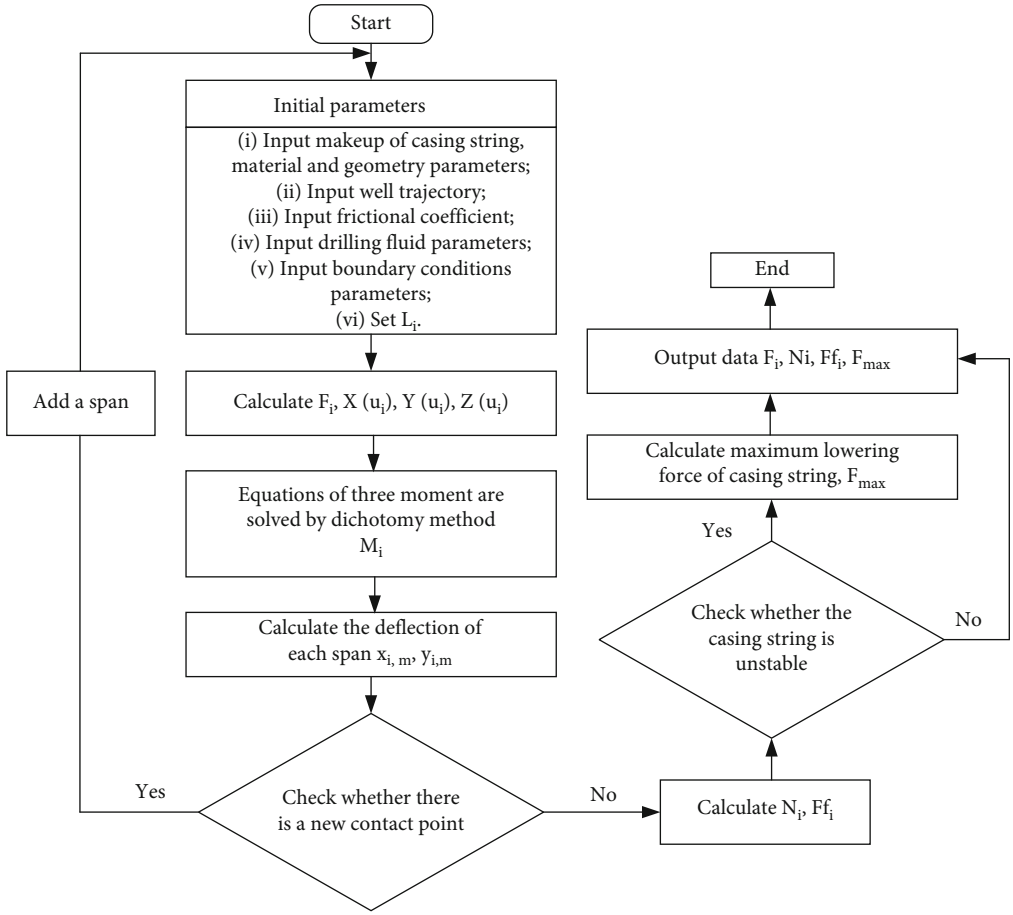

Figure 4: Flowchart of the solution procedure.

where the meanings of the parameters are the same as those above discussed.The boundary conditions at the casing shoe and the upper tangent point in plane Q were as follows:

$$\begin{aligned} M_{0,Q} &= 0, \\ M_{n,Q} &= E \cdot I_n \cdot k_{\phi T} \sin a_T, \end{aligned} \tag{10}$$

where $k_{\phi T}$ is the rate of azimuth change at the tangent point and a_T is the well inclination at the tangent point.

2.4.4. Contact Force. The relationship between the force and deformation of the string is given. An iterative method could be used to solve the deflection function of each span to obtain the deflection, rotation angle, and bending moment of the string after deformation. Combined with Figures 2(b) and 2(c), the contact force at each support in plane P could be calculated:

$$N_{i,P} = \frac{M_{i-1,P} - M_{i,P}}{L_i} + \frac{q_{i,p}L_i}{2} + \frac{M_{i+1,P} - M_{i,P}}{L_{i+1}} + \frac{q_{i+1,p}L_{i+1}}{2}, \quad (i = 1 \text{ to } n-1). \tag{11}$$

Then, the contact force at each support in plane Q was

$$N_{i,Q} = \frac{M_{i-1,Q} - M_{i,Q}}{L_i} + \frac{M_{i+1,Q} - M_{i,Q}}{L_{i+1}}, \quad (i = 1 \text{ to } n-1). \tag{12}$$

2.5. Effect of Initial Bending on Casing Deflection. When the casing string was tripped in the curved section of a wellbore, the deformation of the entire casing string had to be generally consistent with the wellbore axis. Therefore, the maximum deflection of the casing string caused by the initial bending could be obtained [27] (Appendix B):

$$x_{i,\max} = x_{i,0} + x_{i,1} = \frac{2\zeta_{i,P}}{u_i^2}\left(\frac{1}{\cos u_i} - 1\right) = \frac{K_{i,P}EI_i}{F_i}\left(\frac{1}{\cos u_i} - 1\right). \tag{13}$$

2.6. Judgment of Contact Points. Considering the influence of the borehole bending on the casing string deformation, the improved maximum deflection $x_{i,m}$ in plane P and the

improved maximum deflection $y_{i,m}$ in plane Q of the ith span string were calculated as follows:

$$x_{i,m} = \frac{q_{i,p}\Delta L_i^4}{16EI_i u_i^4}\left(\frac{1}{\cos u_i} - 1 - \frac{u_i^2}{2}\right) + \frac{M_{i-1,p} + M_{i,p}}{2F_i \cos(\Delta\alpha_i/2)}\left(1 - \frac{1}{\cos u_i}\right) + \frac{K_P L_i^2}{4u_i^2}\left(\frac{1}{\cos u_i} - 1\right) + \frac{e_{i-1,P} + e_{i,P}}{2},$$

$$y_{i,m} = \frac{M_{i-1,Q} + M_{i,Q}}{2F_i \cos(\Delta\phi_i/2)}\left(1 - \frac{1}{\cos u_i}\right) + \frac{K_Q L_i^2}{4u_i^2}\left(\frac{1}{\cos u_i} - 1\right) + \frac{e_{i-1,Q} + e_{i,Q}}{2}. \quad (14)$$

Therefore, the criterion for generating the new contact points was

$$\sqrt{x_{i,m}^2 + y_{i,m}^2} > \frac{D_w - D_{0i}}{2}, \quad (15)$$

where K_Q is the curvature on the azimuth plane of the well section where the string is located (°/30 m), D_w is the borehole diameter (m), D_{ci} is the centralizer diameter (m), D_{0i} is the casing diameter (m), $e_{i-1} = (D_w - D_{ci-1})/2$, and $e_i = (D_w - D_{ci})/2$.Once the maximum deflection of the casing string between the two supports exceeded the wellbore clearance, there was a new contact point and new support needed to be added to perform the recalculation.

2.7. Tripability Judgment of the Casing String. The contact force and the friction at each contact point could be obtained as follows:

$$N_i = \sqrt{N_{i,p}^2 + N_{i,Q}^2}, \quad F_{fi} = \mu N_i, \quad (16)$$

where μ is the friction coefficient.When the total friction of the casing string was greater than the floating weight of the casing string above the stuck point, the casing string could be considered hindered during the casing running process:

$$\sum F_{fi} > w_i \cdot L_s, \quad (17)$$

where L_s is the length of the casing string above the stuck point (m).

At that time, it was difficult for the casing string to run with its own floating weight and it was possible to run the casing string with the help of the other processes. For example, a lowering force, a pick-up and release technique, and casing floating could be applied. Since the casing string buckled during the running process, it was also necessary to consider the case in which the casing string was hindered by buckling.

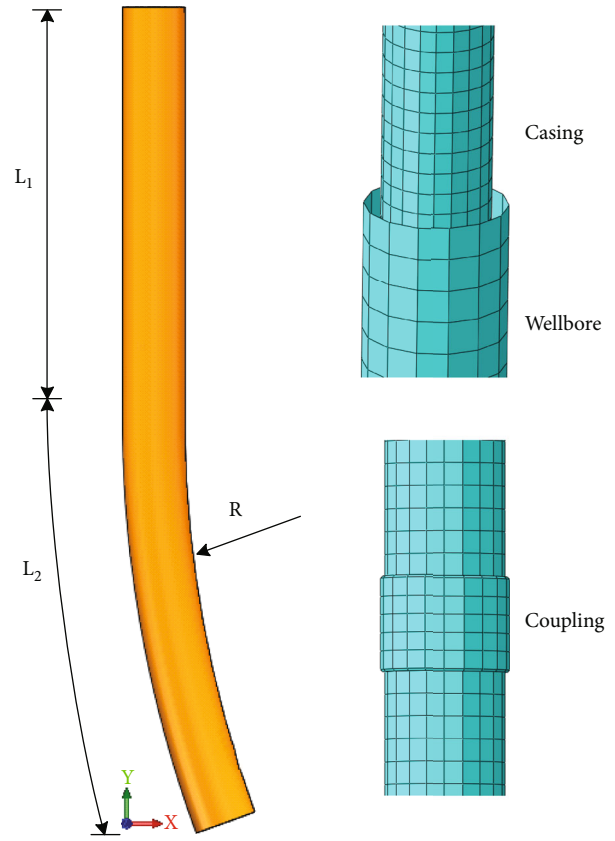

Figure 5: Finite element model of the casing string.

Table 2: Basic calculation parameters.

Name	Value
Well depth	4558 m
Kickoff point	1267 m
Build-up rate	4°/30 m
Radius of curvature, R	430 m
Vertical section, L_1	100 m
Build-up section, L_2	100 m
Diameter (borehole), D_w	215.9 mm
Diameter (casing), D_p	177.8 mm
Diameter (coupling), D_c	200.03 mm
Wall thickness (coupling), D_o	11.12 mm
Young's modulus, E	2.1×10^5 MPa
Poisson's ratio, ε	0.3
Friction coefficient	0.2

2.8. Critical Load for Helical Buckling of the String. Many scholars have obtained the critical load when a string is subjected to spiral buckling in different well sections through theoretical derivations or experiments, as shown in Table 1. Additional friction should be considered when a casing string is spirally buckling and in contact with a

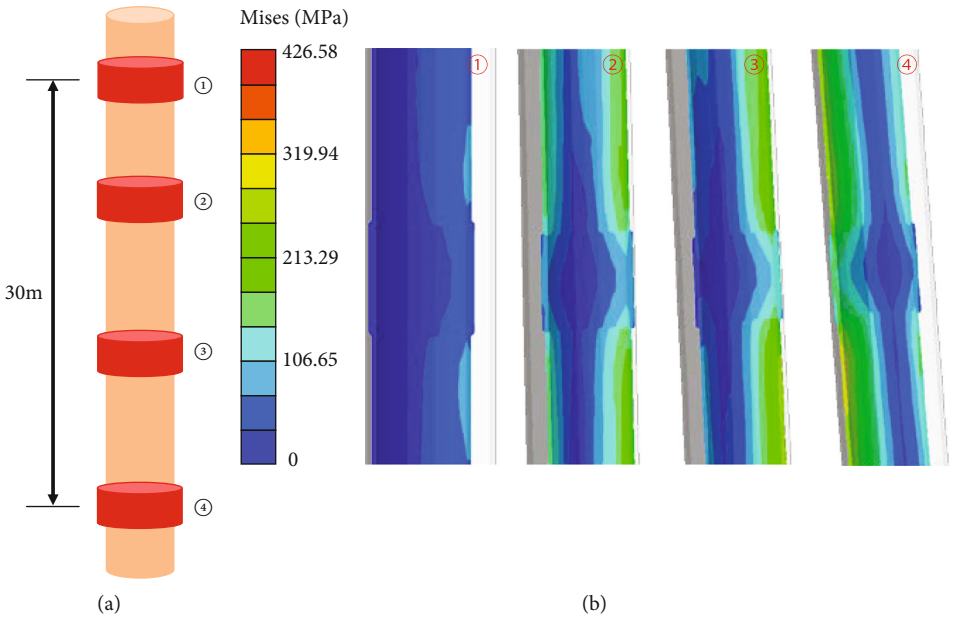

Figure 6: (a) Schematic diagram of casing string combination. (b) Cloud map of contact between the casing string and the wellbore wall.

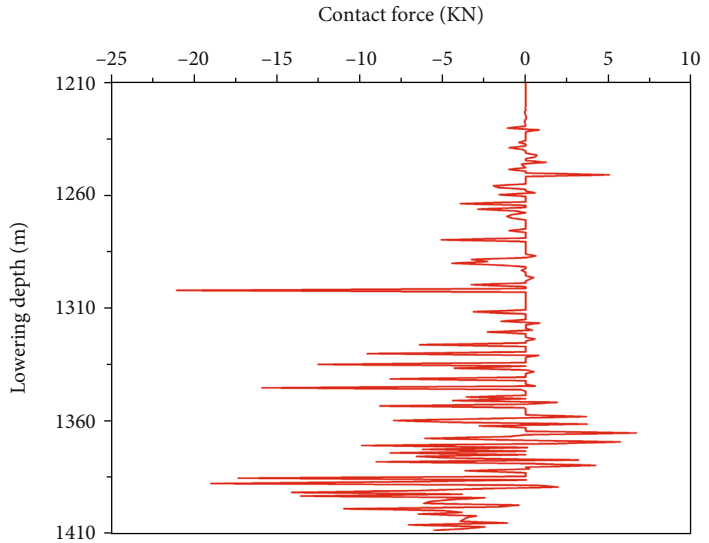

Figure 7: Contact force when the casing string was running in the wellbore.

borehole wall to determine whether the casing string can be successfully tripped in.

2.9. Determine the Maximum Lowering Force. Due to the restrictions of a wellbore, a string will undergo multiple deformation processes with the increase in the lowering force after string buckling. With the combined action of the string weight and the buoyancy of the drilling fluid, the string buckling becomes a spatial spiral shape with a varying pitch. The bending of the string causes contact with the borehole wall, resulting in increased friction, which offsets some of the lowering force and reduces the effective lowering force on the stuck point [28]. Therefore, how to determine the maximum lowering force when applying a load to push down the casing is very important for casing running.

The maximum lowering force $F_{\max}$ can be obtained as follows (Appendix C):

$$F_{\max} = \sqrt{\frac{w_m EI}{3\delta\mu r}}. \tag{18}$$

The maximum effective lowering force $F_{e\,\max}$ can be obtained as follows:

$$F_{e\,\max} = F_{\max} - \frac{\delta\mu r}{w_m EI} F_{\max}^3. \tag{19}$$

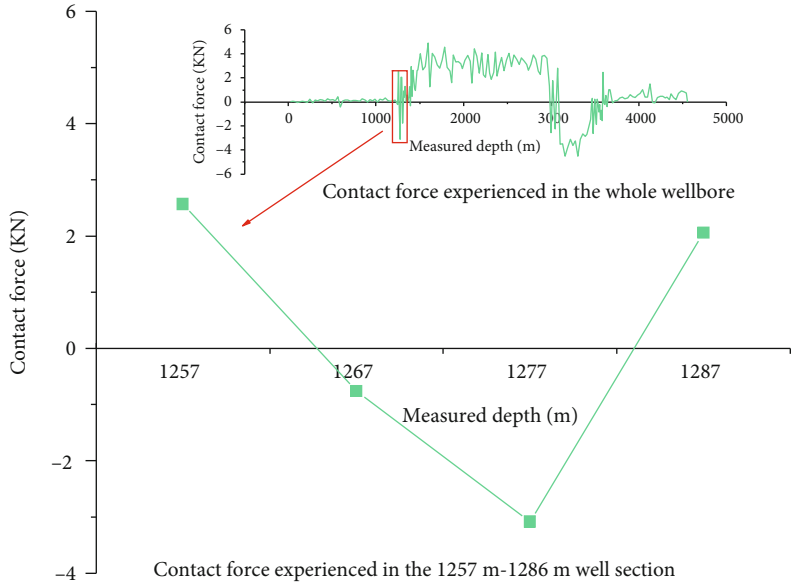

Figure 8: Contact force of the casing string using the improved model.

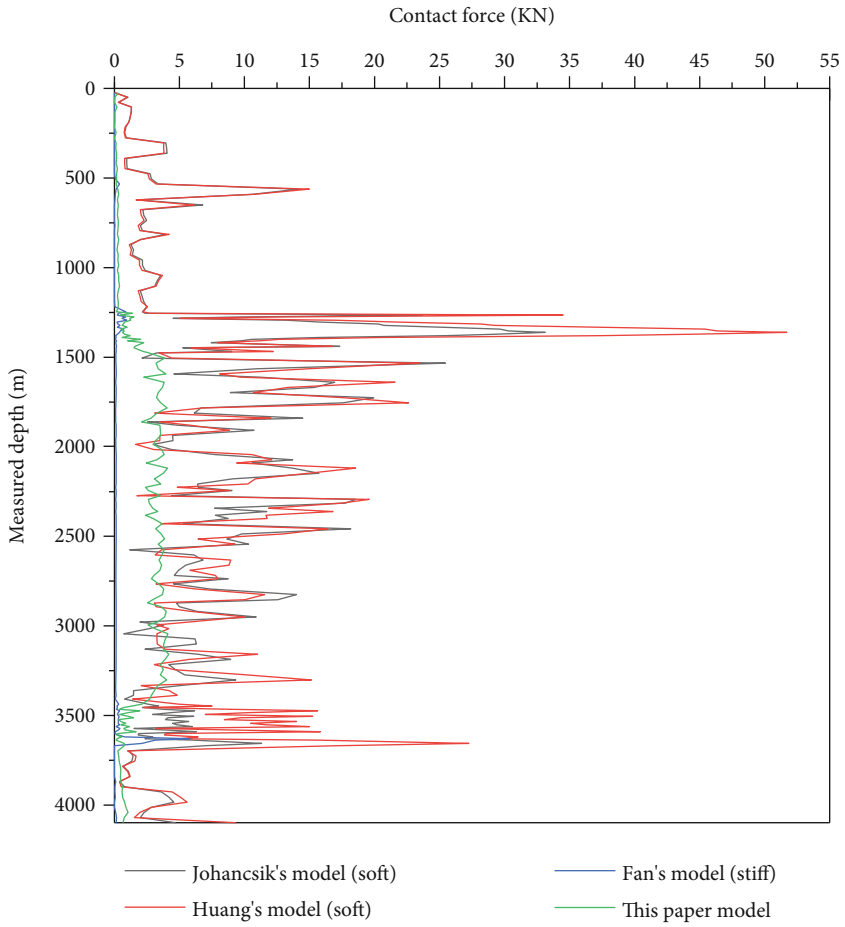

Figure 9: Contact force on the casing string using different models.

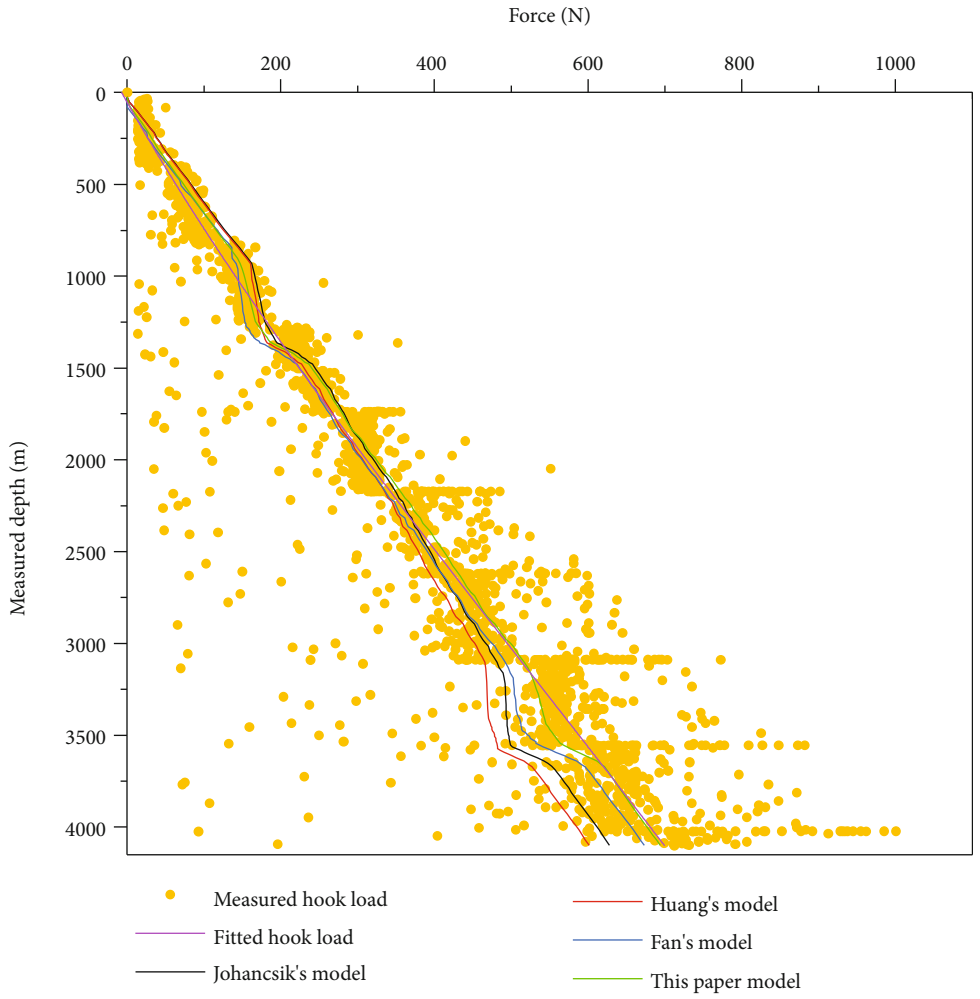

Figure 10: Axial load on the casing string using different models.

2.10. Solution Method. An iterative method [23, 24] was used to apply the simulation model in actual wellbores. The flowchart of the procedure is shown in Figure 4.

3. Model Validation

An example was adapted from an actual FX160 directional well in China. The finite element method was used for verification. Due to the large size of the actual borehole, the establishment of a full-size three-dimensional finite element model of the borehole trajectory and casing string combination required not only a high amount of computational resources but also a long time to perform the calculations. It was believed that the mechanical behavior of a point in the structure would have no effect on the point in space beyond 15 m [29]. Therefore, the well section at 1210–1410 m was selected. This section included the vertical section and the curved section. Considering the influence of the casing string coupling, the deformation and the contact force when the casing string was tripped in were simulated and calculated. The three-dimensional finite element model is shown in Figure 5. The relevant parameters in the model are shown in Table 2.

The dynamic explicit analysis method was used, and the casing running speed was 0.8 m/s. When the casing string was tripped in the wellbore, it deformed and came into contact with the borehole wall due to the influence of the curved borehole. Because the model size was large, the contact state of the entire casing string and the wellbore wall could not be clearly displayed. Therefore, only the contact cloud map of the casing string and the wellbore wall in the 1257–1287 m well section is illustrated in Figure 6. Figure 6(a) shows the schematic diagram of the casing string combination in this well section, and Figure 6(b) shows the corresponding cloud map of the contact between the 30 m casing string and the wellbore wall. As shown in Figure 6(b), the first and fourth couplings were in contact with the downhole wall and the second and third couplings were in contact with the upper wellbore wall. The simulation showed that due to the influence of the curved wellbore, the casing string occasionally came into contact with the upper or lower hole walls of the wellbore during the running process. The calculation results are illustrated in Figure 7. The magnitude and the direction of the contact force were constantly changing when the casing string was tripped in the 1210–1410 m well section.

Table 3: Comparison of model prediction errors.

Wellbore	Relative error (%)			
	Johancsik's model	Huang's model	Fan's model	This paper's model
	33.22	31.64	15.98	15.94
Vertical section	25.08	23.50	15.87	14.09
	13.81	10.56	−1.91	4.60
	17.10	9.01	−2.54	7.80
Build-up section	4.63	−1.92	−5.56	1.33
	9.20	2.70	0.03	7.34
	2.81	−1.70	−2.01	3.97
Sail section	−1.34	−5.16	−2.56	2.80
	−5.08	−8.38	−4.70	0.21
	−6.31	−9.40	−4.27	0.52
Drop-off section	−10.70	−15.04	−8.34	−2.72
	−16.18	−19.14	−10.58	−5.25
	−10.43	−14.64	−3.75	0.02
Inclined section	−10.43	−14.54	−3.83	−0.33
	−10.21	−14.18	−3.70	−0.61
Root mean square error (%)	14.36	14.52	7.41	6.58

The contact force when the casing string was tripped in the wellbore using the improved continuous beam-column model is shown in Figure 8. The casing strings are in contact with the upper or lower borehole wall in the curved section, resulting in changes in the direction and magnitude of the contact force. For the casing strings at 1257–1287 m, the direction of the contact force also changed, similar to the results in Figure 6(b).

The comparison of the results in Figures 7 and 8 showed that the magnitude of the contact force using the improved continuous beam-column model was different from that of the finite element simulation. The magnitude of the contact force calculated using the improved continuous beam-column model represented the contact force of each contact point between the casing string and the borehole wall, while the result of the finite element method was the resultant force of all contact points between the entire casing string and the borehole wall at a certain time. Although the contact force values calculated with the two methods were different, the direction of the contact force reflected the contact state between the casing strings and the wellbore wall when casing strings were tripped in the wellbore, which was more consistent with the actual running operation of the casing strings.

4. Field Applications

With the wellbore trajectory in Section 3 taken as an example, the established tripability analysis model of the casing string was used to calculate the contact force, hook load, and maximum lowering force required during the casing running in the wellbore. The proposed model was compared with the existing friction model of the string and the field drilling data.

Table 4: Casing string combination parameters.

Name	Value
Casing diameter	0.1778 m
Wall thickness	0.0115 m
Unit weight	466.676 N/m
Moment of inertia	2.09×10^{-5} m^4
Borehole diameter	0.2159 m
Young's modulus, E	2.1×10^{11} Pa

4.1. Contact Force on the Casing String. Figure 9 shows that the contact force calculated with the soft model was significantly greater than that of the stiff model. The reason for this was that the soft model assumed that the casing string was in continuous contact with the borehole wall, while the stiff model assumed point contact with the borehole wall. However, the contact force calculated based on the improved continuous beam-column model was also greater than that of Fan's model. The reason for this was that the new model considered the influence of the curved wellbore on the deformation of the casing string. When the string made new contact with the borehole wall due to the initial bending deformation, the additional contact force was included in the total contact force.

4.2. Hook Load of Casing Running. When the casing string was tripped in, its axial load was mainly affected by the floating weight of the string and the friction between the string and the borehole wall. The hook loads calculated by the four models are shown in Figure 10. The hook load calculated by the soft model was less than that calculated by the stiff model in the bottom hole. The reason for this was that the friction calculated by the soft model was larger than that of the stiff

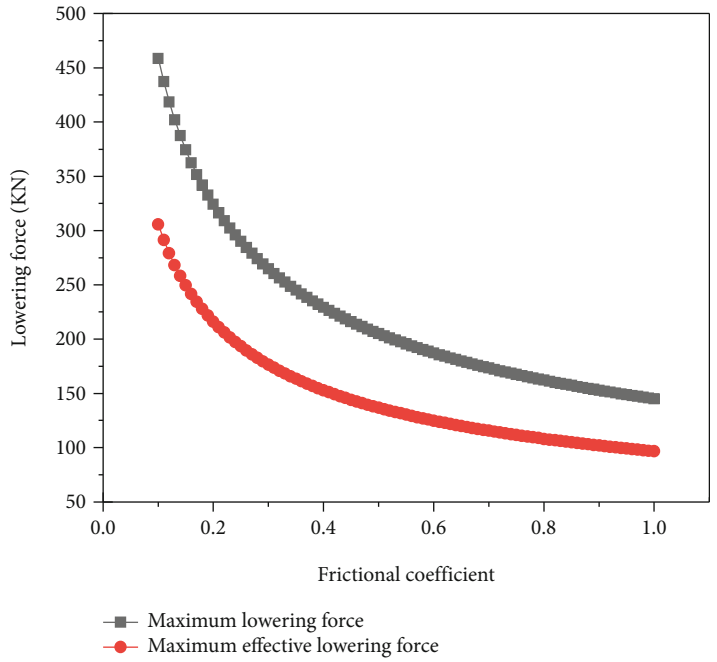

Figure 11: Lowering force on the casing string for different friction coefficients.

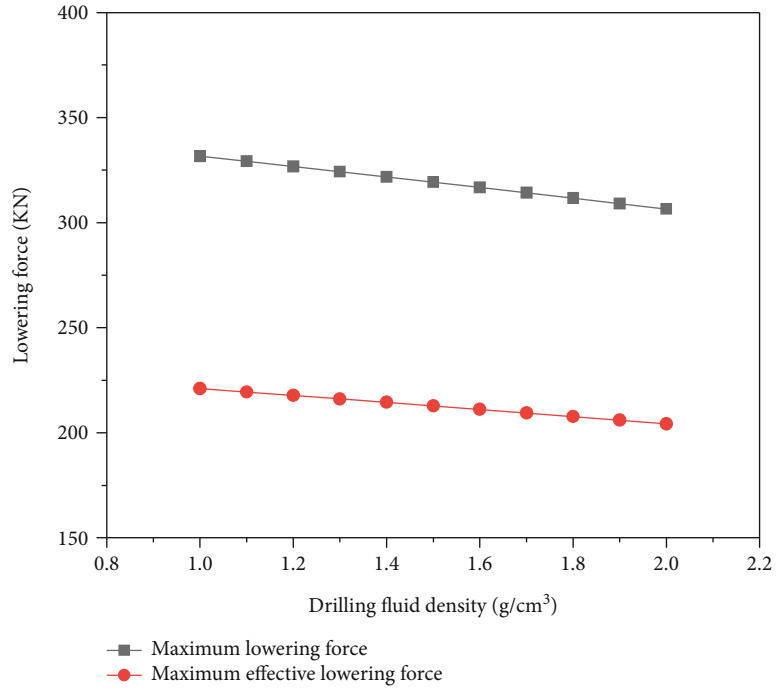

Figure 12: Lowering force on the casing string for different drilling fluid densities.

model and the friction direction was opposite to the movement direction of the casing string, which offset part of the floating weight of the casing string.

The measured hook load was highly affected and sensitive to any change in the drilling operation such as the drill string material gradient, outer diameter, inner diameter, bottom hole assembly, drilling fluid, drilling path, drilling trajectory, or dynamics of the hook. These made the measured hook load data points fluctuate greatly, which was inconvenient for the model verification. Therefore, the hook load data points were fitted with a polynomial function before validation and a fitting curve representing the hook load was obtained, as shown in Figure 10. The accuracies of the four models were verified by comparison with the

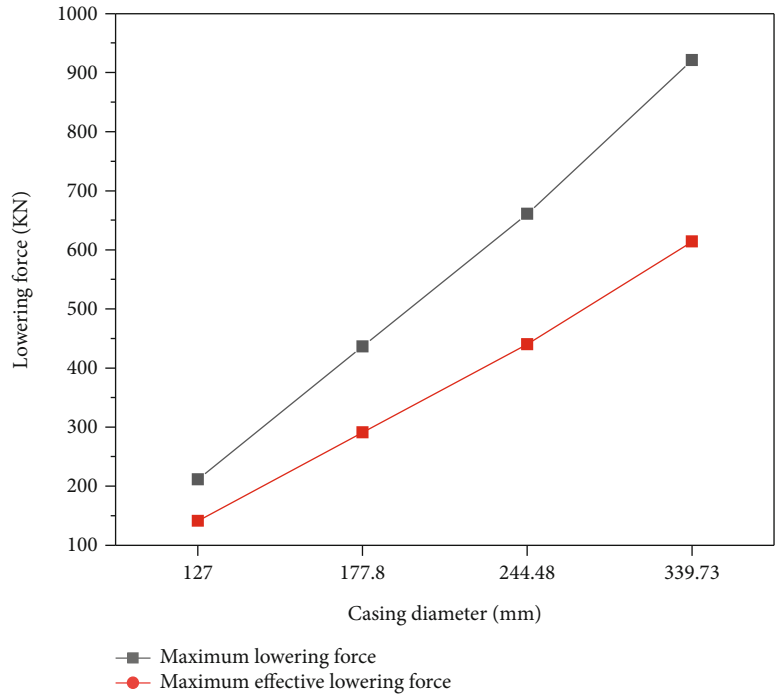

Figure 13: Lowering force on the casing string for different casing diameters.

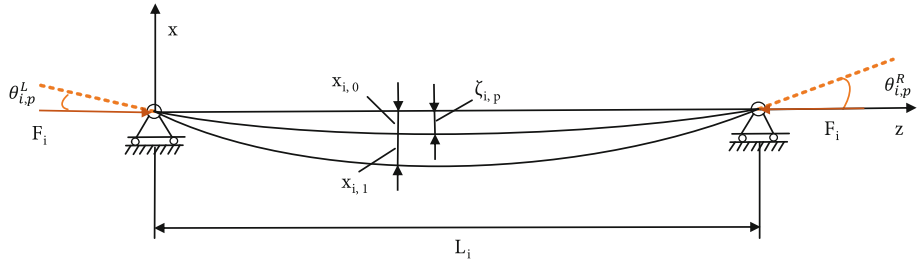

Figure 14: Beam-column with initial bending.

fitted curves. As shown in Table 3, 15 sets of large hook load data points were randomly selected from different well sections for comparison. It can be seen that the improved model had the smallest prediction error, i.e., 6.58%, compared with the existing models.

4.3. Maximum Lowering Force on the Casing String. With the 7-inch (177.8 mm) casing as an example, the parameters are shown in Table 4. The maximum lowering force and the maximum effective lowering force required for the buckled casing string to run in the wellbore were calculated.

Figure 11 shows that the maximum lowering force and the maximum effective lowering force decreased with the increase in the friction coefficient. Adjusting the performance of the drilling fluid at the appropriate time and reducing the friction coefficient increased the maximum lowering force and the maximum effective lowering force, which was conducive to applying a lowering force to the buckled casing during the casing running process.

As shown in Figure 12, the maximum lowering force and the maximum effective running force gradually decreased when the drilling fluid density increased from 1.0 to 2.0 g/cm^3, that is, increasing the drilling fluid density was not conducive to applying a lowering force to the buckled casing during the casing running process.

As shown in Figure 13, with the increase in the casing diameter, the maximum lowering force and the maximum effective lowering force increased and the difference between them also increased. The smaller the casing diameter was, the smaller the maximum lowering force and the maximum effective lowering force were. Therefore, the effect of applying the lowering force to the buckled casing with a smaller diameter was not as good as that for the buckled casing with a larger diameter.

5. Conclusions

(1) The casing string was hindered by buckling during the casing string running process. Improving the performance of the drilling fluid, reducing the friction coefficient, and reducing the drilling fluid density were conducive to applying a lowering force to the casing. The effect of applying the lowering force

to the casing with a smaller diameter was not as good as that for a casing with a larger diameter

(2) Compared with the existing models, the proposed model was no longer limited to the specified point contact range between the casing strings and the wellbore wall. Influenced by factors such as the well trajectory, string assembly, and drilling fluid performance, based on the specified point contact, newly added contact points were dynamically identified. The contact point might include contact with the upper or lower wellbore wall, which was close to the actual working conditions of casing strings running in the wellbore

(3) To account for the influence of the curved wellbore on the initial deformation of the casing strings, based on continuous beam-column theory and buckling theory, a comprehensive model for predicting the friction during casing string running and the lowering force required for hindered casing string running was established. A corresponding computer program was developed. Based on the field data verification, the improved model has the smallest prediction error, i.e., 6.58%, compared with the existing model. Therefore, the comprehensive model could be used for predicting the tripability of casing strings and the conclusions provided necessary theoretical guidance for casing running operations in directional wells

Appendix

A. Three-Moment Equations in Plane P

The rotation angle of the string at the upper tangent point is

$$\theta^R_{n+1,P} = \frac{\sum_{i=1}^{n+1} L_i}{\rho}. \tag{20}$$

The three-moment equations in plane P are

$$\begin{aligned}
\theta^R_{i,P} &= \frac{q_{i,P}L_i^3}{24EI_i}X(u_{i,P}) + \frac{M_{i,P}L_i}{3EI_i}Y(u_{i,P}) + \frac{M_{i-1,P}L_i}{6EI_i}Z(u_{i,P}),\\
\theta^L_{i+1,P} &= \frac{q_{i+1,P}L_{i+1}^3}{24EI_{i+1}}X(u_{i+1,P}) + \frac{M_{i+1,P}L_{i+1}}{3EI_{i+1}}Y(u_{i+1,P})\\
&\quad + \frac{M_{i+1,P}L_{i+1}}{6EI_{i+1}}Z(u_{i+1,P}),\\
\theta^R_{n+1,P} &= \frac{q_{n+1,P}L_{n+1}^3}{24EI_{n+1}}X(u_{n+1,P}) + \frac{M_{n+1,P}L_{n+1}}{3EI_{n+1}}Y(u_{n+1,P})\\
&\quad + \frac{M_{n+1,P}L_{n+1}}{6EI_{n+1}}Z(u_{n+1,P}),
\end{aligned} \tag{21}$$

where

$$\begin{aligned}
X(u_i) &= \frac{3}{u^3}(\tan u - u),\\
Y(u_i) &= \frac{3}{2u}\left(\frac{1}{2u} - \frac{1}{\tan 2u}\right),\\
Z(u_i) &= \frac{3}{2u}\left(\frac{1}{\sin 2u} - \frac{1}{2u}\right),\\
u_i &= \frac{L_i}{2}\sqrt{\frac{F_i}{EI_i}}w_i = w_{\text{pipe}}\left(1 - \frac{\rho_o}{\rho_{\text{pipe}}}\right),\\
q_{i,p} &= w_i \sin\left(\frac{a_{i-1}+a_i}{2}\right),\\
F_i &= -\sum_{j=1}^{i-1}\left[w_j\Delta L_j \cos\left(\frac{a_{j-1}+a_j}{2}\right)\right] - \frac{1}{2}w_i\Delta L_i \cos\left(\frac{a_{i-1}+a_i}{2}\right).
\end{aligned} \tag{22}$$

B. Effect of Initial Bending on Casing Deflection

The initial bending of the casing could be approximately considered to be consistent with the borehole curvature. If the deflection curve of the casing between the two centralizers was assumed to be a quadratic parabola, the approximate value of the maximum initial bending deflection was

$$\zeta_{i,P} = \frac{K_{i,P}L_i^2}{8}, \tag{23}$$

where $K_{i,P}$ is the borehole curvature when the ith span beam was located in plane P (°/30 m).With the action of axial and transverse forces, the initial bending of the casing string had a significant influence on the deformation of the casing string after being stressed. The most common method used to correct the effect of the initial bending is to replace the effect of the initial bending on the deflection with an equivalent transverse load and require the bending moment diagram of the transverse load to be the same as that of the axial force with initial bending. A schematic diagram of the string with initial bending is shown in Figure 14.

In Figure 14, $x_{i,0}$ is the initial bending deflection and $x_{i,1}$ is the bending deflection with the influence of the initial bending in Figure 14. It was assumed that the initial bending deflection curve was a quadratic parabola, namely,

$$x_{i,0} = \frac{4\zeta_{i,P}}{L_i^2}z_i(L_i - z_i), \tag{24}$$

where $\zeta_{i,P}$ is the maximum deflection of the initial bending and $M_{i,P} = F_{i,P}x_{i,0}$. The equivalent lateral load was

$$q_i = -\frac{d^2M_{i,p}}{dz_i^2} = -\frac{d^2(F_{i,P}x_{i,0})}{dz_i^2} = K_{i,P}F_i. \tag{25}$$

By substituting the lateral load into the bending deformation equation with the simultaneous action of a uniform load and an axial force, the maximum deflection of the casing string caused by the initial bending could be obtained:

$$x_{i,\max} = x_{i,0} + x_{i,1} = \frac{2\zeta_{i,P}}{u_i^2}\left(\frac{1}{\cos u_i} - 1\right) = \frac{K_{i,P}EI_i}{F_i}\left(\frac{1}{\cos u_i} - 1\right). \tag{26}$$

C. Determination of the Maximum Lowering Force

The contact force per unit length generated by the casing buckling on the borehole wall is

$$P = \delta \frac{rF^2}{EI}. \tag{27}$$

When the casing is bent in space, the total length of the deformed casing in contact with the borehole wall is

$$l = \frac{F}{w_m}. \tag{28}$$

The friction between the deformed casing and the borehole wall is

$$f = Pl\mu = \frac{\delta \mu r}{w_m EI} F^3. \tag{29}$$

The actual effective lowering force on the casing is

$$F_e = F - f = F - \frac{\delta \mu r}{w_m EI} F^3, \tag{30}$$

where F is the casing lowering force (N), F_e is the actual effective lowering force of the casing (N), and δ is a positive pressure coefficient.Part of the lowering force F applied on the casing is used to overcome the frictional force. It is not difficult to find that when the lowering force F increases, the effective lowering force F_e also increases. When the lowering force increases to a certain value, the effective lowering force has a maximum value. The derivative of the effective lowering force with respect to the lowering force is

$$\frac{dF_e}{dF} = 1 - \frac{3\delta \mu r}{w_m EI} F^2. \tag{31}$$

The maximum lowering force $F_{\max}$ can be obtained as follows:

$$F_{\max} = \sqrt{\frac{w_m EI}{3\delta \mu r}}. \tag{32}$$

The maximum effective lowering force $F_{e\max}$ can be obtained as follows:

$$F_{e\max} = F_{\max} - \frac{\delta \mu r}{w_m EI} F_{\max}^3. \tag{33}$$

Data Availability

The data used to support the findings of this study are available from the corresponding author upon request.

Conflicts of Interest

The authors declare that there are no conflicts of interest regarding the publication of this paper.

Acknowledgments

This paper was supported by the National Natural Science Foundation of China (no. 52104015) and the Natural Science Foundation of Shandong Province (no. ZR2021ME001).

References

[1] W. Li, G. Huang, Y. Jing, F. Yu, and H. Ni, "Modeling and mechanism analyzing of casing running with pick-up and release technique," *Journal of Petroleum Science and Engineering*, vol. 172, pp. 538–546, 2019.

[2] C. A. Johancsik, D. B. Friesen, and D. Rapier, "Torque and drag in directional wells-prediction and measurement," *Journal of Petroleum Technology*, vol. 36, no. 6, pp. 987–992, 1984.

[3] M. C. Sheppard, C. Wick, and T. Burgess, "Designing well paths to reduce drag and torque," *SPE Drilling Engineering*, vol. 2, no. 4, pp. 344–350, 1987.

[4] L. Gorokhova, A. Parry, and N. Flamant, "Comparing Soft-String and Stiff-String Methods Used to Compute Casing Centralization," *SPE Drilling & Completion*, vol. 29, no. 1, pp. 106–114, 2014.

[5] B. S. Aadnoy, M. Fazaelizadeh, and G. Hareland, "A 3D analytical model for wellbore friction," *Journal of Canadian Petroleum Technology*, vol. 49, no. 10, pp. 25–36, 2010.

[6] G. Fan, G. Huang, X. Li, and L. Wang, "Calculation model of friction torque for horizontal well string," *Drilling & Production Technology*, vol. 36, no. 5, pp. 22–25, 2013.

[7] D. Gao, "Down-hole tubular mechanics and its applications," University of Petroleum Press, Dongying, China, 2006.

[8] C. Mason and D. C. K. Chen, "Step changes needed to modernise T&D software," in *In SPE/IADC Drilling Conference*, Amsterdam, Netherlands, February, 2007.

[9] H. S. Ho, "General formulation of drillstring under large deformation and its use in BHA analysis," in *In SPE Annual Technical Conference and Exhibition*, New Orleans, Louisiana, USA, October 1986.

[10] R. F. Mitchell and R. Samuel, "How good is the torque/drag model?," *SPE Drilling & Completion*, vol. 24, no. 1, pp. 62–71, 2009.

[11] M. Fan, Y. Jiao, and W. Yu, "Geometric description of borehole centerline in three-dimensional digital simulation of drag in casing running," *Engineering Mechanics*, vol. 22, no. 2, pp. 195–199, 2005.

[12] Q. Liu, J. Jing, and X. Zhu, "Analysis on the form of contact between a drill string and drilled horizontal wellbore and the effects of friction," *Journal of Southwest Petroleum University (Science & Technology Edition)*, vol. 39, no. 5, pp. 163–169, 2017.

[13] R. F. Mitchell, "New concepts for helical buckling," *SPE Drilling Engineering*, vol. 3, no. 3, pp. 303–310, 1988.

[14] J. Bai and Y. Su, "Deviation control theory and practice," Petroleum Industry Press, Beijing, China, 1990.

[15] Y. Chen, F. Liu, X. Zhang, R. Chen, S. Chen, and Z. Zhong, "Numerical simulation of running process of casing string in

horizontal well," *China Petroleum Machinery*, vol. 38, no. 3, pp. 28–30, 2010.

[16] X. Zhu, Y. Gao, S. Liu, and J. Xu, "Feasibility of casing entering curved part in horizontal well," *Oil Field Equipment*, vol. 40, no. 4, pp. 6–8, 2011.

[17] J. Fu, L. Gong, S. Hu, F. Luo, L. Ma, and L. Shang, "Calculation of frictionnal drag of casing running in horizontal well based on ANSYS," *Oil Drilling & Production Technology*, vol. 29, no. 4, pp. 32–35, 2007.

[18] Y. Yu, H. Wang, and C. Miao, "Applications of ANSYS in tripability analysis of casing through horizontal wells," *Oil Field Equipment*, vol. 36, no. 5, pp. 67–69, 2007.

[19] A. Wu, G. Hareland, and M. Fazaelizadeh, "Torque & drag analysis using finite element method," *Modern Applied Science*, vol. 5, no. 6, p. 13, 2011.

[20] Z. Liu, Z. Lian, and L. Wang, "Stress and contact force analysis of whole hole drill string running in directional well," *China Petroleum Machinery.*, vol. 40, no. 6, pp. 13–16, 2012.

[21] V. Tikhonov, V. Khaydar, and N. Albert, "Dynamic model for stiff string torque and drag," *SPE Drilling & Completion*, vol. 29, pp. 279–294, 2014.

[22] X. Qin, D. Gao, and X. Chen, "Effects of initial curvature on coiled tubing buckling behavior and axial load transfer in a horizontal well," *Journal of Petroleum Science and Engineering*, vol. 150, pp. 191–202, 2017.

[23] Y. Shi, Z. Teng, J. Bai et al., "Improved mechanical model of the static push-the-bit rotary steerable bottomhole assembly," *Journal of China University of Petroleum (Edition of Natural Science)*, vol. 42, no. 5, pp. 75–80, 2018.

[24] H. Liu, T. Ma, P. Chen, X. Wang, and X. Wang, "Mechanical behaviors of bottom hole assembly with bent-housing positive displacement motor under rotary drilling," *Arabian Journal for Science and Engineering*, vol. 44, no. 6, pp. 6029–6043, 2019.

[25] X. Liu, *The Geometry of Wellbore Trajectory*, science press, Beijing, China, 2019.

[26] W. Li, X. Li, and G. Huang, "Method of drill string torque and drag of horizontal well based on beam-column theory," *Science Technology and Engineering*, vol. 13, no. 13, pp. 3577–3582, 2013.

[27] W. Gong, "Calculating position of casing centralizer in directional and horizontal well using three-moment of flexure method," *Oil Drilling & Production Technology*, vol. 18, no. 4, pp. 15–24, 1996.

[28] H. Liu and J. Li, "Determining the maximum load in running casing encountered resistance under deep well," *Journal of Southwest Petroleum Institute*, vol. 24, no. 2, pp. 44-45, 2002.

[29] X. Shen and R. Pounds, "Numerical analysis on the 3D mechanical behavior of completion tubing under subsidence loading," in *In International Petroleum Technology Conference*, Kuala Lumpur, Malaysia, December 2014.

Hindawi
Geofluids
Volume 2022, Article ID 3700109, 13 pages
https://doi.org/10.1155/2022/3700109

Research Article

Pressure Performance Analysis of Inclined Well under Multiple-Well Interference in Offshore Heavy Oil Reservoir

Kuiqian Ma, Gongchang Wang, Yue Gao, Meinan Wang, and Jianguo Liu

Bohai Oilfield Research Institute, Tianjin Branch Company, CNOOC Ltd., Tianjin, China 300459

Correspondence should be addressed to Gongchang Wang; wanggch12@cnooc.com.cn

Received 11 April 2022; Revised 22 May 2022; Accepted 6 June 2022; Published 13 July 2022

Academic Editor: Shuyang Liu

Copyright © 2022 Kuiqian Ma et al. This is an open access article distributed under the Creative Commons Attribution License, which permits unrestricted use, distribution, and reproduction in any medium, provided the original work is properly cited.

Offshore heavy oil reservoirs are developed mainly by inclined wells, and the well distance has been constantly reduced after several well network adjustments. The well test data are often interfered by adjacent wells, resulting in unsatisfactory well test interpretation results, so it is necessary to conduct studies on the multiwell interference well test problem for inclined wells. In this paper, the threshold pressure gradient of heavy oil and the stress sensitive to permeability are considered comprehensively, and a well test model of inclined wells in dual-media reservoirs under multiwell interference is established. The analytical solution in Laplace space is obtained by using Green function and superposition principle. The results show that the typical pressure dynamic curve can be divided into 12 flow regions, and the pressure derivative curve of the central inclined well is upturned and forms multiple "platforms" under the interference of adjacent wells; the adjacent well interference will aggravate the upward of pressure derivative curve; a critical well inclination angle of the inclined well is 40°. When the well inclination angle is greater than 40°, vertical radial flow similar to horizontal wells will appear. The new model is well matched and interpreted in the application of BZ oil field in Bohai Bay, which provides theoretical guidance for multiwell interference test wells in the similar reservoir.

1. Introduction

Currently common well test interpretation methods assume that only one central test well exists in the reservoir. As the field is developed to a later stage, reservoir connectivity becomes more complex, and interference between adjacent wells becomes more pronounced. The test well pressure dynamic curve is often interfered by adjacent wells, causing the late radial flow section to "upturn," which is often treated as a boundary influence in common single-well test models, leading to mishandling of well test data [1–3]. Onur et al. proposed a pressure recovery model including multiproduction well system [4]. Marhaendrajana et al. developed a method to explain the pressure in a multiwell system by considering the "disturbance effect" as a regional pressure drop [5]. Adewole evaluated the connectivity between wells based on the pressure data of test wells under interference [6]. Deng et al. established an interpretation method for pressure recovery under multiple well interference [7]. Cheng et al. used the multiwell interference method to judge the water inflow direction of horizontal wells [8]. Yang et al. developed a novel interference testing model of a multisegment horizontal well (MSHW) to better understand the interference of injection wells when the horizon observation well is open to produce [9]. Kumar et al. established a mathematical interference testing model of the fractured vuggy carbonate reservoirs that then used to test an observation well and two interfering wells in Tarim oilfield [10]. Han et al. presented an integrated approach based on the analysis of tracer and pressure interference data to obtain the degree of interference between fractured horizontal wells in a multiwell pad [11]. Shiqing et al. plotted the type curve of pressure and the pressure derivative of an interference test of wells connected by a large fracture and verified against interference test data [12].

Due to the special characteristics of offshore platforms, inclined wells can adapt to complex geological problems and increase oil seepage area to improve well production and are now widely used in offshore oil fields. Cinco et al. first analyzed and plotted the pressure dynamics of an

inclined well by building an up-and-down closed test well model [13]. Zhang et al. studied the effect of formation heterogeneity on the pressure of inclined wells [14]. Sousa studied the pressure dynamics of inclined wells in homogeneous reservoirs [15]. Li et al. established which belongs to the inclined well in the composite gas reservoir with a conventional internal zone and low-permeability external zone, which comprehensively considered characteristics of stress sensitivity and non-Darcy flow for low-permeability composite gas reservoirs [16].

In summary, there has been no study on the interference of adjacent wells on the pressure dynamic of inclined well. However, as inclined wells are currently the most dominant development method in offshore oil fields, it is important to study an adjacent well interference well test model applicable to inclined wells. In this paper, considering the stress sensitivity to permeability and the threshold pressure gradient of heavy oil, an inclined well test model under multiwell interference in offshore heavy oil reservoirs is established, and the effects of multiple types of sensitive parameters are analyzed. Finally, the model is well applied in the SZ oil field of Bohai Bay.

2. Model Development

2.1. Nonlinear Seepage of Heavy Oil. Heavy oil has high viscosity, large seepage resistance, and large interaction force between liquid-solid interface and liquid-liquid interface [17–19]. Therefore, the seepage characteristics in porous media are different from those of conventional thin oil and generally show nonlinear seepage characteristics (threshold pressure gradient) [20–23]. Only when the displacement pressure gradient exceeds the threshold pressure gradient does the heavy oil begin to flow, and its seepage characteristics are shown in Figure 1.

The core displacement experiments in Bohai SZ oilfield show that the threshold pressure gradient and mobility of heavy oil in porous media conform to the nonlinear relationship, as shown in Figure 2. When the mobility is small, the pressure gradient decreases rapidly with the increase of mobility. With the continuous increase of mobility, the decline of threshold pressure gradient slows down and is matched by exponential function, as shown in Equation (1). The reason for this phenomenon is that with the decrease of viscosity of heavy oil, the content of gum, asphaltene, and high molecular hydrocarbons in heavy oil decreases, resulting in the weakening of structural characteristics of heavy oil, the reduction of intermolecular force during flow, and the reduction of flow resistance. With the increase of permeability, the faster the resistance decreases,

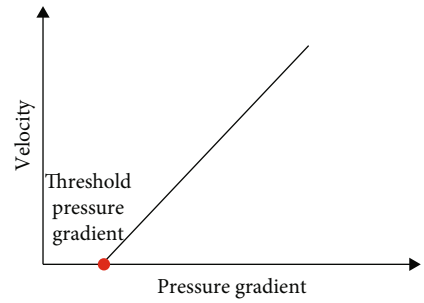

Figure 1: Heavy oil seepage characteristics dynamic curve.

resulting in the gradual decrease of heavy oil threshold pressure gradient with the increase of mobility.

$$\lambda_B = a\left(\frac{K}{\mu_o}\right)^{-b}. \tag{1}$$

2.2. Physical Model. As is shown in Figure 3, there is a central test inclined well in infinite outer boundary reservoir, and the surrounding adjacent wells have good connectivity with it:

(1) The Warren-Root model is adopted to describe the dual-porosity formation

(2) The interporosity flow is calculated through the pseudo-steady-state model

(3) Stress sensitivity of permeability is considered

(4) Heavy oil in porous media has the property of threshold pressure gradient

2.3. Mathematical Model. Considering the permeability stress-sensitive of reservoir and the threshold pressure gradient of heavy oil fluid, the fluid motion equation is improved as follows:

$$v_{fr} = \frac{K_{fh}}{\mu} e^{-\gamma(p_i - p_f)}\left(\frac{\partial p_f}{\partial r} - \lambda_B\right), \tag{2}$$

$$v_{fz} = \frac{K_{fv}}{\mu} e^{-\gamma(p_i - p_f)}\left(\frac{\partial p_f}{\partial r} - \lambda_B\right). \tag{3}$$

By virtue of Equation (1) and Equation (2), the seepage differential equation of central test inclined well describing the threshold pressure gradient of heavy oil in stress sensitive reservoir is obtained:

$$\begin{cases} \dfrac{K_{fh}}{\mu}\dfrac{1}{r}\dfrac{\partial}{\partial r}\left[re^{-\gamma(p_i-p_f)}\left(\dfrac{\partial p_f}{\partial r} - \lambda_B\right)\right] + \dfrac{K_{fv}}{\mu}\dfrac{\partial}{\partial z}\left[e^{-\gamma(p_i-p_f)}\left(\dfrac{\partial p_f}{\partial z} - \lambda_B\right)\right] = (\phi C_t V)_f \dfrac{\partial p_f}{\partial t} - \dfrac{\alpha K_m}{\mu}(p_m - p_f), \\ (\phi C_t V)_m \dfrac{\partial p_m}{\partial t} + \dfrac{\alpha K_m}{\mu}(p_m - p_f) = 0. \end{cases} \tag{4}$$

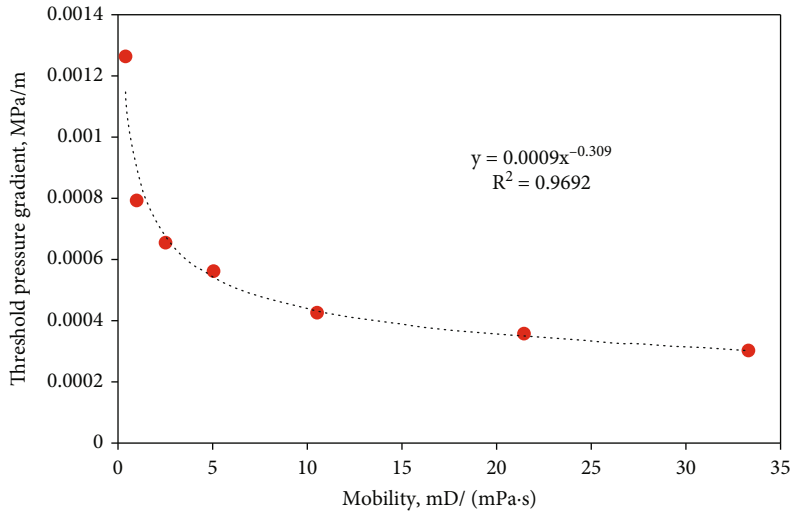

Figure 2: Relation curve between pressure gradient and mobility.

The following is the differential equation of adjacent interference wells:

$$\begin{cases} \dfrac{K_{\mathrm{fh}}}{\mu}\dfrac{1}{r}\dfrac{\partial}{\partial r}\left[re^{-\gamma(p_{\mathrm{i}}-p_{\mathrm{f}})}\left(\dfrac{\partial p_{\mathrm{f}}}{\partial r}-\lambda_{\mathrm{B}}\right)\right]=(\phi C_{\mathrm{t}}V)_{\mathrm{f}}\dfrac{\partial p_{\mathrm{f}}}{\partial t}-\dfrac{\alpha K_{\mathrm{m}}}{\mu}(p_{\mathrm{m}}-p_{\mathrm{f}}), \\ (\phi C_{\mathrm{t}}V)_{\mathrm{m}}\dfrac{\partial p_{\mathrm{m}}}{\partial t}+\dfrac{\alpha K_{\mathrm{m}}}{\mu}(p_{\mathrm{m}}-p_{\mathrm{f}})=0. \end{cases} \tag{5}$$

Since the values of $(\partial p_{\mathrm{f}}/\partial r)\times\lambda_{\mathrm{B}}$ and $(\partial p_{\mathrm{f}}/\partial z)\times\lambda_{\mathrm{B}}$ are small, they can be rounded off and the above equation can be simplified as follows.

Central test inclined well:

$$\begin{cases} K_{\mathrm{fh}}\left[\dfrac{1}{r}\dfrac{\partial}{\partial r}\left(r\dfrac{\partial p_{\mathrm{f}}}{\partial r}\right)+\gamma\left(\dfrac{\partial p_{\mathrm{f}}}{\partial r}\right)^{2}-\dfrac{\lambda_{\mathrm{B}}}{r}\right]+K_{\mathrm{fv}}\left[\dfrac{\partial^{2}p_{\mathrm{f}}}{\partial z^{2}}+\gamma\left(\dfrac{\partial p_{\mathrm{f}}}{\partial z}\right)^{2}\right]=e^{\gamma(p_{i}-p_{\mathrm{f}})}\left[(\phi C_{\mathrm{t}}V)_{\mathrm{f}}\mu\dfrac{\partial p_{\mathrm{f}}}{\partial t}-\alpha K_{\mathrm{m}}(p_{\mathrm{m}}-p_{\mathrm{f}})\right], \\ (\phi C_{\mathrm{t}}V)_{\mathrm{m}}\dfrac{\partial p_{\mathrm{m}}}{\partial t}+\dfrac{\alpha K_{\mathrm{m}}}{\mu}(p_{\mathrm{m}}-p_{\mathrm{f}})=0. \end{cases} \tag{6}$$

Adjacent interference well:

$$\begin{cases} K_{\mathrm{fh}}\left[\dfrac{1}{r}\dfrac{\partial}{\partial r}\left(r\dfrac{\partial p_{\mathrm{f}}}{\partial r}\right)+\gamma\left(\dfrac{\partial p_{\mathrm{f}}}{\partial r}\right)^{2}-\dfrac{\lambda_{\mathrm{B}}}{r}\right]=e^{\gamma(p_{\mathrm{i}}-p_{\mathrm{f}})}\left[(\phi C_{\mathrm{t}}V)_{\mathrm{f}}\mu\dfrac{\partial p_{\mathrm{f}}}{\partial t}-\alpha K_{\mathrm{m}}(p_{\mathrm{m}}-p_{\mathrm{f}})\right], \\ (\phi C_{\mathrm{t}}V)_{\mathrm{m}}\dfrac{\partial p_{\mathrm{m}}}{\partial t}+\dfrac{\alpha K_{\mathrm{m}}}{\mu}(p_{\mathrm{m}}-p_{\mathrm{f}})=0. \end{cases} \tag{7}$$

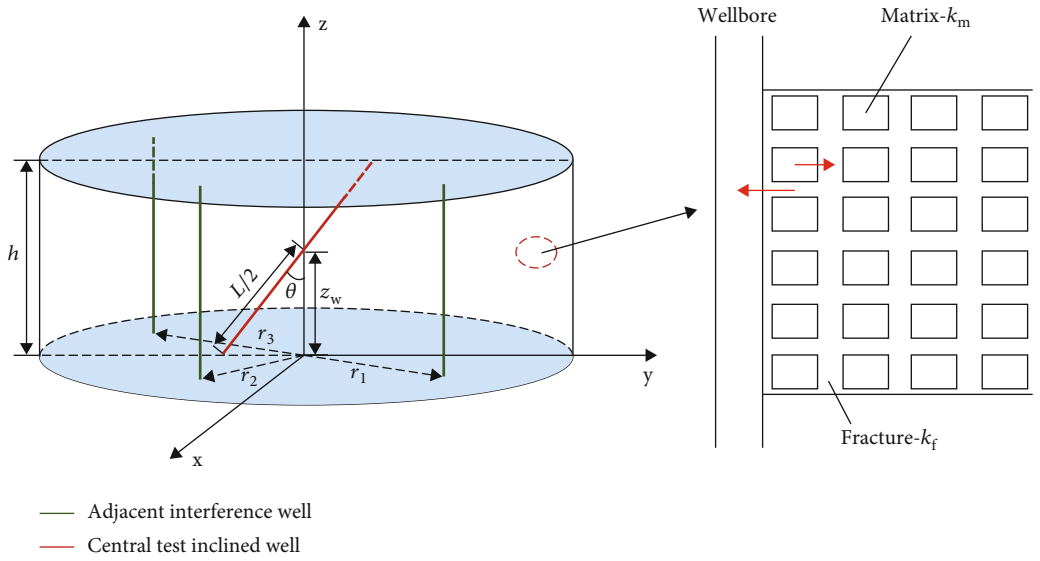

Figure 3: Physical model diagram.

Dimensionless quantities are defined as follows:

$p_{fD} = (2\pi\ K_{fh}h/q\mu)\ (p_i - p_f)\ p_{mD} = (2\pi K_m\ h/q\mu)(p_i - p_m)\ t_D = (K_{fh}t/\mu r_w^2(V\phi C_t)_{f+m})\omega = ((V\phi\ C_t)_f/(V\phi C_t)_{f+m})\lambda_m = \alpha r_w^2\ (K_m/K_{fh})\gamma_D = (q\mu B/K_{fh}h)\gamma\lambda_{BD} = (K_{fh}hr_w/q\mu B)\ \lambda_B\ r_D = (r/r_w)\ z_D = (z/h)C_D = (C/(V\phi C_t)_{f+m}hr\ w^2)L_D = (L/h)\sqrt{K_{fh}/K_{fv}}\ h_D = (h/r_w)\ \sqrt{K_{fh}/K_{fv}}$.

Substituting the above dimensionless quantities into formulas (5) and (6), the dimensionless seepage differential equation is obtained:

$$\begin{cases} \dfrac{1}{r_D}\dfrac{\partial}{\partial r_D}\left(r_D\dfrac{\partial p_{fD}}{\partial r_D}\right) - \gamma_D\left(\dfrac{\partial p_{fD}}{\partial r_D}\right) + \dfrac{\lambda_{BD}}{r_D} + \left[\dfrac{\partial^2 p_{fD}}{\partial z_D^2} + \gamma_D\left(\dfrac{\partial p_{fD}}{\partial z_D}\right)^2\right] = e^{\gamma_D p_{fD}}\left[\omega\dfrac{\partial p_{fD}}{\partial t_D} - \lambda_m(p_{mD} - p_{fD})\right], \\ \omega\dfrac{\partial p_{mD}}{\partial t_D} + \lambda_m(p_{mD} - p_{fD}) = 0, \end{cases} \tag{8}$$

$$\begin{cases} \dfrac{1}{r_{jD}}\dfrac{\partial}{\partial r_{jD}}\left(r_{jD}\dfrac{\partial p_{fD}}{\partial r_{jD}}\right) - \gamma_D\left(\dfrac{\partial p_{fD}}{\partial r_{jD}}\right) + \dfrac{\lambda_{BD}}{r_{jD}} = e^{\gamma_D p_{fD}}\left[\omega\dfrac{\partial p_{fD}}{\partial t_{jD}} - \lambda_m(p_{mD} - p_{fD})\right], \\ \omega\dfrac{\partial p_{mD}}{\partial t_{jD}} + \lambda_m(p_{mD} - p_{fD}) = 0. \end{cases} \tag{9}$$

Central test inclined well is as follows:

Initial condition

$$p_{fD}(r_D, 0) = p_{mD}(r_D, 0) = 0. \tag{10}$$

Outer boundary condition

$$p_{fD}\big|_{r_D\longrightarrow\infty} = p_{mD}\big|_{r_D\longrightarrow\infty} = 0. \tag{11}$$

Inner boundary condition

$$\lim_{\varepsilon\longrightarrow 0}\left[\lim_{r_D\longrightarrow 0}\int_{z_{wD}-\varepsilon/2}^{z_{wD}+(\varepsilon/2)} r_D e^{-\gamma_D p_{fD}}\left(\frac{\partial p_{fD}}{\partial r_D} + \lambda_{BD}\right)dz_D\right] = -h_D\,|z_D - z_{wD}| \le \frac{\varepsilon}{2}. \tag{12}$$

Adjacent interference well ($j = 1, 2, 3 \cdots$) is as follows.
Initial condition

$$p_{\mathrm{fD}}\left(r_{\mathrm{jD}}, 0\right) = p_{\mathrm{mD}}\left(r_{\mathrm{jD}}, 0\right) = 0. \tag{13}$$

Outer boundary condition

$$p_{\mathrm{fD}}\Big|_{r_{\mathrm{jD}}\longrightarrow\infty} = p_{\mathrm{mD}}\Big|_{r_{\mathrm{jD}}\longrightarrow\infty} = 0. \tag{14}$$

Inner boundary condition

$$r_{\mathrm{jD}}\frac{\partial p_{\mathrm{fD}}}{\partial r_{\mathrm{jD}}}\Big|_{r_{\mathrm{jD}}=1} - \lambda_{\mathrm{BD}} = -q_{\mathrm{jD}}. \tag{15}$$

Top and bottom conditions for

$$\frac{\partial p_{\mathrm{fD}}}{\partial z_{\mathrm{D}}}\Big|_{z_{\mathrm{D}}=0} = \frac{\partial p_{\mathrm{mD}}}{\partial z_{\mathrm{D}}}\Big|_{z_{\mathrm{D}}=0} = 0, \tag{16}$$

$$\frac{\partial p_{\mathrm{fD}}}{\partial z_{\mathrm{D}}}\Big|_{z_{\mathrm{D}}=h_{\mathrm{D}}} = \frac{\partial p_{\mathrm{mD}}}{\partial z_{\mathrm{D}}}\Big|_{z_{\mathrm{D}}=h_{\mathrm{D}}} = 0. \tag{17}$$

3. Model Solution

In order to eliminate the quadratic term in the above dimensionless equation, Pedrosa variable substitution and regular perturbation method are used:

$$p_{\mathrm{fD}} = -\frac{1}{\gamma_{\mathrm{D}}}\ln\left(1 - \gamma_{\mathrm{D}}\xi_{\mathrm{D}}\right). \tag{18}$$

Because $\gamma_{\mathrm{D}} \ll 1$, the zero order perturbation solution is taken, and then, Laplace transform is performed on it. Finally, equations (5) and (6) become as follows:

Central test inclined well:

$$\frac{1}{r_{\mathrm{D}}}\frac{\partial}{\partial r_{\mathrm{D}}}\left(r_{\mathrm{D}}\frac{\partial \bar{\xi}_{\mathrm{D0}}}{\partial r_{\mathrm{D}}}\right) + \frac{\lambda_{\mathrm{BD}}}{s r_{\mathrm{D}}} + \frac{\partial^2 \bar{\xi}_{\mathrm{D0}}}{\partial z_{\mathrm{D}}^2} = \omega s\bar{\xi}_{\mathrm{D0}} + (1-\omega)s\bar{p}_{\mathrm{mD}}, \tag{19}$$

$$\bar{p}_{\mathrm{mD}} = \frac{\lambda_{\mathrm{m}}}{\lambda_{\mathrm{m}} + (1-\omega)s}\bar{\xi}_{\mathrm{D0}}, \tag{20}$$

$$\bar{\xi}_{\mathrm{D0}}\big|_{r_{\mathrm{D}}\longrightarrow\infty} = \bar{p}_{\mathrm{mD}}\big|_{r_{\mathrm{D}}\longrightarrow\infty} = 0, \tag{21}$$

$$\lim_{\varepsilon\longrightarrow 0}\left[\lim_{r_{\mathrm{D}}\longrightarrow 0}\int_{z_{\mathrm{wD}}-\varepsilon/2}^{z_{\mathrm{wD}}+(\varepsilon/2)} r_{\mathrm{D}}e^{-\gamma_{\mathrm{D}}p_{\mathrm{fD}}}\left(\frac{\partial \bar{\xi}_{\mathrm{D0}}}{\partial r_{\mathrm{D}}} + \lambda_{\mathrm{BD}}\right)dz_{\mathrm{D}}\right] = -h_{\mathrm{D}}, \left|z_{\mathrm{D}} - z_{\mathrm{wD}}\right| \le \frac{\varepsilon}{2}. \tag{22}$$

Adjacent interference well ($j = 1, 2, 3 \cdots$):

$$\frac{1}{r_{\mathrm{jD}}}\frac{\partial}{\partial r_{\mathrm{jD}}}\left(r_{\mathrm{jD}}\frac{\partial \bar{\xi}_{\mathrm{D0j}}}{\partial r_{\mathrm{jD}}}\right) + \frac{\lambda_{\mathrm{BD}}}{s r_{\mathrm{D}}} = \omega s\bar{\xi}_{\mathrm{D0j}} + (1-\omega)s\bar{p}_{\mathrm{mD}}, \tag{23}$$

$$\bar{p}_{\mathrm{mD}} = \frac{\lambda_{\mathrm{m}}}{\lambda_{\mathrm{m}} + (1-\omega)s}\bar{\xi}_{\mathrm{D0j}}, \tag{24}$$

$$\bar{\xi}_{\mathrm{D0j}}\Big|_{r_{\mathrm{jD}}\longrightarrow\infty} = \bar{p}_{\mathrm{mD}}\Big|_{r_{\mathrm{jD}}\longrightarrow\infty} = 0, \tag{25}$$

$$\frac{\partial \bar{\xi}_{\mathrm{D0j}}}{\partial r_{\mathrm{jD}}} + \frac{\lambda_{\mathrm{BD}}}{s} = -\frac{q_{\mathrm{jD}}}{s}, \tag{26}$$

$$\frac{\partial \bar{\xi}_{\mathrm{D0}}}{\partial z_{\mathrm{D}}}\Big|_{z_{\mathrm{D}}=0} = \frac{\partial p_{\mathrm{mD}}}{\partial z_{\mathrm{D}}}\Big|_{z_{\mathrm{D}}=0} = 0, \tag{27}$$

$$\frac{\partial \bar{\xi}_{\mathrm{D0}}}{\partial z_{\mathrm{D}}}\Big|_{z_{\mathrm{D}}=h_{\mathrm{D}}} = \frac{\partial p_{\mathrm{mD}}}{\partial z_{\mathrm{D}}}\Big|_{z_{\mathrm{D}}=h_{\mathrm{D}}} = 0. \tag{28}$$

According to the superposition principle, the finite cosine integral transform of the model under Laplace space with respect to z_{D}, and then using the Green function and the zero-order regenerative solution, the point source solution of the model can be found as

$$\begin{aligned}\bar{\xi}_{\mathrm{D}} \approx \bar{\xi}_{\mathrm{D0}} + \bar{\xi}_{\mathrm{D0j}} &= \frac{1}{s}K_0\left[r_{\mathrm{D}}\sqrt{sf(s)}\right] \\ &+ \frac{2}{s}\sum_{n=1}^{\infty}K_0\left(r_{\mathrm{D}}\sqrt{sf(s) + \frac{n^2\pi^2}{h_{\mathrm{D}}^2}}\right)\times\cos\left(\frac{n\pi z_{\mathrm{D}}}{h_{\mathrm{D}}}\right)\cos\left(\frac{n\pi z_{\mathrm{wD}}}{h_{\mathrm{D}}}\right) \\ &+ \sum_{\mathrm{j}=1}^{m}\left[\frac{q_{\mathrm{Dj}}\mathrm{K}_0\left(r_{\mathrm{jD}}\sqrt{sf(s)}\right)}{s\sqrt{sf(s)}\mathrm{K}_1\left(\sqrt{sf(s)}\right)} + \int_0^{+\infty}G\left(r_{\mathrm{jD}}, \tau\right)d\tau\right] \\ &+ \int_0^{+\infty}G(r_{\mathrm{D}}, \tau)d\tau.\end{aligned} \tag{29}$$

Assuming that the flow in the wellbore of the central inclined well is evenly inferenced, according to the point source theory, the point source solution is integrated along the wellbore direction, and the bottom hole pressure solution of the central inclined well under multiwell interference can be obtained.

$$\begin{aligned}\bar{\xi}_{\mathrm{wDN}} &= \frac{1}{sL_{\mathrm{D}}}\int_{-L_{\mathrm{D}}/2}^{L_{\mathrm{D}}/2}K_0[\bar{r}_{\mathrm{D}}sf(s)]d\eta \\ &+ \frac{2}{sL_{\mathrm{D}}}\int_{-L_{\mathrm{D}}/2}^{L_{\mathrm{D}}/2}\sum_{n=1}^{\infty}K_0\left(\bar{r}_{\mathrm{D}}\sqrt{sf(s) + \frac{n^2\pi^2}{h_{\mathrm{D}}^2}}\right) \\ &\times\cos\left(\frac{n\pi z_{\mathrm{D}}}{h_{\mathrm{D}}}\right)\cos\left(\frac{n\pi\bar{z}_{\mathrm{wD}}}{h_{\mathrm{D}}}\right)d\eta + \frac{1}{L_{\mathrm{D}}}\int_0^{+\infty}\int_{-L_{\mathrm{D}}/2}^{L_{\mathrm{D}}/2}G(\bar{r}_{\mathrm{D}}, \tau)d\eta d\tau \\ &+ \sum_{\mathrm{j}=1}^{m}\left[\frac{q_{\mathrm{Dj}}\mathrm{K}_0\left(r_{\mathrm{jD}}\sqrt{sf(s)}\right)}{s\sqrt{sf(s)}\mathrm{K}_1\left(\sqrt{sf(s)}\right)} + \int_0^{+\infty}G\left(r_{\mathrm{jD}}, \tau\right)d\tau\right],\end{aligned} \tag{30}$$

$$\bar{r}_{\mathrm{D}} = \sqrt{\left(x_{\mathrm{D}} - x_{\mathrm{wD}} - \eta\sin\theta_{\mathrm{w}}\right)^2 + \left(y_{\mathrm{D}} - y_{\mathrm{wD}}\right)^2}, \tag{31}$$

$$\bar{z}_{\mathrm{wD}} = z_{\mathrm{wD}} + \eta\cos\theta_{\mathrm{w}}, \tag{32}$$

$$\theta_w = \arctan\left(\sqrt{\frac{K_{fv}}{K_{fh}}}\tan\theta\right), \tag{33}$$

$$L_D = \frac{L}{r_w}\sqrt{\frac{K_{fv}}{K_{fh}}\sin^2\theta + \frac{K_{fv}}{K_{fh}}\cos^2\theta}. \tag{34}$$

Duhamel principle and pressure drop superposition principle are used to solve the bottom hole pressure solution of the central inclined well under the interference of multi-wells.

$$\bar{\xi}_{WD} = \frac{s\bar{\xi}_{WDN} + S}{s + C_D s^2\left(s\bar{\xi}_{WDN} + S\right)}. \tag{35}$$

Through Stehfest numerical inversion, the bottom hole pressure solution in real space can be obtained [24, 25]:

$$p_{wD} = -\frac{1}{\gamma_D}\ln\left(1 - \gamma_D\bar{\xi}_{WD}\right). \tag{36}$$

4. Results and Discussion

4.1. Model Verification. When dimensionless threshold pressure gradient (λ_{BD}), dimensionless stress sensitivity coefficients (γ_D), and well inclination angle (θ) are taken as zero, as well there is no interference from adjacent wells, the model is the same as the conventional vertical well pressure drawdown well test model of dual media reservoir. In order to verify the model in the paper, the type curve obtained by the numerical method is compared with the conventional dual media reservoir well test curve obtained by the analytical solution shown in Figure 4.

As shown in Figure 4, the type curve of pressure drawdown well test obtained by the numerical solution and the analytical solution are the same when dimensionless threshold pressure gradient (λ_{BD}), dimensionless stress sensitivity coefficients (γ_D), and well inclination angle (θ) are taken as zero, as well there is no interference from adjacent wells. Thus, the numerical solution in the paper is reliable.

4.2. Type Curves. The pressure solution in real space is obtained by numerical inversion. Taking the existence of three adjacent wells around the central inclined well as an example, its pressure curve and pressure derivative curve are plotted as shown in Figures 5–12; flow regions are identified.

Region 1. The early wellbore storage period: the pressure curve and pressure derivative curve are line segments with a slope equal to "1," reflecting the effect of wellbore reservoir effects

Region 2. The skin effect period: the major influential factor in this period is the skin factor effect, and the pressure derivative curve presents the shape of "hump"

Region 3. Well inclination angle influence period: the pressure derivative curve presents the shape of "concavity," which reflects the influence of well inclination angle. When the well inclination angle is large, it shows the characteristics of vertical radial flow in horizontal wells; when the well inclination angle is small, it shows the characteristics of radial flow for vertical wells

Region 4. Fracture radial flow period: the major influential factor in this period is the flow of fluid from fracture to bottom hole, and the pressure derivative curve is a straight horizontal line

Region 5. Leakage period: the major influential factor in this period is the leakage capacity of matrix to fracture, and the pressure derivative curve presents the shape of "concavity"

Region 6. First radial flow period: the major influential factor in this period is the late radial flow of the central inclined well, and the pressure derivative curve is a straight horizontal line

Region 7. Transitional flow period: transition period between radial flows

Region 8. Second radial flow period: it reflects the radial flow characteristics of the central inclined well interfered by the nearest adjacent well, and the pressure derivative curve is a straight horizontal line

Region 9. Transitional flow period: transition period between radial flows

Region 10. Third radial flow period: it reflects the radial flow characteristics of the central inclined well interfered by the two nearest adjacent well, and the pressure derivative curve is a straight horizontal line

Region 11. Transitional flow period: transition period between radial flows

Region 12. Fourth radial flow period: it reflects the radial flow characteristics of the central inclined well interfered by the three nearest adjacent well, and the pressure derivative curve is a straight horizontal line

4.3. Sensitivity Analysis

4.3.1. Permeability Modulus. As shown in Figure 6, with the increase of permeability modulus, the pressure dynamic curve is gradually upward after region 7, and the larger the permeability modulus is, the greater the degree of upward. The reason for the above phenomenon is that the larger the permeability modulus is, the greater the decrease of permeability with the increase of pressure; therefore, the resistance of fluid flow becomes larger and the pressure required for flow is also larger. When the permeability modulus is large, the reservoir permeability decreases sharply under higher pressure in the late stage of seepage, and the pressure dynamic curve reflects a characteristic similar to a closed outer boundary.

4.3.2. Threshold Pressure Gradient. As shown in Figure 7, the higher the threshold pressure gradient of heavy oil, the greater the upward warping degree of pressure dynamic curve, and the upward warping is obvious after region 7. This is because heavy oil has threshold pressure gradient, the flow capacity of heavy oil in pores is weakened, and the displacement pressure difference required for heavy oil flow is also larger.

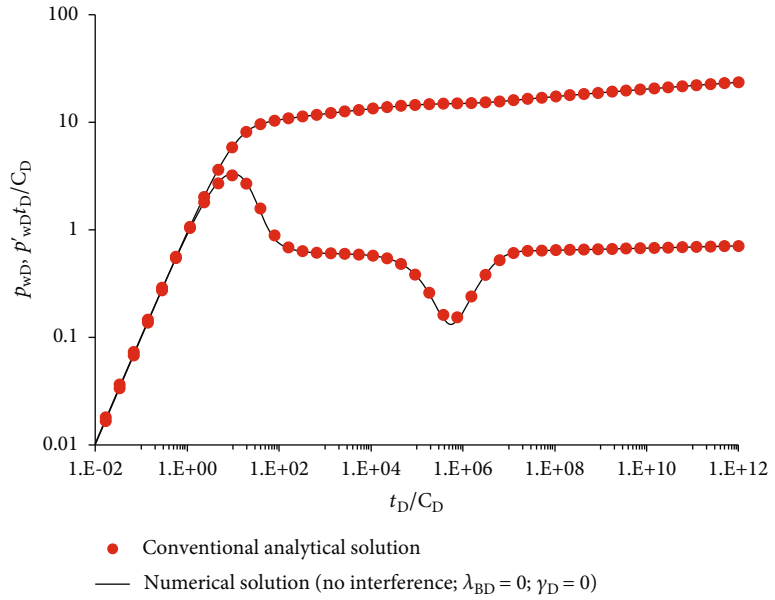

Figure 4: Comparison between the numerical solution and the analytical solution to the pressure drawdown well test.

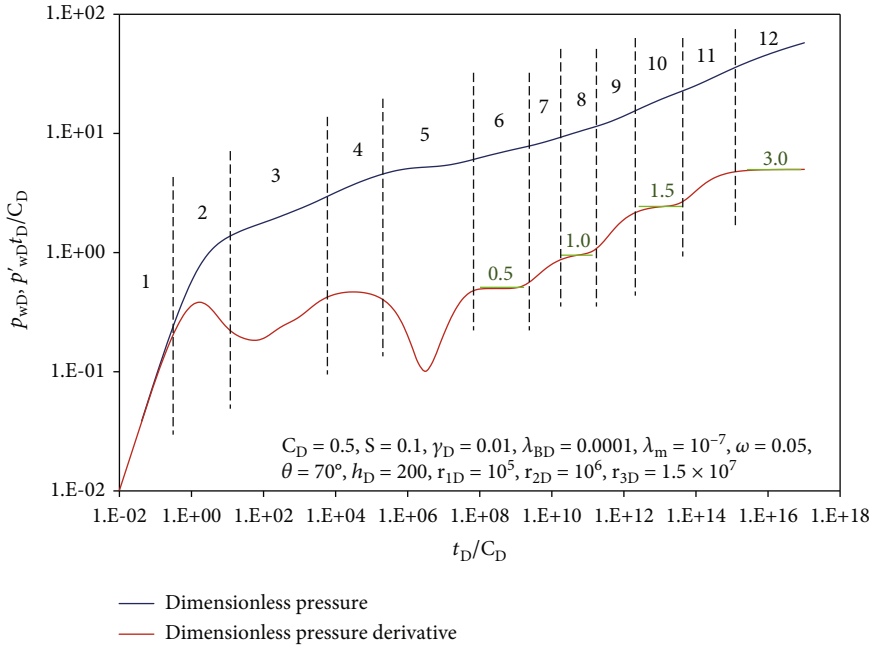

Figure 5: Typical pressure dynamic curves.

4.3.3. Production of Adjacent Wells. As shown in Figure 8, taking the example of the presence of three connected adjacent wells around the central inclined well, the pressure dynamic profile of the central inclined well has four late radial flow stages and the ratio of the N^{th} ($N > 2$) radial flow value to the first radial flow value is equal to $1 + \sum_{j=1}^{k} q_{jD}$ (k is the number of adjacent wells that have an influence on the N^{th} radial flow stage). Taking $q_{1D} = q_{2D} = q_{3D} = 1$ as an example, the third radial flow stage is the result of the joint influence of the test well and the two adjacent wells, so the value of the third radial flow is $0.5 * (1 + 2) = 1.5$.

4.3.4. Well Inclination Angle. As shown in Figure 9, the greater the well inclination angle, the greater the wellbore pressure drop and the lower the pressure dynamic curve. Because the inclined well completely penetrates the formation, the larger well inclination angle is, the longer the wellbore length is. Under the assumption of equal flow in the wellbore, the longer the wellbore length L, the greater the pressure drop in the wellbore. And the well inclination angle mainly affects the flow near the well, when well inclination angle is large ($\theta > 40°$), the curve will show an early vertical radial flow similar to that of a horizontal well, and when

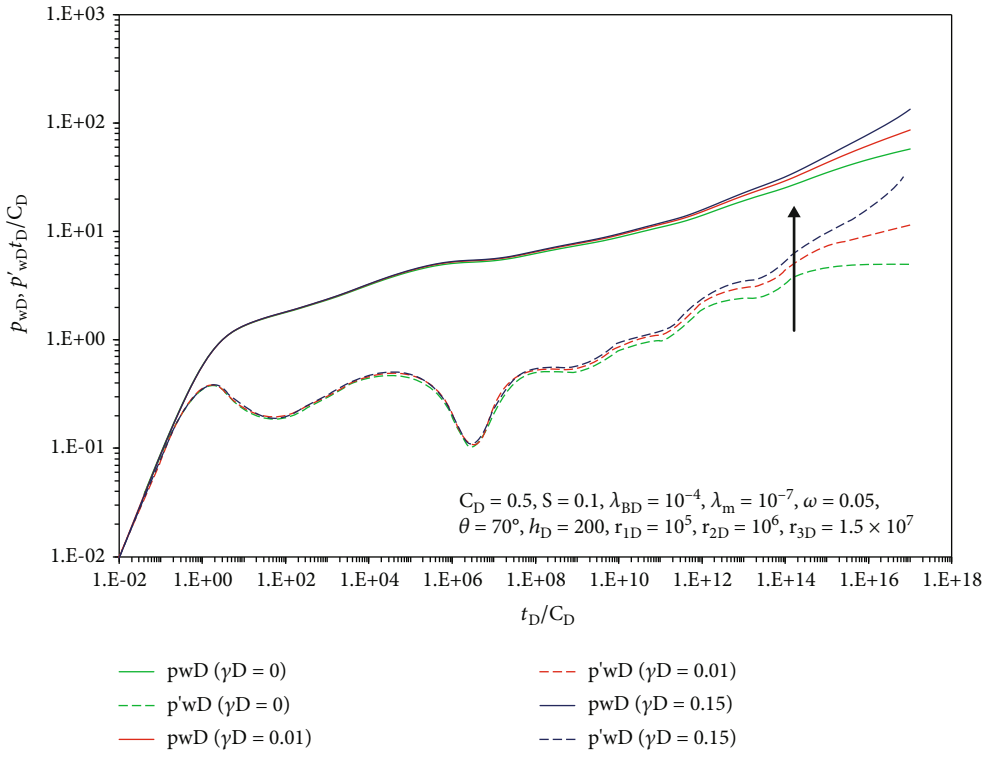

Figure 6: Influence of permeability modulus on pressure dynamic curve.

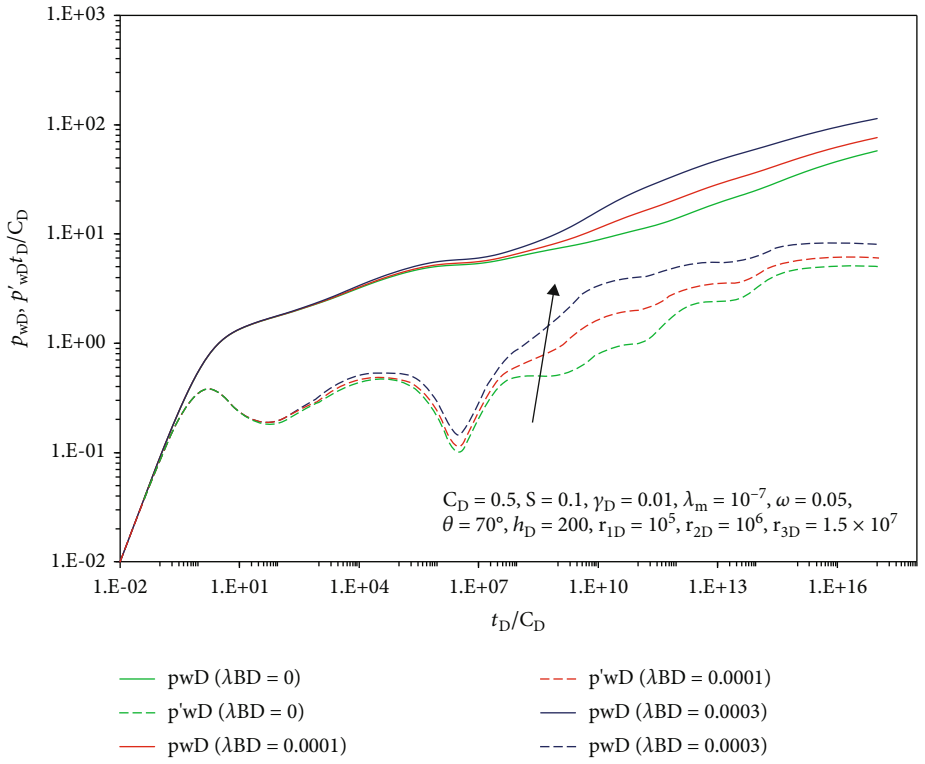

Figure 7: Influence of threshold pressure gradient on pressure dynamic curve.

the well inclination angle is relatively small ($\theta < 40^\circ$), the characteristics of vertical radial flow disappear, which is similar to the radial flow of vertical wells.

4.3.5. Adjacent Well Distance. As shown in Figure 10, as the distance between the adjacent well and the central inclined well increases, the start time of the second radial flow is

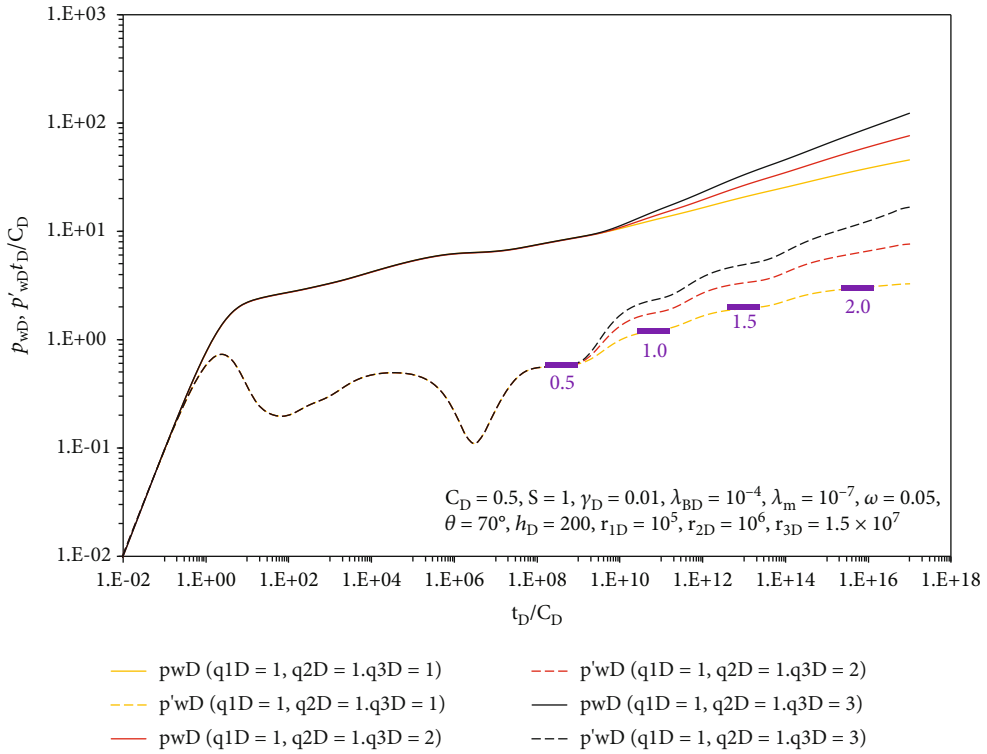

Figure 8: Influence of production of adjacent wells on pressure dynamic curve.

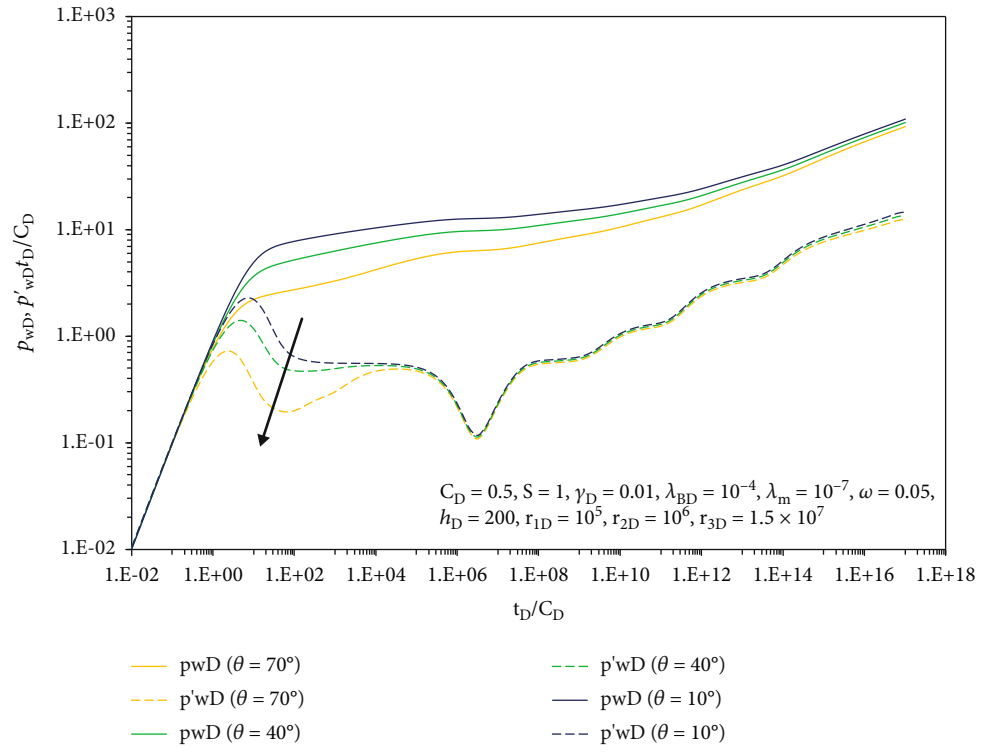

Figure 9: Influence of well inclination angle on pressure dynamic curve.

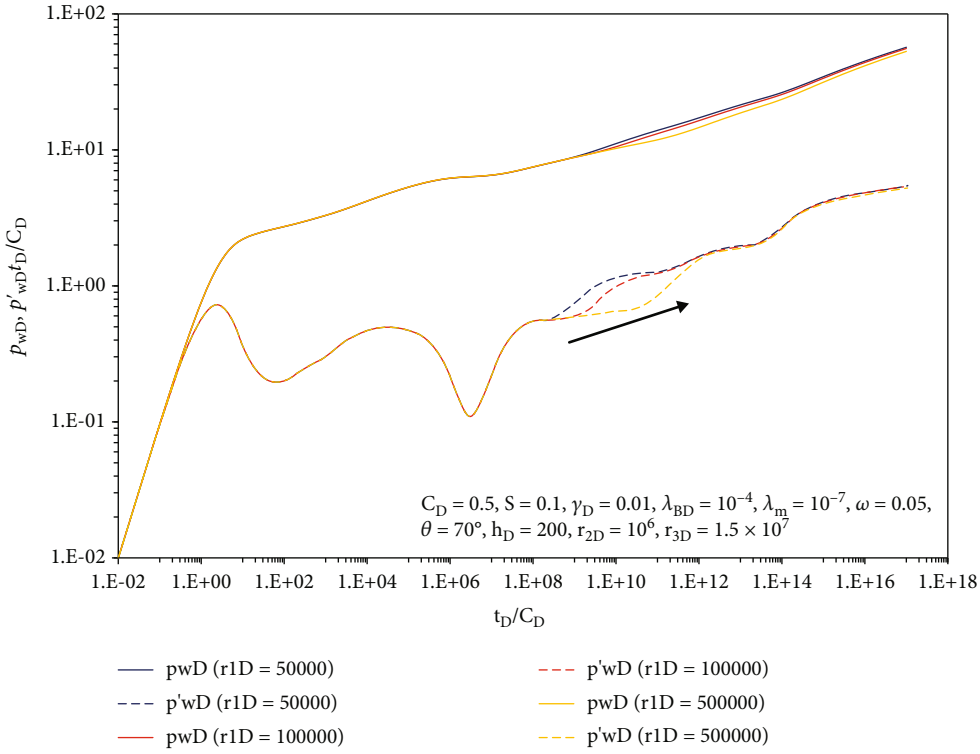

Figure 10: Influence of distance on pressure dynamic curve.

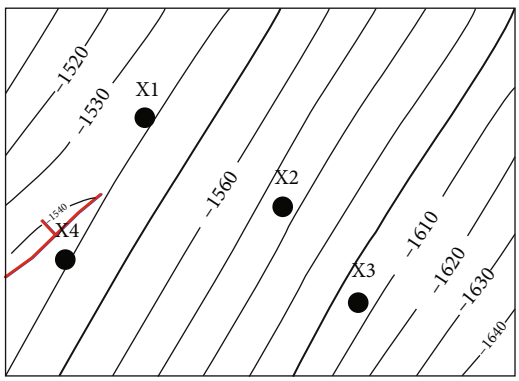

Figure 11: Well location diagram.

delayed and the shift duration becomes shorter. When the distance is short, the second radial flow section gradually disappears and integrates into the third radial flow section.

5. Field Application

5.1. Field Test Data Matching Method. In order to reduce the nonuniqueness, the following steps should be followed when applying the model to well test interpretation of field test data:

(1) Using the actual pressure recovery data, draw the pressure curve and pressure derivative curve. Judging whether there are multiple radial flow period in the later stage of the pressure response curve, if it conforms to the interference well test curve of adjacent wells, the adjacent well interference model is used for parameter interpretation; otherwise, the ordinary single well model is adopted

(2) According to the selected well test interpretation model (without considering the influence of stress sensitivity and threshold pressure gradient), the initial pressure response curve is matched by changing wellbore storage coefficient, skin coefficient, interporosity flow coefficient, and elastic storativity ratio

(3) Input the distance between adjacent wells and the production of adjacent wells to match the multistage radial flow section in the later stage

(4) The interpretation result parameters of adjacent wells in conventional reservoir are taken as the initial parameters and input into the interference well test model of adjacent wells in dual media reservoir considering stress sensitivity and threshold pressure gradient. The pressure response curve is further matched and interpreted by changing the stress sensitivity coefficient and start-up pressure gradient. Finally, the relevant parameters are obtained

5.2. Example Explanation. SZ reservoir is located in Bohai Bay, China. It is a heavy oil reservoir with an average oil viscosity of 320 mPa·s. X2 well is an inclined well in SZ reservoir, with an inclination angle of 73°, and effective thickness of the reservoir is 31.5 m, porosity of 13.5%, and volume coefficient of 1.06. Through the reservoir sand

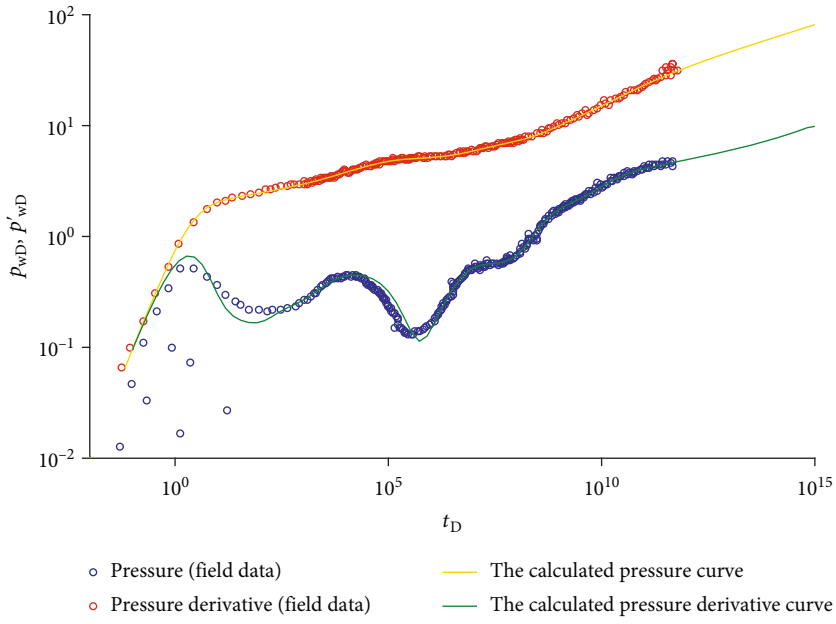

Figure 12: Pressure matching curve.

Table 1: The basic parameters for the investigated reservoir.

Well name	Distance (m)	Daily liquid production (m^3/d)
X1	173	200
X3	162	150
X4	218	200

Table 2: The interpretation results.

Parameters	Value
Wellbore storage coefficient	0.17 m^3/MPa
Skin factor	0.09
Interporosity flow coefficient	5.7×10^{-7}
Permeability	1420 mD
Storativity ratio	5.4×10^{-2}
Threshold pressure gradient	2.4×10^{-4} MPa/m
Permeability modulus	1.5×10^{-2} MPa^{-1}
Interference quantity of X1	72 m^3/d
Interference quantity of X3	10 m^3/d
Interference quantity of X4	0 m^3/d

connectivity analysis, three adjacent wells have good connectivity with it (X1/X3/X4), as shown in Figure 11. When the X2 pressure build-up test was conducted, adjacent wells (X1/X3/X4) were also shut in at the same time, and the locations and parameters of the three interfering wells around the X2 are shown in Table 1. The model proposed in this paper was chosen to match the pressure dynamic curve, as shown in Figure 12. This model was matched with good accuracy, especially for the later stages of the pressure dynamic curve. Table 2 manifests the interpretation results.

6. Conclusion

(1) Aiming at the problem of inclined well test in offshore heavy oil reservoir under multiple well interference, this paper comprehensively considers the permeability stress sensitivity of the reservoir and the threshold pressure gradient of heavy oil and establishes the inclined well test model for dual medium heavy oil reservoir under multiple well interference. And using Green function and superposition principle, the analytical solution under Laplace space is obtained. Finally, the test inclined well pressure dynamic curve is plotted by numerical inversion and with three adjacent wells as an example

(2) The influence law of permeability modulus, threshold pressure gradient, multiwell production, well inclination angle, and well distance for pressure dynamic curve are analyzed in this paper. Under the influence of adjacent wells, the pressure derivative curve of the test inclined well in the later stage warps up and produces multiple "platforms." Through sensitivity analysis, there is a critical well inclination angle of 40° for inclined wells. When the well inclination angle is greater than 40°, vertical radial flow similar to horizontal wells will appear

(3) The new model is applied to the well test interpretation of SZ oilfield in Bohai Bay, and high matching accuracy is obtained. This model not only provides theoretical guidance for multiwell interference well test of the similar type of reservoir but also provides a basis for quantitative characterization of inter well connectivity

Nomenclature

p_f: Fracture system pressure (MPa)
v_{fr}: Radial velocity of fluid in fracture (m/s)
K_{fh}: Fracture horizontal permeability (mD)
v_{fz}: Vertical velocity of fluid in fracture (m/s)
μ: Oil apparent viscosity (mPa·s)
K_{fv}: Fracture vertical permeability
λ_B: Threshold pressure gradient of heavy oil (MPa/m)
p_i: Initial formation pressure (MPa)
r: Distance (m)
ϕ_f: Fracture porosity (dimensionless)
C_{tf}: Fracture compressibility (MPa^{-1})
C_{tm}: Matrix compressibility (MPa^{-1})
V_f: Fracture volume ratio (dimensionless)
K_m: Matrix permeability (mD)
p_m: Matrix system pressure (MPa)
α: Matrix block shape factor (dimensionless)
t: Time (s)
z: Distance (m)
q_{jD}: Dimensionless production of adjacent wells (dimensionless)
r_{jD}: Adjacent well distance (dimensionless)
ξ_D: Perturbation deformation function
s: Laplace factor
ξ_{D0}: Zero order perturbation solution of central inclined well
ξ_{D0j}: Zero order perturbation solution of adjacent well
m: Number of adjacent wells causing interference
η: Wellbore integral factor
θ: Well inclination angle
L: Length of inclined well in reservoir
x_D, y_D, z_D: Coordinate
S: Skin factor.

Data Availability

The data used to support the findings of this study are included within the article.

Conflicts of Interest

The authors declare that they have no conflicts of interest regarding the publication of this paper.

Acknowledgments

This work is supported by the Tianjin Branch of CNOOC Ltd. (YXKY-2018-TJ-04).

References

[1] W. Weilin and A. Hongliang, "Interference pressure analysis model of fractured horizontal well," *Fault-Block Oil & Gas Field*, vol. 26, no. 4, pp. 501–505, 2019.

[2] W. Hongfeng, L. Xiaoping, W. Xiaopei, L. Xiuyu, Z. Songbai, and N. Yanbo, "Application of multi-well interference test technology in exploration and development of Keshen Gasfield," *Petroleum Geology and Recovery Efficiency*, vol. 25, no. 1, pp. 100–105, 2018.

[3] S. Hedong, "Pressure buildup analysis in multi-well systems under interferences from adjacent wells," *Natural Gas Industry*, vol. 36, no. 5, pp. 62–68, 2016.

[4] M. Onur, K. V. Serra, and A. C. Reynolds, "Analysis of pressure-buildup data from a well in a multiwell system," *SPE Formation Evaluation*, vol. 6, no. 1, pp. 101–110, 1991.

[5] T. Marhaendrajana, N. J. Kaczorowski, and T. A. Blasingame, "Analysis and interpretation of well test performance at Arun field," in *The SPE Annual Technical Conference and Exhibition*, Houston, Texas, 1999.

[6] E. S. Adewole, "Interference tests analyses of horizontal and vertical well combinations in a reservoir subject to double-edged water drive," in *The Nigeria Annual International Conference and Exhibition*, Lagos, Nigeria, 2012.

[7] Q. Deng, R.-s. Nie, Y.-l. Jia, X.-l. Wang, Y.-y. Chen, and Y. Xiong, "A new method of pressure buildup analysis for a well in a multiwell reservoir," in *Presented at the SPE North Africa Technical Conference and Exhibition*, Cairo, Egypt, 2015.

[8] Y. He, S. Cheng, J. Qin et al., "Analytical interference testing analysis of multi-segment horizontal well," *Journal of Petroleum Science and Engineering*, vol. 171, pp. 919–927, 2018.

[9] J. Yang, L. I. Qi, F. Chen, Y. Liu, J. Zhang, and D. Gao, "Study on interference testing of fractured-vuggy carbonate reservoirs," *Atlantis Press*, vol. 2017, pp. 510–514, 2017.

[10] A. Kumar, P. Seth, K. Shrivastava, R. Manchanda, and M. M. Sharma, "Integrated analysis of tracer and pressure-interference tests to identify well interference," *SPE Journal*, vol. 25, no. 4, pp. 1623–1635, 2020.

[11] G. Han, Y. Liu, W. Liu, and D. Gao, "Investigation on interference test for wells connected by a large fracture," *Applied Sciences*, vol. 9, no. 1, p. 206, 2019.

[12] C. Shiqing, L. Meng, H. Youwei et al., "A multi-well interference pressure transient analysis method to determine the water source orientation of multi-fractured horizontal well," *Journal of China University of Petroleum(Edition of Natural Science)*, vol. 42, no. 5, pp. 81–88, 2018.

[13] H. Cinco, F. G. Miller, and H. J. Ramey Jr., "Unsteady-state pressure distribution created by a directionally drilled well," *Journal of Petroleum Technology*, vol. 27, no. 11, pp. 1392–1400, 1975.

[14] L. Zhang, M. B. Dusseault, and J. A. Franklin, *Slant Well Production in Media with Permeability Anisotropy*, 1993.

[15] B. R. Sousa, "Slanted well test analysis," *University of Campina(in Portuguese)*, 2012.

[16] H. Li, Q. Zhang, K. Wei, Y. Zeng, and Y. Zhu, "Well test analysis of inclined Wells in the low-permeability composite gas reservoir considering the non-Darcy flow," *Energies*, vol. 15, no. 5, p. 1654, 2022.

[17] Z. Xl, L. Xp, and X. Zhang, "Research on inclined well test model for orthographic fault slabby double porosity reservoir," *Well Testing*, vol. 21, no. 6, 2012.

[18] J. Ruizhong, S. Zeyang, C. Yongzheng, Z. Fulei, Z. Chunguang, and Y. Jianwei, "Dynamical characteristics of inclined well in dual medium low permeability reservoir," *Lithologic Reservoirs*, vol. 30, no. 6, pp. 131–137, 2018.

[19] Y. L. Jia, G. F. Sun, R. S. Nie, J. M. Li, and H. K. Li, "Flow model and well test curves for quadruple-media reservoirs," *Lithologic Reservoirs*, vol. 28, no. 1, pp. 123–127, 2016.

[20] X. Youjie, L. Qiguo, W. Rui, and L. Yicheng, "Pressure transient of fractured horizontal well with complex fracture distribution in composite reservoir," *Lithologic Reservoirs*, vol. 31, no. 5, pp. 161–168, 2019.

[21] C. Zhongliang, W. Nutao, C. Huanghui, J. Tao, and D. Sen, "Well test interpretation about multilayer commingled and inclined well," *Well Testing*, vol. 26, no. 3, pp. 29–32+76, 2017.

[22] G. Li, X. Xin, G. Yu et al., "Effect of asphaltene on threshold pressure gradient of heavy oil in porous media," *Science of Advanced Materials*, vol. 13, no. 2, pp. 273–279, 2021.

[23] D. Zhang, J. Peng, Y. Gu, and Y. Leng, "Experimental study on threshold pressure gradient of heavy oil reservoir," *Xinjiang Petroleum Geology*, vol. 33, no. 2, pp. 201–204, 2012.

[24] H. Stehfest, "Algorithm 368: numerical inversion of Laplace transforms [D5]," *Communications of the ACM*, vol. 13, no. 1, pp. 47–49, 1970.

[25] H. Stehfest, "Remark on algorithm 368: numerical inversion of Laplace transforms," *Communications of the ACM*, vol. 13, no. 10, p. 624, 1970.

Hindawi
Geofluids
Volume 2022, Article ID 7456697, 22 pages
https://doi.org/10.1155/2022/7456697

Research Article

Experimental Study on Production Characteristics of Bottom Water Fractured-Vuggy Reservoir

Hong Cheng, Lin Jiang, and Chenggang Li

Sinopec Northwest Oilfield, Xinjiang Urumqi 830011, China

Correspondence should be addressed to Hong Cheng; 16899612@qq.com

Received 25 March 2022; Accepted 17 May 2022; Published 18 June 2022

Academic Editor: Kai Zhang

Copyright © 2022 Hong Cheng et al. This is an open access article distributed under the Creative Commons Attribution License, which permits unrestricted use, distribution, and reproduction in any medium, provided the original work is properly cited.

To assess the high-pressure production characteristics of double-vug reservoirs with bottom water in the Tahe Oilfield, in this study, a high-pressure physical simulation experiment apparatus is built for double-vug reservoirs with bottom water. The high-pressure production characteristics of "vug-fracture-vug" reservoirs under different bottom water characteristics are studied experimentally, and fracture-vug relationship and oil recovery rates are explored. According to the findings, the oil recovery rate significantly affects the development effect of double-vug reservoirs with bottom water, and bottom water provides sufficient energy for reservoir development. Furthermore, considering the possible occurrence of water invasions, the production rate control must receive close attention in the development process to avoid strong water channeling. Constant-pressure bottom water has sufficient energy and can quickly replenish vug energy. Therefore, the recovery percentage and bottom water invasion and retention volume of fractured-vuggy reservoirs with constant-pressure bottom water are higher than those of fractured-vuggy reservoirs with constant-volume bottom water. Under the appropriate control of production factors, the presence of bottom water can noticeably improve the development effect of fractured-vuggy reservoirs.

1. Introduction

Carbonate reservoirs in the Tahe Oilfield are typical fractured-vuggy reservoirs, which generally contain edge and bottom water. In the development process of such reservoirs, premature water breakthrough often causes an excessively fast increasing water content and a precipitously declining production [1, 2]. Moreover, in the Tahe Oilfield, vuggy carbonate reservoirs with bottom water are buried in deep strata with a formation pressure of about 50 MPa and a formation temperature above 120°C [3, 4]. To study the high-pressure physical properties of vuggy reservoirs with bottom water, laboratory high-pressure experimental models must be built, as ordinary experimental models (such as ordinary glass etching models) cannot endure high-temperature or high-pressure environments [5–7].

So far, few experiments have conducted physical simulations of fractured-vuggy reservoirs. Existing studies on fractured-vuggy reservoirs (both in China and internationally) mostly focused on their production performance characteristics. Ozkan et al. [8] explored the single-well production characteristics of naturally fractured reservoirs under constant-pressure boundary conditions. Olarewaju et al. [9] built a mathematical model suitable for naturally fractured or vugular reservoirs with a radial discontinuity around the wellbore, with which they analyzed the production performance of reservoirs. Guo et al. [10] conducted a case study on the Campeche Bay, Mexico, and modeled it theoretically. Goudarzi et al. [11] built physical models for fracture networks using sandstone cores, and studied the laws of fluid exchange between matrix blocks and fractures as well as the parameters influencing the mechanism of fracture permeability. Li et al. [12] prepared a large-sized porous physical model suitable for the heterogeneity of carbonates and examined oil displacement by water in cores using visualization technology.

Chinese scholars attach great importance to the physical simulation of fractured-vuggy reservoirs through experiments and have developed physical models for both fractured-vuggy and vuggy carbonate reservoirs. Zheng et al. [13, 14] performed physical experiments using carbonate cores, concluding that the recovery efficiency of fractured-vuggy reservoirs with bottom water is related to the bottom water volume.

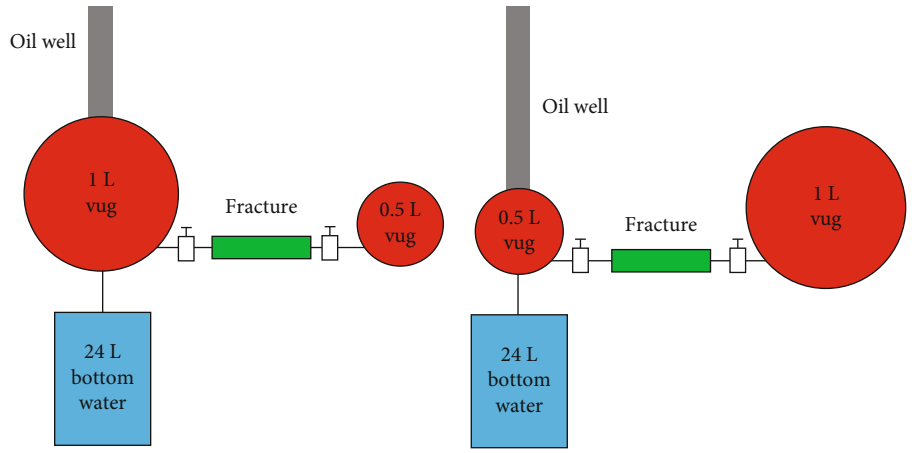

Figure 1: Schematic diagram of the high-pressure physical simulation experiment model for (a) bottom water connected to the large vug and (b) bottom water connected to the small vug.

Figure 2: Pictures of high-pressure physical simulation experiment model for (a) bottom water connected to the large vug and (b) bottom water connected to the small vug.

Liu et al. [15] carried out two-dimensional physical simulation experiments on the production performance of vuggy reservoirs with bottom water and found it to be closely related to the connection type and energy of bottom water. Wang et al. [16] performed visual physical simulation experiments on fractured-vuggy reservoirs and found that injecting water into the bottom of a reservoir effectively improves the development effect of the reservoir; moreover, the intensity of water injection affects both water breakthrough time and recovery percentage. Rong et al. [17] studied fractured-vuggy reservoirs with different interwell connection types using tracers, characterizing fracture-vug connection structures, and improving the water drive effect of fractured-vuggy reservoirs. Zhao et al. [18] probed into the fluid production characteristics and laws of fractured-vuggy reservoirs. Qian et al. [19] explored how the salinity and ion content of injected water affect the recovery efficiency of reservoirs based on carbonate core displacement tests. They reached the conclusion that low-salinity water drive modifies the surface wettability of carbonates, thus increasing recovery efficiency.

Generally, physical simulation experiments are performed on fractured-vuggy reservoirs using physical

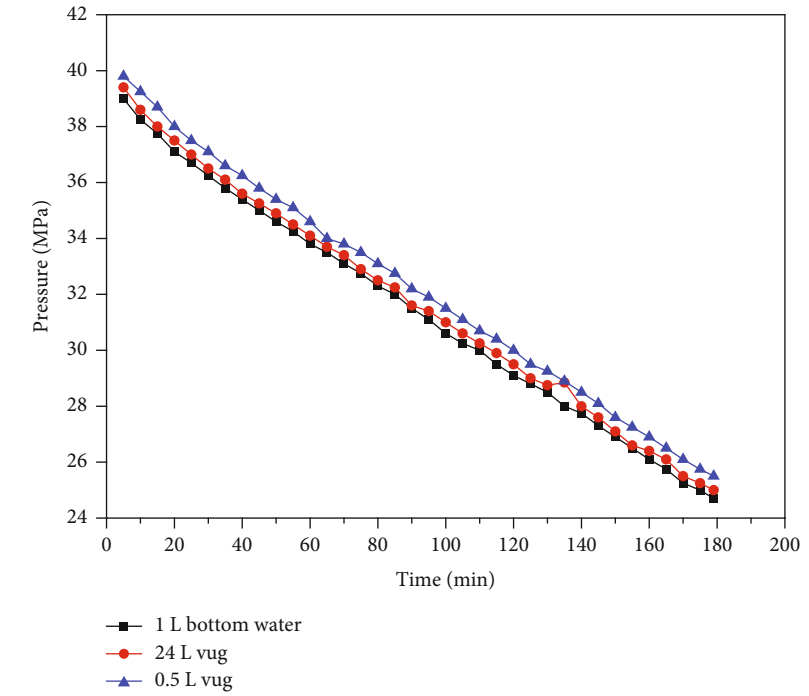

(a)

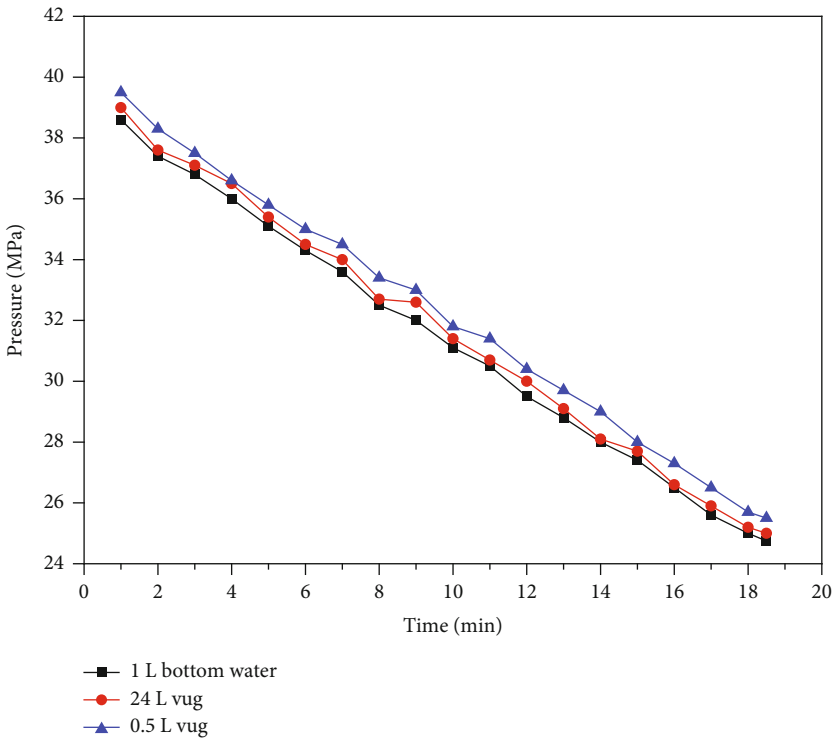

(b)

Figure 3: Continued.

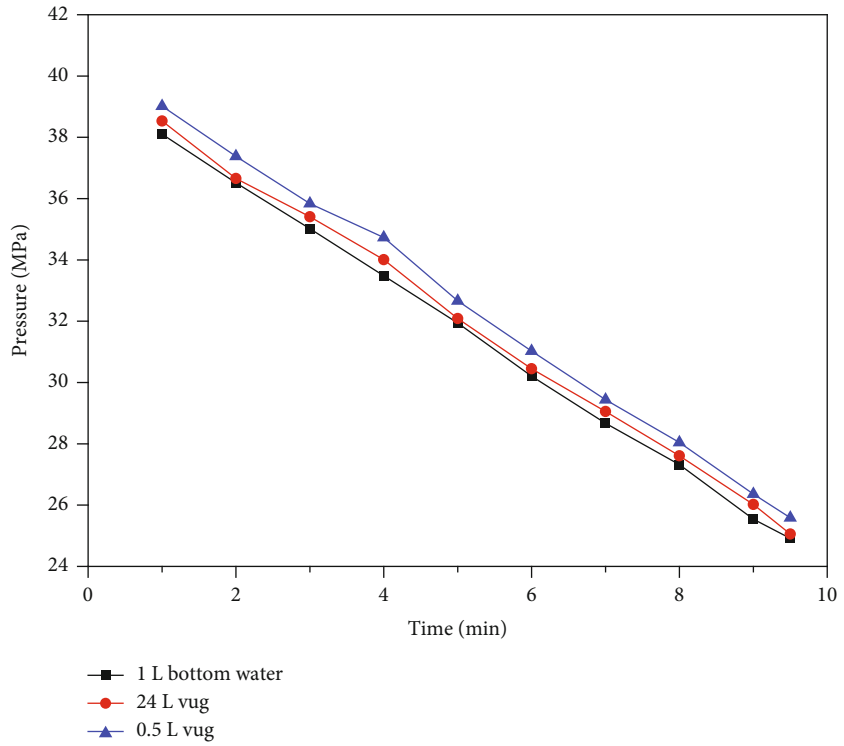

(c)

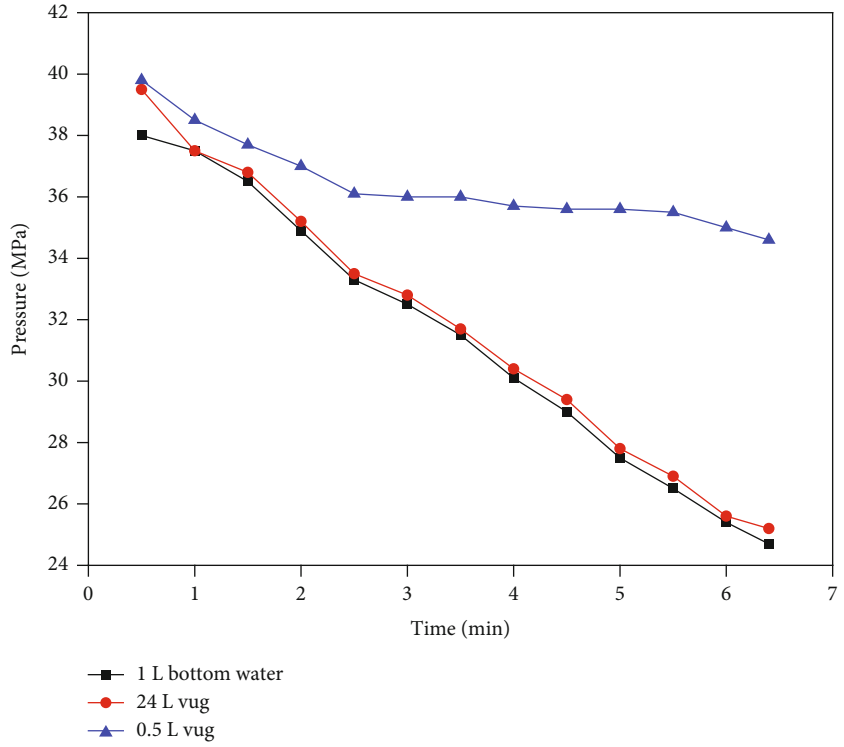

(d)

Figure 3: Pressure variation curves in high-pressure physical property experiments under connection type I (different production rates with (a) 1 mL/min, (b) 10 mL/min, (c) 20 mL/min, and (d) 30 mL/min).

modeling methods such as all-straight well core samples, simulation of fracture generation with unconsolidated sand pack, fracture generation with cores, and vug modeling [20–23]. With regard to carbonate reservoirs with developed vugs, mainly full-diameter cores are used for physical simulation [24–26]. In apparatus modeling, similarities in

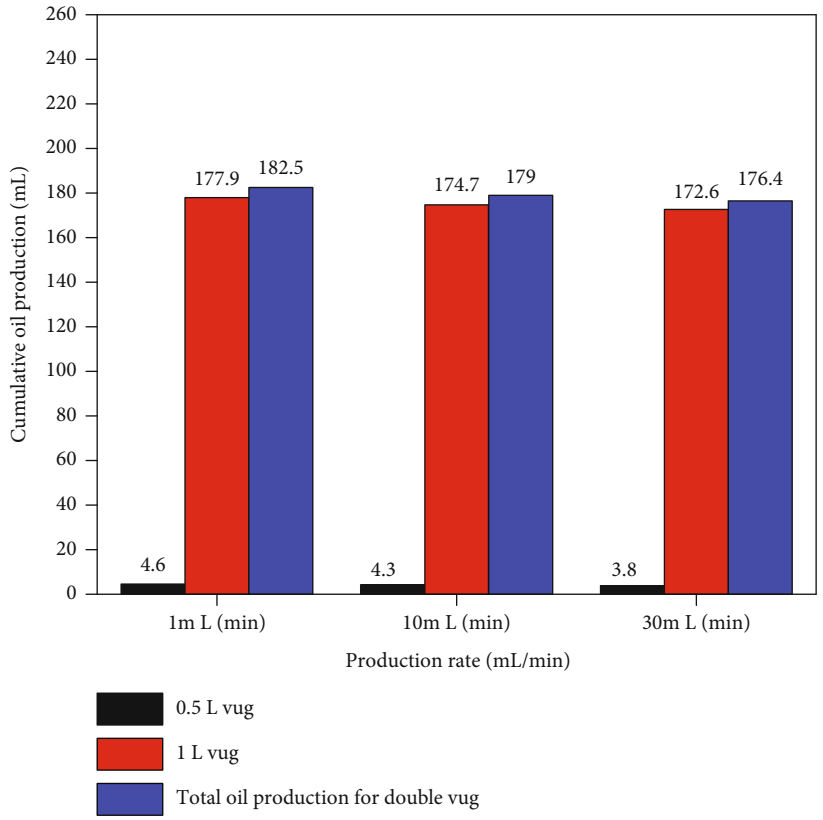

Figure 4: Column chart of cumulative oil production in high-pressure physical property experiments under connection type I (different production rates).

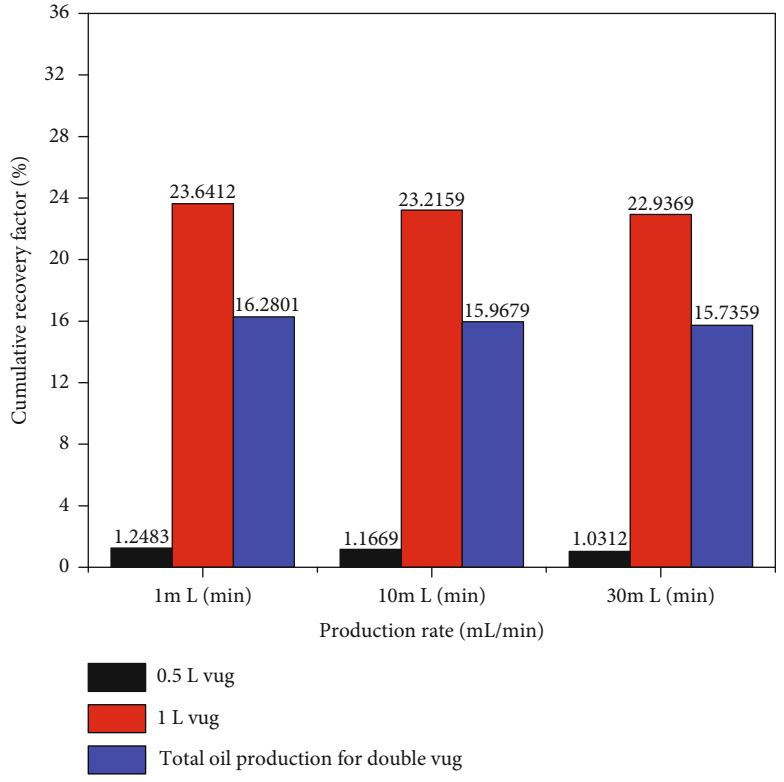

Figure 5: Column chart of cumulative recovery factor in high-pressure physical property experiments under connection type I (different production rates).

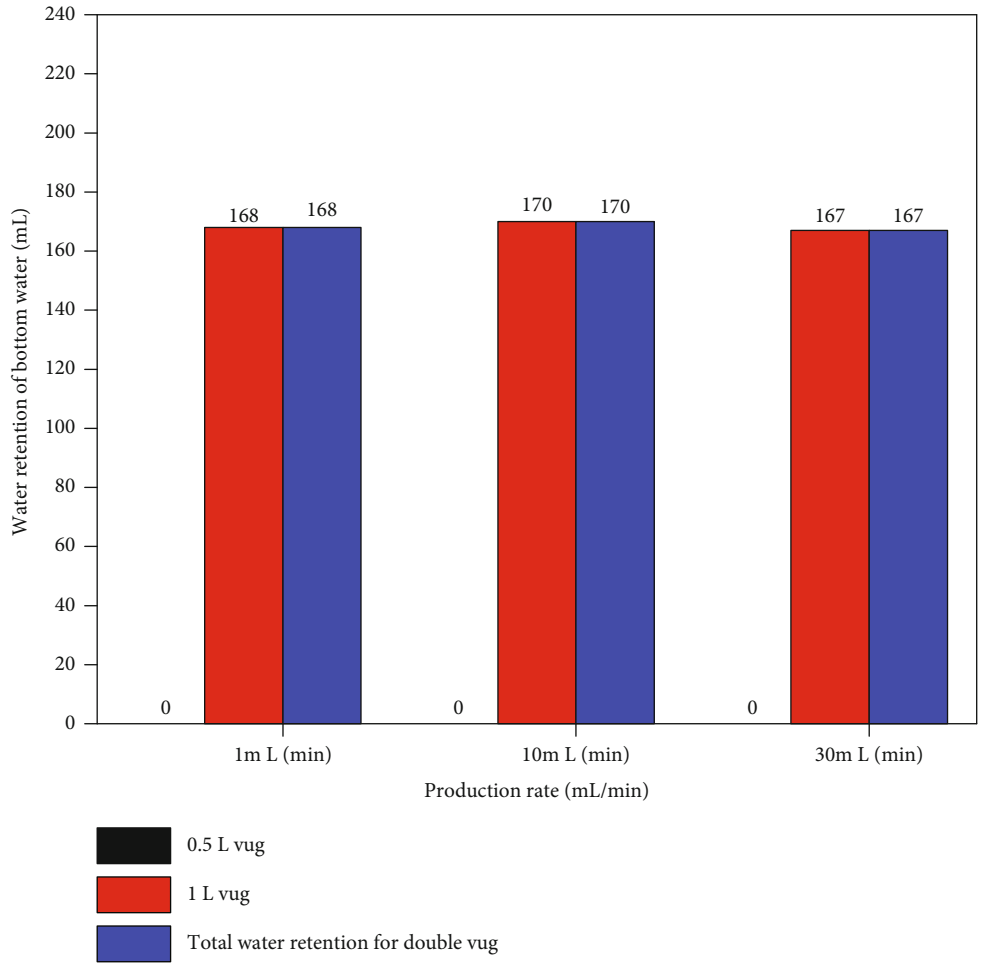

Figure 6: Column chart of bottom water invasion and retention in high-pressure physical property experiments under connection type I (different production rates).

production rate and bottom water type are considered, to ensure comparability real reservoirs [27–29].

Based on conventional models for fractured-vuggy reservoirs, in this paper, a high-pressure physical simulation experiment model for double-vug reservoirs with bottom water is designed. This model can be used for both simulating the bottom water conditions of real reservoirs and equating basic fracture-vug structures, reservoir characteristics, and field working systems of formations. The model is then used to test pressure variation curves and oil/water production variation curves under different bottom water types and production conditions, thus laying a foundation for clarifying development laws and calculating dynamic reserves of fractured-vuggy reservoirs with bottom water.

2. Experiments

2.1. Building a High-Pressure Physical Simulation Experiment Model for Double-Vug Reservoirs with Bottom Water. A 24 L high-pressure intermediate container was used to simulate bottom water. A 1 L intermediate container and a 0.5 L intermediate container (filled with carbonate cores and sediment) were used to simulate two vugs. Relying on simulated fracture generation with an unconsolidated sand pack, a high-pressure physical simulation experiment model was built for double-vug reservoirs with bottom water. The purpose was to explore how bottom water and fracture-vug relationship affect the characteristics of the "vug-fracture-vug" system in high-pressure physical property experiments. The permeability of the unconsolidated sand pack was 0.8-0.9 D, and the initial pressure of the model was 40 MPa. The schematic diagram of the connection relationship between vugs is shown in Figure 1. The pictures of high-pressure physical simulation experiment model for double-vug reservoirs with bottom water are shown in Figure 2. The difference between connection type I and II is the volume of the vug connected to the bottom water.

2.2. Experimental Methods. Experiments were performed to simulate a "vug-fracture-vug" double-vug reservoir with bottom water. Furthermore, the effects of bottom water, fracture-vug relationship, and oil recovery rate on the characteristics of the reservoir were explored in high-pressure physical property experiments.

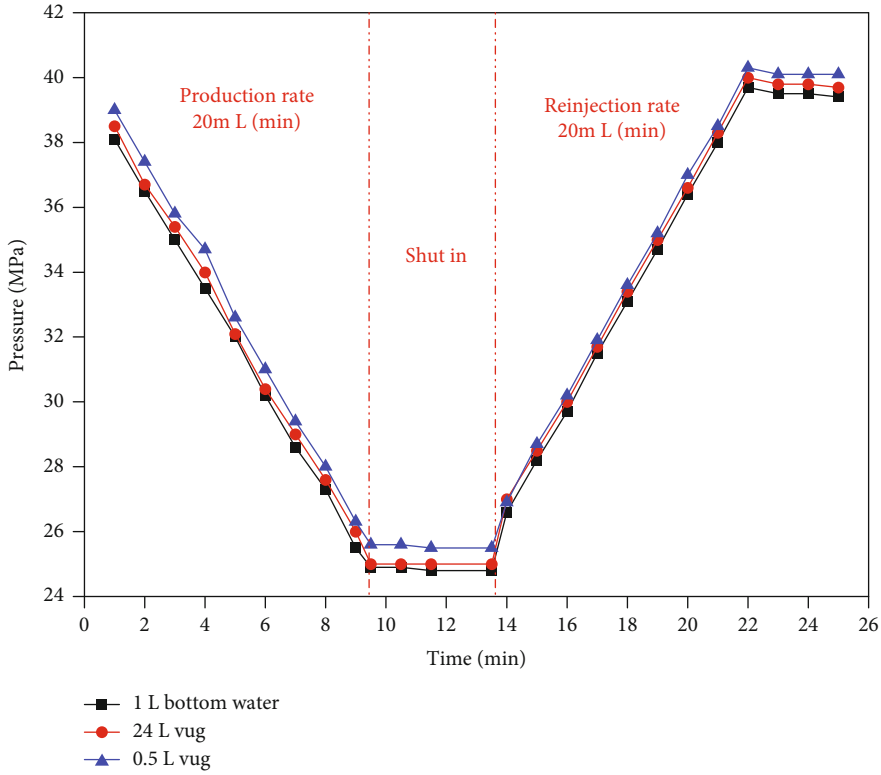

Figure 7: Pressure variation curves of reinjection in high-pressure physical property experiments under connection type I (production rate and reinjection rate = 20 mL/min).

2.2.1. Experiments on Reservoirs with Constant-Volume Bottom Water

(1) The 24 L intermediate container was filled with high-pressure water to simulate bottom water. The 1 L and 0.5 L intermediate containers were filled to simulate vugs. The 30 cm unconsolidated sand pack was filled for fracture simulation

(2) *Model Filling and Crude Oil Saturation*. After completing the model filling step, a vacuum pump was connected to evacuate the intermediate containers to a pressure of -0.09 MPa. Crude oil was connected to the containers at the bottom for oil saturation through self-priming until outflow of oil from the top. An ISCO pump was used to inject oil into the containers until a pressure of 25 MPa was reached. The containers were left to settle for 5 h for pressurized saturation. After pressure relief and discharge of bubbles, intermediate containers were separately injected with oil and pressurized to 40 MPa. The oil consumption of each process was recorded to calculate the initial crude oil saturation capacity of each vug. The original capacities of the 1 L and 0.5 L vugs in the experiments were 752.5 mL and 368.5 mL, respectively

(3) Connection type I was adopted to build the high-pressure physical simulation experiment model for double-vug reservoirs with bottom water. Reduced-pressure production was conducted at the top of the 1 L intermediate container. Production proceeded at rates of 1 mL/min, 10 mL/min, 20 mL/min, and 30 mL/min and stopped when the pressure declined to 25 MPa. The variations of pressure, oil production, and water production in the production process were recorded. For connection type II, reduced-pressure production was conducted at the top of the 0.5 L intermediate container

(4) When the pressure had decreased to 25 MPa, the production valve was quickly closed, and the variations of the pressure buildups of the 24 L, 1 L, and 0.5 L intermediate containers were recorded over time

(5) Steps (1)-(3) were repeated. When the production pressure had decreased to 25 MPa, the valves at the two ends of the intermediate containers and the unconsolidated sand pack were closed, and the two immediate containers emptied. The residual oil contents in the containers were recorded to calculate the contributions of the two vugs to recovery percentage

2.2.2. Experiments on Reservoirs with Constant-Pressure Bottom Water. The same apparatus was used for experiments on reservoirs with constant-pressure bottom water and experiments on reservoirs with constant-volume bottom water. The difference between the two groups of experiments was that a constant-pressure pump was connected with a 24 L intermediate container containing bottom water to

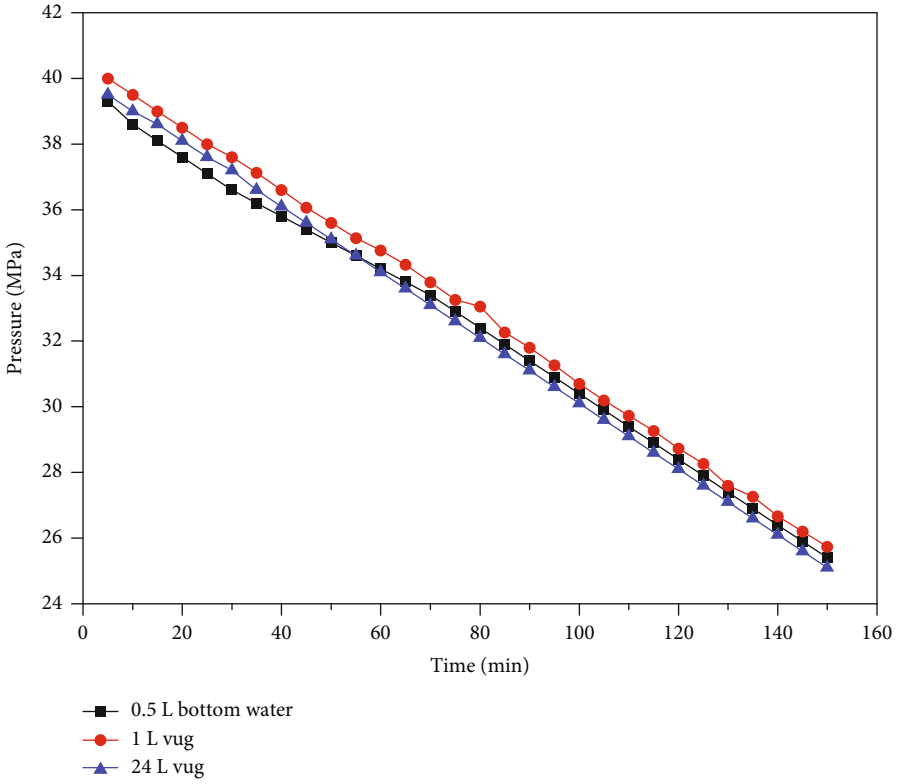

(a)

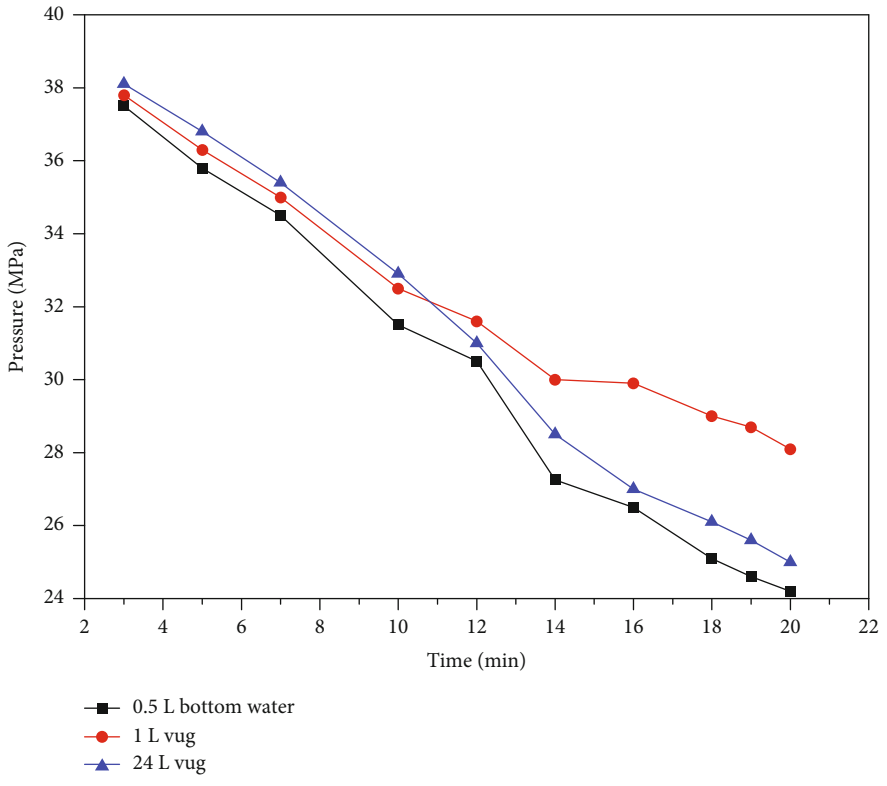

(b)

Figure 8: Continued.

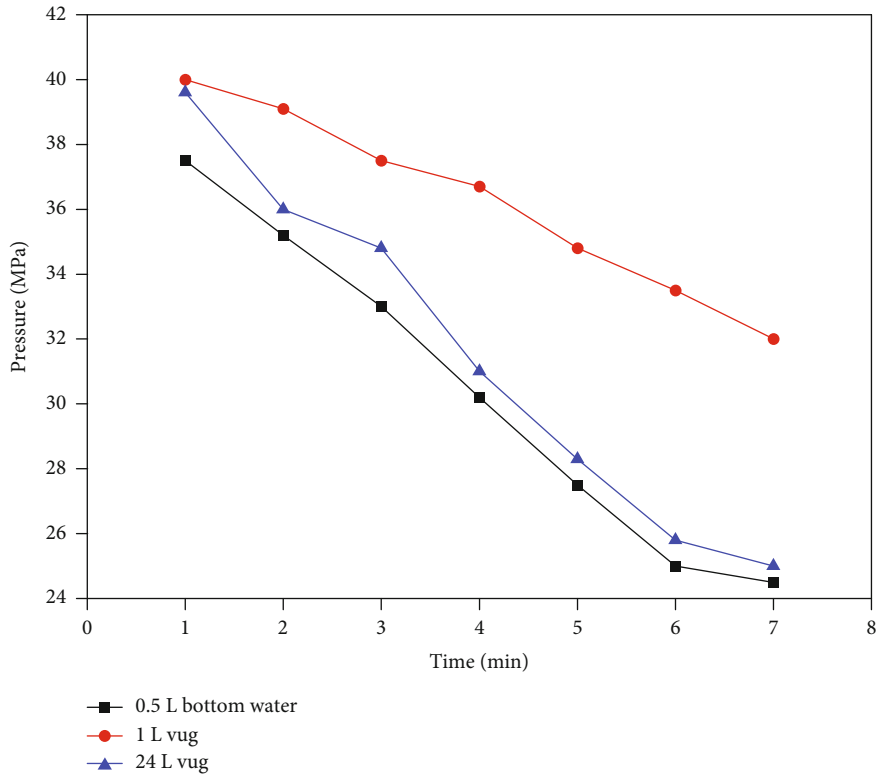

(c)

Figure 8: Pressure variation curves in high-pressure physical property experiments under connection type II (different production rates with (a) 1 mL/min, (b) 10 mL/min, and (c) 30 mL/min).

create the source of constant-pressure bottom water in experiments on reservoirs with constant-pressure bottom water.

(1) The 24 L intermediate container was filled with high-pressure water and connected to a 40 MPa constant-pressure pump to simulate constant-pressure bottom water. The 1 L and 0.5 L intermediate containers were filled to simulate vugs. The 30 cm unconsolidated sand pack was filled for fracture simulation

(2) *Model Filling and Crude Oil Saturation*. After completion of model filling, a vacuum pump was connected to evacuate the intermediate containers to a pressure of -0.09 MPa. Crude oil was connected to containers at the bottom for oil saturation through self-priming until outflow of oil at the top. An ISCO pump was used to inject oil into the containers until a pressure of 25 MPa was reached. The containers were left to settle for 5 h for pressurized saturation. After pressure relief and discharge of bubbles, intermediate containers were separately injected with oil and pressurized to 40 MPa. The oil consumption of each process was recorded to calculate the initial crude oil saturation capacity of each vug. The original capacities of the 1 L and 0.5 L vugs in the experiments were 834 mL and 413 mL, respectively

(3) Connection type I was adopted to build the high-pressure physical simulation experiment model for double-vug reservoirs with bottom water. Reduced-pressure production was conducted at the top of the 1 L intermediate container. Production proceeded at rates of 1 mL/min, 10 mL/min, and 20 mL/min and stopped when the water productivity of the outlet reached 98%. The variations of pressure, oil production, and water production in the production process were recorded. For connection type II, reduced-pressure production was conducted at the top of the 0.5 L intermediate container

(4) At the end of production, the valves at both ends of intermediate containers and the unconsolidated sand pack were closed, and the two vugs were emptied. The residual oil contents in the vugs were recorded to calculate the contributions of the two vugs to recovery percentage

3. Results and Discussions

3.1. High-Pressure Physical Property Experiments on Reservoirs with Constant-Volume Bottom Water

3.1.1. Production Characteristics under Connection Type I. A high-pressure physical simulation experiment model was built for "vug-fracture-vug" reservoirs with bottom water

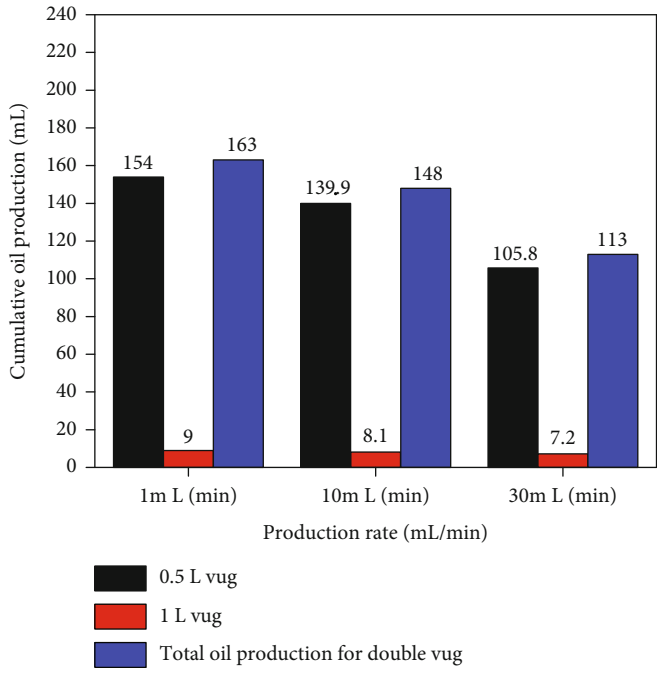

Figure 9: Column chart of cumulative oil production in high-pressure physical property experiments under connection type II (different production rates).

according to connection type I. Different production rates were adopted to assess the production characteristics of double-vug reservoirs with bottom water under different production rates, as shown in Figure 3.

Under connection type I, bottom water exerted a clear effect on the production pressure characteristics of double-vug reservoirs. Compared with vuggy reservoirs without bottom water, double-vug reservoirs with bottom water presented a clearly extended pressure drop time, suggesting that bottom water can significantly increase the natural energy of double-vug reservoir systems.

In addition, the production rate also affected the production characteristics of double-vug reservoirs with bottom water. At a production rate of ≤20 mL/min, the pressures of the 0.5 L vug, the 1 L vug, and the 24 L intermediate container containing bottom water all showed linear decreases. Production pressure differed little between various moments. When the production rate reached 30 mL/min, the pressure variation of the 0.5 L vug clearly differed from pressure variations of the 1 L vug and the 24 L intermediate container containing bottom water, showing a clearly moderated trend of pressure drop. Analysis showed that this phenomenon was mainly attributable to insufficient fracture flow capacity. That is, when the production rate exceeded 30 mL/min, the feed flow from the 0.5 L container to the output end was limited by the fracture, resulting in differences in pressure drop.

Figures 4 and 5 show that bottom water significantly affected the recovery percentage of double-vug reservoirs. Under connection type I, the recovery percentage of reservoirs with bottom water could reach about 16%, which is clearly higher than that of reservoirs without bottom water. Notably, no free water was produced at any stage of reservoir development. Therefore, under circumstances where the structural environment of the reservoir is not liable to water invasion or where there is no apparent water channeling under proper development, the presence of bottom water is conducive to reservoir development. Furthermore, it can provide sufficient energy for the development of fractured-vuggy reservoirs.

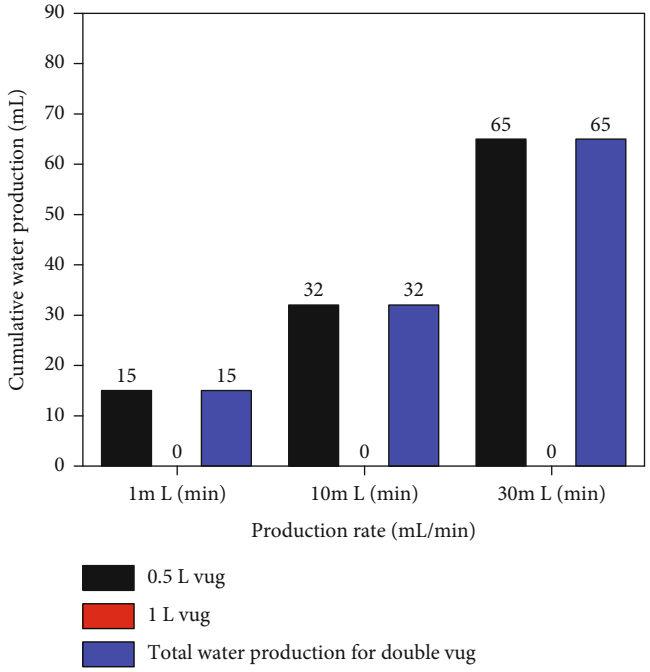

Figure 10: Column chart of cumulative water production in high-pressure physical property experiments under connection type II (different production rates).

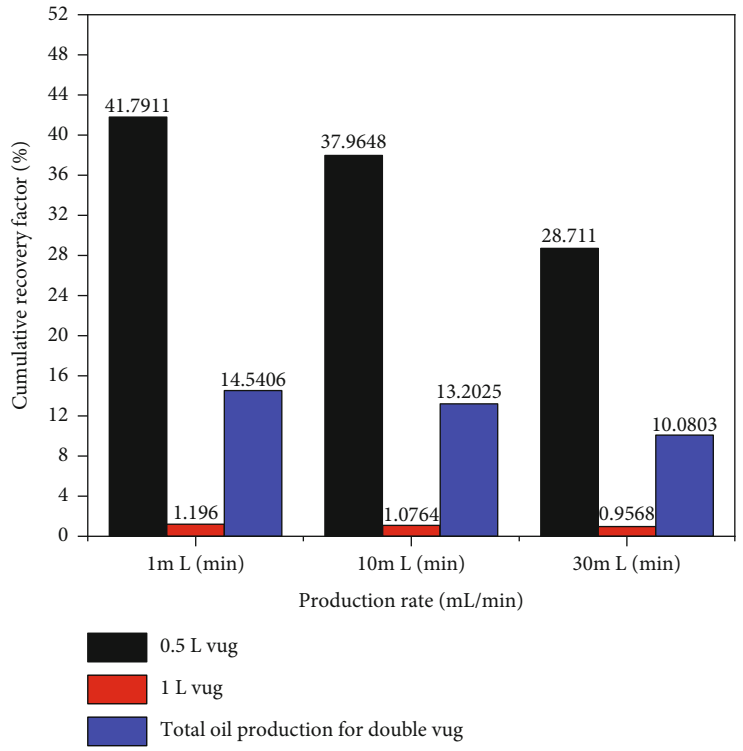

Figure 11: Column chart of cumulative recovery percent in high-pressure physical property experiments (different production rates).

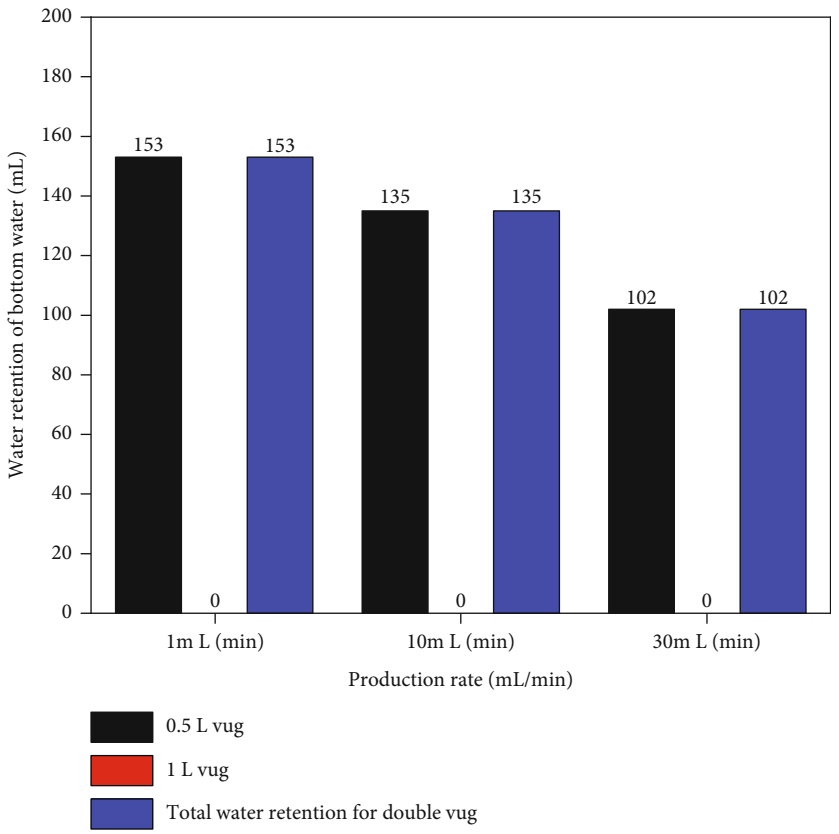

Figure 12: Column chart of bottom water invasion and retention in high-pressure physical property experiments under connection type II (different production rates).

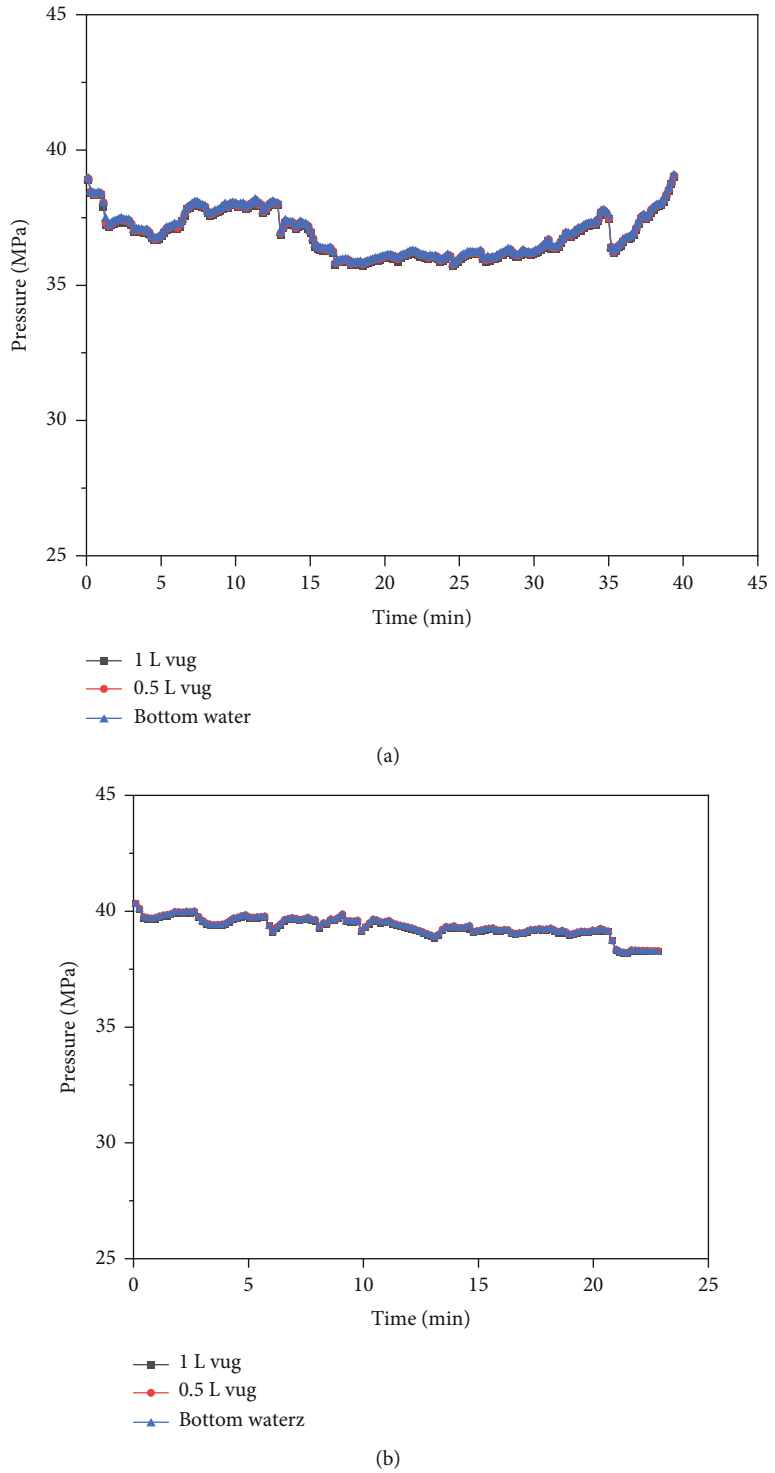

Figure 13: Pressure variation curves for high-pressure physical property experiments on reservoirs with constant-pressure bottom water and production rate of 20 mL/min ((a) production well linked with 1 L vug and (b) production well linked with 0.5 L vug).

Within the range of assessed production rates, recovery percentages differed little between different experiments. This indicated that before water channeling, the production rate exerted little effect on the production of fractured-vuggy reservoirs. However, increasing production rate made it easier for bottom water to occur, which caused the rapid flooding of producing wells, and compromised the overall development effect of reservoirs.

According to Figure 6, bottom water mainly invaded the 1 L vug but did not intrude into the 0.5 L vug, which was consistent with the difference in oil production between both vugs. The 1 L vug experienced severe bottom water invasion,

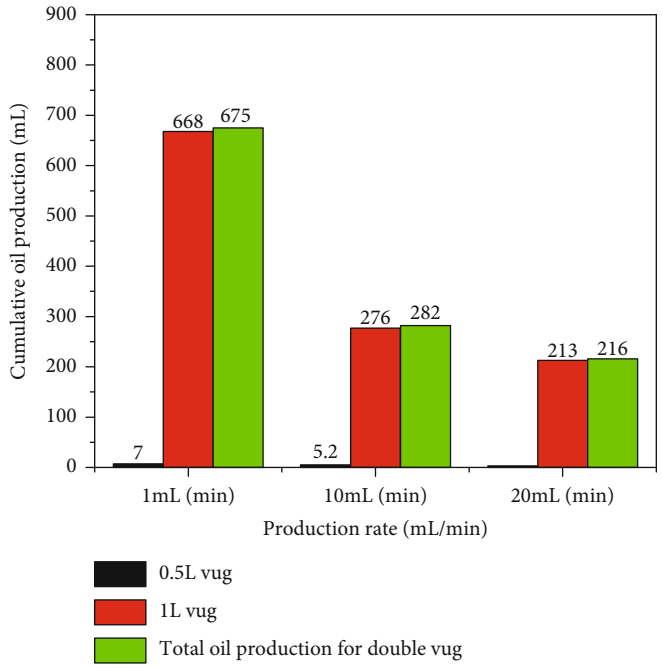

Figure 14: Column chart of cumulative oil production in high-pressure physical property experiments under connection type I (different production rates).

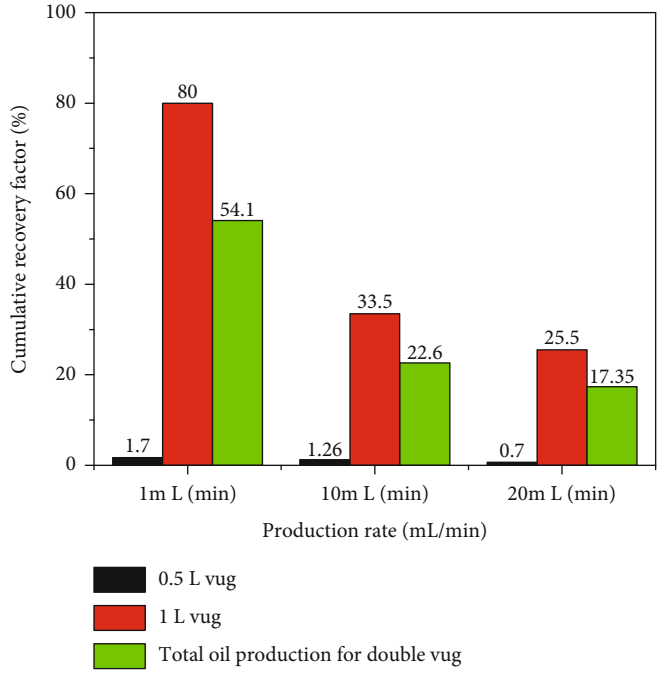

Figure 15: Column chart of crude oil recovery percent in high-pressure physical property experiments under connection type I (different production rates).

and its oil production was also significantly higher than that of the 0.5 L vug. Prior to water breakthrough at the output end, the bottom water invading vuggy reservoirs could displace crude oil and increase the production degree of crude oil in vugs. Therefore, bottom water can increase the natural energy of vuggy reservoirs and can be properly utilized to substantially improve the development effect of fractured-vuggy reservoirs.

Figure 7 shows the depletion pressure drop, pressure buildup, and injection pressure buildup curves of double-vug reservoirs with bottom water under connection type I. Here, production rate and injection rates were set to 20 mL/min.

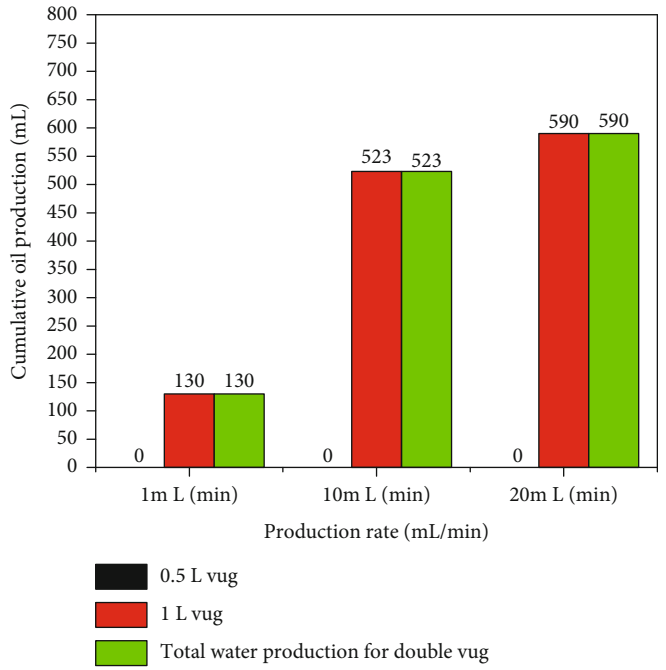

Figure 16: Column chart of cumulative water production in high-pressure physical property experiments under connection type I (different production rates).

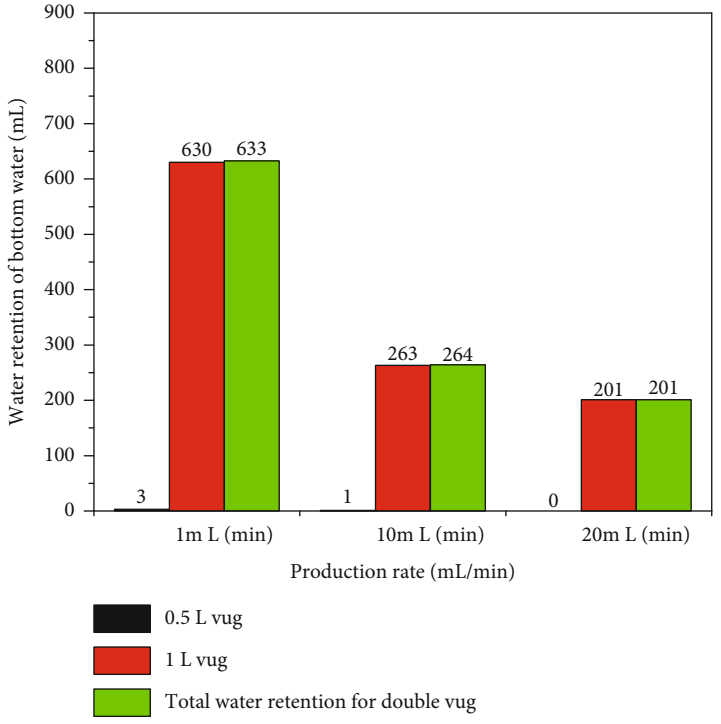

Figure 17: Column chart of bottom water invasion and retention in high-pressure physical property experiments under connection type I (different production rates).

The depletion pressure drop and injection pressure buildup curves both presented linear variations, implying that the fractures did not adversely impact fluid flow and that the fractured-vuggy reservoir could be put into stable production.

3.1.2. Production Characteristics under Connection Type II. A high-pressure physical simulation experiment model was built for "vug-fracture-vug" reservoirs with bottom water according to connection type II. Different production rates were adopted to assess the production characteristics of

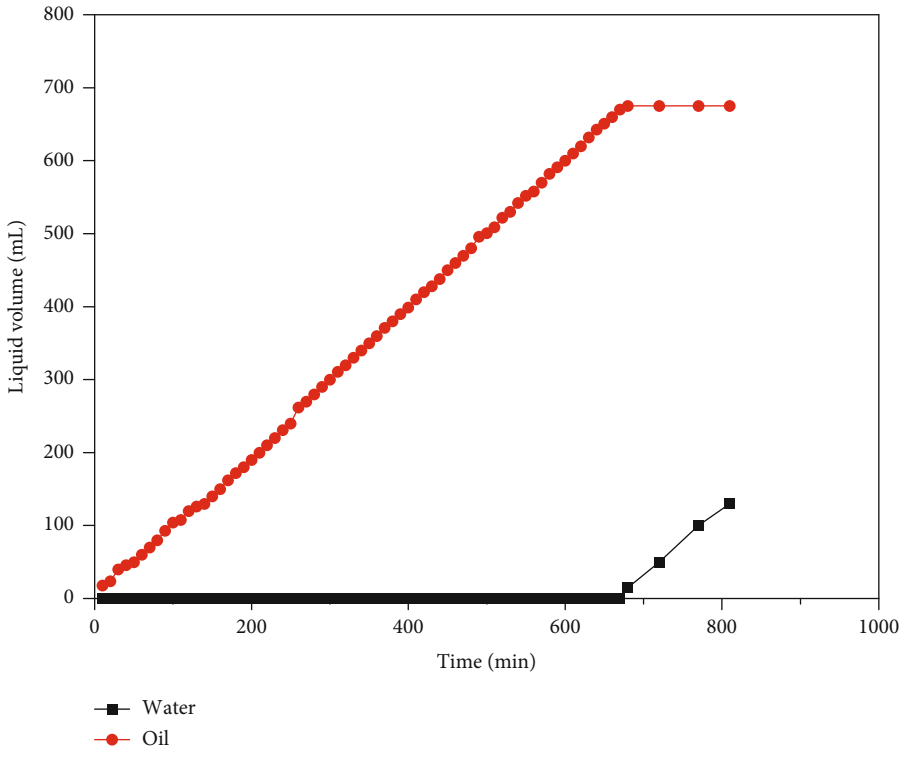

(a)

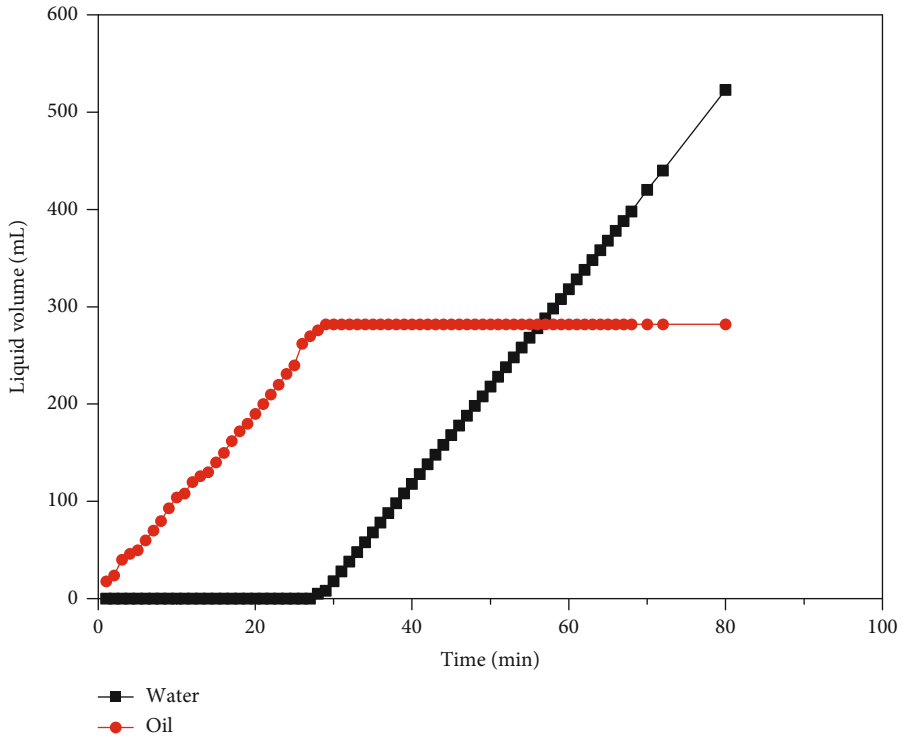

(b)

Figure 18: Continued.

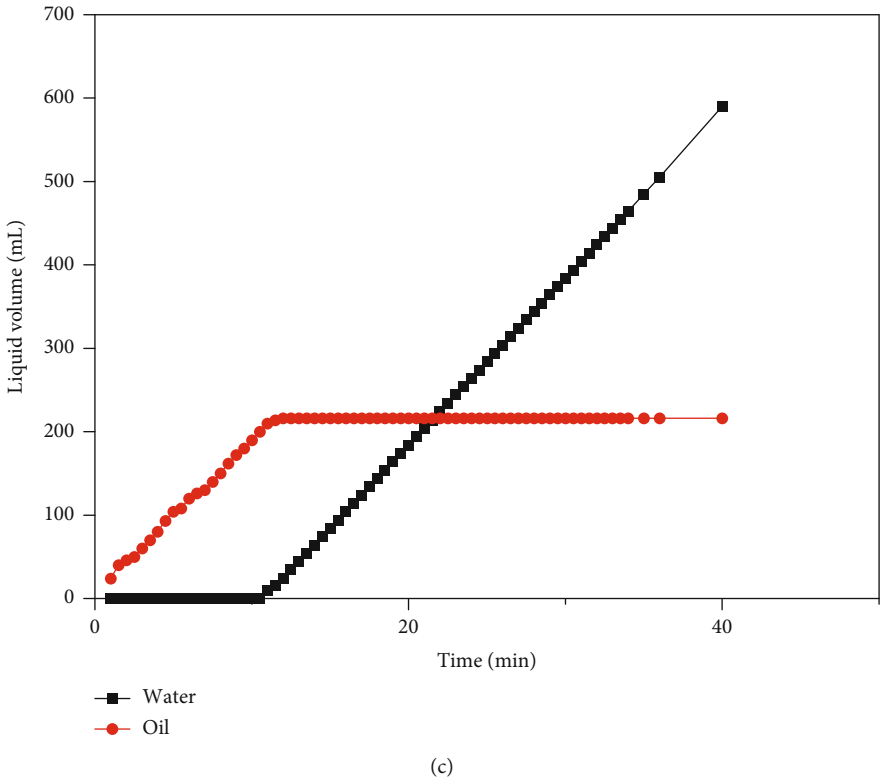

(c)

Figure 18: Oil/water production variation curves under connection type I (different production rates with (a) 1 mL/min, (b) 10 mL/min, and (c) 20 mL/min).

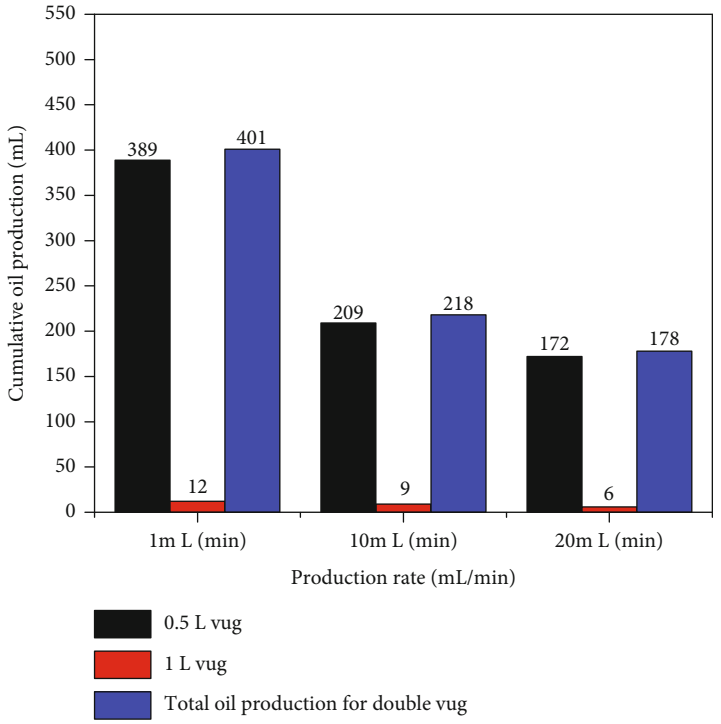

Figure 19: Column chart of cumulative oil production in high-pressure physical property experiments under connection type II (different production rates).

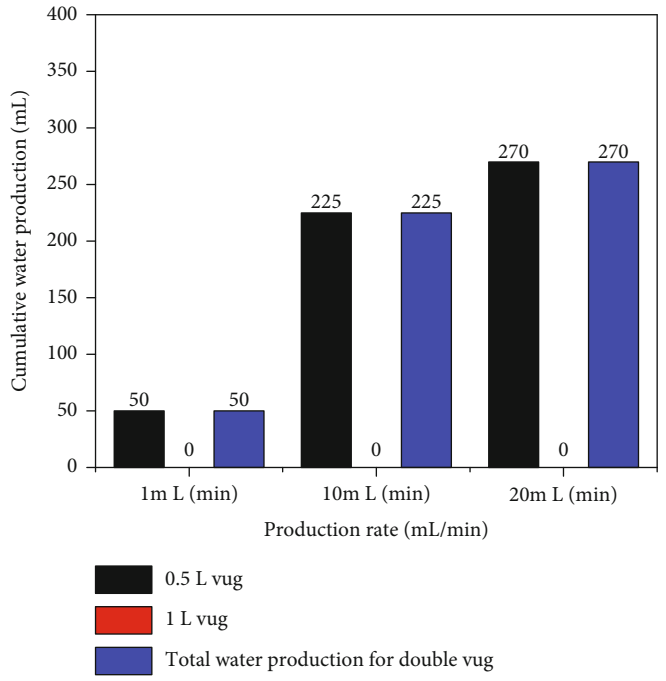

Figure 20: Column chart of cumulative water production in high-pressure physical property experiments under connection type II (different production rates).

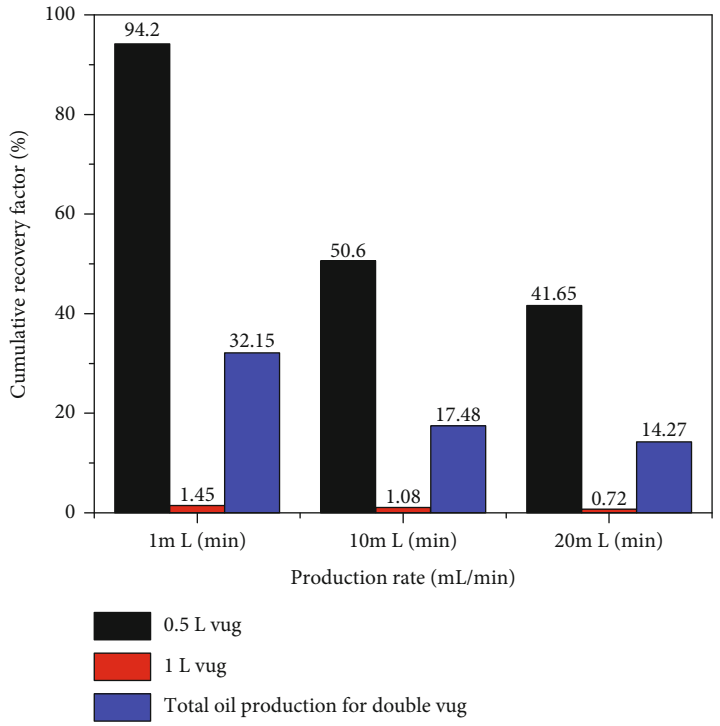

Figure 21: Column chart of crude oil recovery percentage in high-pressure physical property experiments under connection type II (different production rates).

double-vug reservoirs with bottom water under different production rates, as shown in Figure 8.

Under connection type II, production proceeded at the top of the 0.5 L vug, and the production rate clearly affected the production pressure characteristics of double-vug reservoirs with bottom water. At a production rate of 1 mL/min, the pressures of the 0.5 L vug, the 1 L vug, and the 24 L intermediate container containing bottom water all showed linear decreased. Production pressures differed little between various moments. When the production rate reached

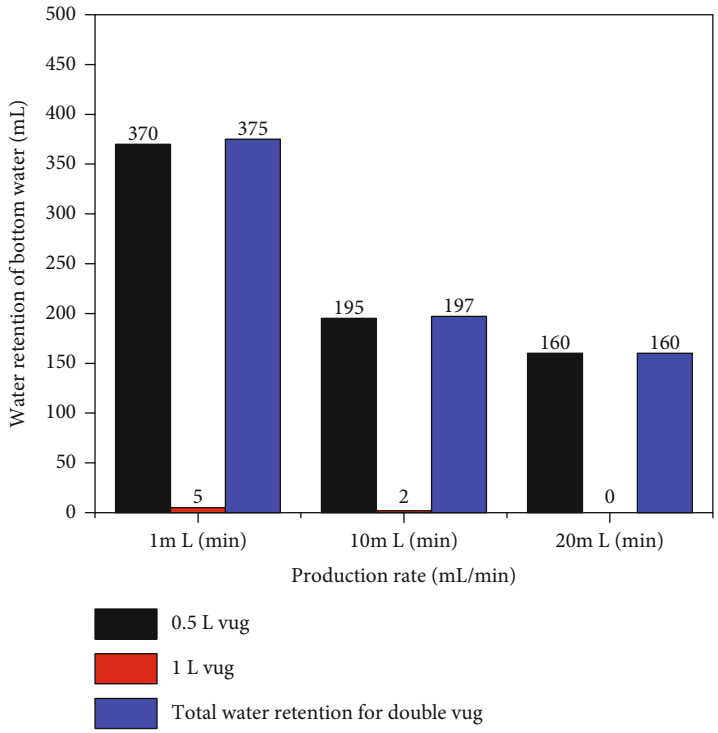

Figure 22: Column chart of bottom water invasion and retention in high-pressure physical property experiments under connection type II (different production rates).

10 mL/min, the pressure variation of the 1 L vug began to deviate from the pressure variations of the 1 L vug and the 24 L intermediate container containing bottom water, showing a clear moderated trend of pressure drop after 14 min of production. When the production rate reached 30 mL/min, the pressure variation of the 1 L vug clearly differed from the pressure variations of the 1 L vug and the 24 L intermediate container containing bottom water. Analysis showed that this phenomenon was mainly attributable to insufficient fracture flow capacity. That is, when the production rate exceeded 10 mL/min, the feed flow from the 1 L container to the output end was limited by the fracture, resulting in differences in pressure drop.

Figures 9–11 show that bottom water significantly affected the recovery percent of double-vug reservoirs. Under connection type II, the recovery percent of reservoirs with bottom water uniformly exceeded 10%, which is higher than that of reservoirs without bottom water. Moreover, bottom water channeling occurred in the production process of the 0.5 L vug at all three production rates, and increasing production rate led to higher water channeling volume and lower cumulative oil production of fractured-vuggy reservoirs. At a production rate of 1 mL/min, the water channeling volume was 15 mL, and the recovery percentage of the vug system was 14.5%. When the production rate increased to 10 mL/min, the water channeling volume was 32 mL, and the recovery percentage of the system was 13.2%. When the production rate further increased to 30 mL/min, the water channeling volume increased to 65 mL, and the recovery percentage of the system decreased to 10.1%. Thus, for reservoirs with bottom water which are susceptible to water channeling, the production rate should be properly controlled in the development process to avoid strong water channeling and fully utilize the elastic energy of bottom water for developing fractured-vuggy reservoirs.

According to Figure 12, bottom water mainly invaded the 0.5 L vug but did not intrude into the 1 L vug, which was consistent with the difference in oil production between the two vugs. The 0.5 L vug experienced substantial bottom water invasion, and its oil production was also significantly higher than that of the 1 L vug. With worsening bottom water channeling, the bottom water retention in vugs decreased, and the recovery percentage of reservoirs with bottom water decreased.

3.2. High-Pressure Physical Property Experiments on Reservoirs with Constant-Pressure Bottom Water

3.2.1. Production Pressure Variations. Figure 13 shows the pressure variation curves of high-pressure physical property experiments on reservoirs with constant-pressure bottom water under connection types I and II at a production rate of 20 mL/min.

In experiments on reservoirs with constant-pressure bottom water, production pressure remained around 38-39 MPa with only slight fluctuation. Neither the production rate nor the fracture-vug relationship exerted any apparent effects on production pressure characteristics. Compared with reservoirs with constant-volume bottom water vuggy reservoir, vuggy reservoirs with constant-pressure bottom water had sufficient natural energy.

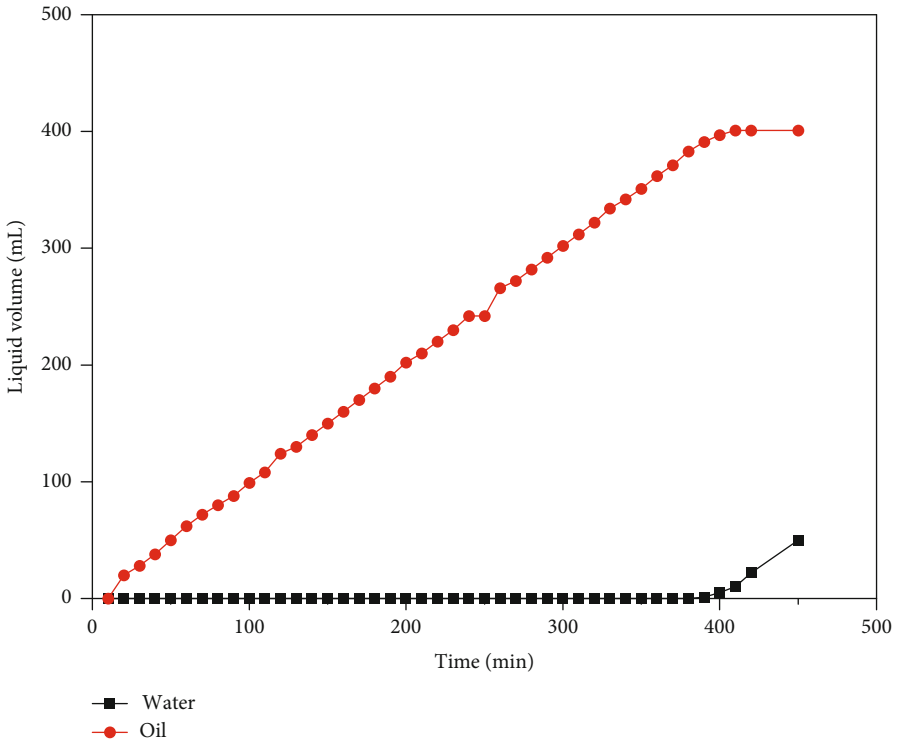

(a)

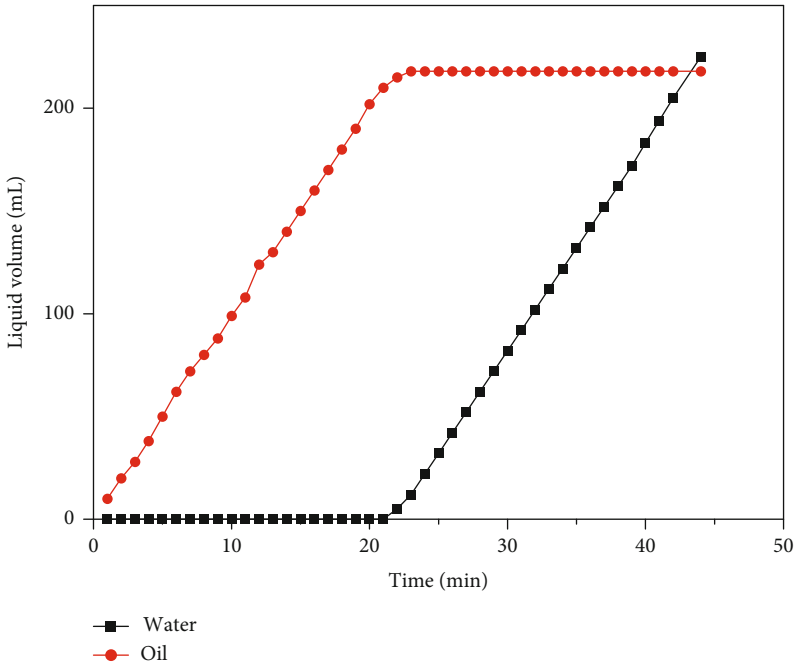

(b)

Figure 23: Continued.

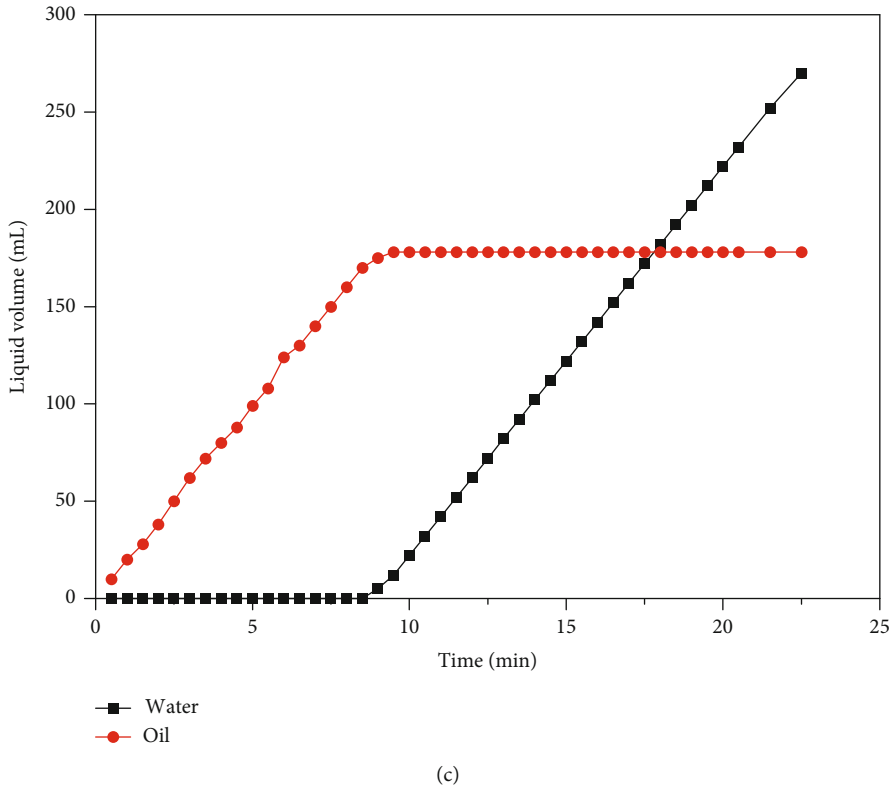

(c)

Figure 23: Oil/water production variation curves under connection type II (different production rates with (a) 1 mL/min, (b) 10 mL/min, and (c) 20 mL/min).

3.2.2. Production Characteristics under Connection Type I. Figures 14–16 show that constant-pressure bottom water significantly affected the recovery percentage of double-vug reservoirs. Under connection type I, the recovery percentage of fractured-vuggy reservoirs with constant-pressure bottom water could uniformly exceed 17% at all three production rates. This is higher than that of fractured-vuggy reservoirs without bottom water and that of fractured-vuggy reservoirs with constant-volume bottom water. In particular, the recovery percentage of fractured-vuggy reservoirs with constant-pressure bottom water reached 54% at a production rate of 1 mL/min. The production rate significantly affected the development effect of fractured-vuggy reservoirs with constant-pressure bottom water. The recovery percentage at 1 mL/min was 3.13 times of that at 20 mL/min. The cumulative water production rates at 10 mL/min and 20 mL/min were far higher than that at 1 mL/min. Thus, given reasonable production systems, bottom water can provide sufficient energy for the development of fractured-vuggy reservoirs with constant-pressure bottom water, thus greatly improving their development effect. Under connection type I, most crude oil production was contributed by the 1 L vug, while the crude oil recovery percentage of the 0.5 L vug was uniformly lower than 1.7%.

According to Figure 17, bottom water mainly invaded the 1 L vug but only slightly intruded into the 0.5 L vug, which was consistent with the difference in oil production between these two vugs. The 1 L vug experienced substantial bottom water invasion and retention, and its oil production was significantly higher than that of the 0.5 L vug.

Figure 18 shows oil/water production variations over time for these experiments. After water breakthrough at the output end in case of fractured-vuggy reservoirs with constant-pressure bottom water, water productivity quickly increased to 100%, and further production basically produced no oil. Increasing the production rate led to shorter water breakthrough time and lower oil production upon water breakthrough.

3.2.3. Production Characteristics under Connection Type II. Figures 19–21 show that constant-pressure bottom water significantly affected the recovery percentage of double-vug reservoirs. Under connection type II, the recovery percentage of reservoirs with bottom water uniformly exceeded 14%.

From this figure, this is clearly higher than that of reservoirs without bottom water and reservoirs with constant-volume bottom water. Moreover, bottom water channeling occurred in the production process of the 0.5 L vug at all three production rates, and increasing the production rate led to higher water channeling volume and lower cumulative oil production of fractured-vuggy reservoirs. At a production rate of 1 mL/min, the water channeling volume was 50 mL, and the recovery percentage of the vug system was 32.2%. When the production rate increased to 10 mL/min, the water channeling volume increased to 225 mL, and the recovery percent of the system was 17.5%. When the

production rate further increased to 20 mL/min, the water channeling volume was 270 mL, and the recovery percentage of the system decreased to 14.3%. Thus, regarding reservoirs with constant-pressure bottom water and sufficient energy, close attention should be paid to production rate control in the development process as this can avoid strong water channeling and fully utilize the elastic energy of bottom water for developing fractured-vuggy reservoirs.

According to Figure 22, bottom water mainly invaded the 0.5 L vug but only slightly intruded into the 1 L vug, which was consistent with the difference in oil production between both vugs. The 0.5 L vug experienced substantial bottom water invasion and retention, and its oil production was significantly higher than that of the 1 L vug. Moreover, with worsening bottom water channeling, the bottom water retention in vugs decreased, and the recovery percentage of reservoirs with bottom also water decreased.

Figure 23 shows oil/water production variations over time in experiments. A comprehensive analysis indicates that, compared with fractured-vuggy reservoirs with constant-volume bottom water, those with constant-pressure bottom water have more sufficient natural energy and greater development potentials. However, in practical development, reasonable production systems should be established to fully utilize the elastic energy of bottom water for developing fractured-vuggy reservoirs.

3.3. Comparison between High-Pressure Physical Property Experiments. For double-vug reservoirs with constant-pressure bottom water, the bottom water supplied during production can sustain energy supply to double-vug production, and pressure variations tend to be consistent. In the case of connection type I, the recovery percentage is higher, and bottom water mainly invades and retains in vugs based on open-well production. Because of water invasion and fracture limitation, production of distal reserves is restricted.

Compared with constant-volume bottom water, constant-pressure bottom water has sufficient energy and can quickly replenish vug energy. Therefore, the recovery percentage and bottom water invasion and retention volume of fractured-vuggy reservoirs with constant-pressure bottom water are both higher than those of fractured-vuggy reservoirs with constant-volume bottom water.

4. Conclusions

(1) Bottom water clearly affects the production pressure characteristics of double-vug reservoirs. Compared with vuggy reservoirs without bottom water, double-vug reservoirs with bottom water have a clearly extended pressure drop time, suggesting that bottom water can significantly increase the natural energy of double-vug reservoir systems

(2) In circumstances where the structural environment of the reservoir is not liable to water invasion or where there is no obvious water channeling under proper development, the presence of bottom water is conducive to reservoir development and can provide sufficient energy for the development of fractured-vuggy reservoirs. Bottom water can be utilized to substantially improve the development effect of fractured-vuggy reservoirs

(3) Worsened bottom water channeling leads to less bottom water retention in vugs and a lower recovery percentage of reservoirs with bottom water. For reservoirs with bottom water which are susceptible to water channeling, the production rate should be appropriately controlled in the development process to avoid strong water channeling. Furthermore, the elastic energy of bottom water should be fully utilized for developing fractured-vuggy reservoirs

(4) For double-vug reservoirs with constant-pressure bottom water, the bottom water supplied during production can sustain energy supply to double-vug production, and pressure variations tend to be consistent. In the case of large vugs, the recovery percentage is higher, and bottom water mainly invades and retains in vugs based on open-well production. Because of water invasion and fracture limitation, production of distal reserves is restricted

(5) Compared with constant-volume bottom water, constant-pressure bottom water has sufficient energy and can quickly replenish vug energy. Therefore, the recovery percentage and bottom water invasion and retention volume of fractured-vuggy reservoirs with constant-pressure bottom water are both higher than those of fractured-vuggy reservoirs with constant-volume bottom water

Data Availability

We checked it carefully and confirmed that all data, models, and code generated at the manuscript could be obtained from the corresponding author.

Conflicts of Interest

The authors declare that they have no conflicts of interest.

Acknowledgments

This research was funded by the National Science and Technology Major Project of China (2016ZX05053) and the Science and Technology Department Project of Sinopec-China Petroleum (P11089).

References

[1] B. Zhang, X. Chen, and P. Yue, "Research on unit mining by elastic drive of fractured-vuggy carbonate reservoir with bottom water by water intrusion," *Reservoir Evaluation and Development*, vol. 10, no. 2, pp. 71–75, 2020.

[2] X. Y. Hu, L. S. Quan, D. S. Qi, and J. G. Hou, "Features of cavern flling in fractured/vuggy carbonate oil reservoirs, Tahe Oilfield," *Specialty Oil & Gas Reservoirs*, vol. 21, no. 1, pp. 18–21, 2014.

[3] X. M. Zhou and M. H. Shahzad Kamal, "Experimental study on the relationship between carbonate reservoir quality index and dynamic parameters of chemical solutions for oil recovery practice," *Energy & Fuels*, vol. 33, no. 10, pp. 9747–9758, 2019.

[4] E. Artun, T. Ertekin, R. Watson, and B. Miller, "Performance evaluation of cyclic pressure pulsing in a depleted, naturally fractured reservoir with stripper-well production," *Petroleum Science and Technology*, vol. 29, no. 9, pp. 953–965, 2011.

[5] Z.-X. Xu, S.-Y. Li, B.-F. Li, D.-Q. Chen, Z.-Y. Liu, and Z.-M. Li, "A review of development methods and EOR technologies for carbonate reservoirs," *Petroleum Science*, vol. 17, no. 4, pp. 990–1013, 2020.

[6] M. R. Hashmet, A. M. AlSumaiti, Y. Qaiser, and S. A. A. Waleed, "Laboratory investigation and simulation modeling of polymer flooding in high-temperature, high-salinity carbonate reservoirs," *Energy & Fuels*, vol. 31, no. 12, pp. 13454–13465, 2017.

[7] M. Bai, Z. Zhang, X. Cui, and K. Song, "Studies of injection parameters for chemical flooding in carbonate reservoirs," *Renewable and Sustainable Energy Reviews*, vol. 75, pp. 1464–1471, 2017.

[8] E. Ozkan, U. Ohaeri, and R. Raghavan, "Unsteady flow to a well produced at a constant pressure in a fractured reservoir," *SPE Formation Evaluation*, vol. 2, no. 2, pp. 186–200, 1987.

[9] J. S. Olarewaju and W. J. Lee, "Rate behavior of composite dual-porosity reservoirs," in *SPE Production Operations Symposium*, Oklahoma City, Oklahoma, 1991.

[10] C. F. Guo, H. B. Li, Y. Tao, L. Y. Lang, and Z. X. Niu, "Water invasion and remaining gas distribution in carbonate gas reservoirs using core displacement and NMR," *Journal of Central South University*, vol. 27, no. 2, pp. 531–541, 2020.

[11] A. Goudarzi, M. Delshad, K. K. Mohanty, and K. Sepehrnoori, "Surfactant oil recovery in fractured carbonates: experiments and modeling of different matrix dimensions," *Journal of Petroleum Science & Engineering*, vol. 125, pp. 136–145, 2015.

[12] Y. Li, D. P. Wan, and J. M. Liu, "Remaining oil enrichment areas in continental waterflooding reservoirs," *Petroleum Exploration and Development*, vol. 32, no. 3, pp. 91–96, 2005.

[13] S. Q. Zheng, M. Yang, Z. J. Kang et al., "Controlling factors of remaining oil distribution after water flooding and enhanced oil recovery methods for fracture-cavity carbonate reservoirs in Tahe Oilfield," *Petroleum Exploration and Development*, vol. 46, no. 4, pp. 786–795, 2019.

[14] J. Wang, H. Q. Liu, J. Zhang et al., "Experimental investigation on water flooding and continued EOR techniques in buried-hill metamorphic fractured reservoirs," *Journal of Petroleum Science and Engineering*, vol. 171, no. 12, pp. 529–541, 2018.

[15] Y. S. Liu, Y. T. Liu, Q. C. Zhang et al., "Large-scale physical simulation experimental study on thick carbonate reservoirs," *Petroleum Geology and Recovery Efficiency (in Chinese)*, vol. 27, no. 4, pp. 117–125, 2020.

[16] J. Wang, H. Q. Liu, J. Xu, and H. F. Zhang, "Formation mechanism and distribution law of remaining oil in fracture-cavity reservoir," *Petroleum Exploration and Development*, vol. 39, no. 5, pp. 624–629, 2012.

[17] Y. S. Rong, J. Z. Zhao, X. B. Lu, X. H. Li, and X. B. Li, "Remaining oil distribution patterns and potential-tapping countermeasures in carbonate fracture-cavity reservoir," *Acta Petrolei Sinica*, vol. 35, no. 6, pp. 1138–1146, 2014.

[18] Q. Zhao, J. J. Zhang, B. D. Ding, and Y. Wang, "Physical simulation of gas enhanced oil recovery for fractured-vuggy carbonate reservoirs in Tahe Oilfield," *Science Technology and Engineering*, vol. 17, no. 18, pp. 56–62, 2017.

[19] Z. Qian, H. Li, L. Qiao, and S. Bai, "Experiment on the mechanism of low salinity waterflooding in carbonate reservoir," *Lithologic Reservoirs*, vol. 32, no. 3, pp. 159–165, 2020.

[20] J. Wang, H. Song, and Y. Wang, "Investigation on the microflow mechanism of enhanced oil recovery by low-salinity water flooding in carbonate reservoir," *Fuel*, vol. 266, p. 117156, 2020.

[21] Z.-J. Song, M. Li, C. Zhao, Y.-L. Yang, and J.-R. Hou, "Gas injection for enhanced oil recovery in two-dimensional geology-based physical model of Tahe fractured-vuggy carbonate reservoirs: karst fault system," *Petroleum Science*, vol. 17, no. 2, pp. 419–433, 2020.

[22] J. Han, S. Han, D. Kang, Y. Kim, J. Lee, and Y. Lee, "Application of digital rock physics using X-ray CT for study on alteration of macropore properties by CO_2 EOR in a carbonate oil reservoir," *Journal of Petroleum Science and Engineering*, vol. 189, article 107009, 2020.

[23] S. H. Zaheri, H. Khalili, M. Sharifi, and M. Sharifi, "Experimental investigation of water composition and salinity effect on the oil recovery in carbonate reservoirs," *Oil & Gas Science and Technology-Revue d'IFP Energies nouvelles*, vol. 75, p. 21, 2020.

[24] S. Mohammadkhani, H. Shahverdi, and M. N. Esfahany, "Impact of salinity and connate water on low salinity water injection in secondary and tertiary stages for enhanced oil recovery in carbonate oil reservoirs," *Journal of Geophysics and Engineering*, vol. 15, no. 4, pp. 1242–1254, 2018.

[25] H. Bijan, A. Amin, K. Mohammad et al., "Experimental investigation of interfacial tension measurement and oil recovery by carbonated water injection: a case study using core samples from an Iranian carbonate oil reservoir," *Energy & Fuels*, vol. 31, no. 3, pp. 2740–2748, 2017.

[26] Z. Fan, K. Li, J. Li, H. Song, L. Hw, and X. Wu, "A study on remaining oil distribution in a carbonate oil reservoir based on reservoir flow units," *Petroleum Exploration and Development Online*, vol. 41, no. 5, pp. 634–641, 2014.

[27] M. Motealleh, R. Kharrat, and A. Hashemi, "An experimental investigation of water-alternating-CO_2coreflooding in a carbonate oil reservoir in different initial core conditions," *Energy Sources, Part A: Recovery, Utilization, and Environmental Effects*, vol. 35, no. 13, pp. 1187–1196, 2013.

[28] J. Fang, G. Zhao, M. Zhao, and C. Dai, "New channel flow control agent for high-temperature and high-salinity fractured-vuggy carbonate reservoirs," *Energy Sources, Part A: Recovery, Utilization, and Environmental Effects*, vol. 43, no. 3, pp. 337–348, 2021.

[29] W. Li, J. Chen, X. Tan, P. Liu, Y. Li, and L. Wang, "Long-core experimental study of different displacement modes on fractured-vuggy carbonate reservoirs," *Geosystem Engineering*, vol. 21, no. 2, pp. 61–72, 2018.

Hindawi
Geofluids
Volume 2022, Article ID 7983330, 9 pages
https://doi.org/10.1155/2022/7983330

Research Article

Study on Reasonable Formation Pressure Maintenance Level for Middle-Deep Reservoirs in the Bohai Sea

Cai Hui, Yang Xiaoyan, Xie Shujian, Zhang Zhanhua, Wang Long, and Gao Yue

Bohai Oilfield Research Institute, Tianjin Branch Company, CNOOC Ltd., Tianjin, China 300459

Correspondence should be addressed to Yang Xiaoyan; yangxy6@cnooc.com.cn

Received 11 April 2022; Revised 13 May 2022; Accepted 19 May 2022; Published 11 June 2022

Academic Editor: Shuyang Liu

Copyright © 2022 Cai Hui et al. This is an open access article distributed under the Creative Commons Attribution License, which permits unrestricted use, distribution, and reproduction in any medium, provided the original work is properly cited.

Reasonable formation pressure maintenance level is significant to high-efficient development of oilfields. In order to study the effects of overlying strata pressure on permeability, oil-water phase permeability curve, and oil displacement efficiency, a physical simulation experiment is designed. Based on the experimental results and the oil-water phase flow theory, the production equation and the mathematical model of oil displacement efficiency considering stress sensitivity are established. And the productivity changes with pressure drop under different permeability are plotted. Then, the permeability coefficients calculated by quantitative characterization of stress sensitivity under different formation pressures are introduced into the numerical simulation model to quantitatively determine the reasonable formation pressure maintenance level of different reservoir properties. Experimental and theoretical studies show that the permeability decreases continuously with the increase in effective overlying strata pressure. In a low permeability reservoir, the more permeability decrease is caused by the increase in effective overlying strata pressure. When reservoir pressure is restored by water injection, the permeability loss is irreversible. With the increase in effective overlying strata pressure, the producer productivity decreases obviously, and the effective seepage capacity and oil displacement efficiency decrease. For reservoirs with permeability below 100 mD and high stress sensitivity, high formation pressure level should be maintained. For reservoirs with permeability of more than 300 mD, lower formation pressure is acceptable in the initial stage. The results are consistent with the actual production characteristics, which effectively guide the establishing of reasonable oilfield development strategy. It has important guiding significance to the oilfield development plans and development of the middle-deep oilfields.

1. Introduction

Pressure is the soul of the oilfield development process. Reasonable formation pressure maintenance is the key to the entire pressure system [1–4]. It not only determines the injection pressure and formation pressure of the injector but also restricts the flow conditions of the producer. Maintaining a reasonable formation pressure is the foundation for achieving stable production in the oilfield. The production pressure difference of the producer is reduced with a low formation pressure, while the seepage capacity is reduced, the energy is insufficient, the productivity of the producer is reduced, and the production cannot meet the demand. However, the high requirements for wellhead equipment will greatly increase the cost while the formation pressure is too high. At the same time, the contradiction between the horizontal and vertical of the oilfield is aggravating. The predecessors [5–9] used an empirical formula method, minimum flow pressure method, reasonable injection-production pressure system method, crude oil loss function method, material balance method, injection-production balance method, and other methods to study the reasonable maintenance level of formation pressure and get some remarkable achievement. But there is no research considering the pressure-sensitive effect caused by the formation pressure drop yet. It is proposed for the first time that the influence of the pressure-

Table 1: Table of core parameters.

Well	Layer	Core depth (m)	Core length (cm)	Core diameter (cm)	Gas permeability (mD)
3	E_2s_3	2569.40	5.58	2.54	10
3	E_2s_3	2563.40	5.52	2.54	30
5	E_2s_3	2491.5	6.48	2.54	100
2	E_2s_3	2554.26	5.37	2.54	300
2	E_2s_3	2454.26	5.37	2.54	1000

sensitive effect is caused by the decrease in formation pressure through physical simulation experiments, reservoir engineering methods, and numerical simulation technology. And then, determine pressure maintenance level under different reservoir conditions.

2. The Impact of Formation Pressure Maintenance Level on Productivity

When the reservoir is not developed, the reservoir rock is in a state of static equilibrium under the combined action of the pressure of the overlying strata, the pore fluid pressure, and the supporting force of the rock skeleton. During the reservoir developing, as the fluid is produced, the pore fluid pressure gradually decreases. With the pressure of the overlying strata unchanged, the supporting force of the rock skeleton continues to increase and the pore throats and microcracks of the rock are compressed, which lead to changing the physical properties of rocks [10–13]. Therefore, the influence of rock stress sensitivity should be considered in the development process.

2.1. Stress Sensitivity Test. The basic principle of the stress sensitivity test is to simulate the effective overlying strata pressure of the oil and gas reservoir [14–16]. Pressurize the rock core to a certain value andthen gradually reduce the pressure to return to the initial overburden pressure. Study the non-steady state of permeability changing with the overburden pressure process [17, 18]. Approximately take the difference between the overlying strata pressure and the pressure of the pore fluid in the rock as the effective overburden pressure, use the confining pressure to simulate the pressure of the overlying formation, and increase the confining pressure to simulate the continuous decrease in the pore pressure of the formation and cause the effective pressure of the rock skeleton to gradually increase.

(1) Number of cores and basic conditions: select cores with a permeability of 10~1000 mD (Table 1), which can better reflect 5 sets of cores with different physical properties for experiment

(2) The conditions of the gas used in the experiment: this experiment uses nitrogen for displacement, the displacement pressure is set to 2 MPa, the temperature is 20°C (room temperature), and the nitrogen viscosity is 0.018 mPa·s

(3) Experimental instruments: the main instruments used in this experimental design are nitrogen bottles, core holders, hand pumps, gasflowmeters, and pressure gauges. The design drawing of the experimental instrument is shown in Figure 1, and the physical photo of the experimental instrument is shown in Figure 2

Experimental process: (1) put the measuring core in the core holder, adopt the gas permeability method, and set the driving pressure to 2 MPa; (2) after the gas flowmeter reading is stable, change the effective stress of the core through the confining pressure pump to simulate formation stress-sensitive environment, and record the experimental data after the gas flowmeter reading is stable; (3) continuously increase the confining pressure with a change of 2 MPa, record the flowmeter reading, and stop after the confining pressure rises to 25 MPa. Then, enter the pressure reduction process.Decrease the confining pressure with a change of2MPa and record the gas flowmeter reading. Repeat the process of lifting andlowering pressure three times to reduce experimental error; (4) after completing three times of lifting and lowering pressure process, relieve the confining pressure pump, turn off the air pump, remove the core holder, replace the core, and repeat the above process.

2.2. Analysis and Quantitative Characterization of Stress-Sensitive Experiment Results. The experimental research results show that with the increase in the effective overburden pressure, the permeability continues to decrease, and the lower the core permeability, the greater the drop in permeability caused by the increase in the effective overburden pressure (Figure 3). Generally speaking, the changes can be divided into two stages. In the first stage, the effective overburden pressure is less than 10 MPa, and the decline is relatively large. Due to the overburden pressure, the rock skeleton is deformed, resulting in a rapid decrease in permeability. In the second stage, the overlying pressure is 10-25 MPa, and the decrease is relatively slow. With the increase in the overlying pressure, the pore structure changes very little, and the drop in permeability is not obvious.

As the effective overburden pressure decreases, the permeability gradually recovers. The lower the core permeability, the greater the permeability loss. Therefore, even if the reservoir pressure is restored by water injection during oilfield development, the permeability can only partially recover, and the permeability loss is irreversible.

Experimental results show that cores with different permeability levels are stress-sensitive, and the difference in

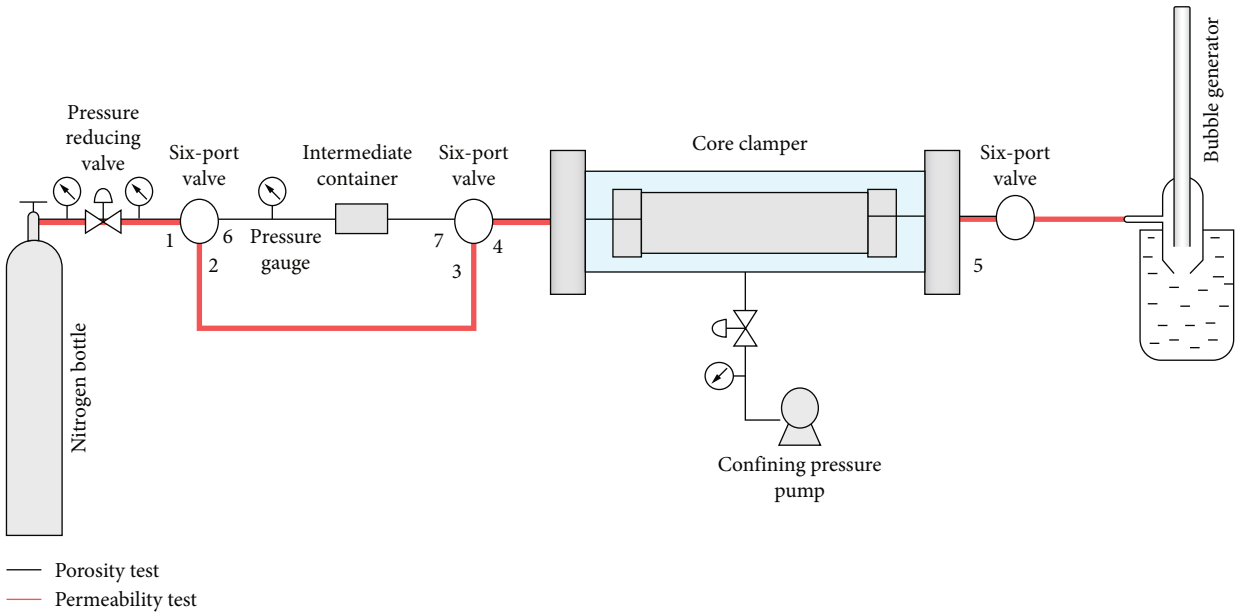

Figure 1: Layout of the experimental apparatus.

Figure 2: Object pictures of experimental instruments.

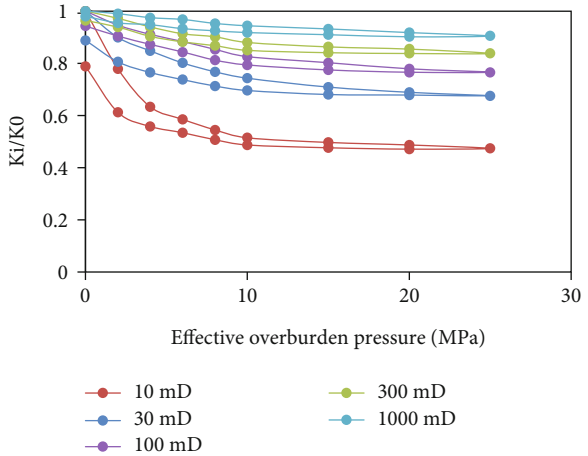

Figure 3: The variation of permeability of different core permeability with effective overburden pressure.

permeability determines the degree of stress sensitivity. As a whole, the permeability under different effective overburden pressures has a power relationship with the effective overburden pressure:

$$\frac{K_i}{K_0} = a \times \sigma^{-s}. \tag{1}$$

In the formula, K_0 is the initial permeability (mD), K_i is the permeability under effective overburden pressure (mD), σ is the effective overburden pressure (MPa), s is the stress sensitivity coefficient, and a is the regression coefficient.

In order to quantitatively characterize the stress sensitivity under different permeability conditions, a quantitative relationship between the stress sensitivity coefficients regressed from 5 sets of data and the initial permeability of the core is established (Figure 4).

Considering that the regression coefficient a is around 1, the quantitative expression of reservoir stress sensitivity is simplified as

$$K_i = K_0 \times \sigma^{-\left(0.4237 \times K_0^{-0.352}\right)}. \tag{2}$$

According to the similarity between the increase in effective overburden pressure (increasing confining pressure) and the actual pore pressure drop in the oilfield, the relationship between the permeability and the pressure in the actual production process of the oilfield can be further obtained:

$$K_i = K_0 \times \left(P_e - P_i\right)^{-\left(0.4237 \times K_0^{-0.352}\right)}. \tag{3}$$

In the formula, P_e is the original formation pressure (MPa) and P_i is the current formation pressure (MPa).

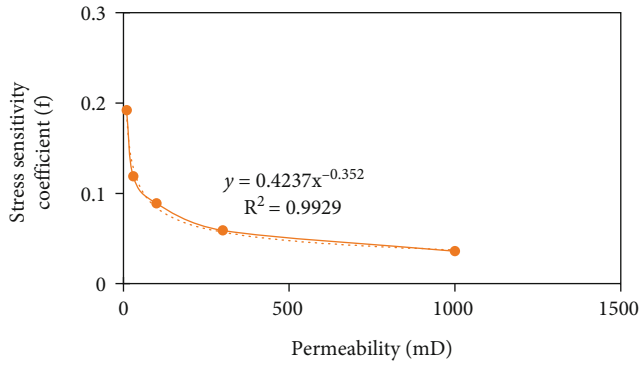

Figure 4: Distribution of stress sensitivity coefficient under different permeability.

Further establish the productivity equation considering the stress sensitivity. The producer plane radial stable seepage equation [19] is formula (4).

$$Q = \frac{2\pi \bullet K_i \bullet h}{\mu_o \bullet B \bullet (\ln (r_e/r_w) + S)} \bullet \Delta P. \quad (4)$$

In the formula, Q is the production (m^3/d), h is the reservoir thickness (m), μ_o is the oil viscosity, mPa·s, B is the oil volume coefficient, r_e is the supply radius (m), r_w is the well radius (m), ΔP is the production pressure differential (MPa), and S is the skin factors.

Considering the stress sensitivity caused by the drop in formation pressure during the production process of a producer, substituting formula (3) into (4) .

$$Q = \frac{2\pi \bullet h}{\mu \bullet B \bullet (\ln (r_e/r_w) + S)} \times K_0 \times (P_e - P_i)^{-\left(0.4237 \times K_0^{-0.352}\right)} \times \Delta P. \quad (5)$$

Incorporate the basic parameters of the oilfield into formula (5), and plot the change of productivity with pressure drop under different permeability of the oilfield (Figure 5). It can be seen that the formation pressure drop has a greater impact on the productivity. At the initial stage of the formation pressuredrop, the large productivity drop is mainly due to the deformation of the rockskeleton and even closure of the pore throats, resulting in a rapid decrease inpermeability. When the pressure of a low-permeability reservoir drops by 5 MPa, the productivity loss exceeds 20%. In the medium permeability reservoir, when thepressure drops by 10MPa, the productivity loss exceeds 10%.And when the pressure in the high-permeability reservoir drops by 15 MPa, the productivity loss exceeds 10%. In general, as the formation pressure decreases, the productivity gradually decreases. The lower the permeability, the greater the productivity loss. The reasonable pressure levels should be determinedaccording to the different physical properties of reservoirs.

In order to ensure the long-term stable development of the oilfield, the maximum pressure drop of middle-deep reservoirs in the Bohai Sea is generally controlled below 5 MPa for reservoirs with permeability less than 50 mD. The maximum pressure drop is generally controlled at 8~9 MPa for reservoirs with permeability between 50 mD and 500 mD. The maximum pressure drop can be widened to 12~15 MPa for reservoirs with permeability greater than 500 mD.

3. The Influence of Formation Pressure Maintenance Level on Oil-Water Two-Phase Seepage

Design five sets of water flooding experiments under different formation pressure conditions (5 MPa, 10 MPa, 15 MPa, 20 MPa, and 25 MPa) to obtain oil-water phase permeation curves under different pressure conditions. Using the JBN method to process the relative permeability data. The experimental results (Figures 6 and 7) show that the stress sensitivity has a great impact on the oil-water relative permeability curve. (1) As the formation pressure decreases, the irreduciblewater saturation increases. The main reason is that the core permeabilitydecreases due to stress sensitivity. And during the process of saturating oil,it is difficult for oil to drive water out of the hydrophilic rock. The resistanceof oil-water flow is increasing, which also leads to the increase ofirreducible water saturation.(2) As the formation pressure decreases, the overall permeability of the core decreases, and the relative permeability of the oil phase and the water phase decreases. The oil phase permeability decreases significantly, which leads to a decrease in producer productivity and an increase in productivity decline. (3) As the formation pressure decreases, the isotonic point decreases, and the overall oil-waterphase permeation curves shift to the left, the oil-water two-phase permeation zone narrows. It is mainly because that the stress sensitivityleads to the narrowing of the pore throats and the reduction of effectiveseepage capacity, which further reduces the oil displacement efficiency. (4) The decrease of formation pressure increases theresidual oil saturation small.

The core water drive efficiency can be expressed as [20]

$$E_r = \frac{1 - S_{wi} - S_{or}}{1 - S_{wi}}. \quad (6)$$

In the formula, E_r is the oil displacement efficiency, S_{wi} is the bound water saturation, and S_{or} is the residual oil saturation.

According to the experimental results, a mathematical model of formation pressure, bound water saturation, and remaining oil saturation is established:

$$S_{wi} = b1 \times P_i + b2, \quad (7)$$

$$S_{or} = c1 \times P_i + c2. \quad (8)$$

In the formula, $b1$, $b2$, $c1$, and $c2$ are fitting coefficients and $b1$ and $c1$ are negative.

Incorporating equations (7) and (8) into equation (6) and combined with experimental fitting data, the oil displacement efficiency equation under different formation pressures can be established.

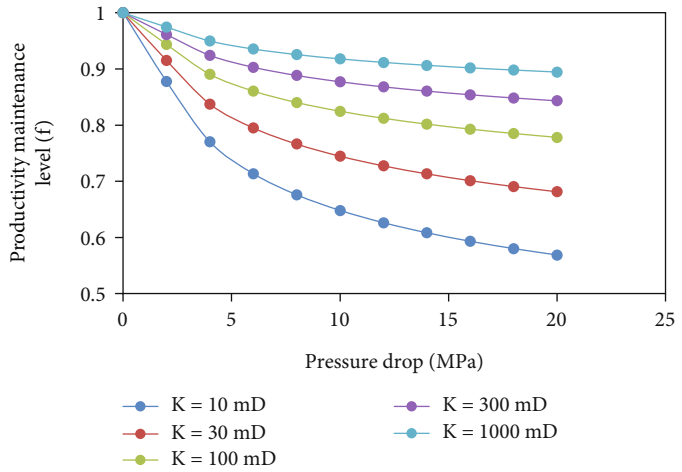

Figure 5: Effect of stress sensitivity on productivity decline (single-phase production).

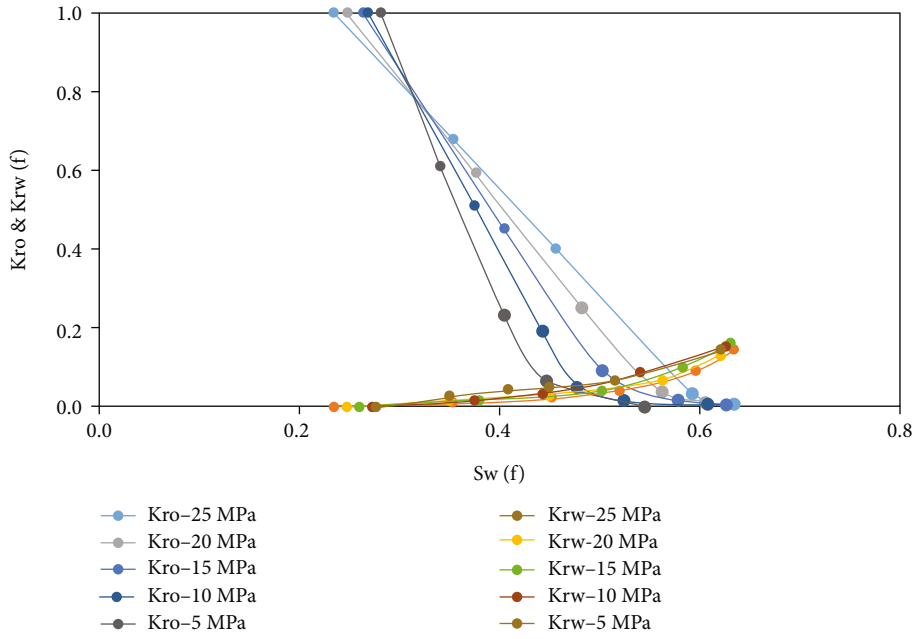

Figure 6: Oil-water phase permeation curves under different formation pressures.

$$E_r = \frac{0.0028P_i + 0.3286}{0.0023P_i + 0.7103}. \quad (9)$$

And the relationship between formation pressureand oil displacement efficiency can be drawn.The lower the formation pressure maintenance level is, the lower the oil displacement efficiency becomes (Figure 8). It is mainly caused by the formation pressure decreases. When the supporting force of the rock skeleton increases, the rock compression is serious, the pore structure is deformed, and the pore space and permeability change. Some parts of the flow channel are even closed, forming dead pores, and the oil stored in the dead pores cannot be displaced effectively.

4. Determination of Reasonable Formation Pressure Maintenance Level considering Stress Sensitivity

Based on experimental results, we interpolated the phase permeation curve in the keyword ROCKTAB and modified it corresponding to different formation pressures by setting the relevant parameters of the keyword ROCKCOMP in the oilfield simulation model, so that the influence of stress sensitivity was considered in the model.

The actual model of KLA oilfield uses the five-point method to deploy wells with a well spacing of 300 × 300 m. The simulation considers the seepage field and production

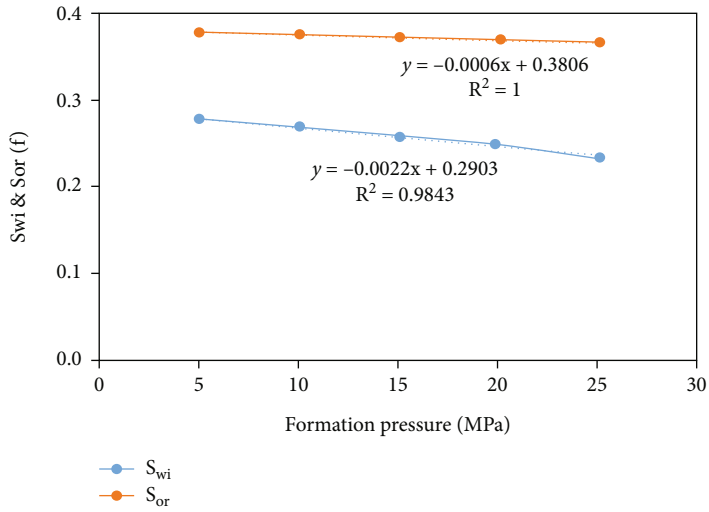

Figure 7: Relationship between S_{wi}, S_{or}, and formation pressure.

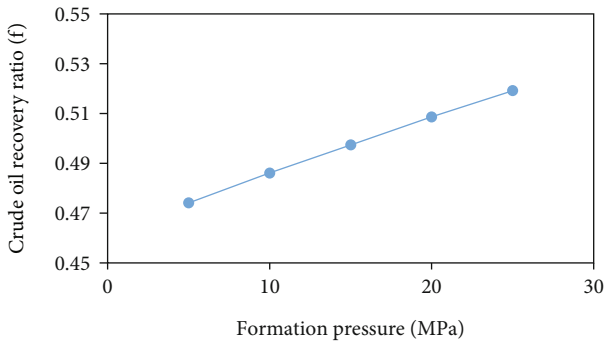

Figure 8: Influence of formation pressure on the crude oil recovery ratio.

characteristics of different development stages under stress sensitivity and clarifies the reasonable formation pressure maintenance level of reservoirs with different permeability levels (Figure 9). For reservoirs with a permeability lower than 100 mD and strong stress sensitivity, high pressure levels should be maintained. This is of great significance for protecting reservoirs near the wellbore, increasing single well production of producers and maintaining efficient and reasonable development of oilfields. For reservoirs with a permeabilityabove 300mD, under the premise that the formation pressure is higher than thesaturation pressure, the pressure can be appropriately reduced.

5. Instance Verification and Application

5.1. Instance Verification. KLA is a complex thin interbed reservoir. The existing seismic data has difficulty identifying the reservoir connectivity and the production capacity. It is necessary to test production, further access information to deepen reservoir understanding, and further identify potential reserves, productivity, and reservoir connectivity. In the marginal part of the well 2 block, the producer A24 encountered an oil layer with a thickness of 50 m and a permeability of 70 mD. A24 works well after it was put into production. The injector A23, which corresponding to A24, encountered an oil layer bottom, and the reserve scale was unclear. In the plan, A23 drains fluid at first and transfers to injection in time after A23 confirms the reserve scale. Since there is no injector in this block before, the formation pressure around A24 drops by 11 MPa, which leads to reservoir stress sensitivity, permeability reduction, and productivity decline. After the A23 transferring to injection in the later period, the productivity of A24 recovered gradually. However, the production capacity is much lower than the initial level (Figure 10). In the well 3 block with a permeability of about 300 mD, the marginal injector B14 drainages to verify the productivity at first. During the drainage, the corresponding producer B12 showed a stable initial liquid volume. After the formation pressure dropped significantly, the production capacity of B12 gradually decreased. And when the B14 transferring to injection in the later period, the production capacity of well B12 rebounded significantly. The actual production is consistent with the theoretical research results. For the wells in the areas with poor permeability, it is recommended to inject water synchronously to maintain the original formation pressure. In the areas with higher permeability, short-term formation pressure drops will not cause reservoir stress sensitivity. And if there is an evaluation requirement, the formation pressure can be appropriately reduced. After the evaluation task was completed, the injectors should recover water injection in time.

5.2. Guide the Preparation of the New Oilfield. The KLB oilfield is divided into multiple well blocks on the plane by the fault. In the ODP plan preparation process, in order to determine the reasonable water injection time of each well block, the stress-sensitive influence is characterized in the numerical model., and the physical properties of the different blocks are determined. Characteristics and natural energy conditions determine the timing of water injection

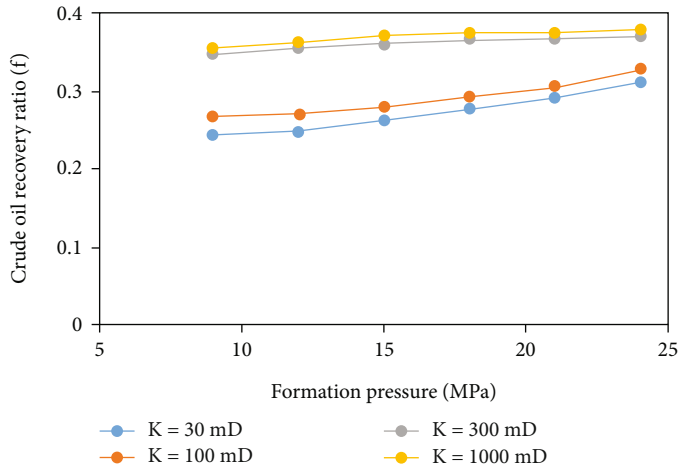

Figure 9: Determination of formation pressure maintenance levels of different reservoir properties.

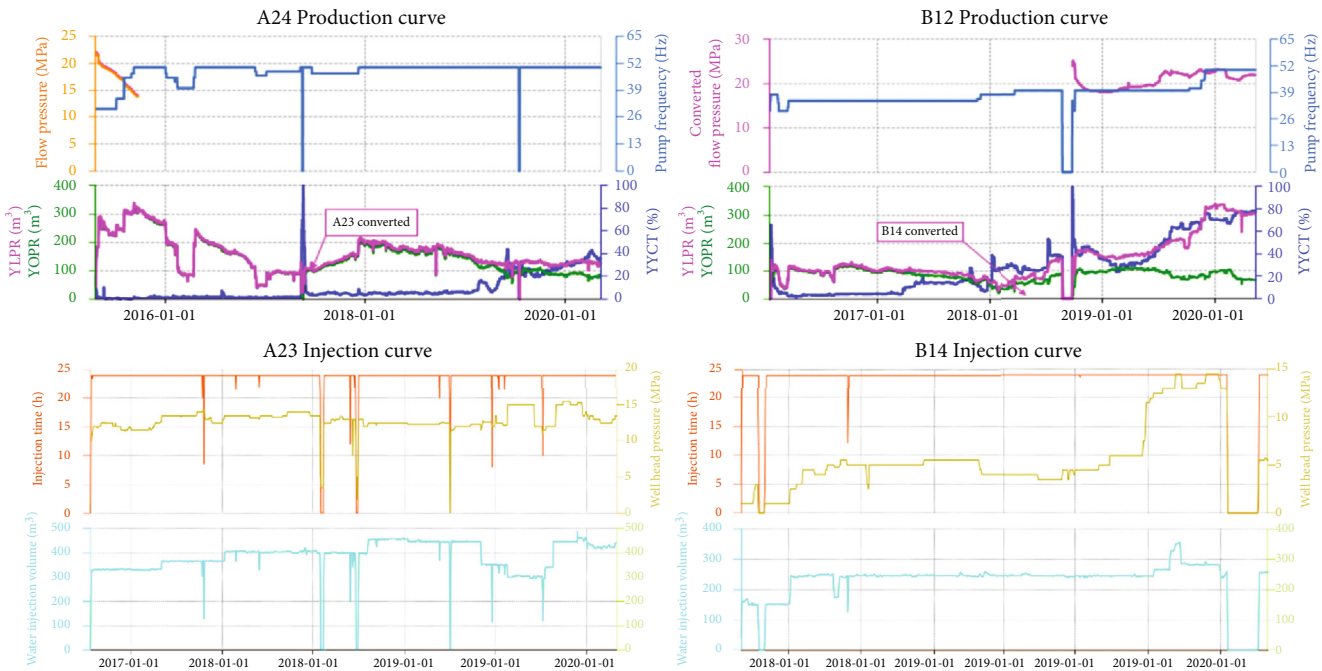

Figure 10: Production curve of A24, B12, A23, and B14.

Table 2: Comparison table of oil recovery under different pressure maintenance levels in different well areas.

Pressure maintenance levels	Well 1 area	Well 2 area	Well 3 area	Well 5 area	Well 6 area	Well 8Sa area
100%	29.8	32.6	20.8	31.8	31.2	30.0
95%	30.2	32.0	20.2	32.3	31.4	29.8
90%	29.5	30.5	19.5	31.4	30.5	29.0
85%	27.8	28.0	18.0	29.5	29.0	27.6

in each well area (Table 2). For the well 1/5/6 area with a reservoir property of 200~300 mD, considering that the ground saturation pressure difference is large and it has a certain natural energy, it is recommended to inject water after half a year after draining fluid from the injector; that is, when the formation pressure is maintained at 95%, perform water injection. For the 8Sa well area with reservoir physical properties below 100 mD, considering that the formation

pressure drops, the reservoir stress will be sensitive, which will have a greater impact on productivity and seepage capacity. The program recommends that the production wells are injected immediately after commissioning to maintain the original formation pressure. For the 2/3 well area, considering that the ground saturation pressure difference is small and the natural energy is insufficient, the program recommends that the production well is put into production and injected immediately to maintain the original formation pressure. The oilfield was put into production in March 2019. After it was put into production, water injection was implemented in accordance with the recommended plan. In the two years since it was put into production, the oilfield's natural decline rate and water cut increase rate have maintained relatively good development indicators.

6. Conclusion

(1) As the formation pressure decreases, the reservoir will become stress-sensitive, resulting in a decrease in permeability and porosity. Under laboratory conditions, the formation pressure decreased by 25 MPa, the permeability of the 10 mD reservoir decreased by 46%, and the permeability of the 300 mD reservoir decreased by 17%. And the loss is irreversible. Even if the pressure returns to the original formation pressure, the permeability of the 10 mD reservoir still drops by 21%, and the permeability of the 300 mD reservoir drops by 5% which leads to a decrease in the productivity of the producers, a greater lapse rate, and a greater impact on the development effect

(2) With the decrease in formation pressure, the oil phase permeability curve is obviously concave, the point of equal permeability moves left, and the irreducible oil saturation increases. Under laboratory conditions, when the pressure decreases by 15 MPa, the irreducible oil saturation increases by 9%. And the effective seepage capacity will decrease, resulting in a decrease in oil displacement efficiency

(3) During the development of middle-deep oilfields, it is necessary to grasp a reasonable timing of water injection to ensure a higher pressure maintenance level to achieve better development results. The research results have a good guiding role in the formulation of KLB oilfield development strategies

Data Availability

The data used to support the findings of this study are included within the article.

Conflicts of Interest

The authors declare that they have no conflicts of interest regarding the publication of this paper.

Acknowledgments

This work is supported by "Thirteenth Five-Year Plan" National Science and Technology Major Project-Bohai Oilfield Efficient Development Demonstration Project (2016ZX05058) and CNOOC Science and Technology Project-High water cut and high recovery degree of Bohai Oilfield Key Technology Research (YXKY-2018-TJ-04).

References

[1] L. Yinsong, Y. Shangkong, and Y. Erlong, "Reasonable formation pressure in the west part of central block in Saertu of Daqing oilfield," *Journal of Petrochemical Universities*, vol. 32, no. 3, pp. 82–86, 2019.

[2] G. Fenzhuan, T. Hai, and L. Dongliang, "Research on rational formation pressure maintenance level in low permeability reservoir," *Special Oil and Gas Reservoir*, vol. 18, no. 1, pp. 90–92, 2011.

[3] Z. Liufang, Z. Guojing, L. Aimin, and Y. Jun, "Study on rational pressure level of 63+4 formation in upper Guantao formation of the west seventh region in Gudong oilfield," *Petroleum Geology and Recovery Efficiency*, vol. 11, no. 2, pp. 45–47, 2004.

[4] T. Li, L. Hui, and J. Xueyuan, "The maintenance level of reasonable formation pressure in Daqing oilfield," *Oil-Gas Field Surface Engineering*, vol. 25, no. 1, pp. 11-12, 2006.

[5] Z. Hongyou, "Determination of reasonable formation pressure in water driven reservoirs using injection-production balance method," *Petroleum Geology and Engineering*, vol. 31, no. 6, pp. 121–124, 2017.

[6] Z. Jie, Z. Yamin, and Z. Shengju, "Reasonable formation pressure maintenance level meeting the water flooding law of oil reservoirs," *Journal of Xi'an Shiyou University (Natural Science Edition)*, vol. 30, no. 1, pp. 38–41, 2015.

[7] L. Yanping, "Research on reasonable pressure of water injection for oil production," *Xinjiang Shiyou Xueyuan Xuebao*, vol. 15, no. 3, pp. 52–56, 2003.

[8] X. Rongkui, T. Shuquan, and L. Baoquan, "Research and application of oilfield injection-production pressure system," *Journal of Oil and Gas Technology (J.JPI)*, vol. 27, no. 3, pp. 383–385, 2005.

[9] D. Liu and J. Sun, "Methods of determining reasonable formation pressure by using production performance data," *Journal of Oil and Gas Technology (J.JPI)*, vol. 31, no. 3, pp. 119–121, 2009.

[10] G. A. O. Jian, L. U. Jing, and W. A. N. G. Jialu, "Evaluation on stress sensibility of low permeability rock under reservoir condition," *Chinese Journal of Rock Mechanics and Engineering*, pp. 3899–3902, 2009.

[11] Y. Xiaoyan and M. Chao, "Experimental study on pressure sensitivity of low permeability reservoir," *Complex Hydrocarbon Reservoirs*, vol. 3, no. 4, pp. 66–68, 2010.

[12] R. Liu, H. Liu, H. Zhang, T. Ye, and L. Ming, "Study of stress sensitivity and its influence on oil development in low permeability reservoir," *Chinese Journal of Rock Mechanics and Engineering*, vol. 30, no. 1, pp. 2697–2702, 2011.

[13] R. L. Luo, L. S. Cheng, J. C. Peng, and H. Y. Zhu, "A new method of determining relationship between permeability and effective overburden pressure for low-permeability reservoirs," *Journal of China University of Petroleum*, vol. 31, no. 2, pp. 87–90, 2007.

[14] C. Zhaohui, X. Yiting, and D. Yong, "Experimental study on sanding stress sensitivity in unconsolidated sandstone reservoirs," *Petroleum Drilling Techniques*, vol. 41, no. 1, pp. 61–64, 2013.

[15] W. Yongkai and L. Lianmin, "Study on stress sensitivity of reservoirs with abnormal high pressure and medium-high permeability," *Logging engineering*, vol. 30, no. 1, pp. 131–134, 2019.

[16] Z. H. E. N. G. Rongchen, W. A. N. G. Xibin, and L. I. U. Chuanxi, "The stress sensitivity test for dense reservoir rocks in low permeability gas pool," *Xinjiang Petroleum Geology*, vol. 27, no. 3, pp. 345–347, 2006.

[17] N. Cao and G. Lei, "Stress sensitivity of tight reservoirs during pressure loading and unloading process," *Petroleum Exploration and Development*, vol. 46, no. 1, pp. 132–138, 2019.

[18] L. Chuanliang, "Evaluation method for stress sensitivity of reservoir rock," *Petroleum geology and oilfield development in Daqing*, vol. 25, no. 1, pp. 40–42, 2006.

[19] Z. Jianguo, D. Dianfa, H. Jian, L. Guanglun, and L. Aiming, *Seepage Flow in Porous Media*, China university of petroleum press, Dongying, 2006.

[20] S. Yang and W. Junzhi, *Reservoir Physics*, Petroleum Indusity Press, Beijing, 2004.

Hindawi
Geofluids
Volume 2022, Article ID 5912732, 16 pages
https://doi.org/10.1155/2022/5912732

Research Article

Well Placement Optimization for Fractured Reservoirs: Coupling StoSAG and EDFM

Jianchun Xu, Wanhang Guo, and Wenxin Zhou

School of Petroleum Engineering, China University of Petroleum (East China), Qingdao 266580, China

Correspondence should be addressed to Jianchun Xu; xujianchun@upc.edu.cn

Received 24 March 2022; Accepted 3 May 2022; Published 25 May 2022

Academic Editor: Kai Zhang

Copyright © 2022 Jianchun Xu et al. This is an open access article distributed under the Creative Commons Attribution License, which permits unrestricted use, distribution, and reproduction in any medium, provided the original work is properly cited.

Well placement optimization is a significant task in oil field development which aims to find the optimal well locations by maximizing the net present value (NPV) or other objective function. It is a highly nonlinear problem involving large number of variables. Despite lots of work has been done on conventional reservoirs, the optimization tool for naturally fractured reservoir (NFR) is still rare. Naturally fractured reservoirs represent significant amounts of oil reserves. The well placement optimization for NFR is challenging due to the high heterogeneity of matrix and fracture system. In this work, a computer-aided well placement optimization method is established for NFR based on the recent advances. The two phases flow discrete fracture numerical simulation model, i.e., the embedded discrete fracture method (EDFM) is used to model the natural fractures as its computational efficiency and flexibility to handle fracture. Then, stochastic simplex approximate gradient (StoSAG) is employed to obtain the approximate gradient by combing the EDFM. The steepest ascent algorithm is used to find the optimal well placement. A series of numerical case studies are set up to examine the performance of the proposed approach. The NPV for water flooding naturally fractured reservoir production optimization substantially increased by using StoSAG.

1. Introduction

Determining the location of wells is crucial during field development process because it can affect the final NPV significantly [1]. Lots of automated well placement optimization methods has been investigated in previous studies [2–5]. However, little has suggested an effective way to assess the well location optimization for naturally fractured reservoir. In recent years, naturally fractured reservoirs receive great attention as its significant amounts of oil reserves [6]. In order to improve the efficiency of reservoir development and enhance oil recovery, well location for NFR should be carefully arranged and optimized.

Well placement optimization is a highly nonlinear problem involving the reservoir response. Reservoir simulation simulators are the common tools to achieve the rates of oil and water. In the optimization process, the reservoir simulation model may require thousands of runs. Thus, the simulator should be computational efficiency. For NFR, simulators are developed based on two classical types of fracture models: dual-continuum method and explicit discrete-fracture and matrix model. Dual-continuum method is widely used in most commercial reservoir simulators such as Eclipse and CMG. Dual-continuum method divides the reservoir domain into fracture and matrix [7–9]. Commonly, it can keep applicability when the fractures are denser and the representative elementary volume (REV) exists [10]. It also loses accuracy in flow calculation when a number of large fractures locates in the reservoir [11]. The fracture and matrix system are coupled by transfer functions. Fracture-matrix flow is controlled mainly by matrix propertied, and the shape factor needs to be determined. Unfortunately, the shape factor is difficult to calculate when considering capillarity, gravity [12]. Explicit discrete-fracture and matrix model or discrete fracture-matrix (DFM) has grown in popularity during recent years. The model deals with every fracture explicitly. Thus, it can capture the fracture geometries and accurately characterize the flow exchange between fracture and matrix. Many DFMs have been developed [13–18]. The unstructured grid is always chosen to discrete the calculation domain. The grid size near

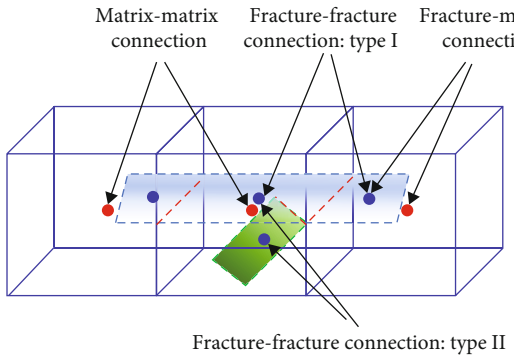

Figure 1: Basic connections for EDFM.

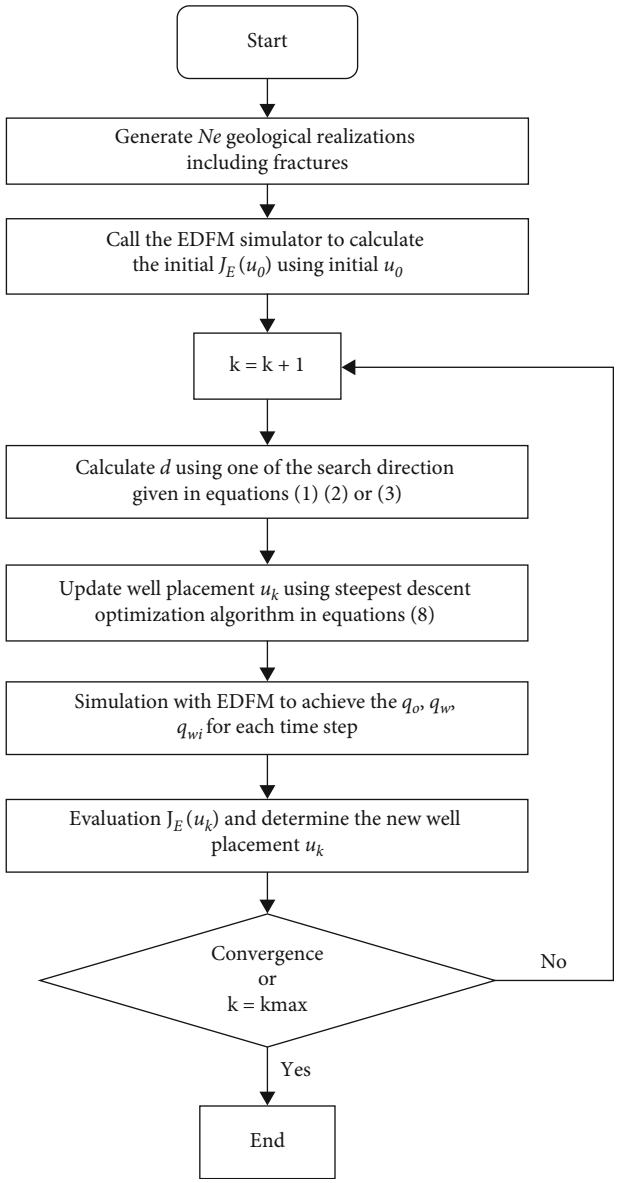

Figure 2: Flow chart of well placement optimization for fractured reservoirs.

the fractures should keep small to exactly simulate the flow between matrix and fracture. However, the local grid refinement leads to large computational load. A recently popular DFM—embedded discrete fracture model (EDFM)—attracts much attention and shows some advantages. The EDFM is firstly proposed as a hierarchical modeling method to deal with multiple length scales in naturally fractured formations [19–21]. Then, it is extended to the flow performance analysis of both naturally fracture reservoirs and hydraulic fractured tight oil reservoirs [22–24]. Some applications of EDFM have been reported. Yao et al. coupled the EDFM and dual-continuum method to inverse multiscale fractures hierarchically using dynamic production data [25, 26]. Yao et al. [27] optimized the fracturing parameters in shale gas reservoir. Yu et al. [28] simulated the pressure response of well interference in tight oil reservoirs with complex–fracture geometries. Alessio et al. [29] employed the EDFM for computing fracture-fracture and matrix-fracture transmissibilities as an upscaling tool. In this study, the EDFM will be used as the simulating tool.

Another important issue for well placement optimization is the chosen of optimization algorithm. Two kinds of optimization algorithms are implemented to find the optimal well placement: (1) gradient-based methods and (2) gradient-free methods. Gradient-based methods mainly include SPSA, finite difference, adjoint method, and descent method. These gradient-based techniques are easy to trap in local optima, and the gradient is difficult to calculate. On the other hand, derivative-free techniques do not require the calculation of derivatives, and they can achieve global search. Many gradient-free methods are used like particle swarm optimization (PSO), genetic algorithm (GA), differential evolution (DE), and covariance matrix adaptation evolution strategy (CMA-ES). Ensemble-based optimization increases popularity recently due to its ability to capture uncertainty of multiple reservoir realizations [30]. Ensemble-based optimization (EnOpt) was first introduced by Lorentzen et al. [31] and Nwaozo [32]. Then, this method is greatly improved and used in reservoir development field [33–35]. In 2017, Fonseca et al. [36] found that not all cases can get the optimal value in the process of robust optimization using this method. Based on this observation, a stochastic simplex approximate gradient (StoSAG) method was proposed. StoSAG improves the EnOpt gradient formula in two aspects, using the initial variable and initial function value to replace the average value of random perturbation position and corresponding function value, respectively. After that, the method is widely used in the field of well location optimization and injection production optimization [37, 38]. In 2019, the researchers of Alamos National Laboratory of the United States proved the advantages of StoSAG in robust optimization theoretically, and the optimal value obtained by StoSAG was significantly higher than that obtained by EnOpt, which provided a strict theoretical basis for the popularization and application of StoSAG. Four kinds of stochastic gradient calculation criteria, which are StoSAG, f-StoSAG, sf-StoSAG, and ss-StoSAG, are proposed. The results show that the optimal injection production control variables can be obtained by using four kinds of gradients. The NPV calculated is greatly improved than EnOpt method [39].

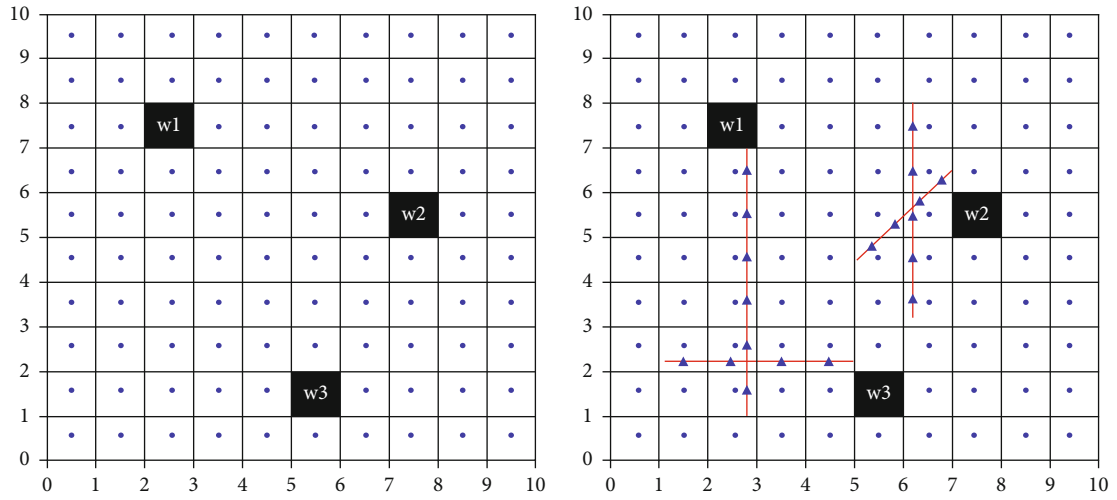

(a) Reservoir without fracture (b) Reservoir with fractures

Figure 3: Illustration of well placement optimization for a reservoir with or without fracture.

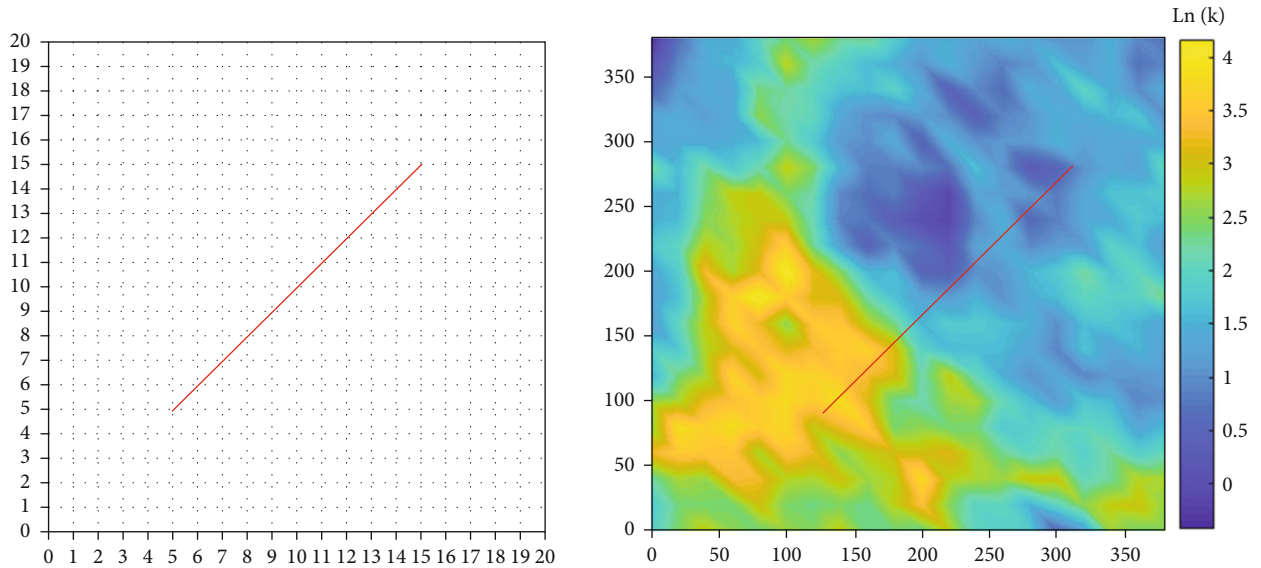

Figure 4: Log-permeability distribution for example 1.

Table 1: Result of optimal well locations.

	Case 1	Case 2	Case 3	Case 4	Case 5	Case 6
Perturbation size	0.1	1	1.414	1	1	1
Initial step size	1	1	1	1	2	3
Optimal injection well location	(19,10)	(19,10)	(20,3)	(19,10)	(18,4)	(16,3)
Optimal production well location	(3,11)	(6,15)	(5,10)	(6,15)	(6,11)	(7,20)

Here, we developed the well placement optimization tool for naturally fractured reservoirs by coupling the EDFM and StoSAG. As far as we know, this is the first well placement optimization tool by introducing the EDFM method. It has broad application prospects. In the tool, the classical EDFM of two-phase flow problem is adopted to simulate the naturally fractures. The detailed geological characteristics of each fracture is kept. The pressure and saturation are solved by Newton-Raphson iteration by carefully setting the time steps to guarantee the convergence. The standard StoSAG is chosen as the optimization algorithm to search for the optimization well placements. The well can connect with the fracture and matrix domain freely. A series of example are test from simple to complex to show the validation of the workflow. Specially, the

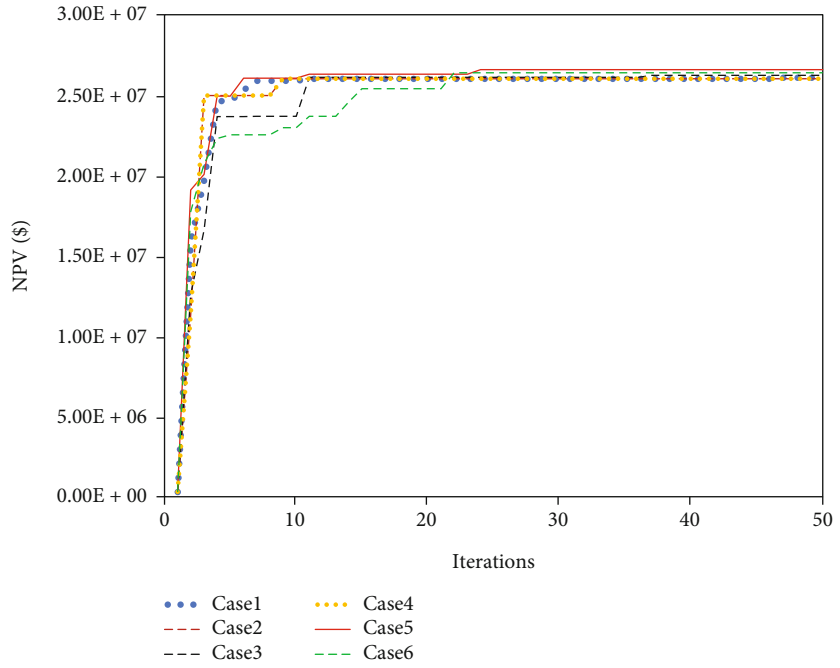

Figure 5: The NPV with respect to number of iteration based on six cases.

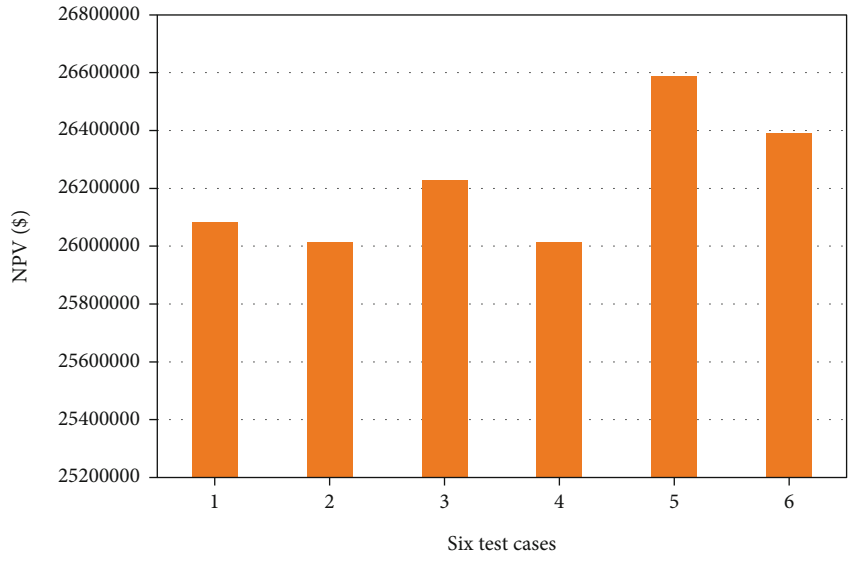

Figure 6: The maximum NPV after 50 iterations for different cases.

robust optimization results are presented. This is the first tool to optimize the well placement by coupling the StoSAG and EDFM. The paper is organized as follows. In Section 2, the theoretical model for well placement optimization is presented. Then, we show the optimization model and results. Finally, discussion is given.

2. Methodology

2.1. Numerical Simulation Model. In order to perform the well placement optimization for naturally fractured reservoir, the numerical simulation model should be carefully prepared. In this work, the embedded discrete fracture method (EDFM) is adopted as the numerical simulation tool for well placement optimization. Figure 1 shows four kinds of connections when using EDFM. The three kinds of NNCs are the fracture-matrix connection in the same matrix grid, the fracture-fracture connection in the same matrix grid, and fracture-fracture connection in different matrix grids. By defining three kinds of NNC in preprocessing program, the in-house numerical simulation code can be called to perform the calculation. Previous research

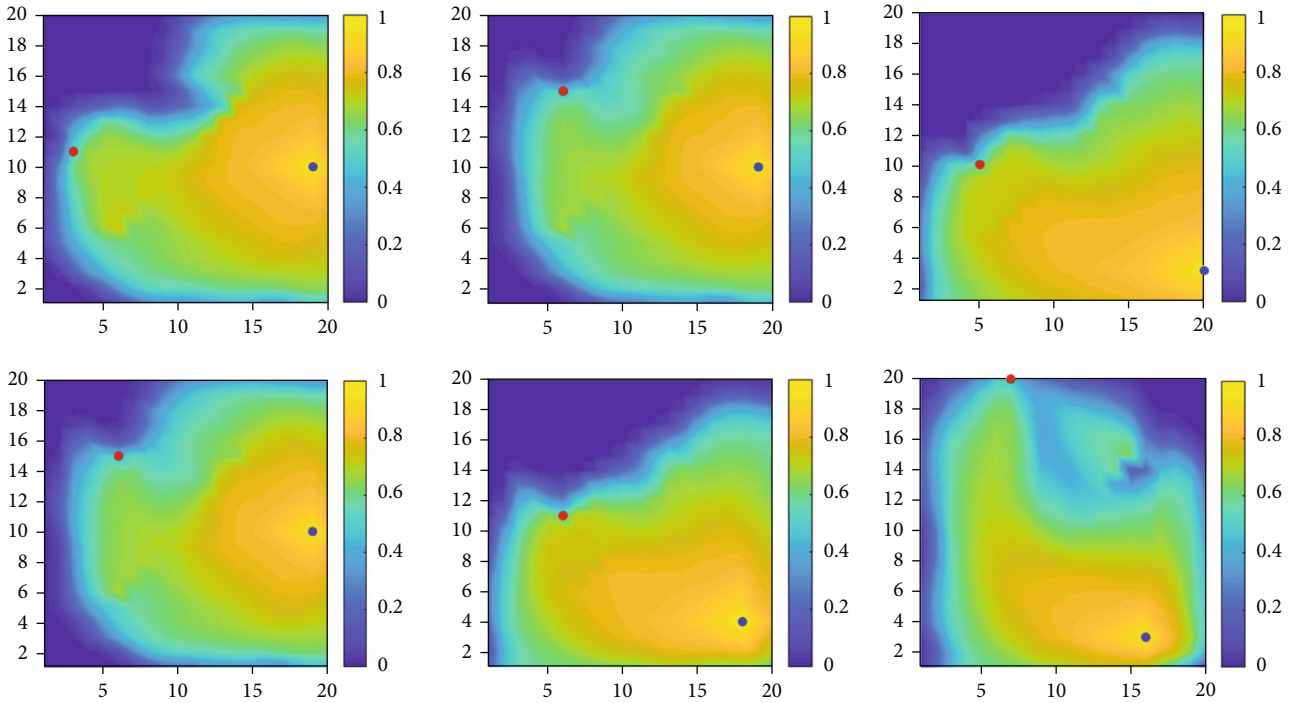

Figure 7: The optimal well locations plotted on the water saturation field.

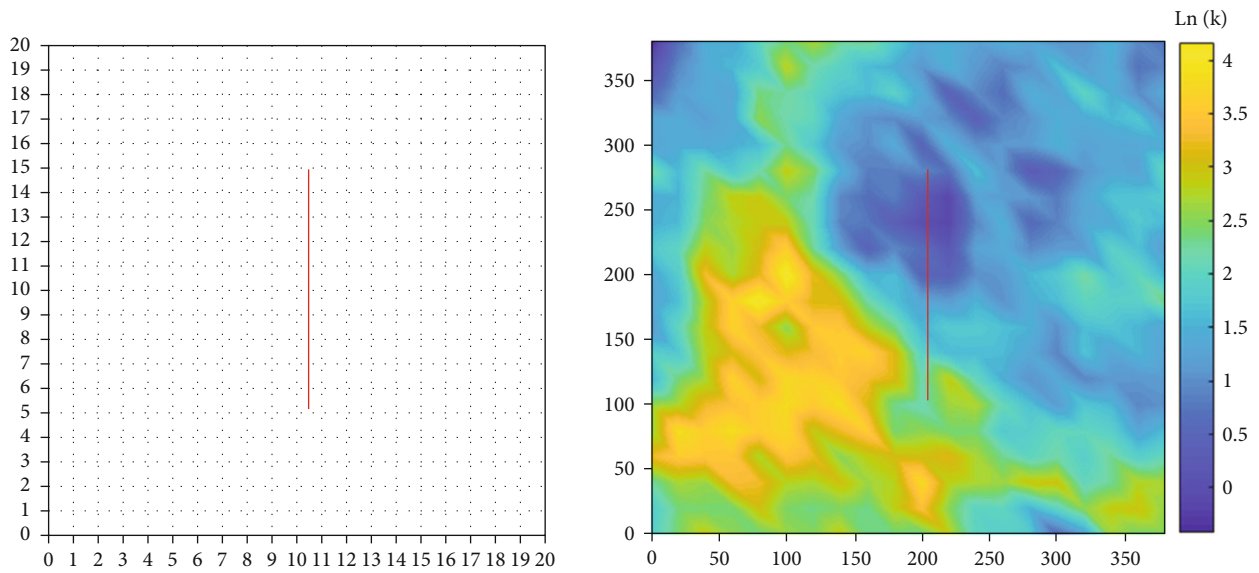

Figure 8: Log-permeability distribution example 2.

Table 2: Result of optimal well locations.

	Case 1	Case 2	Case 3	Case 4	Case 5	Case 6
Perturbation size	0.1	1	1.414	1	1	1
Initial step size	1	1	1	1	2	3
Optimal injection well location	(17,11)	(19,11)	(17,11)	(19,11)	(17,11)	(16,3)
Optimal production well location	(6,11)	(4,10)	(4,10)	(4,10)	(4,10)	(7,20)

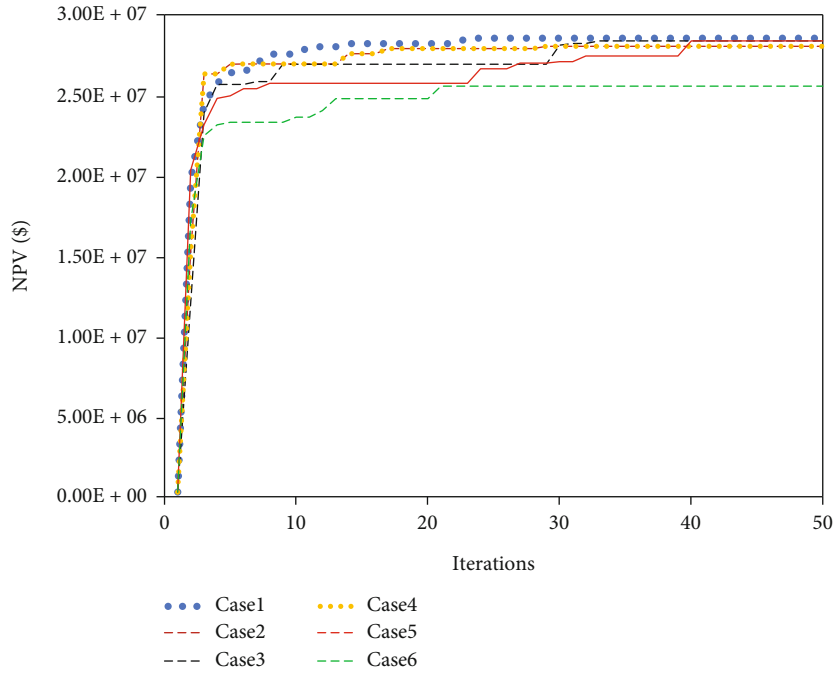

Figure 9: The NPV with respect to number of iteration based on six cases.

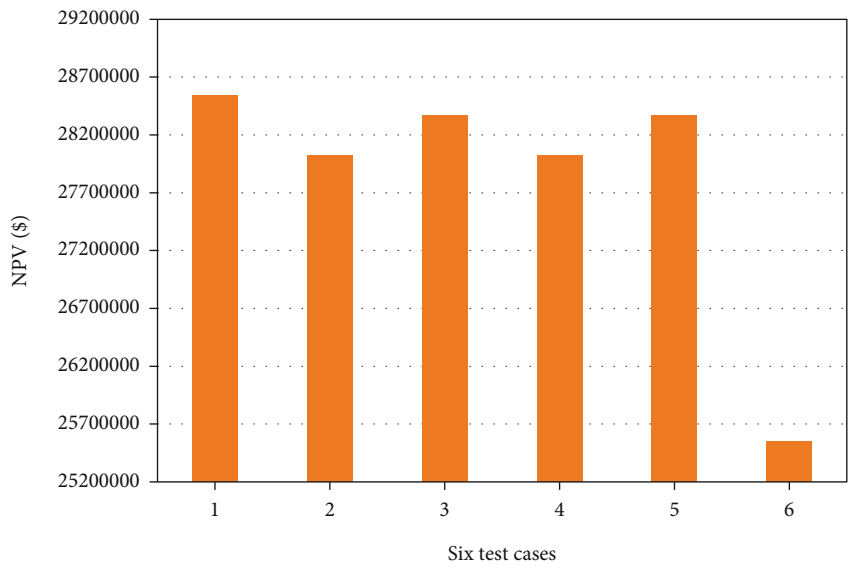

Figure 10: The maximum NPV after 50 iterations for different cases.

results show that pressure distribution, saturation distribution, and the well flow response agree with each other for EDFM, DFM, and LGR. Easy implementation, general applicability, and high computational efficiency are also demonstrated compared to DFM and LGR.

2.2. Optimization Algorithm. Ensemble-based methods show advantages in gradient-based optimization. The motivation is that the real gradient is not always available. The general formulation for StoSAG search direction is given by the following equation [39, 40]:

$$d_l = \nabla_u J_E(u) = \frac{1}{N_e} \sum_{i=1}^{N_e} \nabla_u J(u, m_i), \tag{1}$$

where N_e is the geological model realization number to describe the reservoir uncertainty. $u$contains the placement

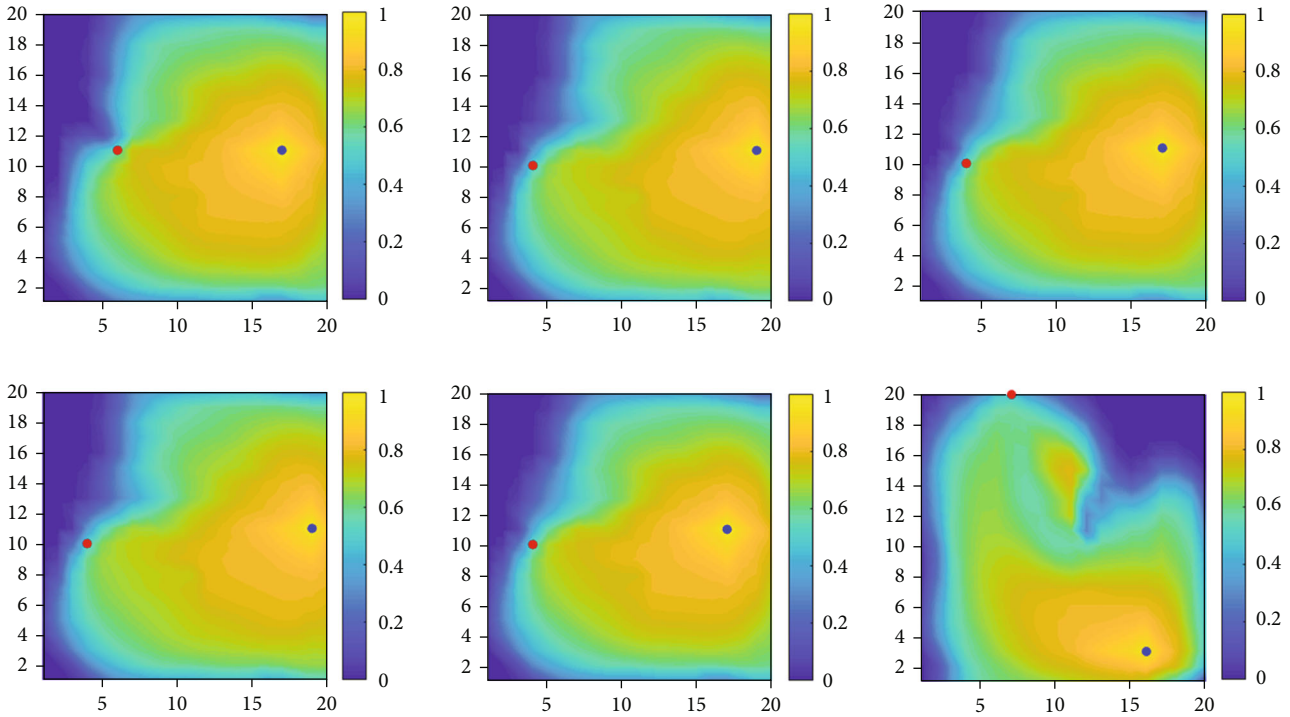

Figure 11: The optimal well locations plotted on the water saturation field.

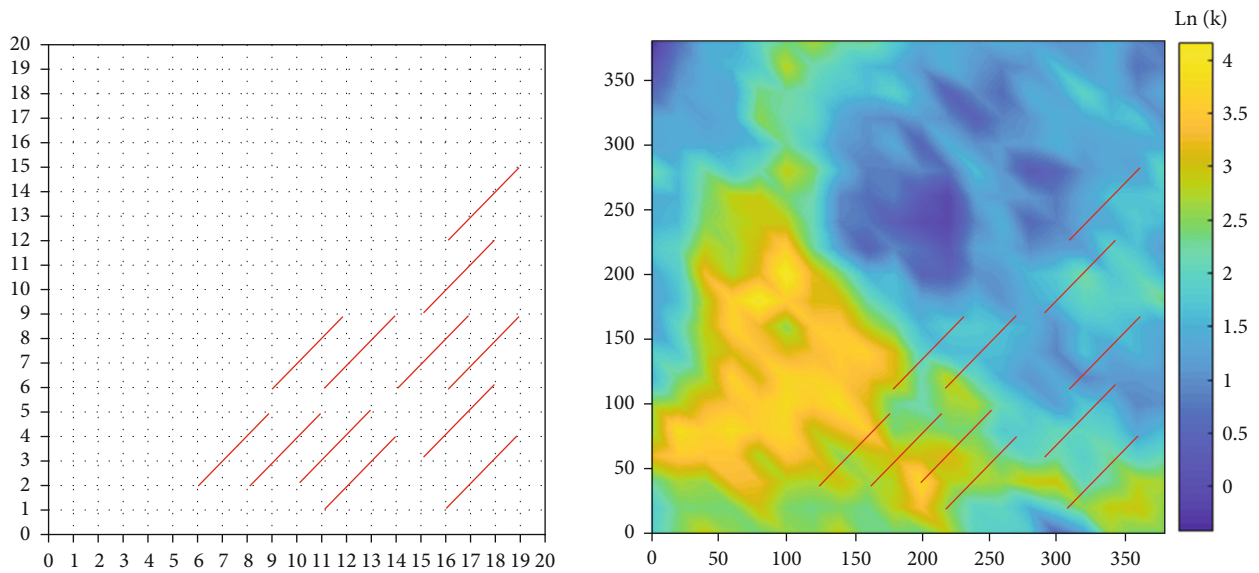

Figure 12: Log-permeability distribution example 3.

information for all wells. $\nabla_u J(u, m_i)$ is the stochastic approximation of the simplex gradient. $\nabla_u J(u, m_i)$ is obtained by

$$\nabla_u J(u, m_i) = \frac{1}{N_s}\sum_{j=1}^{N_s}\left(\delta\hat{u}_{l,j}\left(\delta\hat{u}_{l,j}\right)^T\right)^+\delta\hat{u}_{l,j}\left(J\left(\hat{u}_{l,j}, m_i\right) - J(u_l, m_i)\right). \tag{2}$$

Then, the gradient becomes

$$d_l = \nabla_u J_E(u) = \frac{1}{N_e}\sum_{i=1}^{N_e}\left(\frac{1}{N_s}\sum_{j=1}^{N_s}\left(\delta\hat{u}_{l,j}\left(\delta\hat{u}_{l,j}\right)^T\right)^+\delta\hat{u}_{l,j}\left(J\left(\hat{u}_{l,j}, m_i\right) - J(u_l, m_i)\right)\right). \tag{3}$$

The superscript sign "+" on a matrix denotes the Moore-

Table 3: Result of optimal well locations.

	Case 1	Case 2	Case 3	Case 4	Case 5	Case 6
Perturbation size	0.1	1	1.414	1	1	1
Initial step size	1	1	1	1	2	3
Optimal injection well location	(17,10) (3,19) (17,11)	(11,15) (6,19) (18,4)	(5,18) (10,16) (18,2)	(11,15) (6,19) (18,4)	(3,20) (9,20) (19,3)	(9,20) (5,20) (18,2)
Optimal production well location	(2,4) (10,18) (5,10)	(2,5) (18,19) (3,11)	(8,6) (20,18) (1,3)	(2,5) (18,19) (3,11)	(1,4) (19,17) (4,5)	(2,4) (19,17) (5,6)

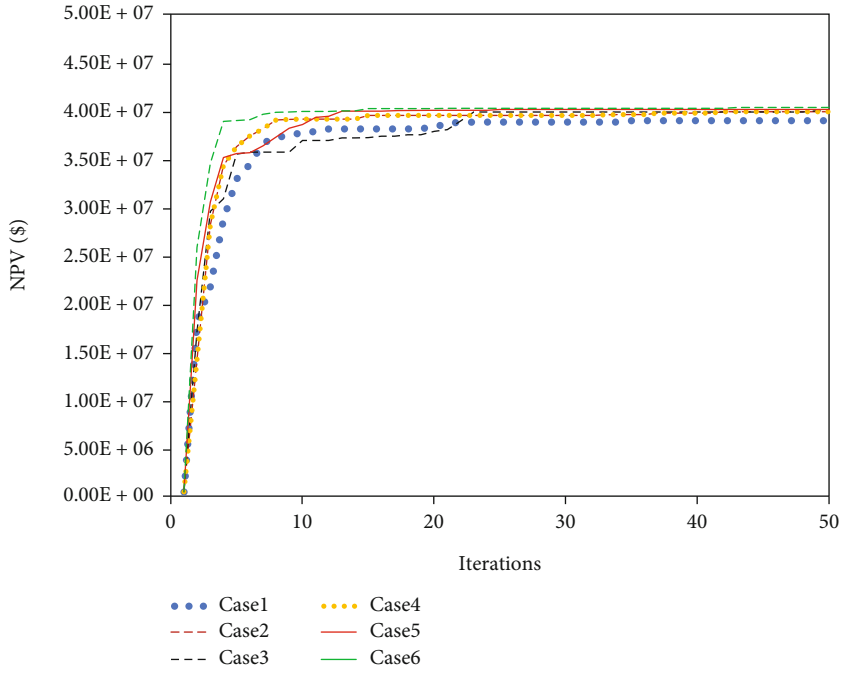

Figure 13: The NPV with respect to number of iteration based on six cases.

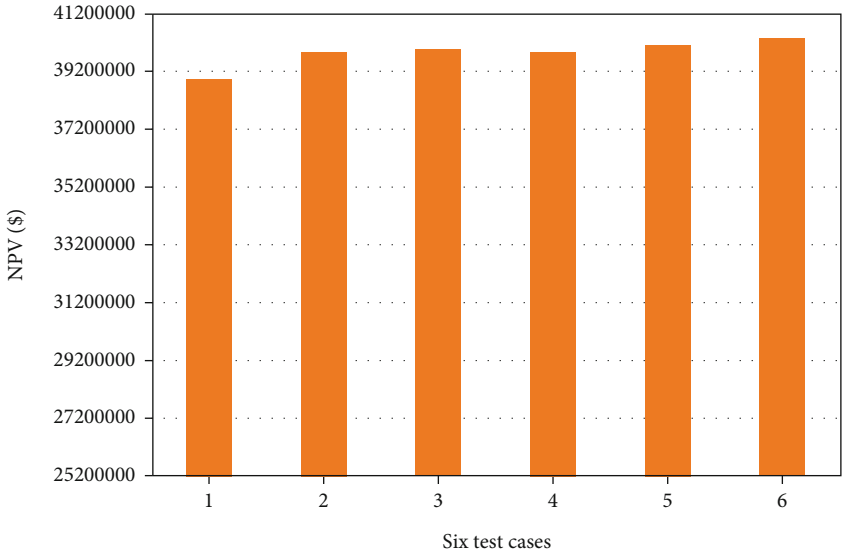

Figure 14: The maximum NPV after 50 iterations for different cases.

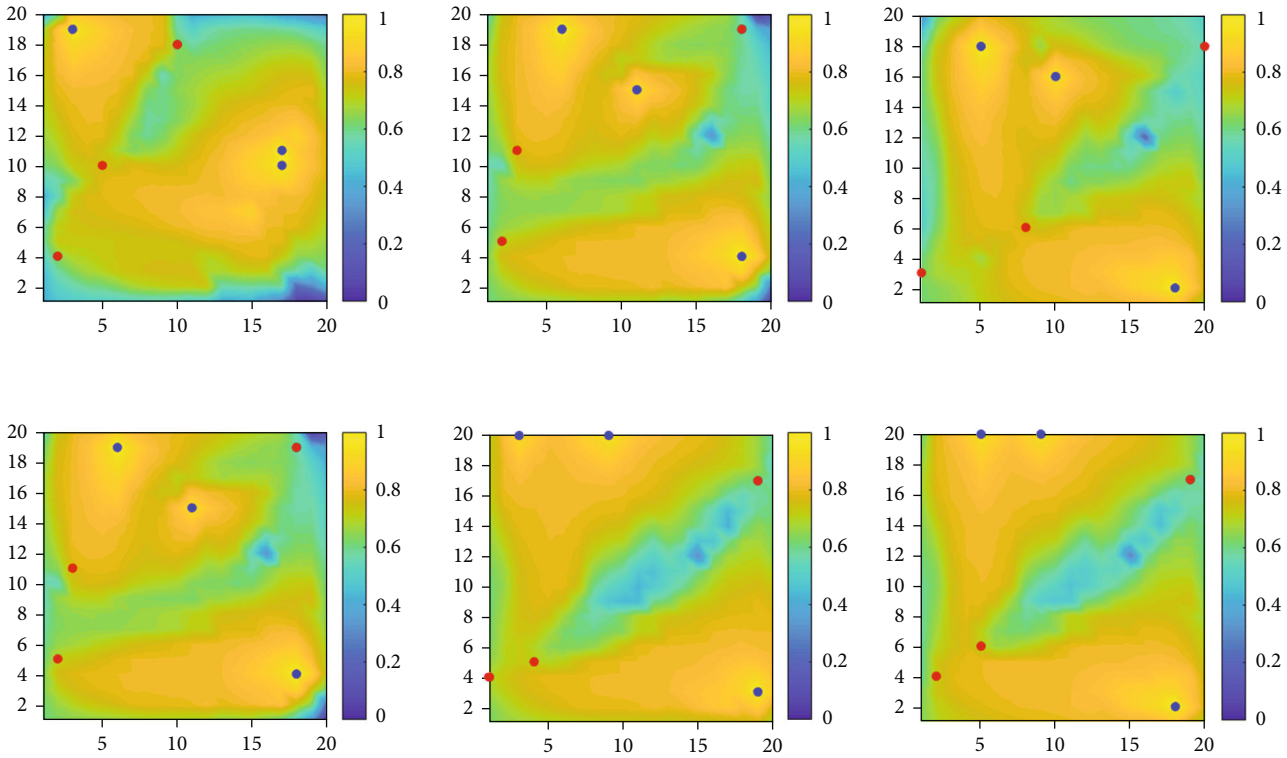

Figure 15: The optimal well locations plotted on the water saturation field.

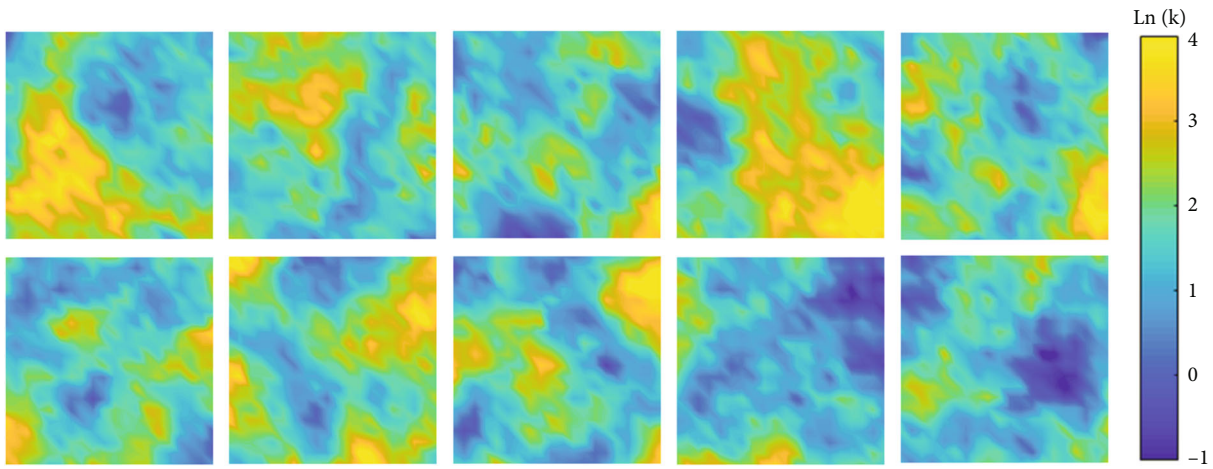

Figure 16: The log-permeability distribution in the horizontal direction for ten realizations.

Table 4: Result of optimal well locations.

	Case 1	Case 2	Case 3	Case 4	Case 5	Case 6
Perturbation size	0.1	1	1.414	1	1	1
Initial step size	1	1	1	1	2	3
Optimal injection well location	(8,12) (19,3) (19,9)	(8,12) (3,13) (19,3)	(2,19) (7,16) (19,2)	(8,12) (3,13) (19,3)	(6,20) (9,13) (20,3)	(17,16) (2,13) (14,13)
Optimal production well location	(5,20) (4,2) (15,19)	(3,1) (18,18) (4,19)	(3,1) (17,20) (8,7)	(3,1) (18,18) (4,19)	(3,2) (20,17) (1,13)	(8,4) (16,1) (8,20)

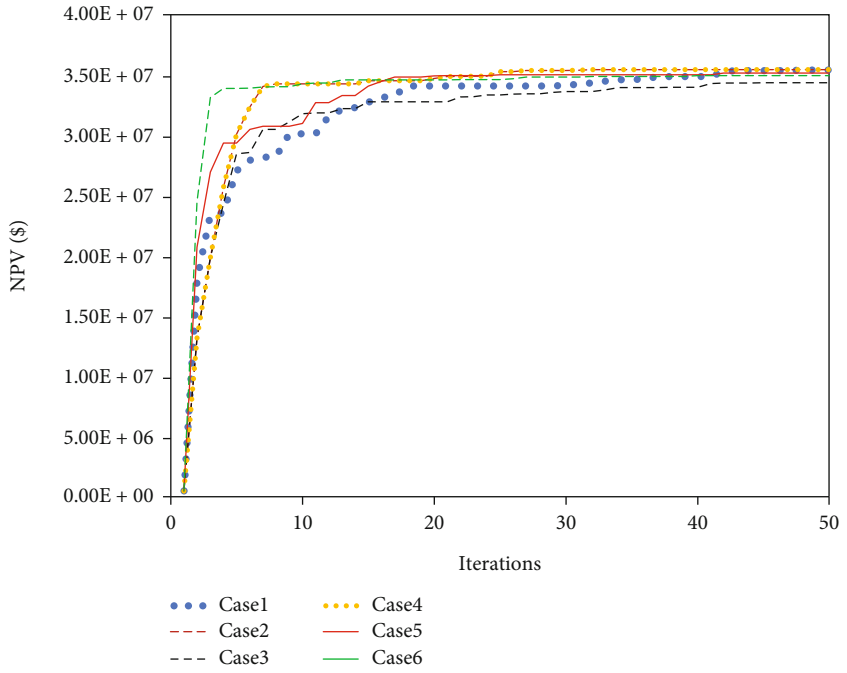

Figure 17: The NPV with respect to number of iteration based on six cases.

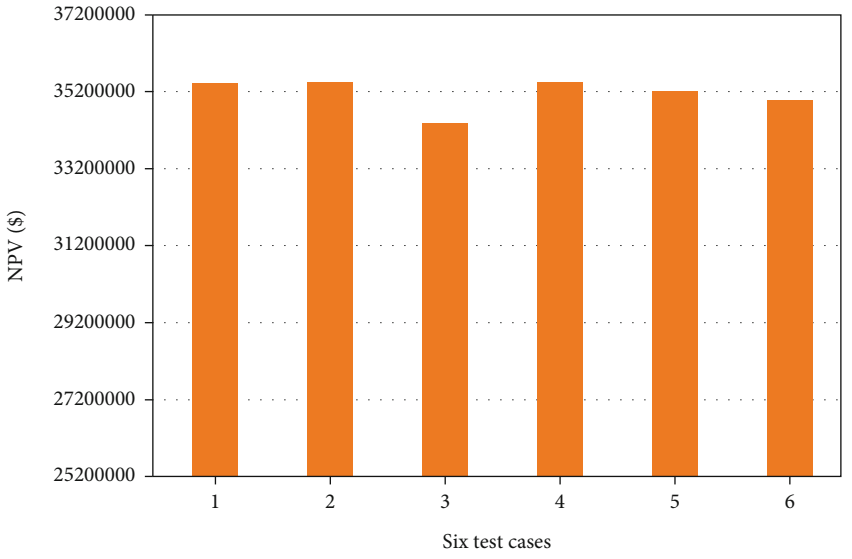

Figure 18: The maximum NPV after 50 iterations for different cases.

Penrose pseudo-inverse, where

$$\delta\hat{u}_{l,j} = \hat{u}_{l,j} - u_l. \tag{4}$$

N_s represents the number of control perturbations. Each control perturbation $\hat{u}_{l,j}, j = 1, 2, \cdots N_s$ at iteration l is generated from the distribution $N(u_l, C_U)$; C_U is a predefined covariance matrix.

2.3. Well Placement Optimization Tool. The objective function commonly used in well placement optimization problem is the NPV, which is defined as

$$J(u, m_i) = \sum_{n=1}^{N_t} \left\{ \frac{\Delta t_n}{(1+b)^{t_n/365}} \left[\sum_{j=1}^{N_p} \left(r_o \cdot \overline{q_{o,j}^n} - c_w \overline{q_{w,j}^n} \right) - \sum_{k=1}^{N_I} \left(c_{wi} \cdot \overline{q_{wi,k}^n} \right) \right] \right\}, \tag{5}$$

where u is a N_u-dimensional column vector which contains all well placement information; $n$denotes the n_{th} time step for the reservoir simulation; N_t is the total number of time steps; the time at the end of the n_{th} time step is denoted by t_n; t_n is the n_{th} time step size; b is the annual discount rate;

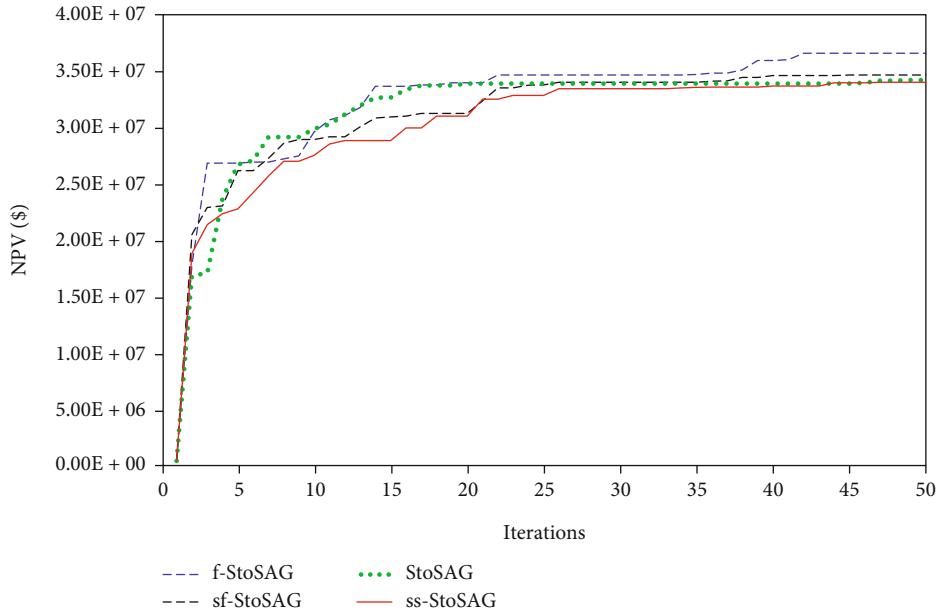

Figure 19: The NPV with respect to number of iterations based on different gradient.

N_P and N_I denote the number of producers and injectors, respectively; r_o is the oil revenue, in \$/STB; c_w and c_{wi} denote the disposal cost of produced water and the cost of water injection in units of \$/STB, respectively; $q_{o,j}$ and $q_{w,j}$, respectively, denote the average oil production rate and the average water production rate for the n_{th} time step, in units of STB/day; and $q_{wi,k}$ denote the average water injection rate at the k_{th} injector for the n_{th} time step, in units of STB/day.

To account for geological uncertainty, robust optimization is performed. The problem is to maximize the expectation for life cycle NPV which is approximated by the average NPV over N_e geological realizations:

$$J_{E(u)} = \frac{1}{N_e}\sum_{i=1}^{N_e} J(u, m_i). \tag{6}$$

We consider only bound constraints and let u^{low} and u^{up} denote the lower bound and upper bound for the well placement variable, respectively. Then, the problem can be expressed as

$$\max_u J_E(u) = \max_u \frac{1}{N_e}\sum_{i=1}^{N_e} J(u, m_i), \quad s.t. u^{low} \le u \le u^{up}. \tag{7}$$

The logarithm transformation to each element of the control vector is used to search the solution of the well placement optimization problem. The steepest descent optimization algorithm is used in which the new search position is updated as

$$x_{k+1} = x_k + \alpha_k \left[\frac{d_k}{\|d_k\|_\infty}\right], \tag{8}$$

for $k = 0, 1, 2 \cdots$ until convergence, where x_0 is the initial guess and x_k is the estimate of the optimal control parameter at the k_{th} iteration; α_k is the step size.

2.4. Workflow. The workflow of well placement optimization using StoSAG and EDFM is shown in Figure 2. Firstly, N_e geological realizations should be generated. In robust optimization, N_e is commonly set to be bigger than 1. The initial well placement u_0 is used to calculate the initial objective function value $J_E(u_0)$. In order to compute the objective function, the EDFM simulator is called. Then, the iteration step is performed. For a certain iteration k, the stochastic simplex approximate gradient is calculated using the search direction. In our work, the ensemble size is set to be 10 for all cases. Figure 3 shows the reservoir model with three wells. The number of grids is 100 for the reservoir without fracture, while the number of grids is 119 for the reservoir with fracture. Note that if there is no fracture in the reservoir, the well placement is located at the center of the matrix grid. However, when fractures exist, the well placements can locate at the centers for both matrix and fracture grids.

3. Case Study

In this section, some synthetic cases are presented to test the new workflow. The examples are set from simply to complex. The 2D models are firstly discussed. Then, the 3D model is presented. A number of wells and fractures also increase for different examples which can test the performance of the new workflow.

3.1. Example 1: 2D Model with Inclined Single Fracture. A water flooding example is considered which is a 2D heterogeneous model. The model size is 400 m ×400 m ×10 m with 20 ×20 × 1 uniform grid. The size for each grid is 20 m ×20 m ×10 m. The horizontal log-permeability

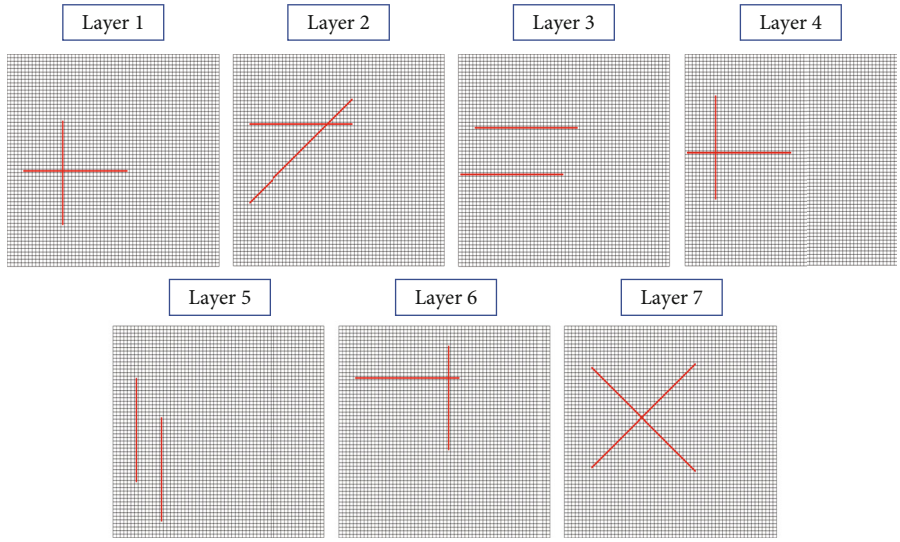

Figure 20: Fracture distribution of different layers for egg model.

distribution is presented in Figure 4. the fracture width is set to be 0.001 m. The matrix porosity is homogenous and equal to 0.1. The initial pressure is set to be 30 MPa. The reservoir lifetime is 2000 days. One production wells and one injection wells are placed in the reservoir. The production well is operated at fixed bottom hole pressure of 10 MPa, and the injection wells are operated with BHP of 40 MPa. To optimize the NPV, the oil price is set equal to USD 60/stb; the water injection cost is USD 5/stb; the cost of disposing produced water is USD 5/stb; the annual discount rate is 0.1. The maximum number of step size cuts is set to be 5. The total maximum allowable iteration is 50.

The performance of the optimization algorithm is always dependent on the setting parameters. In the optimization process, different value of perturbation size and initial step size are taken to examine their effect on the objective function value and optimal placement. Six test cases are conducted, and the optimization results are also presented in Table 1(case 1 and case 4 have the same setting parameters). Figure 5 shows the NPVs after 50 iterations. It can be seen that all cases converge to a steady NPV value after a series of exploring. Compared the initial well placement and the final solution, the NPV increases substantially. At the initial iterations, the NPV increases rapidly, and then the NPV increases slowly. Lastly, the NPV trends to be a constant for different cases. Figure 6 shows the final converged NPV. The highest NPV is $\$2.66 \times 10^7$ for case 5, and the lowest NPV is $\$2.6 \times 10^7$ for case 2. Despite that the final converged NPV value is different, the difference is very small. The NPV evaluation curves follow similar paths which start from small to large value monotonously. Taking a closer look at the six curves calculated from different cases in Figure 5, we can observe that the red curve shows a relatively high converged performance than other for curves. In the initial iteration stage, case 5 has a rapid search efficiency and converges to the highest NPV finally. Though case 6 has a slow search efficiency during the first 25 iterations, it finds a relatively high local optimum. Observing the curves of case 1, case 2, and case 3, the initial stage search efficiency becomes higher if we set a smaller perturbation size. On the other hand, by comparing case 4, case 5, and case 6, we can see that the initial step size also has great effect for the search path. Overall, the results demonstrate that StoSAG generates optimal well placement, so the stochastic simplex approximate gradient can be used in well placement optimization problem. Figure 7 shows the optimal well placement overlapped on water saturation field in 2000 days. The injection well moves along the $+x$ and $-y$ direction, and the production well moves along $-x$ and $+y$ from the initial position. The line connecting two wells trends to be perpendicular to the fracture. The distance between two wells is very close for different cases.

3.2. Example 2: 2D Model with Vertical Single Fracture. A water flooding example is considered shown in Figure 8. The basic model parameter is the same as example 1 except the fracture. A fracture is located at the center of the reservoir. The length of the fracture is 200 m. The fracture width is set to be 0.001 m. Six test cases are conducted, and the optimization results are presented in Table 2. Figure 9 shows the NPVs after 50 iterations. It can be seen that the first five cases are converged to a steady NPV value after 50 iteration. Case 6 is trapped to a local optimum. In this example, case 1 demonstrated an extraordinary ability in research efficiency. For most of the iteration, its NPV is higher than others. Figure 10 is the maximum NPV after 50 iterations. The highest NPV is $\$2.85 \times 10^7$ for case 1, and the lowest NPV is $\$2.55 \times 10^7$ for case 6. Figure 11 shows the optimal well placement overlapped on water saturation field in 2000 days. The injection well moves along the x direction, and the production well moves along $-x$ from the initial position. The line connecting two wells trends to be perpendicular to the fracture for the first five cases. The distance between two wells is very close for the first five cases.

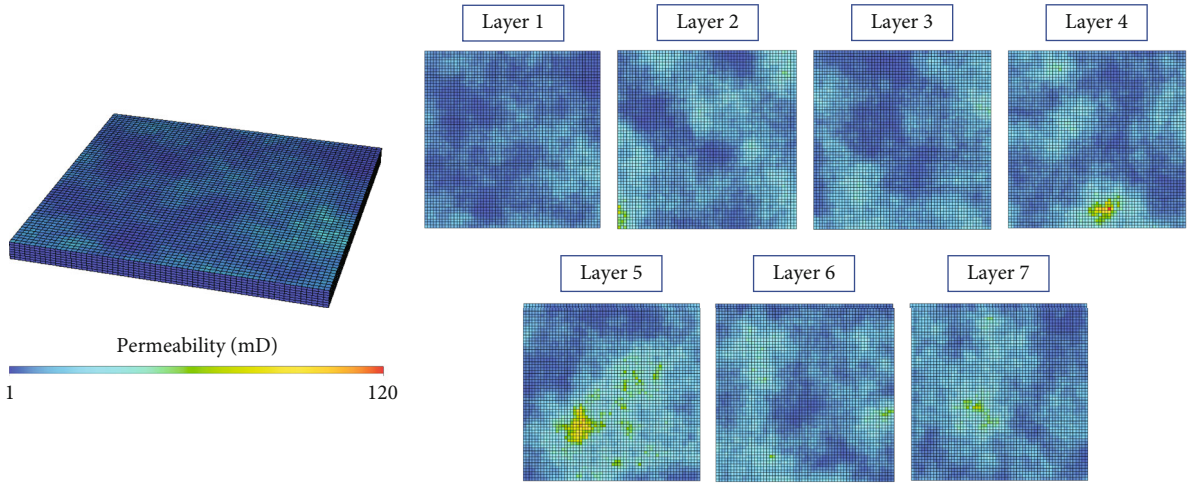

Figure 21: Permeability distribution of different layers for egg model.

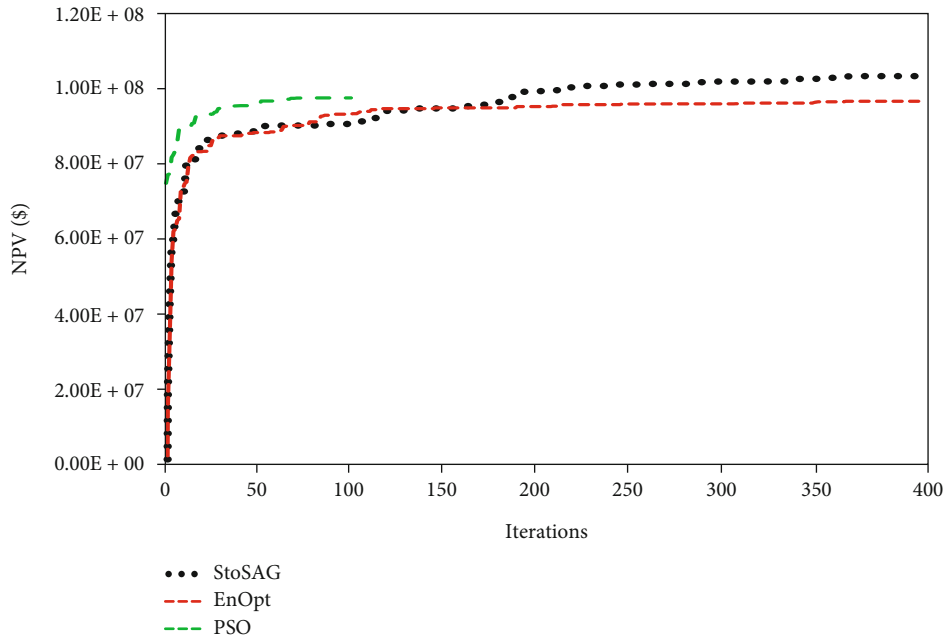

Figure 22: The NPV with respect to number of iterations based on different methods.

3.3. Example 3: 2D Model with Multiple Fractures. In example 3, we set 12 fractures in the reservoir. The position is shown in Figure 12. The orientation of the fractures keeps consistent. The other parameters are the same as example 1. Three injection wells and production wells are arranged in the reservoir. Note that in this model, the number of whole optimization variables is 12 considering the well location coordinates in (x, y)-plane. Six test cases are conducted, and the optimization results are presented in Table 3. Figure 13 shows the NPVs after 50 iterations. It can be seen that the first five cases are converged to a steady NPV value after 50 iteration. In this example, case 6 demonstrated an extraordinary ability in search efficiency. For most of the iteration, its NPV is higher than others. Figure 14 is the maximum NPV after 50 iterations. The highest NPV is \$ 4.03×10^7 for case 6 and the lowest NPV is $\$3.89 \times 10^7$ for case 1. Figure 15 shows the optimal well placement overlapped on water saturation field in 2000 days. The three production wells are located along the diagonal of the reservoir. Two production wells are located at the zone where the permeability is relatively high.

3.4. Example 4: Robust Optimization. In example 4, we consider the robust production optimization. Here, 10 reservoir realizations are randomly chosen, which is used to characterize the reservoir geological uncertainty. Figure 16 shows the log-permeability distribution in the horizontal direction of 10 reservoir models. Like example 3, we set 12 fractures in the reservoir. Three injection wells and production wells are arranged in the reservoir. Table 4 shows the optimal well location. Figure 17 shows the NPVs after 50 iterations. Figure 18 is the maximum NPV after 50 iterations. It can

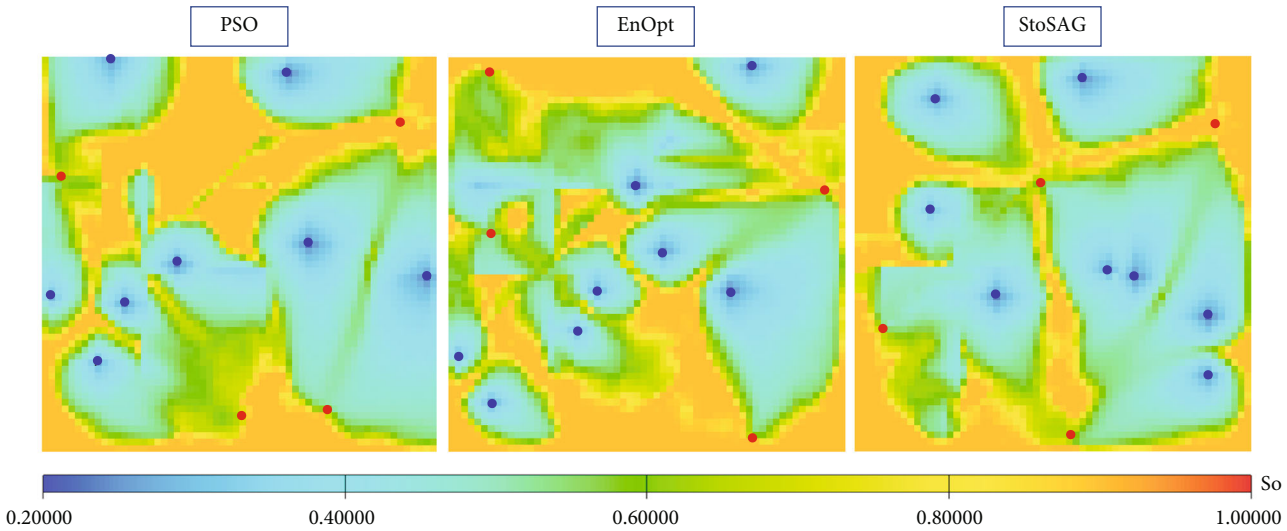

Figure 23: Oil saturation at the final simulation time for different optimization methods.

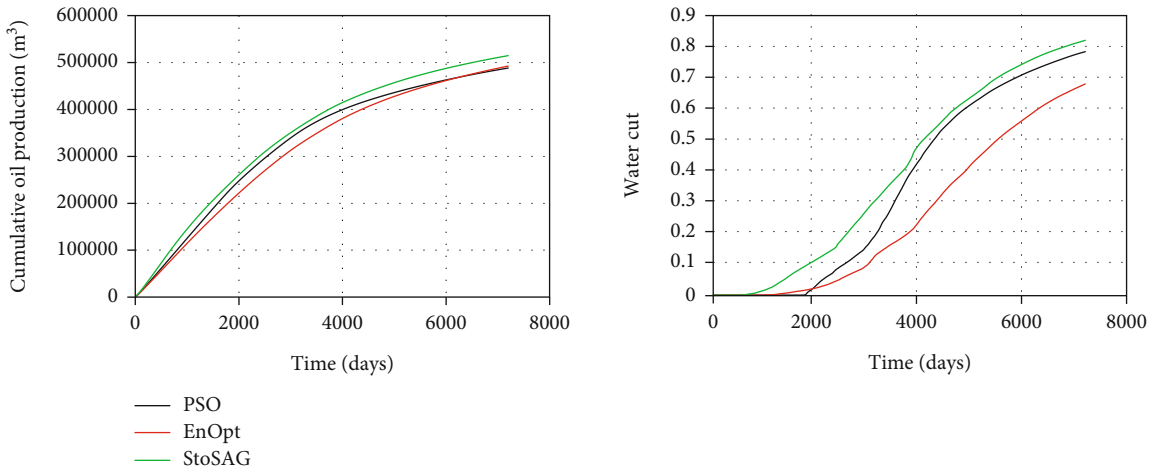

Figure 24: Cumulative oil production and water cut for different optimization methods.

be seen that the highest NPV is $\$3.54 \times 10^7$ for case 4 and the lowest NPV is $\$3.44 \times 10^7$ for case 3. Compared with the results of example 3, the uncertainty decreases the NPV greatly. On the other hand, four types of search methods (f-StoSAG, sf-StoSAG, StoSAG, and ss-StoSAG) for the steepest ascent optimization algorithm are used to optimize the well placement. Figure 19 presents the expected NPV of different methods. As expected, the average NPV generated from different search methods is higher than the initial average NPV. The f-StoSAG obtains a relatively high average NPV.

3.5. Example 5: Modified Egg Model. The egg model has been widely used for well placement and control optimization. The geological parameters, fluids parameters, and production control parameters can be found in Jansen et al. (2014) [41]. The number of gridblocks is 25200 for which (60,60,7) is used to discretize the reservoir in x, y, and z directions, respectively. In this study, all grids are set to be active and will be considered in the simulation runs. The grid block size is set to 8 m ×8 m × 4 m. There are eight injection wells and four production wells. Because the model has no aquifer and no gas cap, primary production is almost negligible. The production wells are operated at fixed bottom hole pressure (BHP) with 39.5 MPa, and the injection wells are operated under a BHP constraint of 42 MPa. Total production time is 7200 days. We seek to optimize the well locations of 8 injection wells and 4 production wells. Figure 20 shows the fracture distribution for each layer. Figure 21 shows the permeability distribution of seven layers for egg model. After defining connections and calculating transmissibility in preprocessing code, the simulation is simple to performance using in-house simulators. Two other typical algorithms, particle-swarm optimization (PSO) and ensemble-based optimization (EnOpt), are both used to study their performance on well placement optimization. Figure 22 shows the NPVs with respect to number of iterations for different methods. Figure 23 shows the oil

saturation (first layer) at the final simulation time for different optimization method. Figure 24 shows the cumulative oil production and water cut for different optimization method. As can be seen, the highest NPV is $\$1.02 \times 10^8$ for by using StoSAG. The final NPV for EnOpt and PSO is $\$9.56 \times 10^7$ and $\$9.65 \times 10^7$, respectively. Also, when using StoSAG, the highest cumulative oil production can be achieved in 7200 days.

4. Conclusions

In this work, we use StoSAG for the well placement optimization. The computer-aided well placement optimization method is established for naturally fractured reservoirs based on the recent advances. The embedded discrete fracture method (EDFM) is used to model the natural fractures as its computational efficiency and flexibility. The stochastic simplex approximate gradient (StoSAG) is employed to obtain the approximate gradient by combing the EDFM. The steepest ascent algorithm is used to find the optimal well placement. A series of numerical case studies are set up to examine the performance of the proposed approach. We also demonstrate that f-StoSAG and StoSAG and sf-StoSAG and ss-StoSAG can achieve fairly close results. The workflow can be taken as an effective tool in well placement optimization for naturally fractured reservoirs.

Data Availability

The data used to support the findings of this study are available from the corresponding author upon request.

Conflicts of Interest

The authors declare that they have no conflicts of interest.

Acknowledgments

This study was supported by the Natural Science Foundation of Shandong Province of China (ZR2019BEE030).

References

[1] M. Zandvliet, M. Handels, G. van Essen, D. R. Brouwer, and J. D. Jansen, "Adjoint-based well-placement optimization under production constraints," *SPE Journal*, vol. 13, no. 4, pp. 392–399, 2008.

[2] O. Badru and C. S. Kabir, "Well placement optimization in field development," in *SPE Annual Technical Conference and Exhibition*, Denver, Colorado, 2003.

[3] S. Ding, R. Lu, Y. Xi, G. Liu, and J. Ma, "Efficient well placement optimization coupling hybrid objective function with particle swarm optimization algorithm," *Applied Soft Computing*, vol. 95, article 106511, 2020.

[4] F. Forouzanfar, G. Li, and A. C. Reynolds, "A two-stage well placement optimization method based on adjoint gradient," in *SPE annual technical conference and exhibition*, Florence, Italy, 2010.

[5] O. Volkov and M. C. Bellout, "Gradient-based constrained well placement optimization," *Journal of Petroleum Science and Engineering*, vol. 171, pp. 1052–1066, 2018.

[6] Y. S. Wu, "Multiphase fluid flow in porous and fractured reservoirs," Gulf professional publishing, 2015.

[7] J. E. Warren and P. J. Root, "The behavior of naturally fractured reservoirs," *Society of Petroleum Engineers Journal*, vol. 3, no. 3, pp. 245–255, 1963.

[8] H. Kazemi, "Pressure transient analysis of naturally fractured reservoirs with uniform fracture distribution," *Society of Petroleum Engineers Journal*, vol. 9, no. 4, pp. 451–462, 1969.

[9] H. Kazemi, L. S. Merrill, K. L. Porterfield, and P. R. Zeman, "Numerical simulation of water-oil flow in naturally fractured reservoirs," *Society of Petroleum Engineers Journal*, vol. 16, no. 6, pp. 317–326, 1976.

[10] J. Jiang and R. M. Younis, "Numerical study of complex fracture geometries for unconventional gas reservoirs using a discrete fracture-matrix model," *Journal of Natural Gas Science and Engineering*, vol. 26, pp. 1174–1186, 2015.

[11] J. Xu, B. Sun, and B. Chen, "A hybrid embedded discrete fracture model for simulating tight porous media with complex fracture systems," *Journal of Petroleum Science and Engineering*, vol. 174, pp. 131–143, 2019.

[12] J. Jiang and R. M. Younis, "An improved projection-based embedded discrete fracture model (pEDFM) for multiphase flow in fractured reservoirs," *Advances in Water Resources*, vol. 109, pp. 267–289, 2017.

[13] M. Karimi-Fard, L. J. Durlofsky, and K. Aziz, "An efficient discrete-fracture model applicable for general-purpose reservoir simulators," *SPE Journal*, vol. 9, no. 2, pp. 227–236, 2004.

[14] Z. Huang, X. Yan, and J. Yao, "A two-phase flow simulation of discrete-fractured media using mimetic finite difference method," *Communications in Computational Physics*, vol. 16, no. 3, pp. 799–816, 2014.

[15] H. Hoteit and A. Firoozabadi, "Compositional modeling of discrete-fractured media without transfer functions by the discontinuous Galerkin and mixed methods," *SPE Journal*, vol. 11, no. 3, pp. 341–352, 2006.

[16] W. Zhang and K. M. Al, "Nonlinear finite volume method for 3D discrete fracture-matrix simulations," *SPE Journal*, vol. 25, no. 4, pp. 2079–2097, 2020.

[17] S. Geiger-Boschung, S. K. Matthäi, J. Niessner, and R. Helmig, "Black-oil simulations for three-component, three-phase flow in fractured porous media," *SPE Journal*, vol. 14, no. 2, pp. 338–354, 2009.

[18] A. Zidane and A. Firoozabadi, "An efficient numerical model for multicomponent compressible flow in fractured porous media," *Advances in Water Resources*, vol. 74, pp. 127–147, 2014.

[19] S. H. Lee, M. F. Lough, and C. L. Jensen, "Hierarchical modeling of flow in naturally fractured formations with multiple length scales," *Water Resources Research*, vol. 37, no. 3, pp. 443–455, 2001.

[20] L. Li and S. H. Lee, "Efficient field-scale simulation for black oil in a naturally fractured reservoir via discrete fracture networks and homogenized media," in *International oil & gas conference and exhibition in China*, China, 2006.

[21] L. Li and S. H. Lee, "Efficient field-scale simulation of black oil in a naturally fractured reservoir through discrete fracture networks and homogenized media," *SPE Reservoir Evaluation & Engineering*, vol. 11, no. 4, pp. 750–758, 2008.

[22] A. Moinfar, W. Narr, M. H. Hui, B. Mallison, and S. H. Lee, "Comparison of discrete-fracture and dual-permeability models for multiphase flow in naturally fractured reservoirs," in *Spe reservoir simulation symposium*, The Woodlands, Texas, USA, 2011.

[23] A. Moinfar, A. Varavei, K. Sepehrnoori, and R. T. Johns, "Development of a coupled dual continuum and discrete fracture model for the simulation of unconventional reservoirs," in *SPE reservoir simulation symposium*, The Woodlands, Texas, USA, 2013.

[24] A. Moinfar, A. Varavei, K. Sepehrnoori, and R. T. Johns, "Development of an efficient embedded discrete fracture model for 3D compositional reservoir simulation in fractured reservoirs," *SPE Journal*, vol. 19, no. 2, pp. 289–303, 2014.

[25] M. Yao, H. Chang, X. Li, and D. Zhang, "Tuning fractures with dynamic data," *Water Resources Research*, vol. 54, no. 2, pp. 680–707, 2018.

[26] M. Yao, H. Chang, X. Li, and D. Zhang, "An integrated approach for history matching of multiscale-fracture reservoirs," *SPE Journal*, vol. 24, no. 4, pp. 1508–1525, 2019.

[27] J. Yao, Z. Li, L. Liu, W. Fan, M. Zhang, and K. Zhang, "Optimization of fracturing parameters by modified variable-length particle-swarm optimization in shale-gas reservoir," *SPE Journal*, vol. 26, no. 2, pp. 1032–1049, 2021.

[28] W. Yu, Y. Xu, R. Weijermars, K. Wu, and K. Sepehrnoori, "A numerical model for simulating pressure response of well interference and well performance in tight oil reservoirs with complex–fracture geometries using the fast embedded–discrete–fracture–model method," *SPE Reservoir Evaluation & Engineering*, vol. 21, no. 2, pp. 489–502, 2018.

[29] A. Fumagalli, L. Pasquale, S. Zonca, and S. Micheletti, "An upscaling procedure for fractured reservoirs with embedded grids," *Water Resources Research*, vol. 52, no. 8, pp. 6506–6525, 2016.

[30] J. Hutahaean, V. Demyanov, and M. Christie, "Reservoir development optimization under uncertainty for infill well placement in brownfield redevelopment," *Journal of Petroleum Science and Engineering*, vol. 175, pp. 444–464, 2019.

[31] R. J. Lorentzen, A. Berg, G. Naevdal, and E. H. Vefring, "A new approach for dynamic optimization of water flooding problems," in *Intelligent Energy Conference and Exhibition*, Amsterdam, The Netherlands, 2006.

[32] J. E. Nwaozo, *Dynamic Optimization of a Water Flood Reservoir*, University of Oklahoma, 2006.

[33] Y. Chen, D. S. Oliver, and D. Zhang, "Efficient ensemble-based closed-loop production optimization," *SPE Journal*, vol. 14, no. 4, pp. 634–645, 2009.

[34] S. T. Do and A. C. Reynolds, "Theoretical connections between optimization algorithms based on an approximate gradient," *Computational Geosciences*, vol. 17, no. 6, pp. 959–973, 2013.

[35] A. S. Stordal, S. P. Szklarz, and O. Leeuwenburgh, "A theoretical look at ensemble-based optimization in reservoir management," *Mathematical Geosciences*, vol. 48, no. 4, pp. 399–417, 2016.

[36] R. R. M. Fonseca, B. Chen, J. D. Jansen, and A. Reynolds, "A Stochastic Simplex Approximate Gradient (StoSAG) for optimization under uncertainty," *International Journal for Numerical Methods in Engineering*, vol. 109, no. 13, pp. 1756–1776, 2017.

[37] R. Lu, F. Forouzanfar, and A. C. Reynolds, "An efficient adaptive algorithm for robust control optimization using StoSAG," *Journal of Petroleum Science and Engineering*, vol. 159, pp. 314–330, 2017.

[38] Y. Zhang, R. Lu, F. Forouzanfar, and A. C. Reynolds, "Well placement and control optimization for WAG/SAG processes using ensemble- based method," *Computers & Chemical Engineering*, vol. 101, pp. 193–209, 2017.

[39] B. Chen and J. Xu, "Stochastic simplex approximate gradient for robust life-cycle production optimization: applied to Brugge field," *Journal of Energy Resources Technology*, vol. 141, no. 9, 2019.

[40] J. Xu, W. Zhou, H. Li, X. Wang, S. Liu, and L. Fan, "Stochastic simplex approximation gradient for reservoir production optimization: algorithm testing and parameter analysis," *Journal of Petroleum Science and Engineering*, vol. 209, article 109755, 2022.

[41] J. D. Jansen, R. M. Fonseca, S. Kahrobaei, M. M. Siraj, G. M. van Essen, and P. M. J. van den Hof, "The egg model – a geological ensemble for reservoir simulation," *Geoscience Data Journal*, vol. 1, no. 2, pp. 192–195, 2014.

Hindawi
Geofluids
Volume 2022, Article ID 4859240, 18 pages
https://doi.org/10.1155/2022/4859240

Research Article

Production Behavior Analysis of Multibranched Horizontal Oil Well considering Reservoir and Well-Type Factors

Shukai Tang,[1] Xiaoxiao Sun,[1] Kai Zheng,[1] Liangbin Xu ,[2] and Qingwen Kong[3]

[1]*Dongsheng Group Company Limited of Shengli Oil Field, Dongying 257099, China*
[2]*Sun Yat-Sen University, Zhuhai 528478, China*
[3]*China University of Petroleum (East China), Qingdao 266580, China*

Correspondence should be addressed to Liangbin Xu; xulb@cnooc.com.cn

Received 29 January 2022; Accepted 12 March 2022; Published 27 April 2022

Academic Editor: Bin Wang

Copyright © 2022 Shukai Tang et al. This is an open access article distributed under the Creative Commons Attribution License, which permits unrestricted use, distribution, and reproduction in any medium, provided the original work is properly cited.

Multibranched horizontal well is an important means to develop low permeability reservoirs. Fishbone multibranched horizontal well has the advantages of increasing drainage area, reducing drilling number, utilizing existing wells, and saving oilfield development cost, especially for marginal oilfield exploitation. The morphological structure of fishbone multibranched horizontal well is very complex, so the numerical simulation study is of great significance to guide the production of fishbone multibranched horizontal well. In this paper, the numerical model is established for fishbone multibranched horizontal well in the oil reservoir. The finite element method is used to numerically solve the mathematic model. The oil well production can be achieved by using the material balance method. Sensitivity analysis is made on the important reservoir and well-type factors that affect the production behavior and transient pressure distribution of fishbone multibranched horizontal well. It is concluded that the effective reservoir thickness and flowing bottomhole pressure have great influence on the productivity, but the influence of heterogeneity is not obvious. The length of main wellbore has great effect on the productivity in the early stage. Fishbone multibranched horizontal wells should be placed in the middle of the reservoir to increase productivity. Branch length, branch angle, branch number, and branch spacing are important parameters affecting the productivity of fishbone multibranched horizontal well. The variation of these parameters has obvious influence on the stimulation effect in the early stage of production, but the influence degree is different. Under the premise of drilling technology and drilling safety, the comprehensive impact of these four factors on productivity should be considered simultaneously. The presented model and obtained results not only enrich production behavior analysis of fishbone multibranched horizontal well but also have significance on formulation of stimulation measures and efficient low permeability reservoir development.

1. Introduction

Multibranch horizontal well refers to one horizontal well as the main borehole, and two or more branch boreholes into oil and gas reservoir are drilled in each part of the horizontal well, which can give play to the advantages of high efficiency and high production of horizontal wells, increase the drainage area, tap the remaining oil potential, increase the recovery rate, and improve the field development effect and is widely used in low-permeability reservoirs, thick oil reservoirs, thin reservoirs, and multilayer reservoirs [1–8]. Multibranch horizontal wells have become an important way to develop low-permeability oil and gas reservoirs, and it is of great significance to study the capacity of multibranch horizontal wells and its influencing factors in depth [9–12]. Each branch of a multibranch horizontal well can be regarded as a horizontal well, and there are more factors affecting the productivity of a multibranch horizontal well than a normal horizontal well. The numerical simulation model can provide an important basis for the determination of the reservoir exploitation plan, especially for the understanding of the sensitivity of various factors in the development process and the environmental impact [13, 14]. Many scholars have already conducted studies on the sensitivity analysis of each influencing factor of multibranch horizontal wells and have preliminary experiences and conclusions.

Fishbone spur horizontal wells are one kind of multibranch horizontal wells, the current research ideas and methods are based on the conventional black oil model, and the numerical solutions are all finite difference method. Due to the limitation of finite difference method, the description of fishbone spur horizontal wells by this method has a large gap with the actual conditions, which is one of the difficulties in the current numerical simulation theory research of fishbone spur horizontal wells [15]. Hu et al. studied the effects of structural parameters such as branch symmetry, number of branches, branch angle, and branch length on the productivity of horizontal wells with fishbone spurs [16]. Ozkan et al. proposed a mathematical model for a two-branch horizontal well and gave an analytical solution based on the branch length, angle, vertical distance, and longitudinal distance of the two branches [17]. Wu et al. established a set of semianalytical capacity prediction model for multibranch horizontal wells. The results of the study indicated that the largest possible branch length, the number of branches with more than three branches, and a branch angle of not less than 30° should be selected [18]. Huang et al. studied the effects of uneven flow density distribution in branch wells and main wellbore and uneven skin distribution in each production section on the bottomhole pressure in herringbone multibranch horizontal wells [19].

In terms of benefits and costs, Ren et al. established a numerical simulation model of coal reservoir. The productivity of different well types is predicted and compared with field data [20]. With the development of numerical simulation software, Dai et al. established a variety of geological models by using ECLIPSE numerical simulation software based on the steady-state productivity calculation formula of horizontal and branch wells and physical property parameters of a domestic oil field [1]. Lv et al. conducted a numerical simulation study on horizontal wells with different branch angles and branch lengths. This study showed that the increase of branch angle has little effect on the time to water and water content of horizontal wells with fishbone spur. The increase of the number of branches has a great effect on the production of horizontal wells with fishbone spur in the early stage of exploitation. The longer the branches, the longer the time to water [21–23]. Duan et al. [24] used the mutual coupling of wellbore flow and reservoir inflow to obtain several multibranched well pressure instability curves and delineate the characteristic sections of seepage flow in different multibranch wells.

In this paper, the numerical model of fishbone multibranch horizontal well in reservoir is established to evaluate the effect of reservoir and well-type factors on well production. To numerically solve the mathematic model, the finite element method is employed. The production rate of fishbone multibranch horizontal well is calculated by using the material balance method. The effects of formation thickness, heterogeneity, production pressure differential, main wellbore length and position, branch length, branch angle, branch numbers, and branch spacing on production behavior and transient pressure distribution characteristics are analyzed. The paper is organized as follows: Section 1 is the introduction; Section 2 is the physics and mathematical model; Section 3 is the solution workflow; Section 4 is the sensitivity analysis; Section 5 is the conclusions.

2. System Description

2.1. Physical Model. There are many forms of multibranched horizontal well, among which fishbone branch well is the most representative one, which can reflect all the characteristics of branch well. Therefore, this paper takes fishbone multibranched horizontal well as an example to study the influence of different factors on productivity. The schematic diagram for the physical model of fishbone multibranched horizontal well in reservoir is shown in Figure 1. In this paper, we consider a fishbone multibranched horizontal well with n branch wells in a reservoir with closed top and bottom, where both the main horizontal well and branch wells are perpendicular to the Z axis. The branch wellbore is at a specific angle to the main wellbore in the XY plane (shown in Figure 1(c)), with single-phase fluid (oil) flowing to both main horizontal and branch wells. It is assumed that the branch wellbores are staggered and evenly distributed on both sides of the main wellbore. In addition, there are some parameters that need to be described: (1) the radius of reservoir can be assumed to be r; (2) the reservoir is horizontal with uniform thickness of h and original pressure p_i; (3) the horizontal permeability is K_h, the vertical permeability is K_v, the comprehensive compressibility is C_t, and the porosity is φ; (4) the influence of gravity and capillary forces is ignored. As shown in Figure 1(b), the length of the main wellbore is L, the main wellbore center coordinate is (x, y, z), the length of each branch wellbore is l, the branch angle between branch wellbore and main wellbore is α, and the branch spacing between two branch wellbores is d.

2.2. Mathematical Model. With orthogonal coordinate system, the flow equation can be expressed as follows.

Flow equation in the reservoir is

$$\frac{\partial}{\partial x}\left(\frac{K_h}{\mu}\frac{\partial p}{\partial x}\right)+\frac{\partial}{\partial y}\left(\frac{K_h}{\mu}\frac{\partial p}{\partial y}\right)+\frac{\partial}{\partial z}\left(\frac{K_v}{\mu}\frac{\partial p}{\partial z}\right)=\phi C_t\frac{\partial p}{\partial t}+q. \tag{1}$$

If the sink or source is ignored, Equation (1) can be simplified into the following.

Flow equation in the reservoir is

$$\frac{\partial}{\partial x}\left(\frac{K_h}{\mu}\frac{\partial p}{\partial x}\right)+\frac{\partial}{\partial y}\left(\frac{K_h}{\mu}\frac{\partial p}{\partial y}\right)+\frac{\partial}{\partial z}\left(\frac{K_v}{\mu}\frac{\partial p}{\partial z}\right)=\phi C_t\frac{\partial p}{\partial t}. \tag{2}$$

Initial condition:

$$p(x, y, z, t=0)=p_i. \tag{3}$$

Outer boundary:

$$\frac{\partial p}{\partial z}=0, \quad z=0 \text{ or } h,$$
$$p=0, r=\infty, \tag{4}$$

where x, y, and z are the directional coordinates, m; K_h and K_v are horizontal permeability and vertical permeability

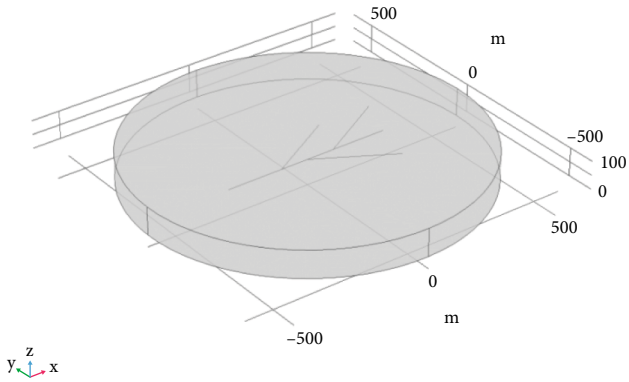

(a) 3D view of reservoir with fishbone multibranched horizontal well

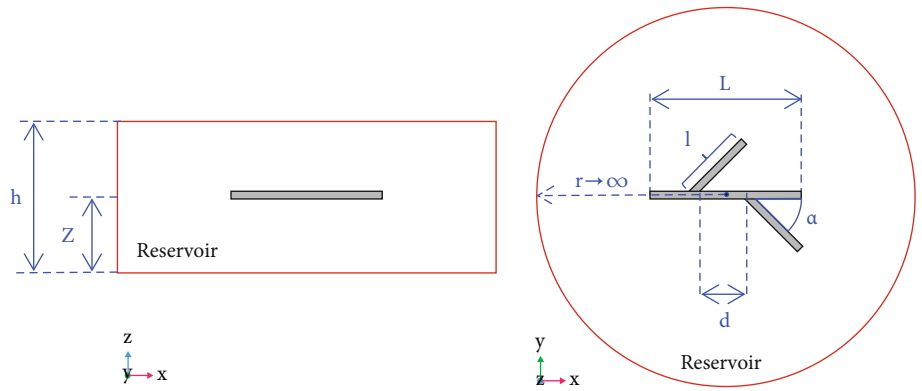

(b) 2D view of reservoir with fishbone multibranched horizontal well

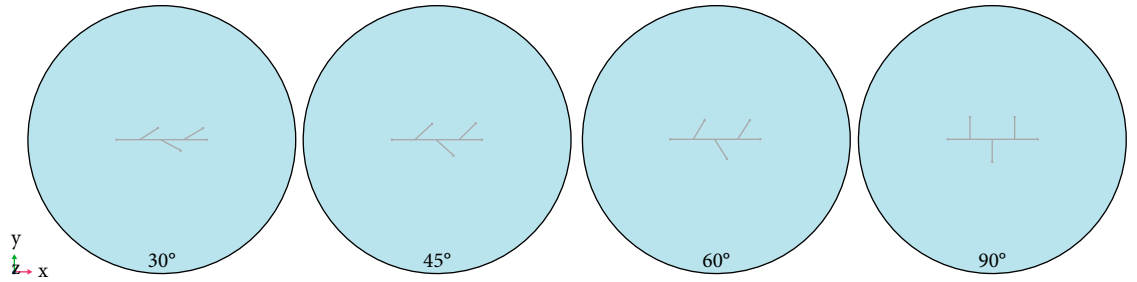

(c) Fishbone multibranched horizontal wells with different branch angles

Figure 1: Physical model of fishbone multibranched horizontal well in oil reservoir.

at any point in reservoir, respectively, m^2; p is reservoir pressure, Pa; p_i is reference pressure, Pa; μ is viscosity of oil, Pa·s; t is time, sec; C_t is comprehensive compressibility factor, 1/Pa; and φ are the formation porosity, fraction.

3. Model Solution

In this study, we use finite element method to solve the equation system. The basic function is defined as

$$N = (N_1, N_2, \cdots, N_n). \tag{5}$$

The displacement function is

$$\tilde{p} = \sum_{i=1}^{n} N_i p_i. \tag{6}$$

We can get the integrating form for reservoir:

$$\iiint_{\Omega_e} N_i \left[\frac{\partial}{\partial x}\left(\frac{K_h}{\mu}\frac{\partial \tilde{p}}{\partial x}\right) + \frac{\partial}{\partial y}\left(\frac{K_h}{\mu}\frac{\partial \tilde{p}}{\partial y}\right) + \frac{\partial}{\partial z}\left(\frac{K_v}{\mu}\frac{\partial \tilde{p}}{\partial z}\right)\right] dV = \iiint_{\Omega_e} (\phi C_t) N_i \frac{\partial \tilde{p}}{\partial t} dV. \tag{7}$$

The final equation form is:

$$\iiint_{\Omega_e}\left\{\left(\frac{K_h}{\mu}\right)\begin{pmatrix}\frac{\partial N_1}{\partial x}\\ \frac{\partial N_2}{\partial x}\\ \vdots\\ \frac{\partial N_n}{\partial x}\end{pmatrix}\begin{pmatrix}\frac{\partial N_1}{\partial x} & \frac{\partial N_2}{\partial x} & \cdots & \frac{\partial N_n}{\partial x}\end{pmatrix}+\left(\frac{K_h}{\mu}\right)\begin{pmatrix}\frac{\partial N_1}{\partial y}\\ \frac{\partial N_2}{\partial y}\\ \vdots\\ \frac{\partial N_n}{\partial y}\end{pmatrix}\begin{pmatrix}\frac{\partial N_1}{\partial y} & \frac{\partial N_2}{\partial y} & \cdots & \frac{\partial N_n}{\partial y}\end{pmatrix}+\left(\frac{K_v}{\mu}\right)\begin{pmatrix}\frac{\partial N_1}{\partial z}\\ \frac{\partial N_2}{\partial z}\\ \vdots\\ \frac{\partial N_n}{\partial z}\end{pmatrix}\begin{pmatrix}\frac{\partial N_1}{\partial z} & \frac{\partial N_2}{\partial z} & \cdots & \frac{\partial N_n}{\partial z}\end{pmatrix}\right\} \tag{8}$$
$$\begin{pmatrix}p_1\\ p_2\\ \vdots\\ p_n\end{pmatrix}dV+\iiint_{\Omega_e}(\phi C_t)\begin{pmatrix}N_1\\ N_2\\ \vdots\\ N_n\end{pmatrix}\begin{pmatrix}N_1 & N_2 & \cdots & N_n\end{pmatrix}\begin{pmatrix}\frac{p_1^n-p_1^{n-1}}{\Delta t}\\ \frac{p_2^n-p_2^{n-1}}{\Delta t}\\ \vdots\\ \frac{p_n^n-p_n^{n-1}}{\Delta t}\end{pmatrix}dV=0.$$

The production rate can be obtained by material balance method.

4. Discussion and Analysis

4.1. Effect of Reservoir Properties

4.1.1. Effect of Formation Thickness (h). The effect of formation thickness on production behavior is discussed in this section. The reservoir properties and main well parameters are shown in Table 1. Basic parameters of branch well to be paid attention to are $n = 3$, $\alpha = 90°$, $l = 100$ m, and $d = 100$ m.

The effect of formation thickness on transient pressure distribution and oil production of fishbone multibranched horizontal well is presented in Figure 2. Figure 2(a) describes the transient pressure distributions characteristics at 5000 d considering different formation thickness. As shown in Figures 2(b) and 2(d), the oil production rate for 30 m of formation thickness is higher than that of the other two scenarios in the early stage of production. However, the influence of formation thickness on production rate can be ignored in the later stage of production. This is because in the late stage of production, the oil production capacity of the formation is close to the limit, the remaining oil around the well is less, and the water cut is too high. The cumulative production for 30 m of formation thickness is higher than that of the other two scenarios in the whole process of production. Figure 2(c) shows that for different time at initial stage of production, oil production rate increases linearly with increasing formation thickness. The formation thickness can be considered as the effective thickness. This indicates that with the increase of effective thickness, oil reserves increase and multibranched well recovery capacity increases.

4.1.2. Effect of Formation Heterogeneity (K_v/K_h). The effect of formation heterogeneity on production behavior is discussed in this section. The reservoir properties and main well parameters are shown in Table 2. It should be noted that the well structure used here is the same as that used in Section 4.1.1.

The effect of formation heterogeneity on production behavior of fishbone multibranched horizontal well is presented in Figure 3. The effect of formation heterogeneity on transient pressure distribution at 5000 d for 100 m of formation thickness is presented in Figure 4. As shown in Figure 3, the effect of K_v/K_h on oil production behavior is sensitive to the formation thickness. In the formation with large h, the difference of oil production behavior is more obvious due to the difference of formation heterogeneity. Figures 3(d) and 3(e) show that with the increase of K_v/K_h value, that is, with the increase of vertical permeability, vertical seepage resistance decreases and productivity increases in the early stage of production. In the later stage of production, the influence of K_v/K_h on production rate can be basically ignored, but a there are some differences in cumulative production. In addition, as shown in Figures 3(c) and 3(f), the production rate at the initial stage of production increases with the decrease of reservoir heterogeneity, but the increase rate gradually decreases. The gradual decrease in the growth rate is mainly due to the existence of the limit oil production capacity of the formation. Figure 4 shows that the pressure drop propagation is slowly due to the small K_v/K_h, that is, the strong heterogeneity of formation. Different K_v/K_h have different effect on area and shape of control area. The vertical permeability of reservoirs has an important influence on the productivity of multibranched horizontal well. When using multibranched horizontal well to develop oil reservoirs with the same other conditions, reservoirs with higher vertical permeability should be given priority.

4.2. Effect of Flowing Bottomhole Pressure (FBHP). The effect of FBHP on production behavior is discussed in this section. The reservoir properties and main well parameters are shown in Table 3. Basic parameters of branch well to be paid attention to are $n = 3$, $\alpha = 90°$, $l = 100$ m, and $d = 100$ m.

Table 1: Input parameters of simulation for considering different formation thickness.

Parameter	Value	Parameter	Value
Formation thickness, h (m)	10, 20, 30	Initial reservoir pressure, p_i (MPa)	20
Porosity, φ	0.4	Flowing bottomhole pressure, p_w (MPa)	10
Permeability, K_h (μm^2)	0.005	Formation heterogeneity, K_v/K_h	1
Formation rock compressibility, C_f (1/MPa)	2×10^{-4}	Formation fluid compressibility, C_l (1/MPa)	10×10^{-4}
Formation fluid viscosity, μ (mP·s)	5	Formation fluid density, ρ (kg/m^3)	1000
Reservoir radius, r_1 (m)	600	Main horizontal well length, L (m)	400
Main horizontal well center coordinates (x, y, z)		$(0, 0, 5)$	

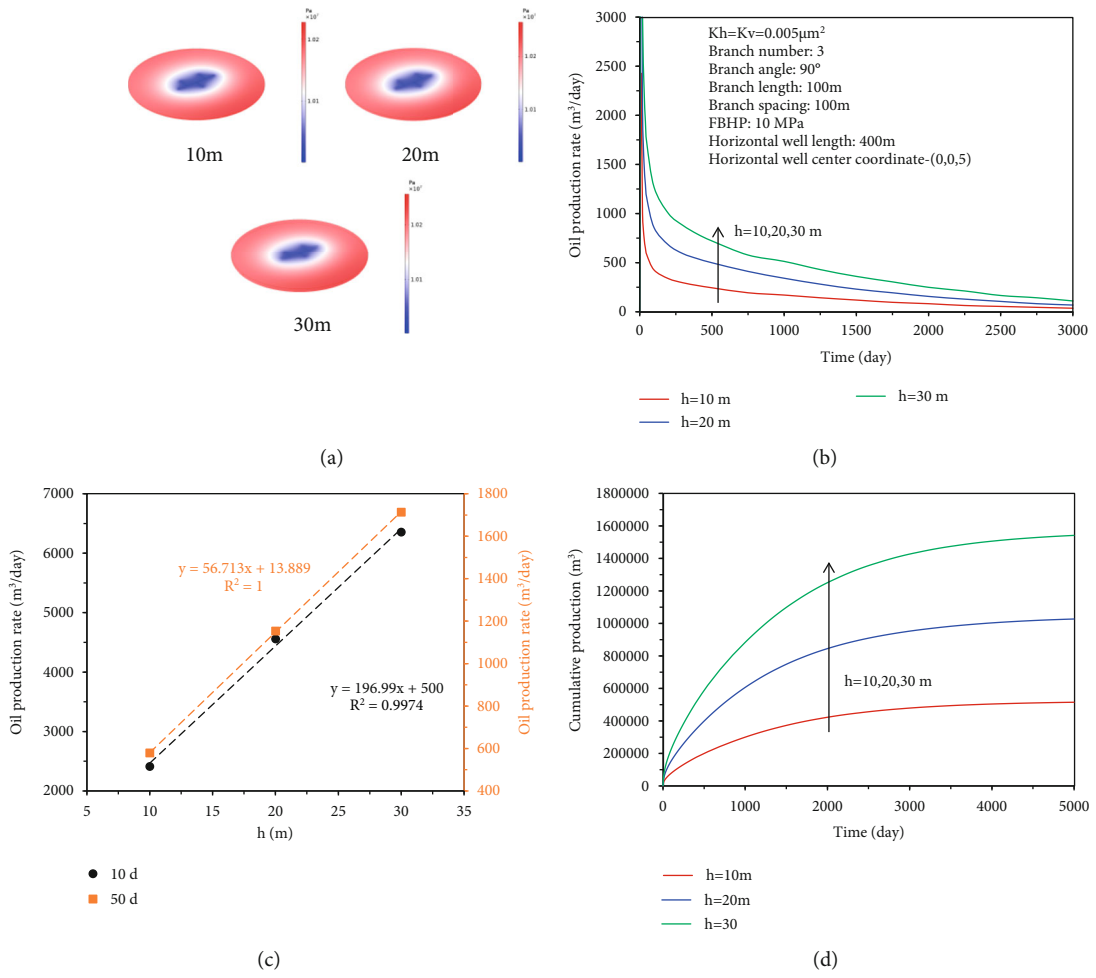

Figure 2: Effect of formation thickness on transient pressure distribution and production behavior.

The effect of FBHP on production behavior of fishbone multibranched horizontal well is presented in Figure 5. The effect of FBHP on transient pressure distribution at 5000 d is presented in Figure 6. It should be noted that different FBHPs represent different production pressure differentials. As shown in Figure 5, as the FBHP decreases (i.e., the production pressure differential increases), the production rate and cumulative production increase in early stage of production, indicating that lower bottom hole pressure (i.e., the larger production pressure differential) results in greater elastic productivity. Figure 5(a) shows that the influence of FBHP on production rate can be ignored in the later stage of production. The cumulative production for 8 MPa of FBHP is higher than that of the other two scenarios in the whole process of production. Figure 5(c) shows that for different times at the initial stage of production, oil production rate increases linearly with increasing production pressure differential. However, the oil production rate increases

Table 2: Input parameters of simulation for considering different formation heterogeneity.

Parameter	Value	Parameter	Value
Formation thickness, h (m)	10,100	Initial reservoir pressure, p_i (MPa)	20
Porosity, φ	0.4	Flowing bottomhole pressure, p_w (MPa)	10
Horizontal permeability, K_h (μm^2)	0.005	Formation heterogeneity, K_v/K_h	1,0.5,0.1,0.05
Formation rock compressibility, C_f (1/MPa)	2×10^{-4}	Formation fluid compressibility, C_l (1/MPa)	10×10^{-4}
Formation fluid viscosity, μ (mP·s)	5	Formation fluid density, ρ (kg/m^3)	1000
Reservoir radius, r_1 (m)	600	Main horizontal well length, L (m)	400
Main horizontal well center coordinates (x, y, z)		$(0, 0, 5)$	

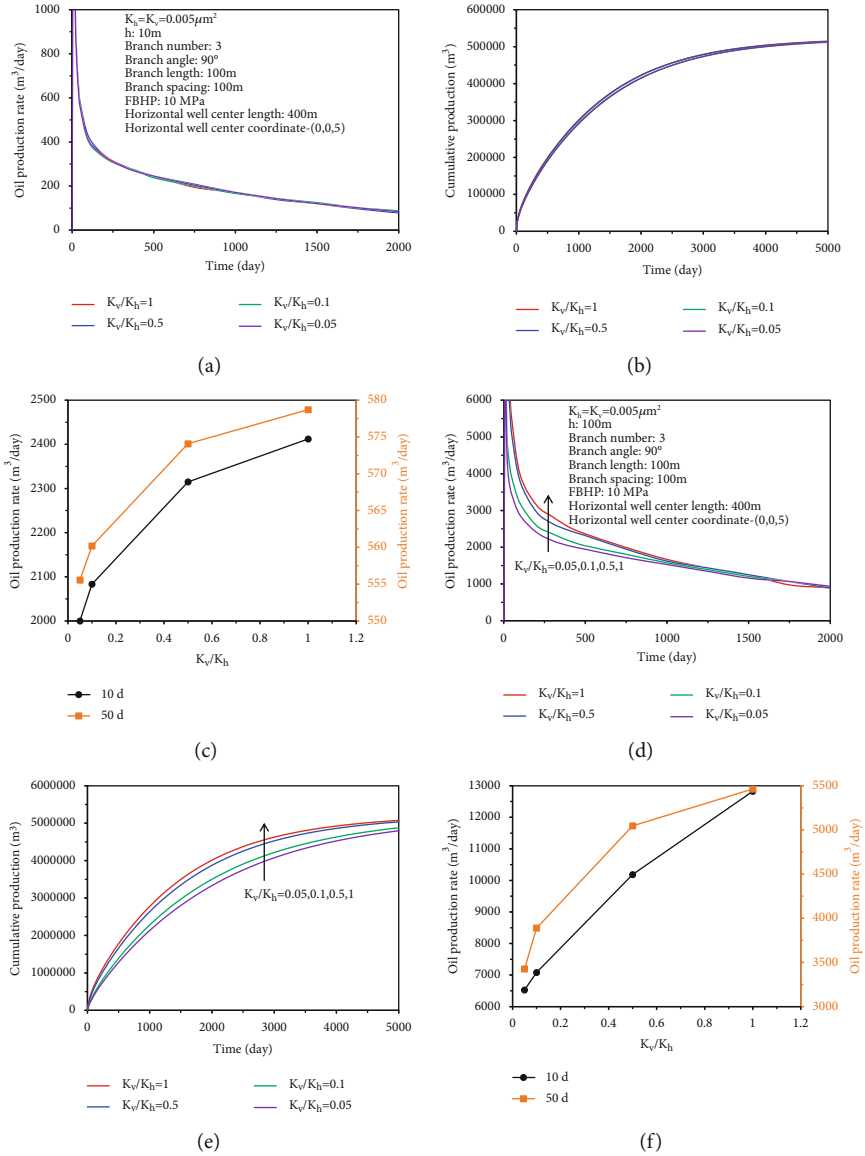

Figure 3: Effect of formation heterogeneity on production behavior.

slowly with increasing production time. Figure 6 shows that the pressure drop propagation is slowly due to the small production pressure differential, that is, the large FBHP.

4.3. Effects of Well-Type Factors. Compared with traditional vertical and horizontal well, fishbone multibranched horizontal well has complex well structure and complex seepage

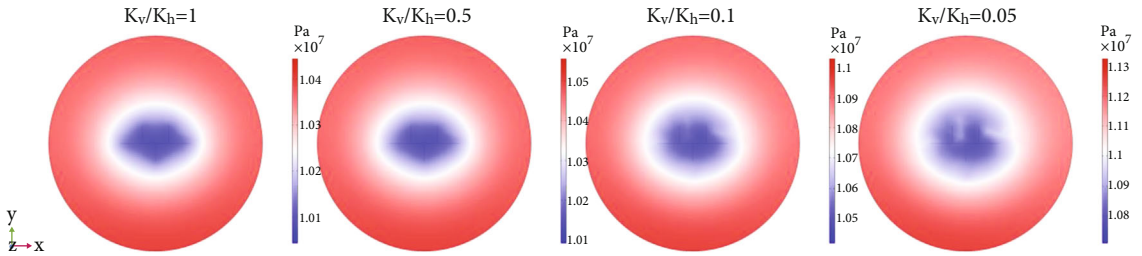

Figure 4: Effect of formation heterogeneity on transient pressure distribution.

Table 3: Input parameters of simulation for considering different FBHP.

Parameter	Value	Parameter	Value
Formation thickness, h (m)	10	Initial reservoir pressure, p_i (MPa)	20
Porosity, φ	0.4	Flowing bottomhole pressure, p_w (MPa)	8,10,12
Horizontal permeability, K_h (μm^2)	0.005	Formation heterogeneity, K_v/K_h	1
Formation rock compressibility, C_f (1/MPa)	2×10^{-4}	Formation fluid compressibility, C_l (1/MPa)	10×10^{-4}
Formation fluid viscosity, μ (mP·s)	5	Formation fluid density, ρ (kg/m^3)	1000
Reservoir radius, r_1 (m)	600	Main horizontal well length, L (m)	400
Main horizontal well center coordinates (x, y, z)		$(0, 0, 5)$	

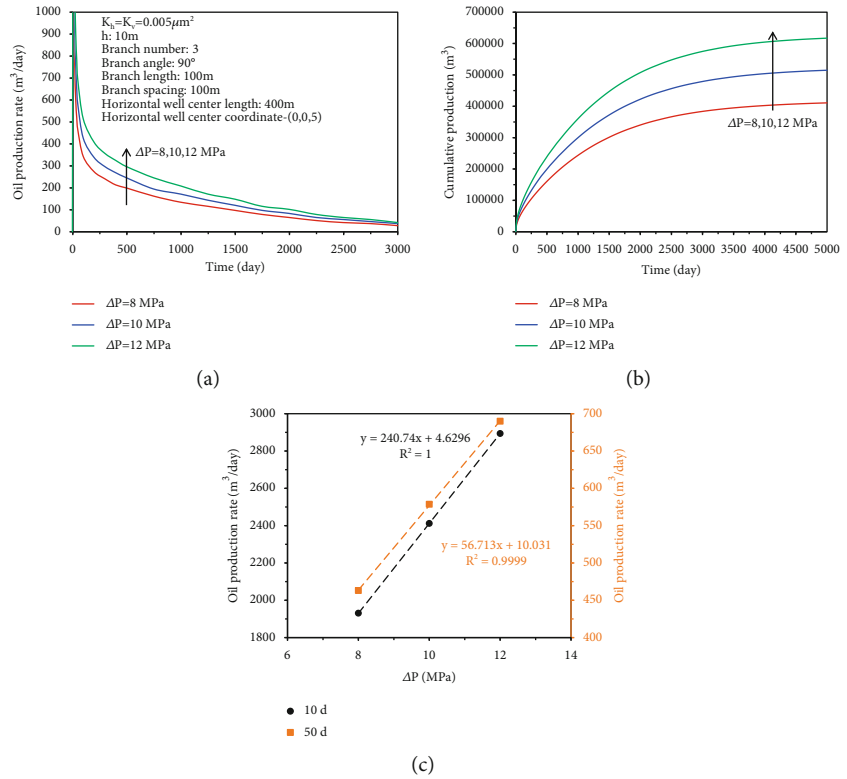

Figure 5: Effect of FBHP on production behavior.

law in the formation near the wellbore. In this section, the effects that various well-type factors on the transient pressure distribution and production behavior in an oil reservoir described mathematically in the previous section are discussed. The well-type factors include the length of main horizontal wellbore, L; the location of main horizontal wellbore in reservoir, (x, y, z); the length of branch wellbore, l; the number of branch wellbore, n; the branch angle between

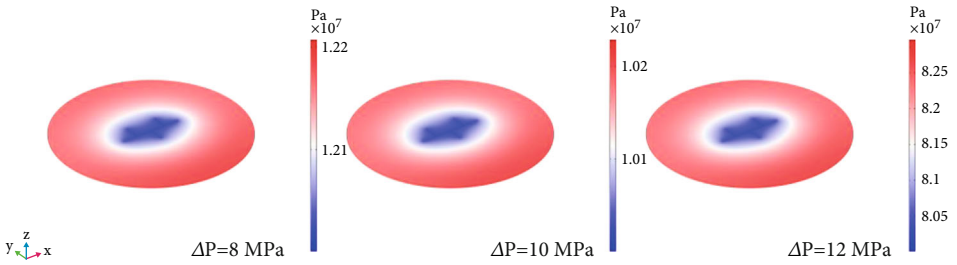

Figure 6: Effect of production pressure differential on transient pressure distribution.

Table 4: Input parameters of simulation for considering different L.

Parameter	Value	Parameter	Value
Formation thickness, h (m)	10	Initial reservoir pressure, p_i (MPa)	20
Porosity, φ	0.4	Flowing bottomhole pressure, p_w (MPa)	10
Horizontal permeability, K_h (μm^2)	0.005	Formation heterogeneity, K_v/K_h	1
Formation rock compressibility, C_f (1/MPa)	2×10^{-4}	Formation fluid compressibility, C_l (1/MPa)	10×10^{-4}
Formation fluid viscosity, μ (mP·s)	5	Formation fluid density, ρ (kg/m^3)	1000
Reservoir radius, r_1 (m)	600	Main horizontal well length, L (m)	400,600,800
Main horizontal well center coordinates (x, y, z)		$(0, 0, 5)$	

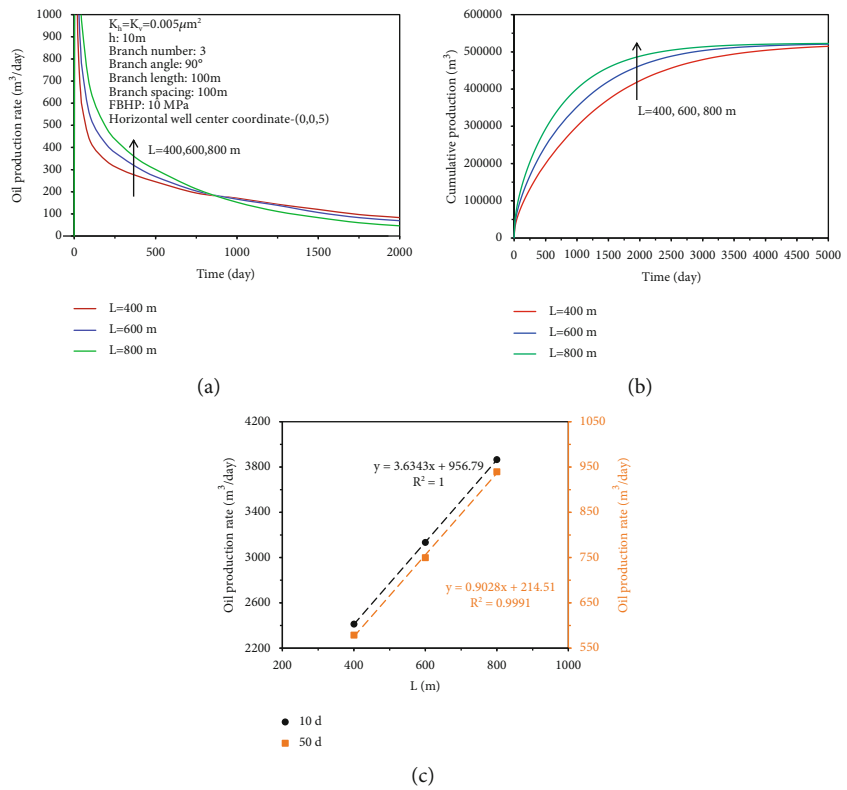

Figure 7: Effect of main wellbore length on production behavior.

branch wellbore and main wellbore, α; and the branch spacing between two branch wellbores, d. Sensitivity analysis of different factors is as follows.

4.3.1. Effect of the Length of Main Horizontal Wellbore (L). The effect of L on production behavior is discussed in this section. The reservoir properties and main well parameters

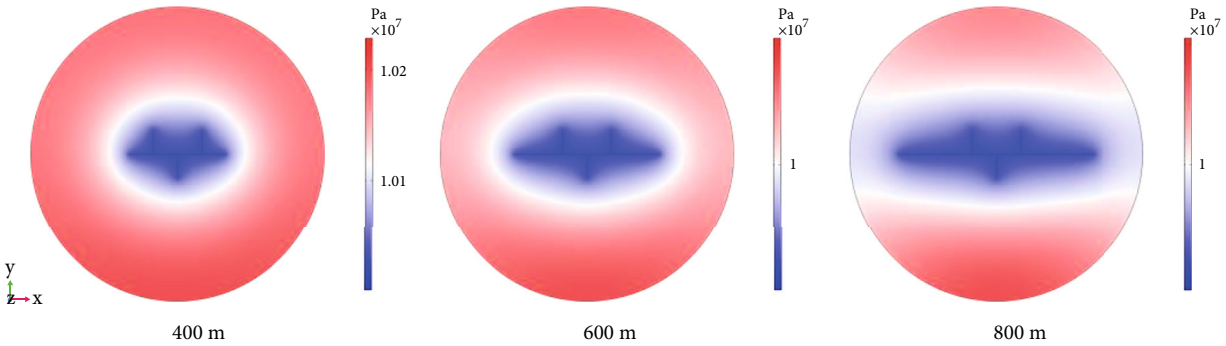

Figure 8: Effect of main wellbore length on transient pressure distribution.

Table 5: Input parameters of simulation for considering different locations of the main horizontal wellbore.

Parameter	Value	Parameter	Value
Formation thickness, h (m)	10,100	Initial reservoir pressure, p_i (MPa)	20
Porosity, φ	0.4	Flowing bottomhole pressure, p_w (MPa)	10
Horizontal permeability, K_h (μm^2)	0.005	Formation heterogeneity, K_v/K_h	1
Formation rock compressibility, C_f (1/MPa)	2×10^{-4}	Formation fluid compressibility, C_l (1/MPa)	10×10^{-4}
Formation fluid viscosity, μ (mP·s)	5	Formation fluid density, ρ (kg/m^3)	1000
Reservoir radius, r_1 (m)	600	Main horizontal well length, L (m)	400
Main horizontal well center coordinates (x, y, z)		z : (0, 0, 10), (0, 0, 25), (0, 0, 50) y : (0, 0, 5), (0,200,5), (0,400,5) x : (0, 0, 5), (150,0, 5), (300,0, 5)	

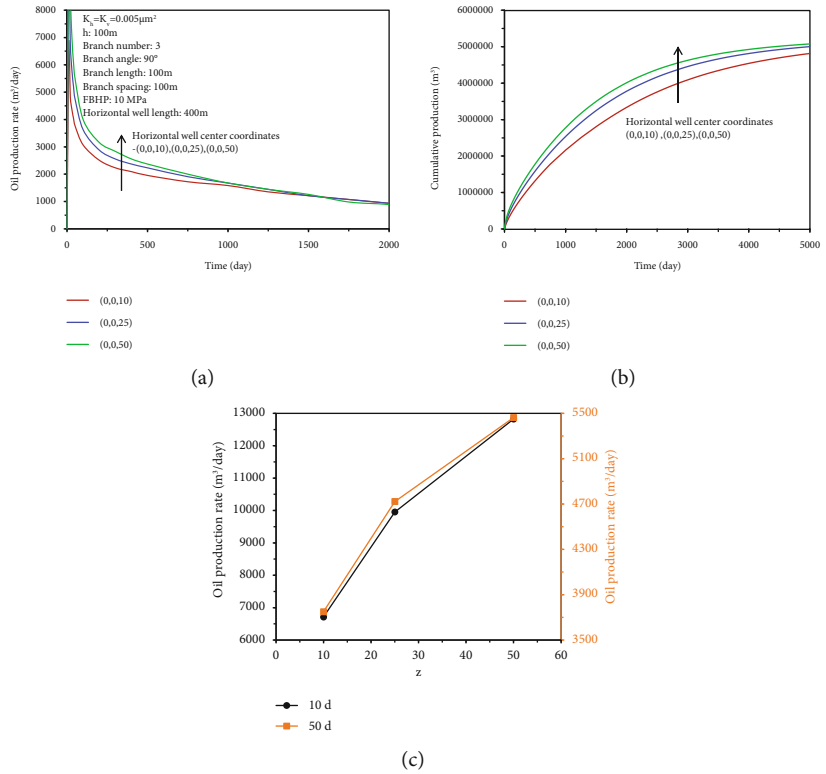

Figure 9: Effect of vertical height of the main wellbore on production behavior.

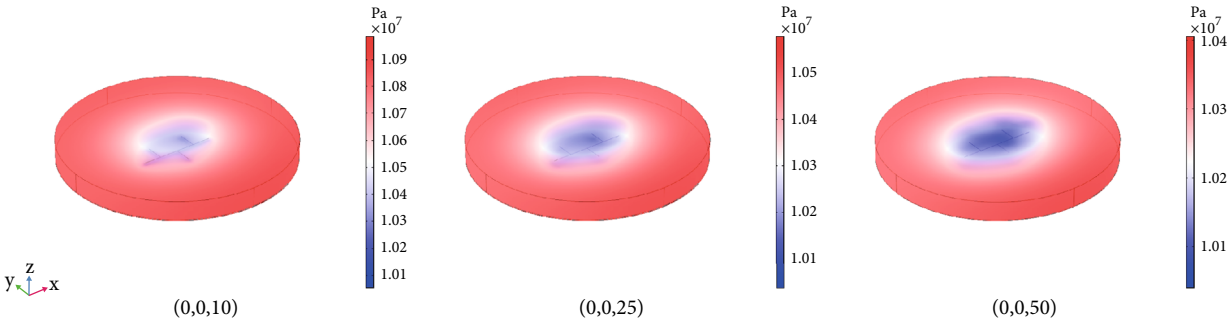

Figure 10: Effect of vertical height of the main wellbore on transient pressure distribution.

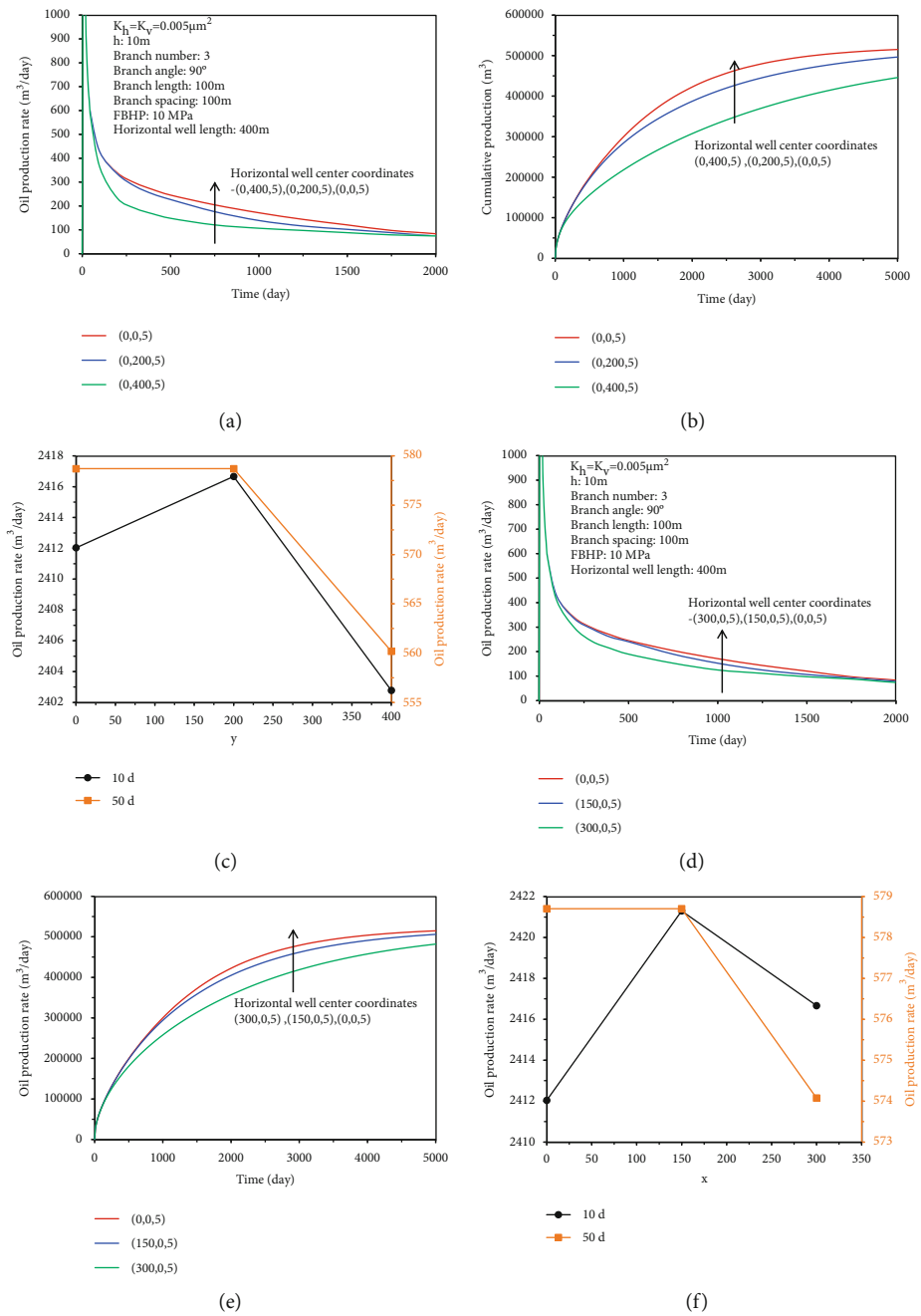

Figure 11: Effect of location of the main wellbore in horizontal plane on production behavior.

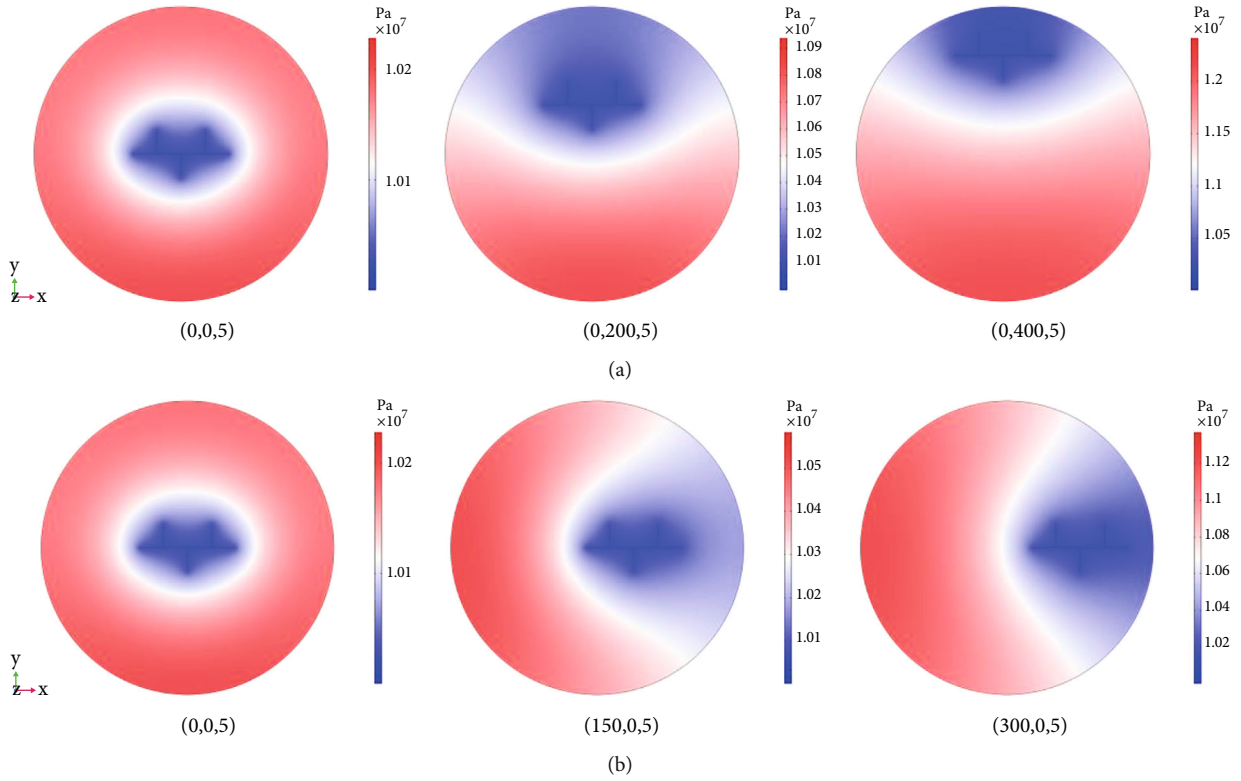

Figure 12: Effect of location of the main wellbore in horizontal plane on transient pressure distribution.

Table 6: Input parameters of simulation for considering different branch well structure.

Parameter	Value	Parameter	Value
Formation thickness, h (m)	10	Initial reservoir pressure, p_i (MPa)	20
Porosity, φ	0.4	Flowing bottomhole pressure, p_w (MPa)	10
Horizontal permeability, K_h (μm^2)	0.005	Formation heterogeneity, K_v/K_h	1
Formation rock compressibility, C_f (1/MPa)	2×10^{-4}	Formation fluid compressibility, C_l (1/MPa)	10×10^{-4}
Formation fluid viscosity, μ (mP·s)	5	Formation fluid density, ρ (kg/m^3)	1000
Reservoir radius, r_1 (m)	600	Main horizontal well length, L (m)	400
Main horizontal well center coordinates (x, y, z)		$(0, 0, 5)$	

are shown in Table 4. Basic parameters of branch well to be paid attention to are $n = 3$, $\alpha = 90°$, $l = 100$ m, and $d = 100$ m.

The effect of L on production behavior of fishbone multibranched horizontal well is presented in Figure 7. The effect of L on transient pressure distribution at 5000 d is presented in Figure 8. As shown in Figure 7, as L decreases, both the production rate and cumulative production of multibranch well increase at the early stage of production. It indicates that large length of the main wellbore results in the increase of the initial production capacity. Figure 7(b) shows that the influence of L on cumulative production can be ignored in the later stage of production, but a there are some differences in production rate. Figure 7(c) shows that for different times at the initial stage of production, oil production rate increases linearly with increasing production pressure differential. Figure 8 shows that the contact area (i.e., drainage area) with reservoir can be increased by increasing the length of the main wellbore, and the pressure propagation can quickly spread to the boundary and provide a stable energy supply, which helps to increase the productivity.

4.3.2. Effect of the Location of Main Horizontal Wellbore in Reservoir (x, y, z). The effect of location of main horizontal wellbore in reservoir on production behavior is discussed in this section. The reservoir properties and main well parameters are shown in Table 5. It should be noted that the well structure used here is the same as that used in Section 4.3.1.

(1) Effect of Vertical Height of the Main Wellbore (z). The effect of vertical height of the main wellbore (z) on production behavior of fishbone multibranched horizontal well for 100 m of formation thickness is presented in Figure 9. The effect of vertical height on transient pressure distribution at

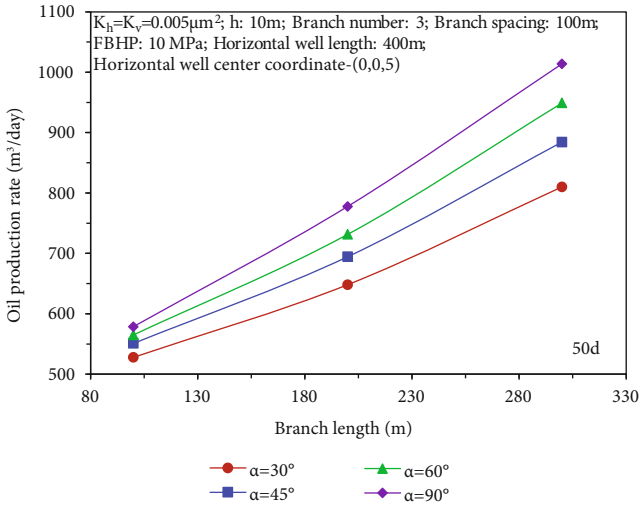

Figure 13: Effect of branch length on production rate.

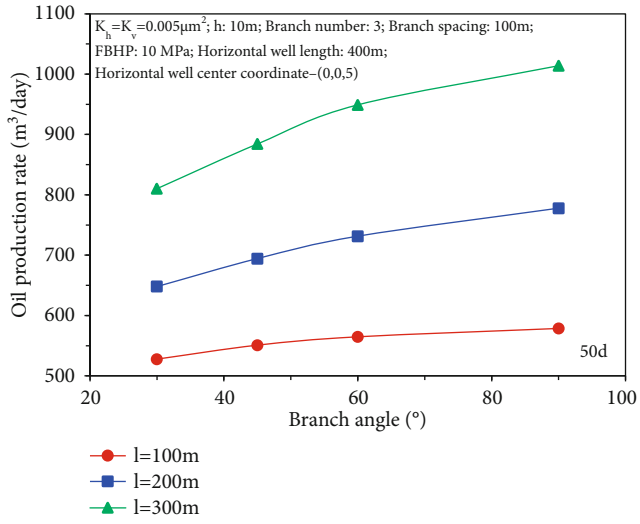

Figure 14: Effect of branch angle on production rate.

5000 d for 100 m of formation thickness is presented in Figure 10. As shown in Figures 9(a) and 9(b), as z increases from 10 to 50, both the production rate and cumulative production increase at initial stage of production. That indicates that well locating in the middle of the reservoir results in higher early production. In the later stage of production, the influence of vertical height on production rate can be basically ignored, but a there are some differences in cumulative production. In addition, as shown in Figure 9(c), the production rate at the initial stage of production increases with increasing z, but the increase rate gradually decreases. Figure 10 shows that the pressure drop propagation is slowly due to the small z (i.e., the closer the well is to the bottom boundary), thus leading to the relatively weak productivity.

(2) Effect of Location of the Main Wellbore in Horizontal Plane (x and y). The effect of location of the main wellbore in horizontal plane on production behavior for 10 m of h is presented in Figure 11. The effect of location in horizontal plane on transient pressure distribution at 5000 d for 10 m of formation thickness is presented in Figure 12. As shown in Figures 11(a), 11(b), 11(d), and 11(e), as the x or y decreases, both the production rate and cumulative production increase at the early stage of production. That indicates that well located in the middle of the reservoir resulted in higher early production. In the later stage of production, the influence of x or y on production rate can be basically ignored, but there are some differences in cumulative production. In addition, as shown in Figures 11(c) and 11(f), the production rate for $y = 200$ or $x = 150$ at 10 d are higher than other two scenarios, respectively. However, at 50 d, the production rate for $y = 0$ and 200 are equal, as well as or $x = 0$ and 150, and the production rate for $y = 400$ or $x = 300$ are the lowest. Figure 12 shows that the pressure drop propagation is slowly due to the big y or x (i.e., the closer the well is to the vertical boundary), thus leading to the relatively weak productivity.

4.3.3. Effect of the Branch Well Structure. The effect of branch well structure on production behavior is discussed in this section. The reservoir properties and main well parameters are shown in Table 6.

(1) Effect of the Length of Branch Well (l). The effect of l on production behavior is discussed in this section. Basic parameters of branch well to be paid attention to are $n = 3$ and $d = 100$ m. The initial production rate at production time of 50 d was taken as the comparison target. The effect of different branch lengths on production rate of multibranched horizontal well is shown in Figure 13. The production rate of multibranched horizontal well increases approximately linearly with the increase of branch length, and the increase rate gradually increases. The reason for this is that the larger the branch length, the less the increase in the length of the branch is affected by the main wellbore, and the greater the stimulation effect for each additional length of the branch. It can also be seen from Figure 13 that the effect of increasing branch length is different with different branch angles. The larger the branch angle is, the longer the branch length is, which makes the control area of the multilateral horizontal wells larger, the mutual interference between the lateral wells is weakened, the influence of the main well on the lateral wells is weakened, and the growth rate of the production rate is greater.

(2) Effect of the Branch Angles (α). The effect of α on production behavior is discussed in this section. Basic parameters of branch well to be paid attention to are $n = 3$ and $d = 100$ m. The initial production rate at production time of 50 d was taken as the comparison target. The effect of the number of branches on the production rate of multibranched horizontal well is shown in Figure 14. The production rate of multibranched horizontal well increases approximately linearly with the increase of branch angle, and the increase rate gradually decreases. The angle at which the increase rate slows down is generally around 45°. The larger the branch length, the greater the effect of the branch angle on production rate. The reason is that when the branch angle is small,

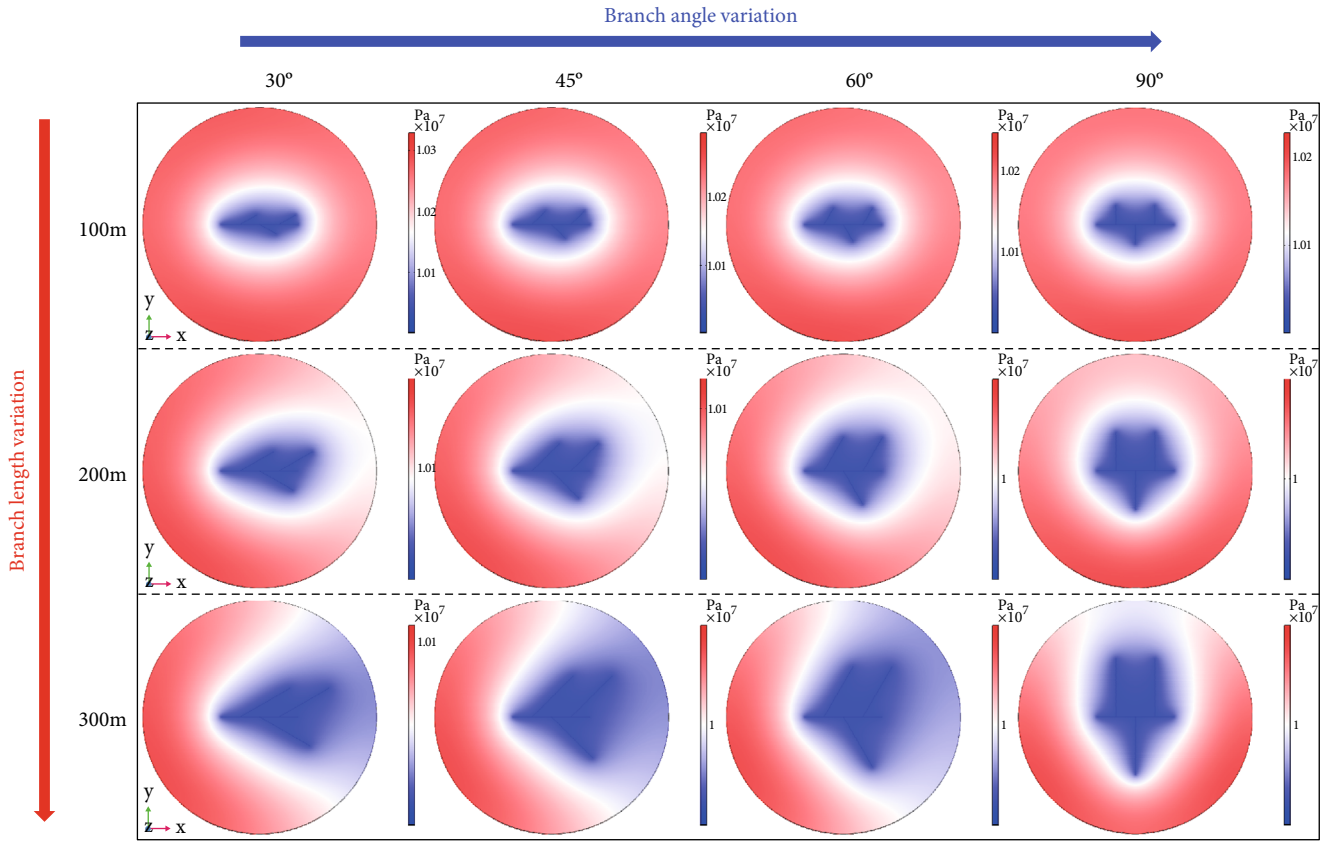

Figure 15: Effect of branch length and angle on transient pressure distribution at 5000 d.

the effect of the main wellbore on the branch wellbores decreases rapidly with each additional angle, and the contribution of the branch well to production rate increases rapidly. However, when the branch angle is large, the effect of the branch wellbores on the main wellbore becomes less obvious every time the angle increases, and the contribution of the branch well to the production rate is relatively small. Therefore, with the increase of the branch angle, the increase rate of production rate of the multibranched horizontal well gradually decreases. In the design of multibranched well, the angle between the branch wellbore and the main wellbore should be larger as far as possible.

The effects of branch length and angle on transient pressure distribution at 5000 d are presented in Figure 15. We can find that at a given branch length, with the increase of branch angle, the control area of fishbone multibranched horizontal well increases, and the interference between branch wellbore and main wellbore decreases. Similarly, at a given branch angle, with the increase of branch length, the control area increases, and the interference between branch wellbore and main wellbore decreases. It can also be seen that the increase of branch angle has different effects on the shape and area of control area of fishbone multibranched horizontal well under different branch lengths. The longer the branch length, the greater the influence of branch angle on the shape and area of control area.

After comparison, it can be concluded that the increase of branch length has a greater effect on the increase of control area (drainage area) of fishbone multibranched horizontal well than the increase of branch angle, thus resulting in the greater stimulation effect on production rate. Therefore, under the premise of drilling technology and drilling safety, the influence of branch length should be given priority, and longer branch length and larger branch angle should be selected.

The effect of branch angle on evolution of transient pressure distribution for different production stage is presented in Figure 16. At 10 d, the initial stage of production, the low-pressure area rapidly diffused outward. With further production, the low-pressure area begins to increase gradually. With the increase of branch angle, the change trend of the pressure field is similar to that of the branch angle of 30°, but the diffusion speed of the low-pressure area gradually becomes faster, and the area of the low-pressure area gradually becomes larger. In the late production period, the area of low-pressure area gradually tends to be stable, and the area of low-pressure area of the fishbone multibranched horizontal well with larger branch angle is larger.

(3) Effect of the Numbers of Branch Well (n). The effect of n on production behavior is discussed in this section. Basic parameters of branch well to be paid attention to are $\alpha = 45°$ and $d = 100$ m. The initial production rate at production time of 50 d was taken as the comparison target. The effect of the number of branches on the production rate of multibranched horizontal well is shown in Figure 17. With the

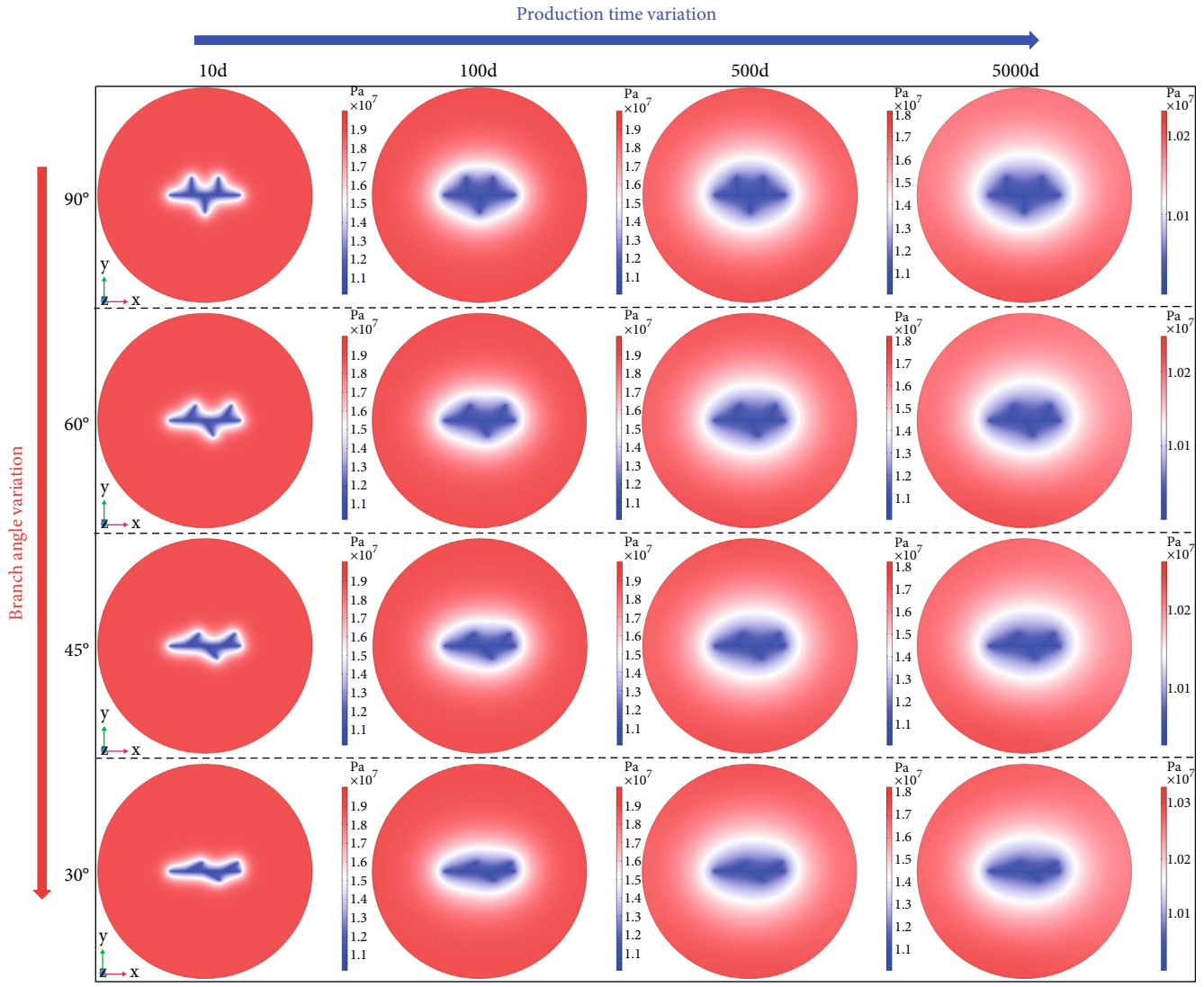

Figure 16: Effect of branch angle on evolution of transient pressure distribution.

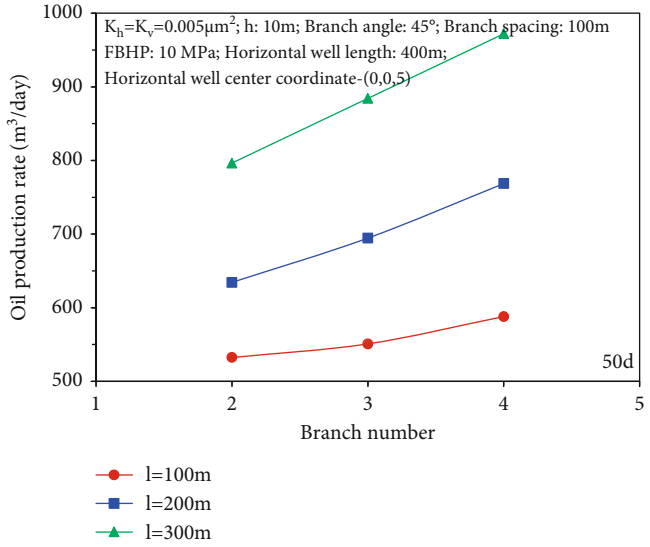

Figure 17: Effect of branch numbers on production rate.

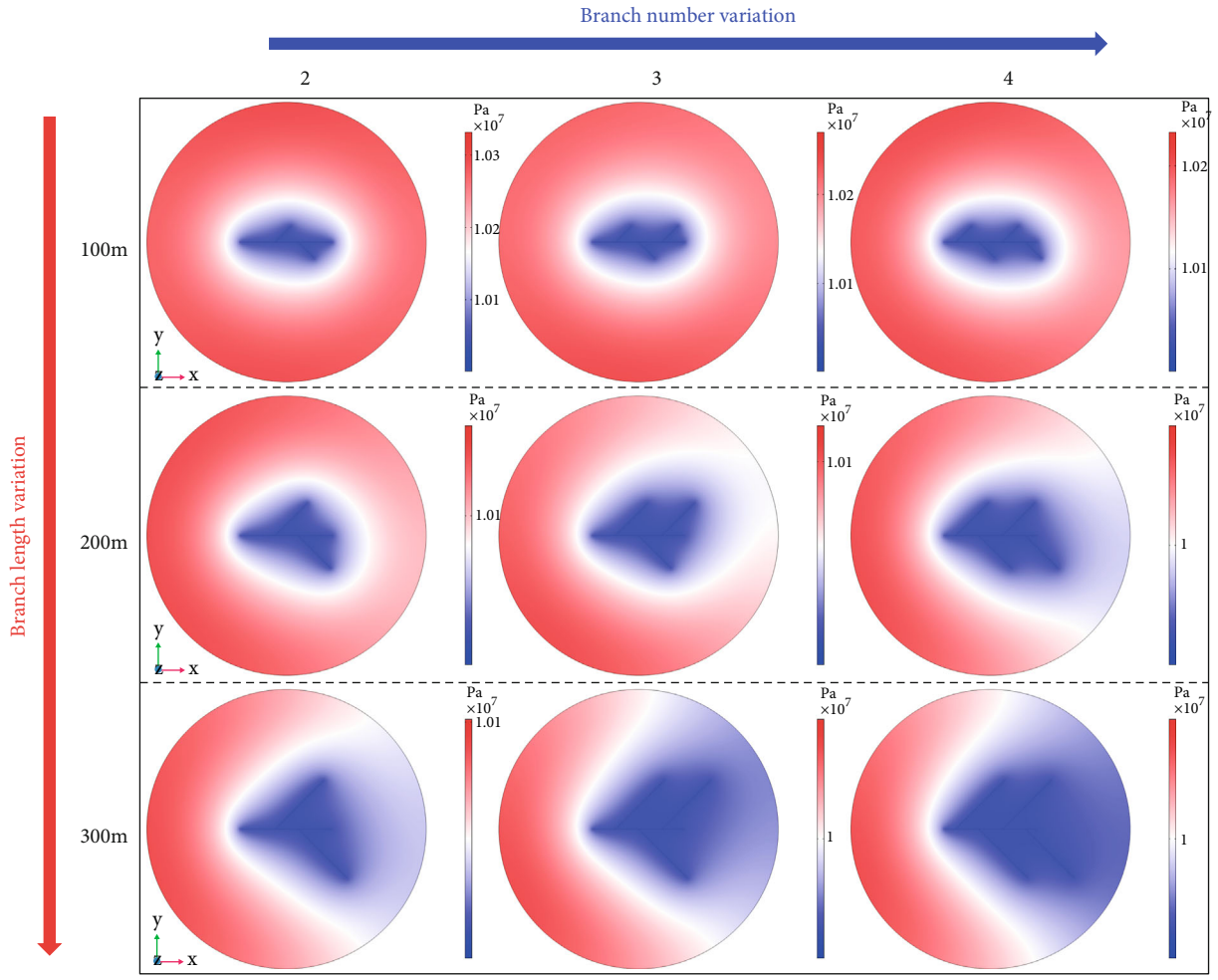

Figure 18: Effect of branch numbers on transient pressure distribution at 5000 d.

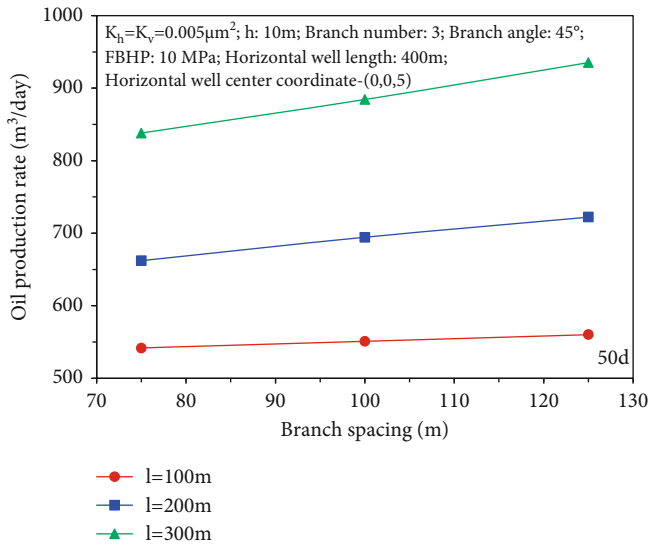

Figure 19: Effect of branch spacing on production rate.

increase of the numbers of branch well, the total production rate of multibranched well increases approximately linearly, but the effect of increasing branch numbers varies greatly under the condition of different branch lengths. When the branch length is 100 m, the increase of the branch numbers causes a slight increase in total production rate, while when

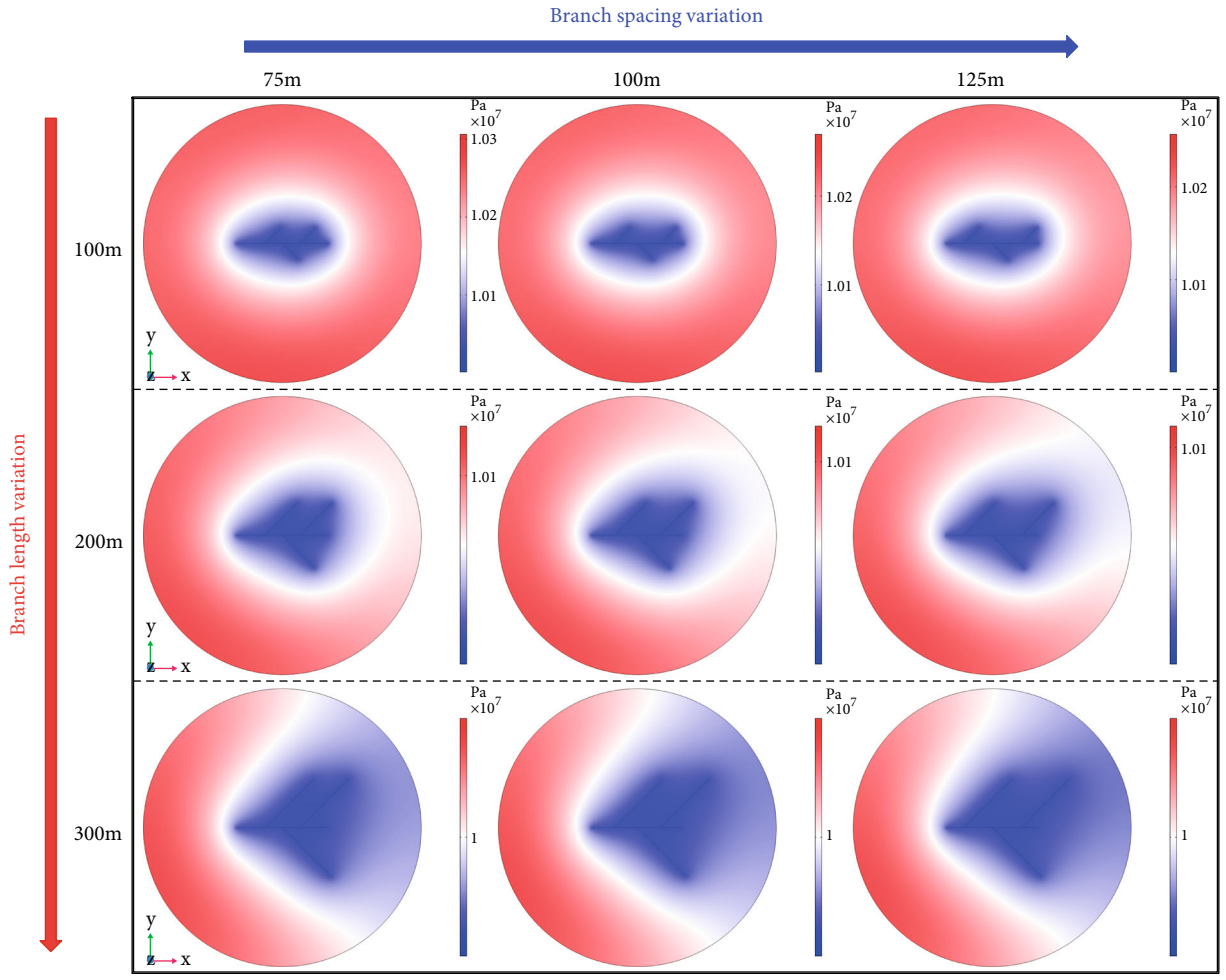

Figure 20: Effect of branch spacing on transient pressure distribution at 5000 d.

the branch length is 300 m, the increase of branch numbers can significantly increase the total production rate of the multibranched horizontal well.

The effects of branch numbers and length on transient pressure distribution at 5000 d are presented in Figure 18. We can find that at a given branch length, with the increase of branch numbers, the control area of fishbone multibranched horizontal well increases, but the interference between branch wellbore and main wellbore increases. Similarly, at given branch numbers, with the increase of branch length, the control area increases, and the interference between branch wellbore and main wellbore decreases. It can also be seen that the increase of branch numbers has different effects on the shape and area of control area of fishbone multibranched horizontal well under different branch lengths. The longer the branch length, the greater the influence of branch numbers on the shape and area of control area.

(4) Effect of the Spacing between Two Branch Wells (d). The effect of d on production behavior is discussed in this section. Basic parameters of branch well to be paid attention to are $n = 3$ and $\alpha = 45°$. The initial production rate at production time of 50 d was taken as the comparison target. The effect of the branch spacing on the production rate of multibranched horizontal well is shown in Figure 19. With the increase of the branch spacing, the total production rate of multibranched well increases linearly, but the effect of increasing branch spacing varies greatly under the condition of different branch lengths. When the branch length is 100 m, the increase of the branch spacing causes a slight increase in total production rate, while when the branch length is 300 m, the increase of branch spacing can significantly increase the total production rate of the multibranched horizontal well.

On the one hand, the reason is that when the branch length is small, the effect of the main wellbore on the branch wellbores decreases slowly with each additional spacing, and the contribution of the branch well to production rate increases slowly. On the other hand, when the branch spacing is large, the interference between branch wellbores becomes less obvious, and the contribution of the branch

well to the production rate is relatively big. Therefore, the influence of branch length should also be considered when choosing proper branch spacing.

The effects of branch spacing and length on transient pressure distribution at 5000 d are presented in Figure 20. We can find that at a given branch length, with the increase of branch spacing, the control area of fishbone multibranched horizontal well increases, and the interference between branch wellbore and main wellbore decreases. Similarly, at a given branch spacing, with the increase of branch length, the control area increases, and the interference between branch wellbore and main wellbore decreases. It can also be seen that the increase of branch length has different effects on the shape and area of control area of fishbone multibranched horizontal well under different branch spacing. The larger the branch spacing, the greater the influence of branch length on the shape and area of control area.

5. Conclusions

In this paper, we investigated the production behavior and transient pressure distribution characteristics of fishbone multibranched horizontal well in an oil reservoir by numerical simulation considering different reservoir and well-type factors. From the above analysis, the following conclusions can be drawn:

(1) The numerical model of fishbone multibranched horizontal oil well is established. The mathematical model is numerically solved by finite element method, and oil production rate is calculated using material balance method. The different transient pressure distribution characteristics and production behavior are caused by various reservoir and well-type factors

(2) The reservoir properties, as well as FBHP, have important effect on the production behavior and transient pressure distribution. With the increase of effective thickness, oil reserves increase and multibranched well recovery capacity increases. With the increase of heterogeneity, vertical seepage resistance increases and productivity decreases. Different heterogeneity has different effect on area and shape of control area, and the vertical permeability has an important influence on the productivity. Lower FBHP results in greater elastic productivity. The pressure drop propagation is slowly due to the large FBHP

(3) The length and location of the main wellbore have an important effect on the production behavior and transient pressure distribution. The large length of the main wellbore results in the increase of the production capacity. When the horizontal section of the multibranched well is located in the middle of the reservoir, the daily production and cumulative oil production of the multibranched well are the largest under any circumstances. In addition, at the horizontal plane, deviating from the middle of the reservoir perpendicular to the main well has a greater impact on productivity

(4) The branch well structure which is an important factor affecting the productivity of fishbone multibranched horizontal well includes branch length, branch numbers, branch angle, and branch spacing. With the increase of branch length, the production rate increases more obviously with large branch angle, and the increase rate gradually increases. With the increase of branch angle, the production rate increases more obviously with large branch length, but the increase rate gradually decreases. With the increase of branch numbers, the production rate increases more obviously with large branch length. With the increase of branch spacing, the production rate increases more obviously with large branch length. The increase of branch length has a greater effect on the increase of production rate and control area than the effect of other factors. Hence, a longer branch length should be selected under the premise of drilling technology and drilling safety

(5) The analysis results show that the new method and model in this study have important significance to production behavior analysis for practical application. The new method not only enriches production analysis of fishbone multibranched horizontal well in reservoir considering different influencing factors and provides some valuable advice for drilling but also provided a useful tool in performance analysis of other multibranched well with complex structure in two-region composite reservoirs

Data Availability

The data in this study are available. If you need to obtain the data in this study, please contact "z19020014@s.upc.edu.cn" by email.

Conflicts of Interest

The authors declare that they have no conflicts of interest.

References

[1] S. G. Dai, C. T. Zhang, J. Zhu, and Q. Li, "Multi-branch horizontal well productivity factors affecting research," *Journal of chongqing institute of technology (natural science edition)*, vol. 14, no. 4, pp. 32–34, 2012.

[2] Z. Q. Jiang, "Study on productivity evaluation and parameter optimization of multi-branch horizontal well," *China University of Geosciences Beijing*, 2009.

[3] T. Wan, J. Wang, Z. Sha et al., "Tough+multilateral well model construction based on mView in numerical simulation of natural gas hydrate," *Marine Geology Frontiers*, vol. 37, no. 11, pp. 60–69, 2021.

[4] W. J. Tank, B. C. Curran, and E. E. Wadleigh, "Targetinghorizontal wells efficient oil capture and fracture insights," *SPE Reservoir Evaluation & Engineering*, vol. 37, no. 751, pp. 601–605, 1997.

[5] J. R. Gilman, J. L. Bowzer, and B. W. Rothkopfr, "Application of short radius horizontal boreholes in thenaturally fractured Yates Field," *SPE Reservoir Engineering*, vol. 28, no. 568, pp. 21–25, 1994.

[6] D. T. Vo, E. L. Marsh, L. J. Sienkiewicz, M. D. Mueller, and R. S. May, "Gulfof Mexico horizontal well improves attic-oil recoveryin active water-drive reservoir," *SPE Reservoir Engineering*, vol. 12, no. 3, pp. 163–168, 1997.

[7] D. A. Bodnar, P. J. Clifford, J. S. Isby et al., "First horizontal water injectors in Prudhoe Bay Field, Alaska," *SPE Reservoir Engineering*, vol. 12, no. 2, pp. 104–108, 1997.

[8] F. M. Giger, "Low permeability reservoirs development using horizontal wells," *SPE/DOE Joint Symposium on Low Permeability Reservoirs*, vol. 16, no. 406, pp. 173–183, 1987.

[9] W. L. Jiang, J. P. Ye, and D. W. Qiao, "The recent process and developing tendency in CBM multi-branch horizontal well," *China mining*, vol. 19, no. 1, pp. 101–103, 2010.

[10] L. I. Mingzhong, C. H. E. N. Huijuan, and Z. H. A. N. G. Xiansong, "Wellbore pressure and inflow rate distribution of multilateral horizontal well for coalbed methane," *Journal of China university of petroleum edition of natural science*, vol. 38, no. 1, pp. 92–97, 2014.

[11] B. J. Duan, W. Y. Yao, and W. S. Wang, "Of coalbed methane multi-branch horizontal well test analysis method research," *Journal of Yangtze university*, vol. 13, no. 1, 2016.

[12] J. J. Guo, H. T. Wang, L. H. Zhang, Q. G. Liu, Y. Y. Feng, and C. Q. Li, "Well testing model and pressure dynamics for multilateral horizontal wells in naturally fractured gas reservoirs," *Journal of China university of petroleum (edition of natural science)*, vol. 38, no. 6, pp. 106–112, 2014.

[13] Y. Huang, *Research on Productivity Prediction of Multi-Branch Horizontal Wells*, Yangtze University, 2015.

[14] D. P. Hou, *Research on Productivity and Interference of Multi-Branch Horizontal Wells*, Northeast Petroleum University, 2015.

[15] M. Sun, Y.-s. Yang, H.-y. Zhu, and L. Wang, "Impact of fishbone well structure on production performance," *Special oil and gas reservoirs*, vol. 19, no. 2, 2012.

[16] B. Hu, S. Cheng, Z. Yuan, X. Sui, and L. I. Xiaojing, "Experimental research on fishbone wells by electric field analogue model," *Journal of liaoning technical university natural science edition*, vol. 28, no. S1, pp. 127–130, 2009.

[17] E. Ozkan, T. Yildiz, and F. Kuchuk, "Pressure behavior of dual lateral wells," *SPE Journal*, vol. 3, no. 2, pp. 181–190, 1998.

[18] X. Wu, A. N. Yongsheng, G. Han, and X. Sui, "Sensitivity analysis of multilateral horizontal well productivity," *Oil drilling & production technology*, vol. 31, no. 6, pp. 19–22, 2009.

[19] H. Yao, C. Shiqing, H. Youwei, and Y. Haiyang, "Transient pressure analysis of fishbone multi-lateral horizontal well with non-uniform flux density," *Journal of shenzhen university science and technology edition*, vol. 33, no. 2, pp. 202–210, 2016.

[20] J. Ren, L. Zhang, S. Ren et al., "Multi-branched horizontal wells for coalbed methane production: field performance and well structure analysis," *International Journal of Coal Geology*, vol. 131, pp. 52–64, 2014.

[21] C. Lu, H. T. Yang, H. Z. Wang, J. B. He, S. K. Liu, and L. Y. Xu, "Influence of branch angle on productivity of fish bone spur horizontal well," *Chemical Engineering and Equipment*, vol. 7, pp. 5–8, 2016.

[22] L. V. Chong, Y. Haitao, H. Jinbao, and X. Liyan, "The effect of branch length on productivity on herringbone well," *Petrochemical Industry Technology*, vol. 23, no. 5, pp. 133-134, 2016.

[23] C. Lu, H. T. Yang, H. Z. Wang et al., "Branch number of fish bone spur the influence of the horizontal well productivity research," *Journal of modern chemical industry*, vol. 6, pp. 1207–1210, 2016.

[24] Y. Duan, W. Chen, T. Huang, and X. Yan, "Seepage characteristics and unsteady pressure performance of multi-lateral wells," *Journal of Xi 'an Shiyou University Natural Science Edition*, vol. 2, 2007.

Hindawi
Geofluids
Volume 2022, Article ID 1795369, 13 pages
https://doi.org/10.1155/2022/1795369

Research Article

Well Interference Analysis of Shale Gas Wells Based on Embedded Discrete Fracture Model

Qing Zhang

Shale Gas Exploration and Development Department, CNPC Chuanqing Drilling Engineering Co., Ltd., Chengdu, Sichuan 610051, China

Correspondence should be addressed to Qing Zhang; zhangpetro@126.com

Received 16 November 2021; Accepted 15 January 2022; Published 19 April 2022

Academic Editor: Shuyang Liu

Copyright © 2022 Qing Zhang. This is an open access article distributed under the Creative Commons Attribution License, which permits unrestricted use, distribution, and reproduction in any medium, provided the original work is properly cited.

Well interference is commonly observed in shale gas reservoirs due to the small well spacing, and it significantly affects the shale gas production. Effective evaluation of well interference is important to increase the gas production of shale gas wells. Previous researches mainly focus on the well interference phenomenon and production optimization using numerical simulation so that the quantitative analysis of shale gas well interference is rare. Therefore, this paper is aimed at analyzing the well interference of shale gas wells through production type curves. First, the complex fracture networks are described by using the embedded discrete fracture model (EDFM). Second, different cases are designed to characterize different types and degrees of well interference in shale gas reservoirs. Third, numerical modelling is conducted to simulate the well interference and its effect on gas production. Fourth, the type curves are obtained to quantitatively analyze and compare the impact of well interference on shale gas production. Results show that well interference caused by hydraulic fractures mainly reduce the gas production of the parent well while the gas production of child well can be increased owing to the larger equivalent stimulated area. The pressure depletion is obvious when the well communication degree becomes higher. Differences can be found from early to late periods by the combination of log-log and Blasingame type curves. This work provides a method for well interference evaluation, and it can be used to obtain well spacing and adjust fracturing parameter in shale gas reservoirs.

1. Introduction

The permeability and porosity of shale gas reservoirs are ultralow due to abundant nanopores [1–5]. Stimulation technology is required to obtain commercial productivity [6]. Horizontal well drilling and hydraulic fracturing technologies have been commonly used to generate high-permeability fracture networks [7–11]. Multiwell pad is further introduced to decrease the drilling and fracturing costs, and each well pad is usually composed of six to eight horizontal wells [12, 13]. However, well interference is observed in shale gas reservoirs due to the small well spacing (e.g., 300 m to 500 m). How to characterize and analyze the well performance in shale gas reservoirs is important for enhancing the ultimate shale gas production [14].

In recent years, the well interference phenomena in unconventional oil and gas reservoirs have attracted much research interest [15–17]. The well interference is modelled using different methods. Lawal et al. simulated and forecasted frac hits in shale gas wells and indicated that the gas production reduction was caused by the flow resistance due to the multiphase flow in the fracture network or the permeability decrease around the wells [18]. Moradi and Angus modelled the frac hits by using dynamic microseismicity-constrained enhanced fracture regions [19]. Guo et al. conducted numerical investigation about the effects of subsequent parent well injection on interwell fracturing interference using reservoir-geomechanics-fracturing modelling approaches [20]. Mohaghegh presented dynamic simulation of frac hit based on artificial intelligence and machine learning methods [21]. The impact of fracturing interference on gas production performance is also analyzed [22]. The mechanisms of well interference and different types of well interference types in shale reservoirs are further investigated [23–25]. Various methods are developed to evaluate the well interference caused by hydraulic fracturing in the shale reservoirs. Sardinha et al.

applied frac pressure hits and production interference analysis to estimate the well connectivity [26]. Gupta et al. focused on identifying the well interference by forecasting long-term production and residual analysis [27]. Molina established an analytical model to assess the fraction of frac fits in multiwell pads [28]. Kumar et al. performed integrated analysis of tracer and pressure-interference tests to identify well interference [29]. Arman et al. forecasted the mid and far field frac hits at an Eagle Ford and Wolfcamp well based on shale pressure depletion and well performance using geomechanical constraints [30]. GIS Platform was used to evaluate the risks of frac hits in the Aishwarya Barmer-Hill Field [31]. Magneres et al. developed a workflow to estimate the well interferences and its maximum expected well head pressure using magnitude forecast methodology [32]. To enhance the shale gas production, well spacing needs to be optimized to decrease well interference [33–35]. Except for well spacing, the stimulation design also needs to be optimized [36]. Different fracturing technologies are applied to prevent well interference, including fracture geometry control technology [37] and adaptive fracturing [38]. Other prevention methods are also proposed to mitigate the well interference especially the frac hits, including preloading depleted parent wells or fluid injection [39–41], chemical or mechanical treatments such as refracturing or solvent/surfactant chemistry blend [42–44]. Also, there are some filed case studies about the mitigation measures for well interference [45, 46]. However, the remedial costs are huge and the recovering effect is uncertain by the prevention measures. A quick and accurate evaluation of well interference is important for selecting measures to reduce the effect of well interference on shale gas production. Exact characterization of complex fracture networks is required for shale gas wells, especially for the multiple wells with fracture interference [47–49]. The embedded discrete fracture model (EDFM) is able to accurately and efficiently deal with both natural fractures and hydraulic fractures, which does not require local grid refinement nearby fractures through nonneighboring connections [50–53]. PTA and RTA are methods to analyze well interference, which can identify the characteristics of well interference in some specific periods [54–59].

The current research mainly focuses on the phenomenon, reason, mechanism, and mitigation suggestions for well interference. The quantitative analysis method for shale gas well interference evaluation needs to be further investigated. Thus, this paper tries to analyze the well interference of shale gas wells through production type curves based on numerical simulation using EDFM technology.

2. Fracture Characterization and Calculation

Complex fracture networks are generated through large-scale hydraulic fracturing in shale gas formations. How to characterize and calculate the formed fracture networks including both hydraulic and natural fractures becomes a crucial issue for efficient development of shale gas resources. The dual porosity and dual permeability models belong to the continuum media, which is unavailable for the fracture description in shale gas reservoirs [60]. A discrete fracture model is more accurate to characterize the hydraulic fractures and natural fractures [61]. Although the discrete fracture model based on unstructured grids shows good performance in representing complex fracture geometries, the huge number of grids and big differences among grid scale result in high computation costs and poor convergence as well as difficulty on gridding [62]. Therefore, it is hard to efficiently handle the complex fractures by using the discrete fracture model based on unstructured grids. In recent years, the EDFM was developed to meet the accuracy of discrete fracture models with structured gridding especially in the unconventional oil and gas reservoirs [63]. The grid number is significantly reduced since the refinement near the fractures is not required compare to the discrete fracture model with unstructured gridding. Furthermore, the gridding is easier and the convergence is better based on EDFM.

2.1. Nonneighboring Connections. The nonneighboring connections (NNCs) are proposed to handle the different intersections among natural fractures, hydraulic fractures, and matrices [62]. The fracture can be divided into multiple segments through matrix cells and generate NNCs. The fluid flow between the fracture and matrix can be efficiently modelled using the transmissibility of NNCs [63].

The NNCs can be divided into three categories (see Figure 1), including the connection between the matrix grid and fracture segment, connection between different fracture segments within the same fracture, and connection between different fractures.

2.1.1. Transmissibility of Connection between Matrix Grid and Fracture Segment. The schematic of fracture-matrix connection can be found in Figure 1(a). Its transmissibility can be calculated by [62]

$$T_{f-m} = \frac{2A_f(\overrightarrow{\overrightarrow{K}} * \overrightarrow{n}) * \overrightarrow{n}}{d_{f-m}}, \tag{1}$$

$$d_{f-m} = \frac{\int_V X_n dV}{V}, \tag{2}$$

where A_f is the area of the fracture plane. $\overrightarrow{\overrightarrow{K}}$ denotes the permeability tensor. $\overrightarrow{n}$ is the normal vector of the fracture plane. d_{f-m} represents the distance between the matrix and fracture segment. V means the fracture volume. X_n denotes the distance from the matrix unit to the fracture segment.

2.1.2. Transmissibility of Connection between Fracture Segments within the Same Fracture. The connection between fracture segments from the same fracture is shown in Figure 1(b). Its transmissibility can be obtained and expressed as [62]

$$T_{\text{seg}} = \frac{T_1 T_2}{T_1 + T_2}, \tag{3}$$

$$T_1 = \frac{k_f A_c}{d_{\text{seg }1}}, T_2 = \frac{k_f A_c}{d_{\text{seg }2}}, \tag{4}$$

where k_f is the fracture permeability. A_c means the common

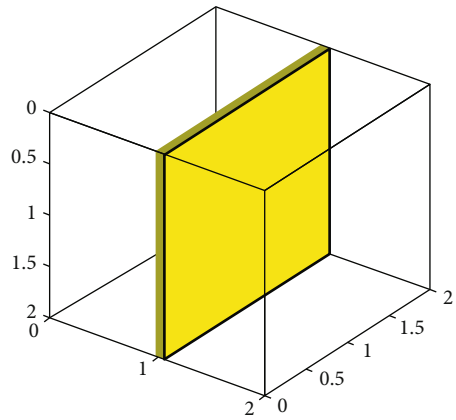

(a) Connection between the matrix grid and fracture segment

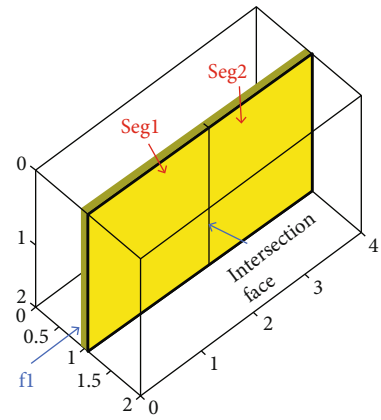

(b) Connection between fracture segments within the same fracture

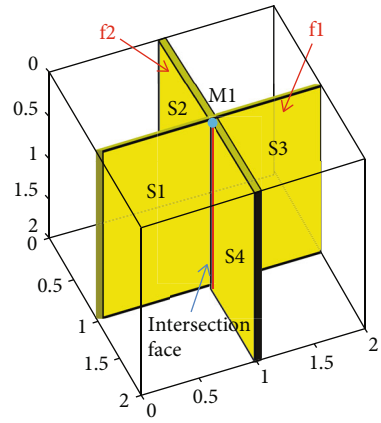

(c) Connection between different fractures

FIGURE 1: Three kinds of connections between the fracture and matrix.

plane area of two fracture segments. d_{seg1} denotes the distance from the center of fracture segment 1 to the common plane. d_{seg2} denotes the distance from the center of fracture segment 2 to the common plane.

2.1.3. Transmissibility of Connection between Different Fractures. Figure 1(c) shows the intersection between two different fractures. The transmissibility between them can be calculated by [62]

$$T_{\text{int}} = \frac{T_1 T_2}{T_1 + T_2}, \tag{5}$$

$$T_1 = \frac{k_{f1} w_{f1} L_{\text{int}}}{d_{f1}}, T_2 = \frac{k_{f2} w_{f2} L_{\text{int}}}{d_{f2}}, \tag{6}$$

where L_{int} is the length of the intersection line. k_{f1} and k_{f2} represent the permeability of fracture 1 and fracture 2, respectively. d_{f1} and d_{f2} denote the weighted average distance from the intersection line to the fracture 1 and fracture 2, respectively. w_{f1} and w_{f2} are the fracture aperture of fracture 1 and fracture 2, respectively.

2.2. Well Index. The well index in EDFM can be calculated through the effective well index of the fracture segment intersecting with the horizontal wellbore, as shown in [62]

$$WI_f = \frac{2\pi k_f w_f}{\ln\left(r_e / r_w\right)}, \tag{7}$$

$$r_e = 0.14\sqrt{L^2 + W^2}, \tag{8}$$

where k_f and w_f are the permeability and aperture of the fracture. r_e and r_w represent the supply radius and well radius. L means the fracture length, and W is the fracture height.

After the calculation of transmissibility of different NNCs and the well index, the EDFM model can be coupled with commercial reservoir simulators for numerical simulation efficiently [64].

3. Well Interference Modelling

3.1. Model Design. Based on the well distribution and fracture features in shale gas reservoirs, six physical models are designed to analyze the effect of well interference on production performance. The distribution of horizontal well, hydraulic fractures, and natural fractures of two MFHWs are presented in Figure 2.

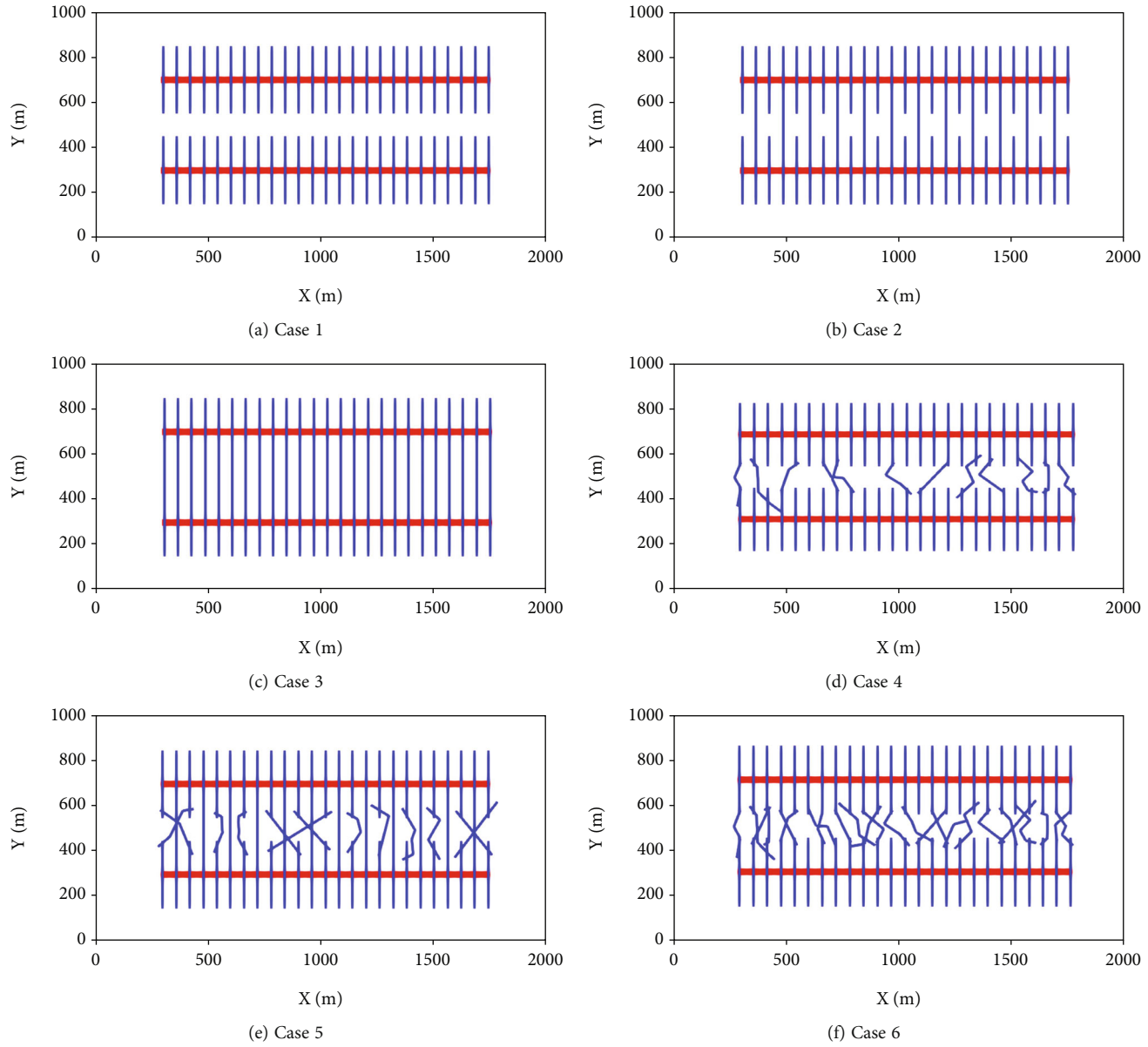

Figure 2: Distribution of horizontal wells and hydraulic fractures as well as natural fractures. (a) Two horizontal wells are not directly connected. (b) Two horizontal wells are connected through partial hydraulic fractures. (c) Two horizontal wells are connected through all hydraulic fractures. (d) Two horizontal wells are connected through partial natural fractures. (e) Two horizontal wells are connected through both hydraulic fractures and natural fractures. (f) Two horizontal wells are connected through numerous natural fractures.

Case 1. Two horizontal wells are not directly connected (see Figure 2(a)). Pressure interference is dominated through matrix.

Case 2. Two horizontal wells are connected through 50% hydraulic fractures (see Figure 2(b)). And well interference is composed of fracturing interference and pressure interference through hydraulic fractures and matrix.

Case 3. Two horizontal wells are connected through all hydraulic fractures (see Figure 2(c)). And well interference is composed of fracturing interference and pressure interference through all hydraulic fractures and matrix.

Case 4. Two horizontal wells are connected through partial natural fractures (see Figure 2(d)). And well interference is composed of fracturing interference and pressure interference through natural fractures and matrix.

Case 5. Two horizontal wells are connected through both hydraulic fractures and natural fractures (see Figure 2(e)). Well interference is caused by fracturing interference and pressure interference through hydraulic, natural fractures, and matrix.

Case 6. Two horizontal wells are connected through lots of natural fractures (see Figure 2(f)). The well interference is

Table 1: Basic parameters of formation, horizontal wells, and fractures.

Parameters	Value	Parameters	Value
Formation permeability	0.0001 mD	Well length	1460 m
Porosity	0.06	Number of hydraulic fractures	50
Formation height	35 m	Hydraulic fracture conductivity	20 mD m
Compressibility coefficient	$1.0e-7$ 1/kPa	Natural fracture conductivity	2 mD m
Initial pressure	60000 kPa	Well radius	0.1 m

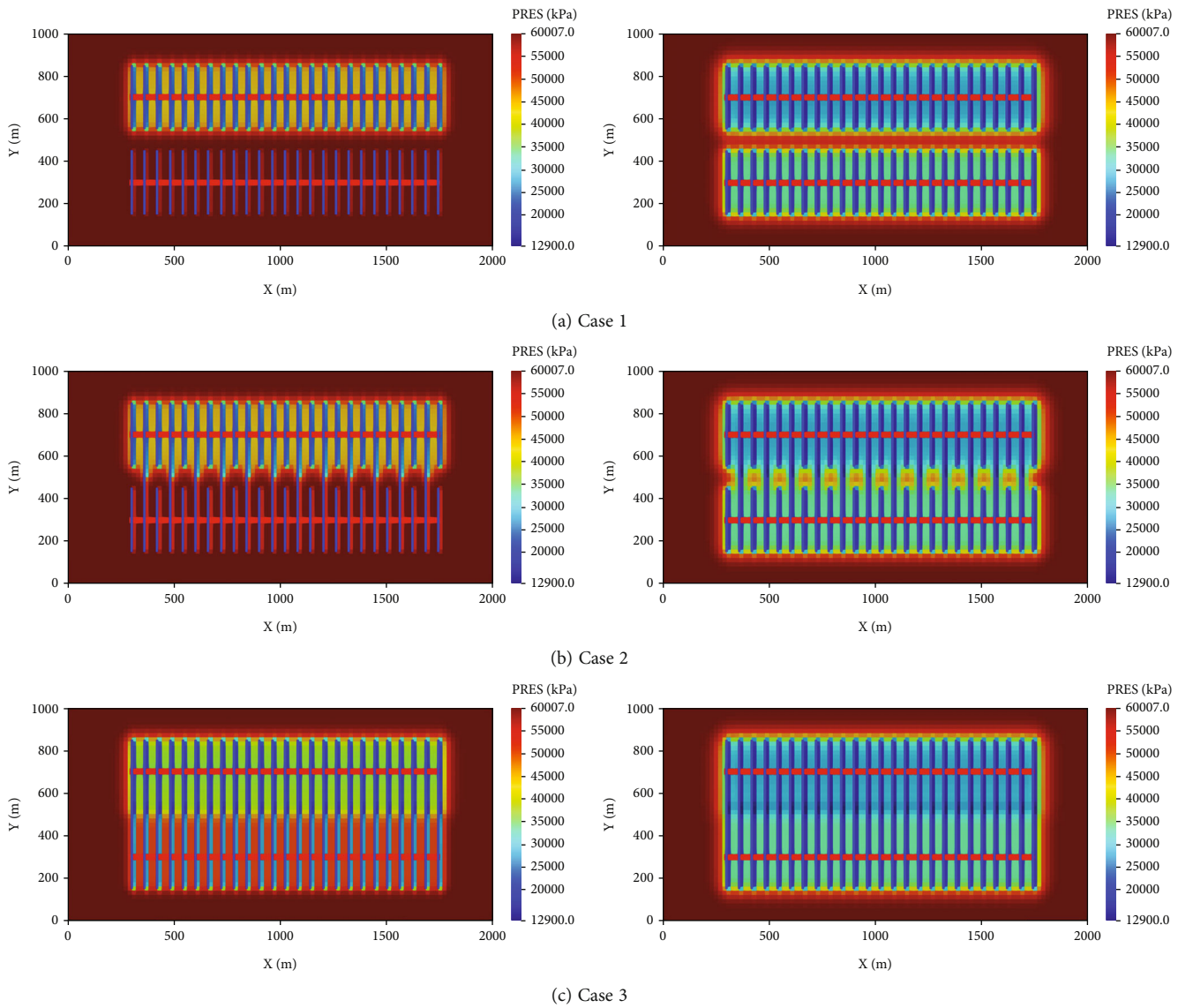

(a) Case 1

(b) Case 2

(c) Case 3

Figure 3: Pressure distribution of two MFHWs considering only hydraulic fractures in different time steps. (a) Two horizontal wells are not directly connected. (b) Two horizontal wells are connected through partial hydraulic fractures. (c) Two horizontal wells are connected through all hydraulic fractures.

caused by fracturing interference and pressure interference through lots of natural fractures and matrix.

The basic parameters of shale gas reservoirs, horizontal wells, and fractures can be seen in Table 1.

3.2. Pressure Distribution. To consider the effect of fracturing fluid on gas production, fluids are injected into the parent well from Jan 2, 2020 to Jan 20, 2020, and the well was further shut in for 11 days. From Feb 1, 2020, the parent well was put into production. The designed gas production is 250000 m^3/d and the minimum bottom-hole pressure (BHP) is set as 5 MPa. After about two years, the child well was fractured beginning from Jan 1, 2022 to Jan 20, 2022. The child well began to produce gas and water from Feb 1,

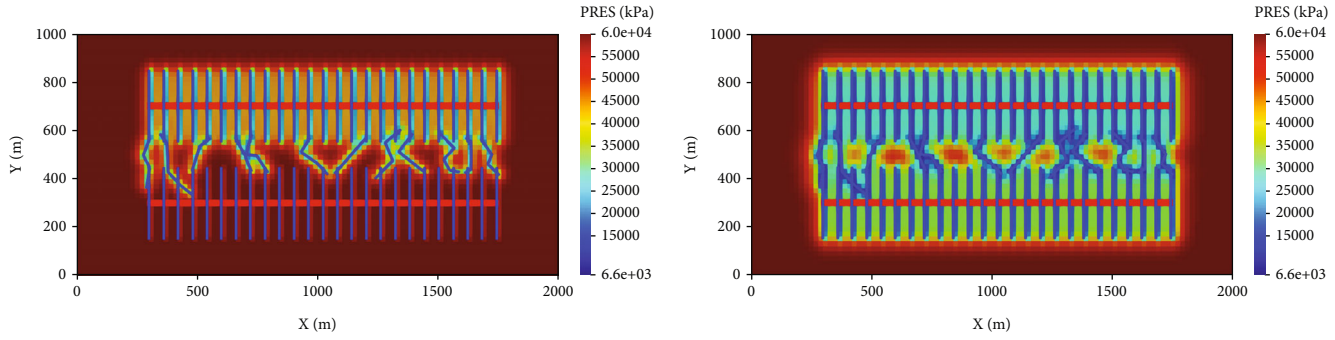

(a) Case 4

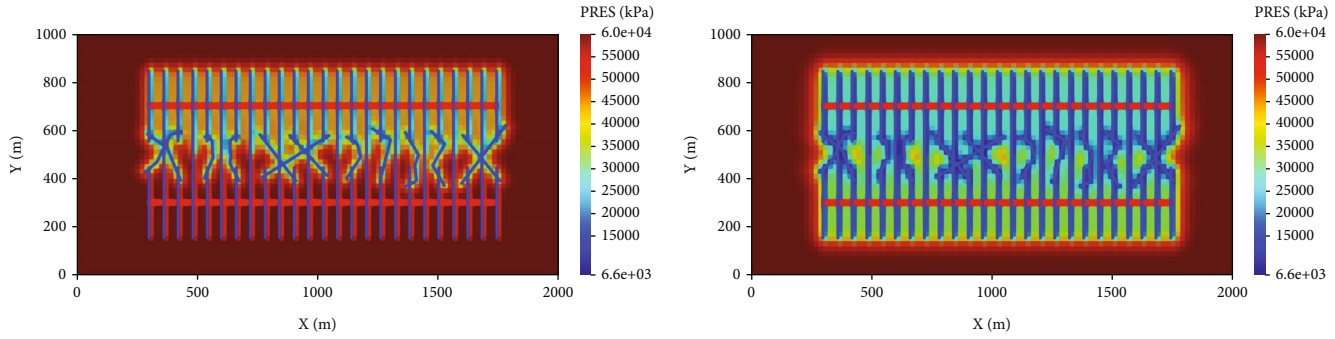

(b) Case 5

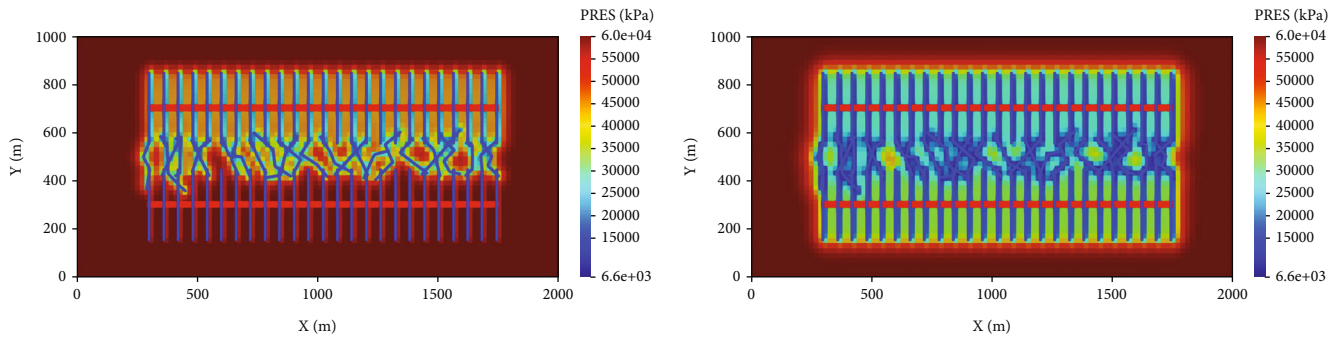

(c) Case 6

Figure 4: Pressure distribution of two MFHWs considering both hydraulic fractures and natural fractures. (a) Two horizontal wells are connected through partial natural fractures. (b) Two horizontal wells are connected through both hydraulic fractures and natural fractures. (c) Two horizontal wells are connected through numerous natural fractures.

2022. For the child well, the gas production is also set as 250000 m^3/d and the minimum bottom-hole pressure (BHP) is 5 MPa.

To compare the well interference of different cases, the pressure distribution in different time steps (Mar 2022 and Dec 2025) of two MFHWs considering only hydraulic fractures (Cases 1 to 3) are obtained as shown in Figure 3. In the early period, the difference of pressure distribution between Case 1 and Case 2 is not obvious as shown in Figures 3(a) and 3(b). However, the difference gradually becomes bigger since the well interference becomes stronger when two horizontal wells are connected with partial hydraulic fractures. If the two wells are totally connected through all hydraulic fractures (see Figure 3(c)), the well interference is obvious and the impact of well interference on the pressure distribution is significant. The pressure depletion is obvious when the well communication degree becomes higher, which can provide guidance for well spacing optimization.

Except for the effect of hydraulic fractures on well interference and pressure distribution, the impact of natural fractures also needs to be investigated. The pressure distribution of two MFHWs considering hydraulic fractures and natural fractures under three kinds of well connection conditions are shown in Figure 4. Firstly, the pressure distribution of Case 4 (see Figure 4(a)) is quite different with Case 1 (see Figures 3 (a)). It indicates that well interference is obvious when two horizontal wells are directly connected through hydraulic fractures or natural fractures. In addition, the impact of natural fractures on pressure distribution is relatively weaker than hydraulic fractures especially for the late period (see Figures 4(b) and 4(c)). However, it is hard to quantitatively evaluate the well interference and its impact on gas production only based on the pressure distribution.

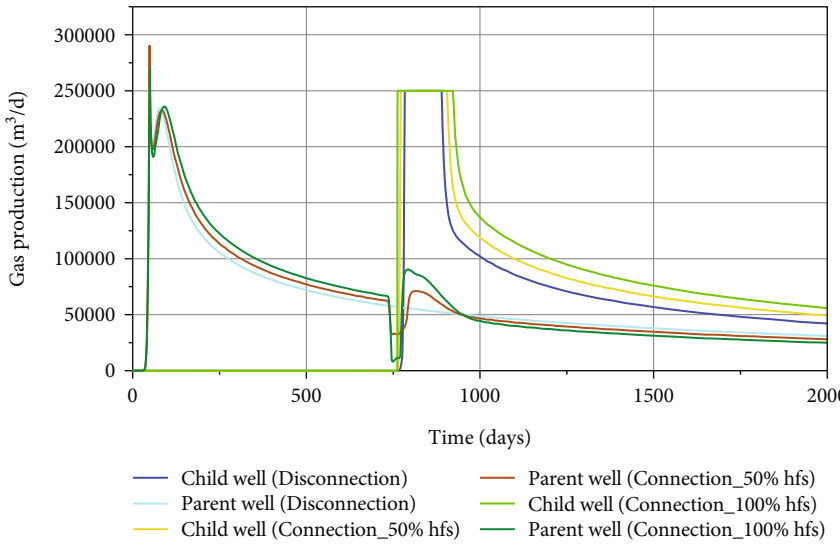

FIGURE 5: Production curves of two MFHWs considering only hydraulic fractures.

4. Well Interference Analysis

Type cures are developed to further quantitatively analyze the well interference, including the log-log type curve and Blasingame type curve. The feature on log-log type curve and Blasingame type curve under different well connections are identified to evaluate well interference.

4.1. Log-Log Type Curve. The log-log type curve is composed of the rate normalized pressure integral and rate normalized pressure integral derivative. The rate normalized pressure integral can be defined as

$$P_{\mathrm{rni}} = \frac{1}{t_e}\int_0^{t_e} \frac{p_i - p_{wf}(\tau)}{q(\tau)}\,d\tau. \tag{9}$$

On the basis of Equation (9), the rate normalized pressure integral derivative can be obtained shown as Equation (10).

$$P_{\mathrm{rniD}} = \frac{\partial}{\partial \ln t_e}\left[\frac{1}{t_e}\int_0^{t_e} \frac{p_i - p_{wf}(\tau)}{q(\tau)}\,d\tau\right], \tag{10}$$

where p_{rni} and p_{rniD} represent the rate normalized pressure integral and its derivative, respectively. P_i is the initial formation pressure. P_{wf} is the bottom-hole pressure. q is the gas production. t_e is the equivalent time, and $t_e = Q(t)/(2q(t))$.

4.2. Blasingame Type Curve. The Blasingame type curves are proposed to handle the production data under changeable pressure and production rate [65]. It is composed of pressure normalized rate, pressure normalized rate integral, and pressure normalized rate integral derivative curves.

The pressure normalized rate is defined as

$$R_{\mathrm{pn}} = \frac{q(\tau)}{p_i - p_{wf}(\tau)}. \tag{11}$$

The pressure normalized rate integral can be calculated

$$R_{\mathrm{pni}} = \frac{1}{t_e}\int_0^{t_e} \frac{q(\tau)}{p_i - p_{wf}(\tau)}\,d\tau. \tag{12}$$

Based on Equation (12), the pressure normalized rate integral be expressed as

$$R_{\mathrm{pniD}} = \frac{\partial}{\partial \ln t_c}\left[\frac{1}{t_c}\int_0^{t_c} \frac{q(\tau)}{p_i - p_{wf}(\tau)}\,d\tau\right], \tag{13}$$

where R_{pn}, R_{pni}, and R_{pniD} represent the pressure normalized rate, pressure normalized rate integral, and its derivative, respectively. P_i is the initial formation pressure. t_c means the material balanced time, and $t_c = Q(t)/q(t)$.

4.3. Well Interference Type Curve. To compare the impact of hydraulic fractures and natural fractures, we separate the six cases into two groups. The first group consists of Cases 1, 2, and 3. The second group is composed of Case 1, 4, 5, and 6.

Firstly, the production data needs to be analyzed and compared. The production curves of two MFHWs considering only hydraulic fractures under three kinds of well connection conditions (Cases 1 to 3) are shown in Figure 5. After the wells are connected through hydraulic fractures, the gas production of the parent well decreases rapidly and the water production increases quickly. Bigger decline of gas production for the parent well can be identified with the increase of well communication degree (e.g., from Case 2 to Case 3). Although it begins to recover in the later stage, it is still lower than that of parent wells with lower well communication degree. However, the gas production of child well shows the opposite characteristics. Higher communication degree between wells through hydraulic fractures results in the stimulation area or degree for the child well so that the gas production is slightly higher than that with lower communication degree or even disconnection. It indicates that

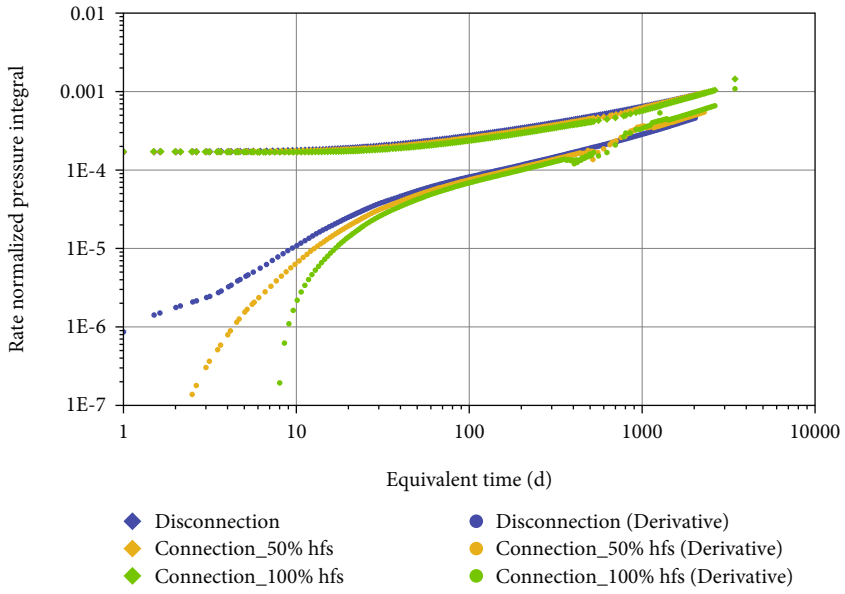

Figure 6: Log-log type curves of different well connection conditions considering only hydraulic fractures.

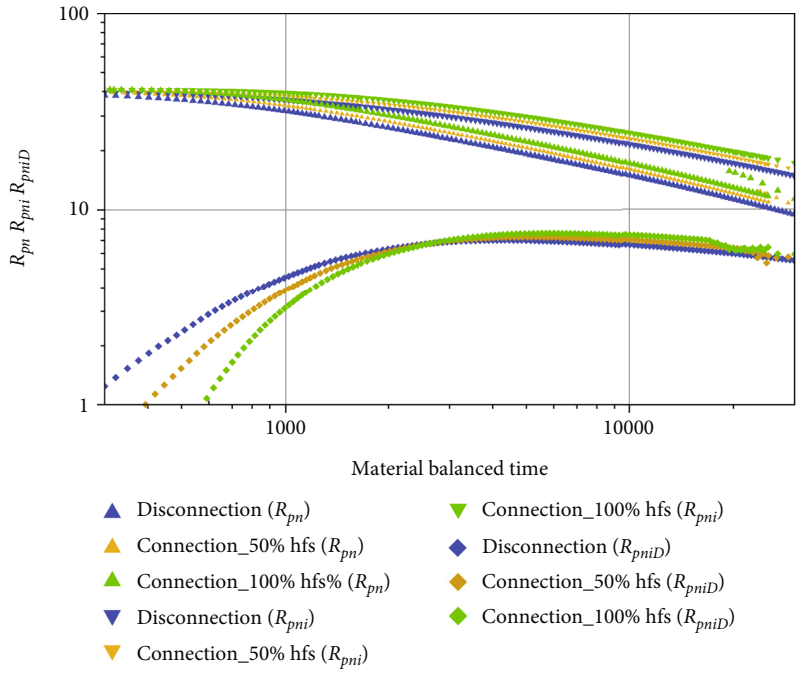

Figure 7: Blasingame type curves of different well connection conditions considering only hydraulic fractures.

well interference caused by hydraulic fractures mainly reduce the gas production of the parent well while the gas production of child well can be increased owing to the larger equivalent stimulation area and degree.

Then, the production and pressure data can be processed by using the Equations (9) and (10). The log-log type curves are generated for the MFHWs considering only hydraulic fractures under three different well connection conditions (Cases 1 to 3), shown in Figure 6. Obvious differences can be found from early to late periods in the log-log type curves when two horizontal wells are connected with hydraulic fractures (Cases 2 and 3) or two wells are not directly connected with hydraulic factures (Case 1). Especially, the distinctions during early period are more obvious. The rate normalized pressure integral derivative drops a lot with the increase of well connectivity, while it becomes larger under late period with the increase of well connectivity. Therefore, well interference can be identified using the log-log type curves.

Furthermore, the Blasingame type curves can also be obtained using the Equations (11) and (13) based on the production and pressure data. Figure 7 shows the Blasingame type

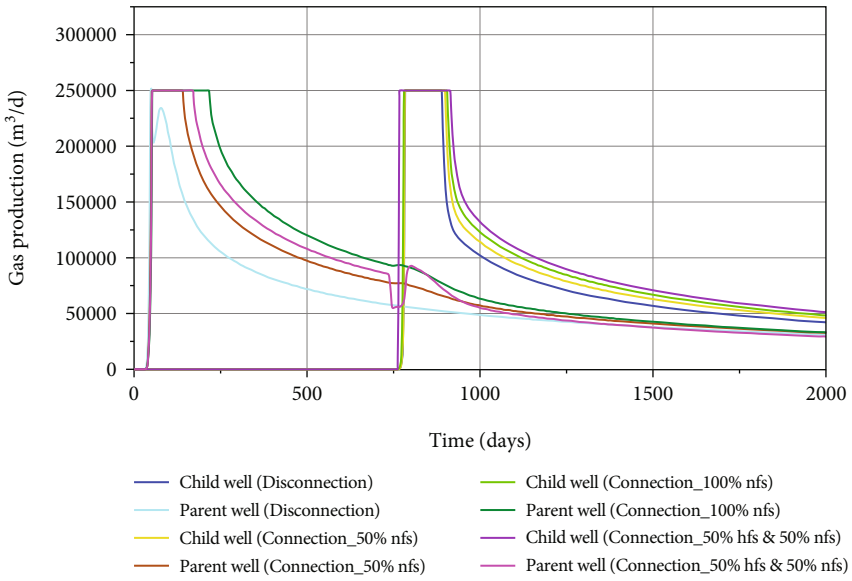

Figure 8: Production curves of two MFHWs considering both hydraulic fractures and natural fractures.

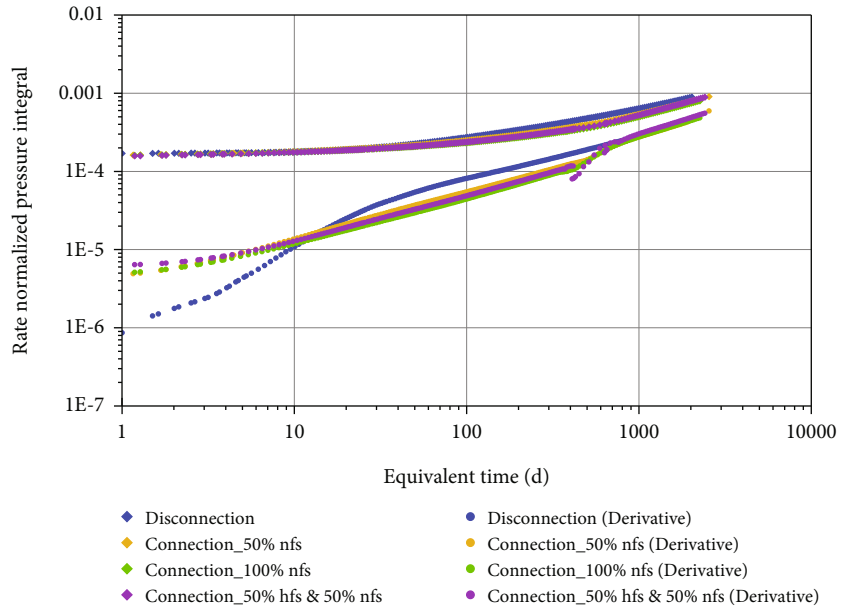

Figure 9: Log-log type curves of different well connection conditions considering both hydraulic fractures and natural fractures.

curves for the MFHWs considering only hydraulic fractures under three different well connection conditions (Cases 1 to 3). Distinctions can be observed on the type curves among different well connection conditions by the combination of pressure normalized rate, pressure normalized rate integral, and pressure normalized rate integral derivative, especially during early and late periods. When two wells are communicated directly through hydraulic fractures, the pressure normalized rate integral derivative drops a lot during the early stage with the increase of well connectivity, while it moves up under late period with the increase of well connectivity. The differences during the late period on the Blasingame type curves among three cases are bigger than that on the log-log type curves, while the features during early period on the log-log type curves are clearer. Thus, the well interference of shale gas reservoirs can be identified by the combination of the log-log and Blasingame type curves.

In this part, the impact of natural fractures on the production data and type curves will be analyzed. The production curves of two MFHWs considering both hydraulic fractures and natural fractures under three kinds of well connection conditions (Cases 4 to 6) are shown in Figure 8. Case 1 was included in this part to show the comparison. Compared to Case 1, more fractures are added in to Cases 4 to 6 so that the gas production is improved owing to bigger simulated area. When the fracturing interference

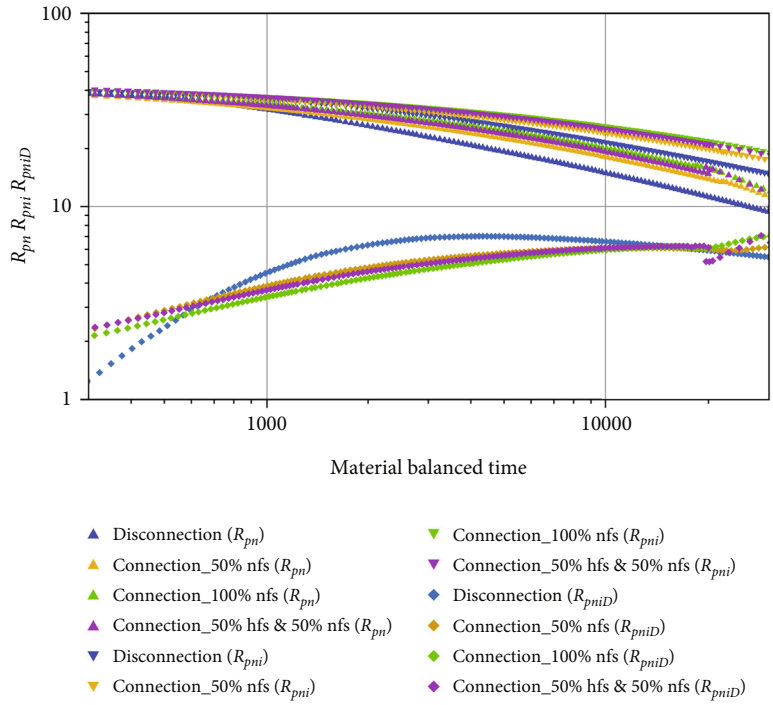

Figure 10: Blasingame type curves of different well connection conditions considering both hydraulic fractures and natural fractures.

occurs, the gas production of the parent well decreases due to the impact of fracturing fluids from the child well. Different from Figure 5, the decline degree of gas production is minor when child well is connecting parent well only through natural fractures (Cases 4 and 6). But, if two wells are communicated with natural and hydraulic fractures, the gas production of the parent well decline a lot (Case 5). We can conclude that well interference caused by natural fractures is much weaker compared to hydraulic fractures.

To identify the impact of well interference caused by natural fractures, log-log type curves are generated as shown in Figure 9. On the one hand, differences can be observed between Case 1 and Cases 4 to 6, especially on the rate normalized pressure integral derivative curves. On the other hand, the distinctions are minor if the parent well and child well are communicated with only natural fractures (Cases 4 and 6). Additionally, the impact of fracturing interference caused by hydraulic fractures or numerous natural fractures can be identified using the rate normalized pressure integral derivative curve (Case 5 and 6).

The feature of fracturing interference is not obvious enough on the log-log type curves so that the Blasingame type curves are developed based on the production and pressure data of Cases 1, 4, 5, and 6 (see Figure 10). It is obvious that major differences during early, middle, and late periods can be found on the Blasingame type curves under different well communication degrees. And the signal of fracturing interference caused by the natural fractures is more obvious.

5. Conclusions

This paper focuses on the well interference analysis of shale gas wells. EDFM technology is introduced to deal with the hydraulic fractures and natural fractures as well as model the well interference caused by hydraulic and natural fractures.

(1) After the wells are communicated through hydraulic fractures, the gas production of the parent well declines a lot due to the fracturing fluids from the child well. However, if two wells are connected only through natural fractures, the decline degree of gas production is much minor. Well interference caused by natural fractures is much weaker compared to hydraulic fractures

(2) For wells connected through hydraulic fractures, the differences during the late period on the Blasingame type curves are clearer than that on the log-log type curves, while the features during early period on the log-log type curves are easier to distinguish

(3) For wells connected through only natural fractures, the distinctions are minor if the parent well and child well are communicated with only natural fractures, the signal of fracturing interference caused by the natural fractures are more obvious on the Blasingame type curves

Thus, the well interference of shale gas reservoirs can be identified by the combination of log-log and Blasingame type curves. This work can be helpful for understanding the well interference feature and its impact on shale gas production.

Data Availability

The data used to support the findings of this study are included in the article.

Conflicts of Interest

The author declares that there is no conflict of interest regarding the publication of this paper.

Acknowledgments

This work was financially supported by the Chuanqing scientific project (CQXN-2020-09).

References

[1] F. Javadpour, D. Fisher, and M. Unsworth, "Nanoscale gas flow in shale gas sediments," *Journal of Canadian Petroleum Technology*, vol. 46, no. 10, 2007.

[2] D. J. Ross and R. M. Bustin, "The importance of shale composition and pore structure upon gas storage potential of shale gas reservoirs," *Marine and Petroleum Geology*, vol. 26, no. 6, pp. 916–927, 2009.

[3] K. Liu, L. Wang, M. Ostadhassan, J. Zou, B. Bubach, and R. Rezaee, "Nanopore structure comparison between shale oil and shale gas: examples from the Bakken and Longmaxi Formations," *Petroleum Science*, vol. 16, no. 1, pp. 77–93, 2019.

[4] X. Zhao, L. Zhou, and X. Pu, "Formation conditions and enrichment model of retained petroleum in lacustrine shale: a case study of the Paleogene in Huanghua depression, Bohai Bay Basin, China," *Petroleum Exploration and Development*, vol. 47, no. 5, pp. 916–930, 2020.

[5] L. Huang, W. Zhou, H. Xu, L. Wang, J. Zou, and Q. Zhou, "Dynamic fluid states in organic-inorganic nanocomposite: implications for shale gas recovery and CO_2 sequestration," *Chemical Engineering Journal*, vol. 411, p. 128423, 2021.

[6] J. Liu, L. Xie, B. He, P. Zhao, and H. Y. Ding, "Performance of free gases during the recovery enhancement of shale gas by CO2 injection: a case study on the depleted Wufeng–Longmaxi shale in northeastern Sichuan Basin, China," *Petroleum Science*, vol. 18, no. 2, pp. 530–545, 2021.

[7] D. Rahm, "Regulating hydraulic fracturing in shale gas plays: the case of Texas," *Energy Policy*, vol. 39, no. 5, pp. 2974–2981, 2011.

[8] M. B. Seales, T. Ertekin, and J. Yilin Wang, "Recovery efficiency in hydraulically fractured shale gas reservoirs," *Journal of Energy Resources Technology*, vol. 139, no. 4, article 042901, 2017.

[9] J. Xie, J. Tang, R. Yong et al., "A 3-D hydraulic fracture propagation model applied for shale gas reservoirs with multiple bedding planes," *Engineering Fracture Mechanics*, vol. 228, p. 106872, 2020.

[10] Y. He, J. Qin, S. Cheng, and J. Chen, "Estimation of fracture production and water breakthrough locations of multi- stage fractured horizontal wells combining pressure-transient analysis and electrical resistance tomography," *Journal of Petroleum Science and Engineering*, vol. 194, p. 107479, 2020.

[11] C. Ou, C. Liang, Z. Li, L. Luo, and X. Yang, "3D Visualization of Hydraulic Fractures Using Micro-Seismic Monitoring: Methodology and Application," *Petroleum*, vol. 8, no. 1, pp. 92–101, 2022.

[12] J. Zhao, L. Ren, and T. Jiang, "Ten years of gas shale fracturing in China: review and prospect," *Natural Gas Industry*, vol. 41, no. 8, pp. 121–142, 2021.

[13] S. Mao, Z. Zhang, T. Chun, and K. Wu, "Field-scale numerical investigation of proppant transport among multi-cluster hydraulic fractures," *SPE Journal*, vol. 26, no. 1, pp. 307–323, 2021.

[14] Y. Duan, H. Wang, M. Wei, L. Tan, and T. Yue, "Application of ARIMA-RTS Optimal Smoothing Algorithm in Gas Well Production Prediction," *Petroleum*, 2021.

[15] A. Ajani and M. Kelkar, "Interference study in shale plays," in *SPE Hydraulic Fracturing Technology Conference*, The Woodlands, Texas, USA, February 2012.

[16] A. Morales, K. Zhang, K. Gakhar et al., "Advanced modeling of interwell fracturing interference: an Eagle Ford shale oil study-refracturing," in *SPE Hydraulic Fracturing Technology Conference*, The Woodlands, Texas, USA, February 2016.

[17] B. Lin, H. Meng, J. Pan, and S. Chen, "Porothermoelastic response of an oil sand formation subjected to injection and micro-fracturing in horizontal wells," *Petroleum Science*, vol. 17, no. 3, pp. 687–700, 2020.

[18] H. Lawal, G. Jackson, N. Abolo, and C. Flores, "A novel approach to modeling and forecasting frac hits in shale gas wells," in *EAGE Annual Conference and Exhibition incorporating SPE Europec*, London, UK, June 2013.

[19] P. Moradi and D. Angus, "Modeling frac-hits using dynamic microseismicity-constrained enhanced fracture regions," in *SPE/AAPG/SEG Unconventional Resources Technology Conference*, Denver, Colorado, USA, July 2019.

[20] X. Guo, K. Wu, C. An, J. Tang, and J. Killough, "Numerical investigation of effects of subsequent parent well injection on interwell fracturing interference using reservoir-geomechanics-fracturing modeling," *SPE Journal*, vol. 24, no. 4, pp. 1884–1902, 2019.

[21] S. D. Mohaghegh, "Frac-hit dynamic modeling using artificial intelligence and machine learning," in *SPE/AAPG/SEG Unconventional Resources Technology Conference, Virtual*, July 2020.

[22] A. Khodabakhshnejad, "Impact of frac hits on production performance- a case study in Marcellus Shale," in *SPE Western Regional Meeting*, San Jose, California, USA, April 2019.

[23] R. Esquivel and T. A. Blasingame, "Optimizing the development of the Haynesville shale - lessons learned from well-to-well hydraulic fracture interference," in *SPE/AAPG/SEG Unconventional Resources Technology Conference*, Austin, Texas, USA, July 2017.

[24] X. Guo, K. Wu, J. Killough, and J. Tang, "Understanding the mechanism of interwell fracturing interference with reservoir/geomechanics/fracturing modeling in Eagle Ford Shale," *SPE Reservoir Evaluation and Engineering*, vol. 22, no. 3, pp. 842–860, 2019.

[25] Y. He, J. Guo, Y. Tang et al., "Interwell fracturing interference evaluation of multi-well pads in shale gas reservoirs: a case study in WY Basin," in *SPE annual Technical Conference and Exhibition, Virtual*, October 2020.

[26] C. Sardinha, C. Petr, J. Lehmann, and J. Pyecroft, "Determining interwell connectivity and reservoir complexity through frac pressure hits and production interference analysis," in *SPE/CSUR Unconventional Resources Conference–Canada*, Calgary, Alberta, Canada, September 2014.

[27] I. Gupta, C. Rai, D. Devegowda, and C. Sondergeld, "Haynesville shale: predicting long-term production and residual analysis to identify well intereference and frac hits," in *SPE Oklahoma City Oil and Gas Symposium*, Oklahoma City, Oklahoma, USA, April 2019.

[28] O. M. Molina, "Analytical model to estimate the fraction of frac hits in multi-well pads," in *SPE/AAPG/SEG Unconventional Resources Technology Conference*, Denver, Colorado, USA, July 2019.

[29] A. Kumar, P. Seth, K. Shrivastava, R. Manchanda, and M. M. Sharma, "Integrated analysis of tracer and pressure-interference tests to identify well interference," *SPE Journal*, vol. 25, no. 4, pp. 1623–1635, 2020.

[30] A. Khodabakhshnejad, Y. Aimene, N. Mistry, A. Bachir, and A. Ouenes, "A fast method to forecast shale pressure depletion and well performance using geomechanical constraints - application to poro-elasticity modeling to predict mid and far field frac hits at an Eagle Ford and Wolfcamp Well," in *SPE Eastern Regional Meeting*, Lexington, Kentucky, USA, October 2017.

[31] S. Pathak, R. Tibbles, A. Bohra, S. Tiwari, P. Godiyal, and A. Deo, "Evaluation of frac hit risks in Aishwarya Barmer-Hill field development utilising GIS platform," in *SPE Asia Pacific oil and gas conference and exhibition*, Brisbane, Australia, October 2018.

[32] R. D. Magneres, M. Castello, F. Bertoldi, and M. Griffin, "Vaca Muerta frac-hit occurrence and magnitude forecast methodology," in *SPE/AAPG/SEG Latin America Unconventional Resources Technology Conference, Virtual*, November 2020.

[33] R. Cao, R. Li, A. Girardi, N. Chowdhury, and C. Chen, "Well interference and optimum well spacing for Wolfcamp development at Permian Basin," in *SPE/AAPG/SEG Unconventional Resources Technology Conference*, Austin, Texas, USA, July 2017.

[34] Y. Zhao, N. Li, J. Yang, and S. Cheng, "Optimization of deep shale gas well spacing based on geology-engineering integration: a case study of Weirong shale gas field," *Petroleum Reservoir Evaluation and Development*, vol. 11, no. 3, pp. 340–347, 2021.

[35] R. Manchanda, J. Hwang, P. Bhardwaj, M. M. Sharma, M. Maguire, and J. Greenwald, "Strategies for improving the performance of child wells in the permian basin," in *SPE/AAPG/SEG unconventional resources technology conference*, Houston, Texas, USA, July 2018.

[36] A. Rangriz Shokri, R. J. Chalaturnyk, and D. Bearinger, "Deployment of pressure hit catalogues to optimize multi-stage hydraulic stimulation treatments and future re-fracturing designs of horizontal Wells in Horn River Shale Basin," in *SPE annual Technical Conference and Exhibition*, Calgary, Alberta, Canada, September 2019.

[37] K. Vidma, P. Abivin, D. Fox et al., "Fracture geometry control technology prevents well interference in the Bakken," in *SPE Hydraulic Fracturing Technology Conference and Exhibition*, The Woodlands, Texas, USA, February 2019.

[38] M. Paryani, R. Smaoui, S. Poludasu et al., "Adaptive fracturing to avoid frac hits and interference: a Wolfcamp shale case study," in *SPE Unconventional Resources Conference*, Calgary, Alberta, Canada, February 2017.

[39] S. Zheng, R. Manchanda, D. Gala, and M. Sharma, "Pre-loading depleted parent wells to avoid frac-hits: some important design considerations," in *SPE Annual Technical Conference and Exhibition*, Calgary, Alberta, Canada, September 2019.

[40] D. P. Gala, R. Manchanda, and M. M. Sharma, "Modeling of fluid injection in depleted parent wells to minimize damage due to frac-hits," in *SPE/AAPG/SEG Unconventional Resources Technology Conference*, Houston, Texas, USA, July 2018.

[41] T. Whitfield, M. H. Watkins, and L. J. Dickinson, "Pre-loads: successful mitigation of damaging frac hits in the Eagle Ford," in *SPE Annual Technical Conference and Exhibition*, Dallas, Texas, USA, September 2018.

[42] G. E. King, M. F. Rainbolt, and C. Swanson, "Frac hit induced production losses: evaluating root causes, damage location, possible prevention methods and success of remedial treatments," in *SPE Annual Technical Conference and Exhibition*, San Antonio, Texas, USA, October 2017.

[43] C. Swanson, W. A. Hill, G. Nilson et al., "Post-frac-hit mitigation and well remediation of Woodford horizontal wells with solvent/surfactant chemistry blend," in *SPE/AAPG/SEG Unconventional Resources Technology Conference*, Houston, Texas, USA, July 2018.

[44] M. F. Rainbolt and J. Esco, "Frac hit induced production losses: evaluating root causes, damage location, possible prevention methods and success of remediation treatments, part II," in *SPE Hydraulic Fracturing Technology Conference and Exhibition*, The Woodlands, Texas, USA, January 2018.

[45] P. A. Bommer and M. A. Bayne, "Active well defense in the Bakken: case study of a ten-well frac defense project, Mckenzie county, ND," in *SPE hydraulic fracturing technology conference and exhibition*, The Woodlands, Texas, USA, January 2018.

[46] D. C. Johnson, B. B. Yeager, C. D. Roberts, and B. W. Fowler, "Offset fracture events made simple: an operator's collaborative approach to observe parent child interactions, measure frac hit severity and test mitigation strategies," in *SPE Hydraulic Fracturing Technology Conference and Exhibition*, The Woodlands, Texas, USA, February 2020.

[47] C. L. Cipolla, E. Lolon, J. Erdle, and V. S. Tathed, "Modeling well performance in shale-gas reservoirs," *SPE/EAGE Reservoir Characterization and Simulation Conference*, 2009, Abu Dhabi, UAE, October 2009, 2009.

[48] A. Mhiri, T. A. Blasingame, and G. J. Moridis, "Stochastic modeling of a fracture network in a hydraulically fractured shale-gas reservoir," in *SPE Annual Technical Conference and Exhibition*, Houston, Texas, USA, September 2015.

[49] Y. Wu, L. Cheng, J. Killough et al., "Integrated characterization of the fracture network in fractured shale gas reservoirs–stochastic fracture modeling, simulation and assisted history matching," *Journal of Petroleum Science and Engineering*, vol. 205, article 108886, 2021.

[50] Y. Xu and K. Sepehrnoori, "Development of an embedded discrete fracture model for field-scale reservoir simulation with complex corner-point grids," *SPE Journal*, vol. 24, no. 4, pp. 1552–1575, 2019.

[51] M. X. Fiallos, W. Yu, R. Ganjdanesh et al., "Modeling interwell interference due to complex fracture hits in eagle ford using EDFM," in *International Petroleum Technology Conference*, Beijing, China, March 2019.

[52] W. Yu, K. Wu, M. Liu, K. Sepehrnoori, and J. Miao, "Production forecasting for shale gas reservoirs with nanopores and complex fracture geometries using an innovative non-intrusive EDFM method," in *SPE Annual Technical Conference and Exhibition*, Dallas, Texas, USA, September 2018.

[53] Y. He, Y. Qiao, J. Qin, Y. Tang, Y. Wang, and Z. Chai, "A novel method to enhance oil recovery by inter-fracture injection and production through the same multi-fractured horizontal well," *Journal of Energy Resources Technology*, vol. 144, no. 4, article 043005, 2022.

[54] M. Onur, C. Ayan, and F. J. Kuchuk, "Pressure-pressure deconvolution analysis of multi-well interference and interval pressure transient tests," in *International Petroleum Technology Conference*, Doha, Qatar, December 2009.

[55] E. Yaich, O. C. Diaz De Souza, R. A. Foster, and I. Abou-Sayed, "A methodology to quantify the impact of well interference and optimize well spacing in the Marcellus Shale," in *SPE/CSUR Unconventional Resources Conference – Canada*, Calgary, Alberta, Canada, September 2014.

[56] C. Xiao, Y. Dai, L. Tian et al., "A semianalytical methodology for pressure-transient analysis of multiwell-pad-production scheme in shale gas reservoirs, part 1: new insights into flow regimes and multiwell interference," *SPE Journal*, vol. 23, no. 3, pp. 885–905, 2018.

[57] J. Qin, Y. Xu, Y. Tang et al., "Impact of complex fracture networks on rate transient behavior of wells in unconventional reservoirs based on embedded discrete fracture model," *Journal of Energy Resources Technology*, vol. 144, no. 8, article 083007, 2022.

[58] H. Chu, X. Liao, C. Wei, and J. Lee, "Rate/pressure transient analysis of a variable bottom hole pressure multi-well horizontal pad with well interference," in *SPE Annual Technical Conference and Exhibition*, Dubai, UAE, September 2021.

[59] Y. He, Y. Xu, Y. Tang, Y. Qiao, W. Yu, and K. Sepehrnoori, "Multi-phase rate transient behaviors of the multi-fractured horizontal well with complex fracture networks," *Journal of Energy Resources Technology*, vol. 144, no. 4, article 043006, 2022.

[60] Y. Xu, *Implementation and application of the embedded discrete fracture model (EDFM) for reservoir simulation in fractured reservoirs*, Doctoral dissertation. The University of Texas at Austin, Texas, USA, 2015.

[61] A. Yaghoubi, "Hydraulic fracturing modeling using a discrete fracture network in the Barnett Shale," *International Journal of Rock Mechanics and Mining Sciences*, vol. 119, pp. 98–108, 2019.

[62] Y. Xu, J. Cavalcante Filho, W. Yu, and K. Sepehrnoori, "Discrete-fracture modeling of complex hydraulic-fracture geometries in reservoir simulators," *SPE Reservoir Evaluation and Engineering*, vol. 20, no. 2, pp. 403–422, 2017.

[63] Z. Chai, H. Tang, Y. He, J. Killough, and Y. Wang, "Uncertainty quantification of the fracture network with a novel fractured reservoir forward model," in *SPE Annual Technical Conference and Exhibition*, Dallas, Texas, USA, September 2018.

[64] W. Yu, K. Wu, L. Zuo, J. Miao, and K. Sepehrnoori, "Embedded discrete fracture model assisted study of gas transport mechanisms and drainage area for fractured shale gas reservoirs," in *SPE/AAPG/SEG Unconventional Resources Technology Conference*, Denver, Colorado, USA, July 2019.

[65] T. A. Blasingame, T. L. McCray, and W. J. Lee, "Decline curve analysis for variable pressure drop/variable flowrate systems," in *SPE Gas Technology Symposium*, Houston, Texas, January 1991.